M.Sc. thesis report

Performance analysis of the Trilogy mission concept. Expected improvements in planetary ephemerides and asteroid mass estimations

Lluc R. Busquets i Soler

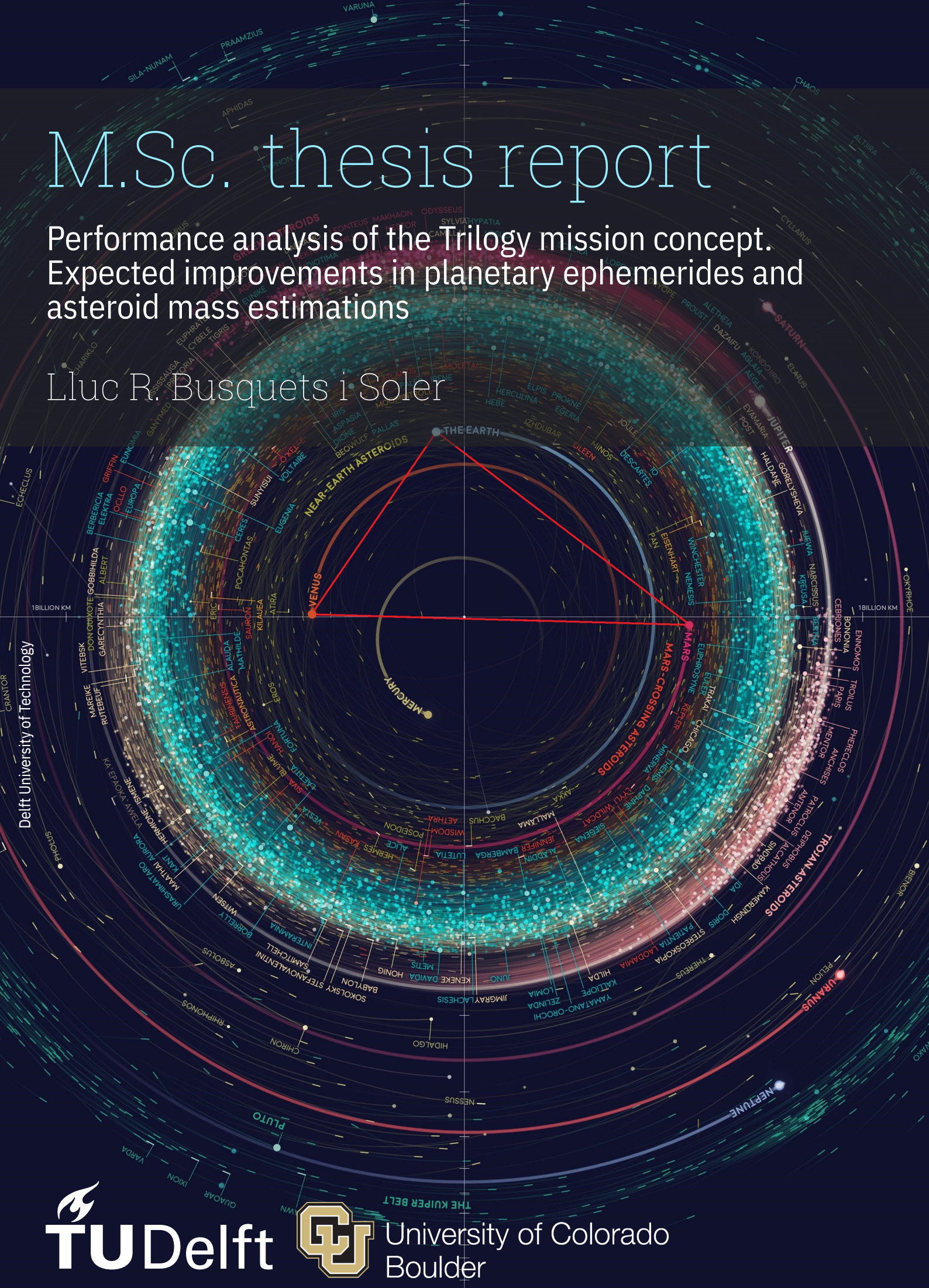

Delft University of Technology

TU Delft

University of Colorado Boulder

M.Sc. thesis report

Performance analysis of the Trilogy mission concept. Expected improvements in planetary ephemerides and asteroid mass estimations

by

Lluc R. Busquets i Soler

Student Number

5838231

Supervisor 1:	Dominic Dirkx
Supervisor 2:	Steve Nerem
Project Duration:	February - December 2024
Location:	Delft, Netherlands / Boulder, Colorado
Faculty:	Faculty of Aerospace Engineering, Delft / Ann and H.J. Smead Aerospace Engineering Sciences, Boulder
Report date:	Friday 27th December, 2024

Cover:	Visualization of the orbits of all planets and 18000 minor bodies in the Solar System (logarithmic scale). Authorship of original image: Eleanor Lutz. Trilogy links added by Lluc Busquets.
Style:	TU Delft Report Style, with modifications by Daan Zwaneveld and Lluc Busquets

TU Delft University of Colorado **Boulder**

Abstract

Our current knowledge of Solar System dynamics is limited by a combination of unknowns, including the masses of most asteroids and the mass loss rate and oblateness of the Sun. Highly precise Interplanetary Laser Ranging (ILR) measurements have been suggested to enable the reconstruction of subtle dynamical effects, allowing the determination of several of such unknowns. Following the mission proposal by the name of Trilogy, we simulate a triple ILR setup obtaining frequent range measurements between space-based transceivers orbiting the Earth, Mars and Venus. Simultaneous spacecraft orbit determination allows for the generation of highly accurate planet-to-planet ranges by adding constant range biases as parameters to estimate at every orbit determination arc. We find that such resulting ranges can reach millimetric precision and accuracy, assuming state-of-the-art ILR hardware, accurate spacecraft dynamical modeling and favorable geometry between the ILR links and the spacecraft orbital planes. The usage of such measurements alone in a planetary batch estimation after a five-year mission is found capable of estimating the radial positions of the three planets with millimetric true errors, whereas only a few tens among the 350 main perturbing asteroids are found to get their true and formal errors reduced by a significant amount (i.e., one order of magnitude). We make a series of recommendations for future studies, including the testing of alternative mission architectures (e.g., placing one vertex around a Main Belt asteroid instead of Venus to reach more sensitivity to the asteroid perturbations) or more complex orbit estimation methods (e.g., coupled, constrained multi-arc) to get the most information out of the inter-spacecraft laser range measurements.

Contents

List of Figures

List of Tables

Acronyms and symbols

ASTROD-GW Astrodynamical Space Test of Relativity using Optical Devices optimized for Gravitational Waves. 56
AU astronomical unit. 51

CCR corner cube reflector. 17

DE Developmental Ephemerides. vi, xii, xiii, 45, 46, 51, 62, 143–145
DECIGO DECi-hertz Interferometer Gravitational wave Observatory. 56
DR data release. 47
DSOC Deep Space Optical Communications. 24

EMB Earth-Moon Barycenter. xii, 62, 64, 66, 75, 78–80, 83, 129, 144, 145, 147–149, 152, 153
EP Equivalence Principle. 55
EPM Ephemerides of the Planets and the Moon. 45–48, 51
ESA the European Space Agency. 47
EVM Expected Value Method. 61

GNSS Global Navigation Satellite System. 11, 22, 79, 129
GOPEX Galileo Optical Experiment. 24, 25
GPS Global Positioning System. 34, 50
GR General Relativity. 3, 4, 32, 50–52, 54–56
GRACE Gravity Recovery and Climate Experiment. 25
GRACE-FO GRACE Follow-On. 25, 26
GTE Global Truncation Error. 133
GW gravitational wave. 10, 25, 26, 56, 57

IAA Institute for Applied Astronomy. 45
IAU International Astronomical Union. 68
ICRF International Celestial Reference Frame. 50
IERS International Earth Rotation Service. 23
ILR interplanetary laser ranging. x, xi, xxi, 3, 9–12, 15, 21–27, 34, 43, 64, 66, 67, 73, 76–81, 85–90, 92, 93, 127, 129
ILRS International Laser Ranging Service. 23
ILTN Interplanetary Laser Trilateration Network. 3, 10, 11, 50, 52
IMCEE Celestial Mechanics and Ephemerides Calculations Institute. 45
INPOP Planetary Numerical Integrator of the Paris Observatory. vi, xii, xiii, 45–49, 55, 56, 61–64, 143–146

JPL Jet Propulsion Laboratory. 45, 46, 61
JUICE Jupiter Icy Moons Explorer. 42, 46, 76, 95

KBO Kuiper Belt Object. 45, 47–49

LADEE Lunar Atmosphere and Dust Environment Explorer. 24
LIDAR light detection and ranging. 25
LIGO Laser Interferometer Gravitational-Wave Observatory. 56
LISA Laser Interferometry Space Antenna. 10, 12, 25, 26, 56, 57
LLR lunar laser ranging. 15, 17, 21, 24, 46, 52, 55, 78

LOLA Lunar Observer Laser Altimeter. 25
LPE Lagrange Planetary Equations. xii, 152, 153
LRI Laser Ranging Interferometer. 25, 26
LRO Lunar Reconaissance Orbiter. 25, 78
LT Lense-Thirring. 9, 32, 53, 54
LTT laser time transfer. 20, 24, 25

MAB Main Asteroid Belt. 67
MESSENGER Mercury Surface, Space Environment, Geochemistry and Ranging. 25, 42, 51, 54–56, 76
MGS Mars Global Surveyor. 25
MLA Mercury Laser Altimeter. 25
MOLA Mars Orbiter Laser Altimeter. 25
MRO Mars Reconaissance Orbiter. 45, 56

NAIF Navigation and Ancilliary Information Facility. 61
NASA National Aeronautics and Space Administration. 24, 25, 47, 61
NEA near-Earth asteroid. 66
NRLMSISE Naval Research Laboratory Mass Spectrometer and Incoherent Scatter Radar Exosphere. 33

OSIRIS-REx Origins, Spectral Interpretation, Resource Identification, and Security – Regolith Explorer. 47
OSSOS the Outer Solar System Origins Survey. 49

Pan-STARRS Panoramic Survey Telescope and Rapid Response System. 49
PBH primordial black hole. 49
PPN parametrized post-Newtonian. xx, 54, 55
PRIDE Planetary Radio Interferometry and Doppler Experiment. 46

RK Runge-Kutta. 133
RKDP Runge-Kutta-Dormand-Prince. 133
RKF Runge-Kutta-Feagin. 133, 139, 141
RMS root mean square error. xii, 34, 62, 145, 146

SiMDA Size, Mass and Density of Asteroids. ix, 47, 48, 61, 62, 64, 66, 68
SLR satellite laser ranging. 15, 17, 21–25, 79
SRP solar radiation pressure. xii, 11, 34, 157
SSA Space Situational Awareness. 45
SSB Solar System barycenter. 55
SSSA Solar System Situational Awareness. 45

TNO Trans-Neptunian Object. ix, xiii, 3, 4, 45, 47–49, 65, 66, 68, 153

USM Unified State Model. xvii, xix, xx, 31, 137, 140, 141
USSA76 U.S. Standard Atmosphere 1976. 33
UTC Universal Coordinated Time. 63

VLBI very long-base interferometry. 15, 42, 45, 46, 50

Symbol	Definition
a	Orbit semimajor axis
$\mathbf{a}$	Acceleration vector
A	Area enclosed by the Trilogy triangle
$\overline{A}$	Non-dimensional area enclosed by the Trilogy triangle
$\mathbf{A}$	Generic area-normal vector
$\boldsymbol{A}$	Generic matrix
$\mathcal{A}$	Subindex indicating all asteroids are included in the simulation
$\mathcal{A} \setminus \{i\}$	Subindex indicating all asteroids but asteroid i are included in the simulation
b	Impact parameter of a laser beam with respect to the Sun
b_{XY}	Estimated bias of a range observation between ends X and Y
c	Speed of light in vacuum
	Generic considered parameter
C	First USM element
$\boldsymbol{C}$	Covariance matrix of the considered parameters
C_D	Drag coefficient
C_L	Lift coefficient
C_{lm}	Spherical harmonic coefficient of degree l and order m
$\bar{C}_{lm}$	Normalized spherical harmonic coefficient of degree l and order m
C_r	Radiation pressure coefficient
C_S	Lateral force coefficient
d_{XY}	distance between bodies X and Y
e	Orbit eccentricity
$E[.]$	Mathematical expectancy
f	State vector derivative function
	second modified equinoctial element
$\mathbf{F}$	Force vector acting in the RSW frame
F_R	Component of vector $\mathbf{F}$ acting in the R direction of the RSW frame
F_S	Component of vector $\mathbf{F}$ acting in the S direction of the RSW frame
fs	Femtosecond
F_W	Component of vector $\mathbf{F}$ acting in the W direction of the RSW frame
$F_{i,0}$	Function that integrates a state x at t_0 to a later state t_i
$F_{\chi^2_\nu}$	Cumulative distribution function of the chi-square distribution of ν degrees of freedom
g	Third modified equinoctial element
G	Graviational constant
$\dot{G}$	Time derivative of the gravitational constant
G_∞	Gravitational constant at an infinite distance of a gravitational source
h	Norm of the angular momentum vector
	Fourth modified equinoctial element
	Altitude
	Plancks' constant
$\mathbf{h}$	Orbit angular momentum vector
	Observation function
$\boldsymbol{H}$	Design matrix, i.e., Jacobian matrix of observation function h with respect to state $\mathbf{x}$
$\boldsymbol{H}_\mathbf{c}$	Equivalent to matrix $\boldsymbol{H}$, but with respect to the considered parameters $\mathbf{c}$
H_s	Atmospheric scale height
i	Orbit inclination
I	Seventh modified equinoctial element
$\boldsymbol{I}$	Identity matrix
$\mathbf{J}$	Angular momentum vector
J_2	Second zonal harmonic coefficient of a non-spherical gravity field
$J_{2,\odot}$	Second zonal harmonic coefficient of the solar gravity field
J_4	Fourth zonal harmonic coefficient of a non-spherical gravity field
k	Fifth modified equinoctial element
$\boldsymbol{K}_i$	Kalman gain matrix at instant t_i

Symbol	Definition
L	Sixth modified equiinoctial element
l	Confidence boundary of ucnertainty ellipsoid
$l(t)$	Length function of a Trilogy leg through time
m	Mass of particle
	Number of observations in a vector **z**
m_I	Inertial mass
m_G	Gravitational mass
m_g	Mass of the graviton
M	Generic mass of a massive mody
	Mean anomaly
$\boldsymbol{M}_{\mathbf{yc}}$	Auxiliary matrix used in a consider covariance analysis
$\bar{\boldsymbol{M}}_{\mathbf{yc}}$	Auxiliary matrix used in a consider covariance analysis
$\mathbf{M}$	Vector of asteroid masses
M_i	Mass of asteroid i
$\bar{M}_i$	Reference (*a priori*) mass of asteroid i
$M_\odot$	Solar mass
$\dot{M}_\odot$	Time derivative of the solar mass
n	Orbital mean motion
	Number of components of a full state vector **y**
N	Number of observations
$\mathbf{N}$	Auxiliary vector used in batch estimation
n_c	Number of considered parameters
n_p	Number of parameters in a parameter vecotr **p**
p	Orbital semilatus rectum
	Confidence boundary expressed as probability
	Integrator order
$\mathbf{p}$	Vector of environmental parameters
	Vector of estimable environmental parameters
ps	Picosecond
P	Total radiative power of a radiation source
$\boldsymbol{P}$	Final covariance matrix of estimated state after applying a consider covariacne analysis
$\bar{\boldsymbol{P}}_0$	A priori covariance matrix of state at instant t_0
$\bar{\boldsymbol{P}}_{\mathbf{x},i}$	A priori covariance matrix of state **x** at instant i
$\bar{\boldsymbol{P}}_{\mathbf{x}_0}$	A priori covariance matrix of planetary initial states
$\bar{\boldsymbol{P}}_{\mathbf{x}_{\mathrm{S/C}}}$	A priori covariance matrix of spacecraft initial states
$\bar{\boldsymbol{P}}_{0_{\mathrm{S/C}}}$	A priori covariance matrix of estimated vector $\mathbf{y}_{\mathrm{S/C}}$
$\boldsymbol{P}_{\mathbf{y}}$	Covariance matrix of estimated state **y**
$\boldsymbol{P}^{(\mathbf{c})}_{\mathbf{y}_0}$	Extra covariance matrix of estimated state **y** due to the covariance of the considered parameters
$\boldsymbol{P}_{\mathbf{yc}}$	Covariance matrix between the estimated parameters **y** and the considered parameters **c**
$\boldsymbol{P}_{\mathbf{z}}$	Covariance matrix of observations **z**
$\boldsymbol{P}_{\mathbf{z}_i}$	Covariance matrix of a set of observations $\mathbf{z}_i$, obtained at time t_i
$\boldsymbol{P}_{\mathbf{M}}$	Covariance matrix of asteroid masses
P_{lm}	Legendre polynomial of degree l and order m
$\bar{P}_{lm}$	Normalized Legendre polynomial of degree l and order m
$\mathbf{r}$	Generic position vector
$\mathbf{r}_p$	Position vector of perturbing asteroid
$\mathbf{r}(t)$	Generic position vector history
$\mathbf{r}'(t)$	Position vector history resulting from numerical integration with half the step size
$\bar{\mathbf{r}}_X$	*A priori* position vector of body X
$\mathbf{r}_{\mathrm{S/C\,X}}$	Position vector of spacecraft around body X
r	Norm of a generic position vector
$\dot{\mathbf{r}}$	Time derivative of a position vector
$\ddot{\mathbf{r}}$	Second time derivative of a position vector

Symbol	Definition
$r_I^{\mathrm{S/C}}$	Position component of spacecraft
R	Reference radius
	Radial position component
	Perturbing potential function
$\dot{\mathbf{R}}$	Rotation rate of a non-inertial reference frame
R_{f1}	Second USM element
R_{f2}	Third USM element
$\boldsymbol{R}^{A/B}$	Rotation matrix to change from basis B to basis A
$\mathbf{r}_A$	Position vector of station/particle A
s	Generic, errorless range measurement
$\tilde{s}$	Generic, error-affected range measurement
$\hat{s}$	Estimated value of range measurement after introducing error corrections
$s_{BA}^{(1)}$	One-way range measurement from A to B
$s_{BA}^{(2)}$	Two-way range measurement, from A to B and back to A
$\overline{s}_{BA}^{(2)}$	Two-way range measurement between A and B generated from the *a priori* position history of A and B
$\hat{s}_{BA}^{(2)}$	Estimated two-way range measurement between planets A and B generated by correcting $\overline{s}_{BA}^{(2)}$ with the addition of a fitted range bias
$\dot{s}_{BA}^{(2)}$	Two-way range-rate (Doppler) measurement, from A to B and back to A
$s_{XY_r}^{(i)}$	i-way range measurement referenced at the reception time
$s_{XY_t}^{(i)}$	i-way range measurement referenced at the transmission time
S	Cross-sectional area
	Along-track position component
$\boldsymbol{S}(t)$	Sensitivity matrix at instant t
S_{lm}	Spherical harmonic coefficient of degree l and order m
$\bar{S}_{lm}$	Normalized spherical harmonic coefficient of degree l and order m
$\mathbf{S}_\odot$	Solar angular momentum
t_0	Simulation start epoch
t_f	Simulation end epoch
t_i	Time at isntant i
t_r	Time of pulse reception
$\tilde{t}_r$	Error-affected measurement of time of pulse reception
t_t	Time of pulse transmission
$\tilde{t}_t$	Error-affected measurement of time of pulse transmission
U_B	Gravitational potential caused by massive body B
U_N	Generic Newtonian gravitational potential
$\mathbf{u}$	Vector of control accelerations
$\mathbf{u}_{XY}$	Unit vector pointing to Y from X
v_t	Orbital tangential velocity
v_r	Orbital radial velocity
v_R	Orbital radial velocity
v_S	Orbital along-track velocity
v_W	Orbital cross-track velocity
$\mathbf{v_{rel}}$	Airspeed velocity vector
$\mathbf{v}_{\mathrm{S/C\,X}}$	Velocity vector of spacecraft around body X
$v_I^{S/C}$	Velocity component of spacecraft
W	Cross-track position component
$\boldsymbol{W}$	Generic weights matrix
W_X	Weights associated to the X component of cartesian position observations
W_Y	Weights associated to the Y component of cartesian position observations
W_Z	Weights associated to the Z component of cartesian position observations
$\mathbf{x}$	State vector
$\mathbf{x}_0$	Initial state vector

Symbol	Definition
$\dot{\mathbf{x}}$	Time derivative of the state vector
$\mathbf{x}_i$	State vector at time t_i
$\mathbf{x}_i^*$	Reference state at instant t_i
$\overline{\mathbf{x}}$	*A priori* planetary ephemerides state history
$\overline{\mathbf{x}}_0$	*A priori* initial state
$\hat{\mathbf{x}}_i$	Estimated state vector at time t_i
$\mathbf{x}_{\mathrm{S/C}_X}$	State history of spacecraft around planet X
$\mathbf{x}_{0_{\mathrm{S/C}_X}}$	*A priori* state of spacecraft around planet X
x_A	Generic position of station A
$\mathbf{y}$	Full/extended state vector, consisting of the concatenation of $\mathbf{x}$ and $\mathbf{p}$
$\mathbf{y}_0$	Full state vector at time t_0
$\mathbf{y}_{\mathrm{S/C}}$	Vector of estimated parameters in a joint spacecraft estimation
$\overline{\mathbf{y}}_{\mathrm{S/C}}$	Initial guess of the vector of estimated parameters in a joint spacecraft estimation
$\hat{\mathbf{y}}_0$	Estimationm of full state vector at time t_0
$\mathbf{z}$	vector of observations
α	Solar separation angle
	Fifth force model parameter
α_1	parameter of the PPN formalism
α_2	parameter of the PPN formalism
β	parameter of the PPN formalism
γ	parameter of the PPN formalism
δ	Parameter of violation of the weak equivalence prinicple
δt	Response time of a synchronous transponder
$\Delta\mathbf{r}_X$	Position vector error of spacecraft X
$\Delta s_{BA}^{(1)}$	Increase in one-way range observable due to effects not modeled by the main equation
Δt	Numerical integration step size
$\Delta\mathbf{y}$	Increment of the estimated $\mathbf{y}_0$ vector in the iterative batch algorithm
$\Delta\mathbf{z}$	difference between observed and predicted observations
$\hat{\epsilon}$	Estimate of error in a range observation
ϵ_{O1}	Fourth USM element
ϵ_{O2}	Fifth USM element
ϵ_{O3}	Sixth USM element
ζ	Generic convergence parameter
ζ_1	parameter of the PPN formalism
η	Nordtvedt parameter
η_O	Seventh USM element
θ	Orbital true anomaly
	Longitude in spherical coordinates
	Generic angle between two position vectors
λ	Compton wavelength of a particle
	Fifth force exponential parameter
	USM auxiliary parameter
λ_g	Compton wavelength of the graviton
$\mathbf{\Lambda}$	Auxiliary matrix used in batch estimation
μ	Generic gravitational parameter
$\dot{\mu}$	Time derivative of generic gravitational parameter
$\hat{\mu}$	Estimated mean of a statistical distribution
$\mu_\odot$	Solar gravitational parameter
$\dot{\mu}_\odot$	Time derivative of the solar gravitational parameter
μ_p	Gravitational parameter of perturbing asteroid
ν	True anomaly
ξ	parameter of the PPN formalism
ρ	Atmospheric density
ρ_0	Atmospheric reference density

Symbol	Definition
$\boldsymbol{\rho}$	Position vector of a purely Keplerian trajectory
$\hat{\boldsymbol{\rho}}$	Unit vector in the direction of a range observation
$\dot{\boldsymbol{\rho}}$	Time derivative of the position vector of a purely Keplerian trajectory
$\hat{\sigma}$	Estimated standard deviation of a statistical distribution
$\sigma_{b,i}$	Uncertainty in measurement error of Trilogy leg i
	a priori covariance of the range bias corresponding to Trilogy leg i
	Post-fit formal error of the range bias corresponding to Trilogy leg i
$\sigma_{\bar{M}_i}$	Nominal (*a priori*) uncertainty of the mass of asteroid i
σ_{obs}	Noise level of observations
σ_{ρ}	Total uncertainty in planet-to-planet range measurement
$\sigma_{\rho_{\text{S/C}}}$	Uncertainty in spacecraft-to-spacecraft range measurement
$\boldsymbol{\sigma}_{\mathbf{r}_{\text{S/C}}}$	Uncertainty in spacecraft position
σ_x^2	Variance of random variable x
$\sigma_x \sigma_y$	Covariance of random variables x and y
ϕ	Latitude
$\Phi(t_i, t_j)$	State transition matrix between instant t_j and instant t_i
φ	Angle between spacecraft orbital plane and ILR link
$\boldsymbol{\Psi}(t_i, t_j)$	Horizontal concatenation of matrices $\Phi(t_i, t_j)$ and $\boldsymbol{S}(t_j)$
$\boldsymbol{\omega}$	Angular velocity vector of a celestial body
ω	Orbital argument of perigee
Ω	Orbital right ascension of the ascending node
	Gravitational self-energy
$\boldsymbol{\Omega}$	Rotation rate with respect to inertial space
$\hat{\cdot}$	Estimated magnitude
$\tilde{\cdot}$	Error-affected magnitude
$\cdot\vert_a$	Magnitude evaluated at a

Part I

Introduction

1 Introduction

1.1. Background and motivation

Our understanding of the Solar System has dramatically improved since the beginning of the space age. Manned missions to the Moon placed laser retrorreflectors to allow high-precision ranging from Earth, and extraterrestrial probes with advanced instrumentation have studied all of the eight planets in-situ, allowing to measure, among others, their gravity fields and direct distances to Earth. This, combined with the direct study of the Sun, both ground-based and space-based, and the newest generations of ground-based telescopes that allow the discovery of objects beyond the orbit of Neptune that had remained undetected for centuries, has allowed the modeling, reconstruction and prediction of Solar System dynamics with remarkable exactness. The most updated version of such knowledge is materialized by planetary ephemerides models (section 5.1), which are largely based on range measurements to other planets conducted thanks to interplanetary missions.

Despite this great progress, significant uncertainties still persist. The cycle of mass burn and gravity field variation of the Sun remains poorly understood (section 5.5.2), most known asteroids lack reliable mass estimates (section 5.2) and the potential presence of undiscovered, massive Trans-Neptunian Objects (TNOs) perturbing the orbits of the outer planets is still an active research topic (section 5.3). Additionally, the validity of General Relativity (GR) is still being discussed, and subtle variations from the classical formulation of the theory might result in observable dynamical discrepancies within the Solar System (section 5.5.3). All these existing unknowns do not only represent problems to be solved for the sake of knowledge itself, but can still be found to have non-negligible impact, for instance, in the predictions of hazardous events for planetary defense (Farnocchia et al., 2021). The existing uncertainties will only be solved in the future as long as more and more accurate observations are conducted in order to reconstruct the underlying dynamical phenomena to greater nuance. With this in mind, proposals of space missions aimed to contributing to this endeavor are recurrent (e.g., Gan et al., 2019; Smith et al., 2018; Turyshev et al., 2024).

In particular, the study that set the basis for this thesis is the Trilogy mission proposal by Smith et al. (2018). Their suggestion is to place three spacecraft around the Earth, Mars and Venus aimed at measuring the distance to each other, thus obtaining precise range measurements between the three planets, which would potentially shed light into the variation of the Sun's gravitational parameter (section 5.5.1) were they precise enough. Such precision, although practically infeasible with traditional radio-based ranging, is within the limits of ILR. Despite the lack of past missions employing ILR, the technology is available and it has been tested to work in the past (section 3.3).

The Trilogy mission concept has been re-visited by other studies (section 2), who confirmed its scientific potential not only regarding the measurement of the Solar System expansion but also the mass distribution of the Solar System and relativistic parameters in the search of deviations from GR. Different studies were put together in the Interplanetary Laser Trilateration Network (ILTN) workshop in early 2023, the minutes of which concluded that higher fidelity simulations were needed to get further confirmation on the scientific potential of the mission. With the aim of making a contribution in this regard, the present thesis topic was chosen. The exact definition of the research objectives is detailed below.

1.2. Description of the research objectives

1.2.1. Overview

The highly precise range measurements obtained by Trilogy are expected to be used to generate new highly accurate ephemerides of Venus, the Earth and Mars, together with the estimation of collateral science objectives. Such potential scientific output can be relative to several different sub-fields, each of which is detailed in a separate section in chapter 5.

Each of these different possible research lines was studied during the early stages of this work with the aim of making a well founded decision on which theme to focus on. Based on this analysis, it was decided to focus on the potential scientific output related to the mass distribution of the Solar System, mainly by means of asteroid mass determinations from the highly precise range measurements obtained by Trilogy. Although the whole story is thoroughly presented in chapter 5, the individual assessments on each of the different potential research lines can be summarized as follows:

- **Measurement of the variation of the Sun's gravitational parameter**: despite being the initial objective for which Trilogy was conceptualized, it was concluded that this analysis would require to be complemented with the assessment on how the uncertainty in the mass distribution of the Solar System is expected to affect the results. Today, estimations of $\dot{\mu}_\odot$ significantly degrade when asteroid masses are also considered (section 5.5.1), and the assessment on whether or not this would still happen with Trilogy will require to introduce asteroid mass uncertainties in the simulations. Alternatively, proving that Trilogy would help reducing such asteroid mass uncertainties, as suggested by Fienga (2023a), would pave the way for the estimation of $\dot{\mu}_\odot$ without as much of a strong limitation caused by the mass distribution uncertainty.
- **Estimation of asteroid masses**: this has been the chosen scientific topic, together with the estimation of planetary ephemerides. The main motivation for this decision has been the current state of the art of asteroid mass estimations, many of which show inconsistencies between different methods and with mean uncertainties around 50% (section 5.2).
- **Discovery and mass determination of TNOs**: this is considered to be an extension of the asteroids objective. In fact, the asteroid catalog employed in the simulations (section 5.2) does include TNOs, and these have been mixed with the rest of asteroids when assessing their influence to the Trilogy measurements (section 6.2). The assessment on the location of unknown, significantly massive TNOs (section 5.3.2) has finally not been assessed due to time constraints, although it would have been a straightforward continuation of the implemented simulations.
- **Estimation of the Solar System rotation rate**: although the Trilogy mission has been found to possess potential for the accurate determination of the Solar System rotation (section 5.4), recent advancements that already constrain current knowledge to sub-milliarcsecond levels (Liu et al., 2023) lead to judging this science objective as less valuable, as the remaining uncertainty has smaller impact in the remaining unknowns of Solar System dynamics.
- **Deviations from GR**: after having studied the state of the remaining possibilities of GR violations (section 5.5), GR has been assumed to be true in this entire work. Mainly, because GR is consistent with all experimental evidence so far (Fienga & Minazzoli, 2024; Will, 2014) and there is not any significant hint that points to a promising direction where such violations could be detected. Moreover, the measurement of relativistic parameters in the search of GR deviations has been suggested to be conducted with other mission architectures (Turyshev et al., 2024) more suitable than Trilogy for fundamental physics research.

Initially, the proposed research questions were intended to give an answer to the expected number of asteroid and TNO mass improvements starting from an operational scenario in which virtual measurements are not directly assumed to be taken between the centers of mass of the different planets but between the spacecraft themselves, thus considering the impact of orbital perturbations and imperfect orbit determination. During the development of this work, however, it became more evident that these are two separate problems, each of which might deserve entire theses on their own: on the one hand, the estimation of third-body masses from planet-to-planet ranges, and on the other hand, the generation of such planet-to-planet ranges from spacecraft-to-spacecraft measurements. The only case where these are not necessarily separate problems is if a coupled estimation approach (section 4.2.2) is followed, but this was discarded due to technical limitations (section 7.1).

With this in mind, one might formulate the research questions with the aim of analyzing what the expected quality on the generated planet-to-planet range measurements is from Trilogy range measurements as compared to current methods. In the end, after different iterations on what the main simulation of this work needed to aim for (section 7.1), this sub-topic was introduced in the final research questions, which were set to be less exclusively related to the scientific output of asteroid masses alone. This was driven, in great part, by the finding of numerical instabilities under some configurations in the simulation cases with planet-to-planet measurements only (section 6.3.2), which did not allow to conduct an analysis as thorough as it should had it been the main research focus.

1.2.2. Formulation of the research questions

1. What is the expected sensitivity of Trilogy to the present uncertainty in asteroid masses?
2. How well can the existence of enclosed, highly accurate inter-satellite range measurements at interplanetary distances improve the spacecraft orbit determination and the quality of the generated planet-to-planet ranges?

3. Is this measurement quality enough to get current uncertainty levels in planetary ephemerides and asteroid masses significantly reduced by using a straightforward batch estimation?

1.3. Report structure

The structure of this report is as follows: Part II contains the background information related to the Trilogy mission (chapter 2), laser ranging technology (chapter 3), orbit propagation and estimation (chapter 4) and the different studied fields with potential scientific output from the Trilogy mission (chapter 5); Part III describes the implemented simulations, both with planets and asteroids only (chapter 6) and the complete pipeline including spacecraft (chapter 7); and Part IV includes the summary of the complete thesis in a scientific paper format spanning 21 pages. The reader is advised to focus mainly on Part IV, and refer to Parts II and III as a means of consulting more extensive explanations for any points that remain too vague in the paper due to the extension constraints.

It must be pointed out that Part II is essentially the document delivered as literature review at the first stage of this thesis, which was due in late March 2024. Although the whole document has been revised to make it consistent as a final report, it is possible that the expert reader identifies certain statements, phrasings or figures in the scientific paper (Part IV) to be more precise, elaborate or current than their counterparts in Part II. Should any contradictions have been overlooked and remain in this final version of the report, Part IV takes precedence.

Finally, Part VI contains appendices that support the body of this report: Appendix A includes all the figures of the integrator analyses that led to the final choices of integrator and propagator settings for both planetary and spacecraft propagations; Appendix B details the procedure followed to obtain a representative covariance matrix for the planetary initial states; Appendix C includes some findings related to analytical developments on the sensitivity of asteroid masses to Trilogy measurements, which were developed in parallel to the main work but were not given as much focus; and Appendix D includes the details on some issues found with the TU Delft Astrodynamics Toolbox (Tudat), wihch is the software used in all the simulations of this thesis.

Part II

Background

2

Trilogy mission overview

2.1. Background and motivation

The mission concept of Trilogy was first introduced by Smith et al. (2018), who suggested that a triple ILR setup linking the Earth, Venus and Mars—represented in Figure 2.1—would provide range measurements precise enough to accurately monitor the expansion of the Solar System. Such expansion is caused by the variability of the gravitational parameter of the Sun $\mu_\odot$, and an accurate understanding of this phenomenon would in turn provide significant insight on both the solar mass burn rate $\dot{M}_\odot/M_\odot$ and the hypothesis of the universal gravitational constant G not being actually constant. Although measurements of both $\dot{M}_\odot/M_\odot$ and $\dot{G}/G$ have been carried out in the past, it is still required to further reduce the error margins in order to get a deeper understanding of the cyclic variations of internal solar dynamics and to find stronger confirmation or rebuttal of alternative gravitational theories (see subsection 5.5.1).

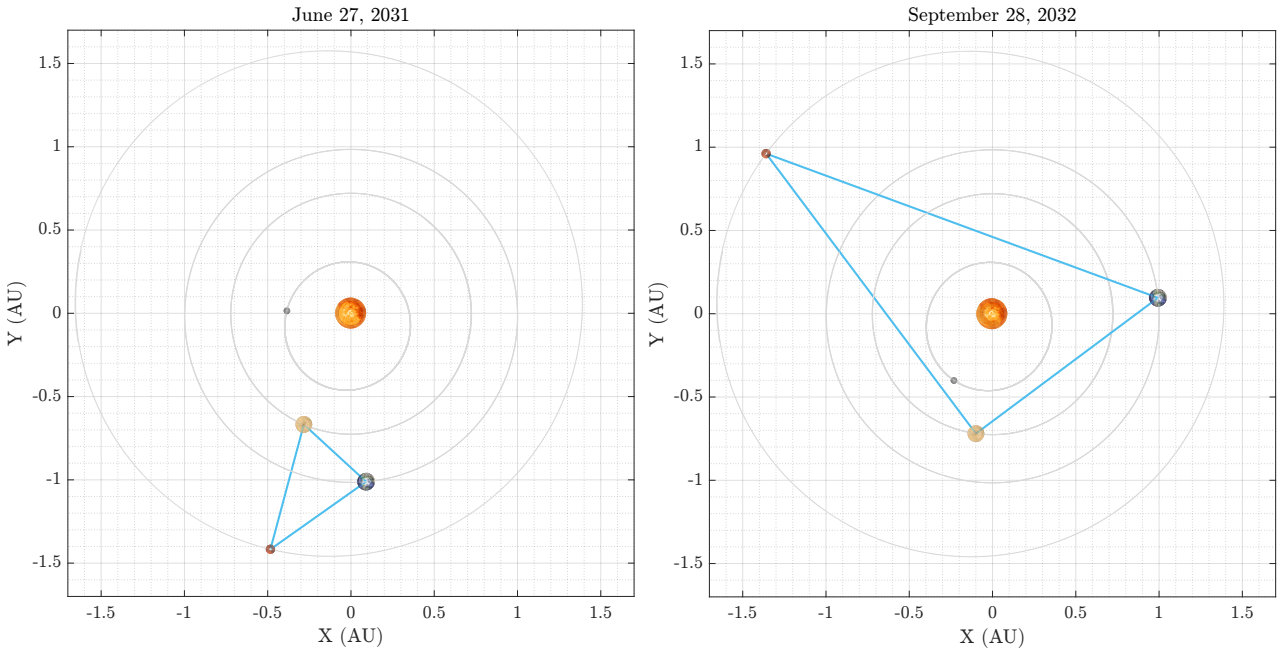

Figure 2.1: Trilogy laser links shown in two different dates of the early 30's. Sun scale: 20; planets scale: 1250.

Besides the direct measurement of the inner Solar System's expansion rate, the authors also acknowledged the relevance of the proposal to many other scientific matters. These include other astrophysical concepts subject to active research, such as the testing of the equivalence principle, the Lense-Thirring (LT) effect or the certainty of values of the relativistic parameters (section 5.5); scientific research on the very planets hosting the Trilogy orbiters, including the more accurate determination of their obliquity, tides and moment of inertia; and the improvement of their planetary ephememerides, which are a direct result of having more exact range measurements to the planets themselves (section 5.1).

Today, the only missions planned for launch in the next decade employing an enclosed laser link between three spacecraft are conceived for the detection of gravitational waves (GWs), and most of them plan smaller triangles in comparison (subsection 5.5.4). In fact, laser ranging at interplanetary distances has never been used on a regular basis in past missions, although the feasibility of the technology has been demonstrated in several occasions (subsection 3.3.2). Trilogy would be the first mission employing continuous interplanetary laser ranging between celestial bodies other than the Earth.

Cascioli et al. (2019) suggested different variations of the Trilogy architecture, with orbiters around Mercury and Jupiter (see section 2.2), with the aim of estimating different relativistic and planetary parameters. They concluded that Trilogy could provide "substantial improvements in the determination of planetary orbital dynamics in the short time scale", outperforming other architectures that do not take advantage of the closed triangle concept. More follow-up work was conducted by Bills and Skillman (2022) and Bills and Gorski (2022), which explored, respectively, the Trilogy setup as a Solar-System-sized gyroscope (section 5.4) and as a trilateration antenna to locate unobserved masses in the Solar System (section 5.3). Finally, preliminary calculations by Fienga (2023a), estimating the accuracy improvement in the computation of planetary ephemerides with Trilogy measurements, concluded it to be a "very promising option for the measurement of the distribution of mass in the Solar System and of $\dot{\mu}_\odot/\mu_\odot$". The non-Earth-based ranging link was found to provide significant gain regardless of the mission duration and the accuracy of the range measurements.

Following these studies, the ILTN Workshop[1] was held in February 2023. This event gathered the authors of the original studies with other experts in the fields of laser ranging and planetary estimation with the aim of putting past findings in common and defining the needs for future efforts. The final minutes detailed different key aspects to work on, including full perturbed simulations of the Solar System to better assess the expected accuracy of measurements and science output.

No further work has been published since, yet it is worth mentioning that an independent study by Bassi et al. (2022) assessing future proposals for space-based research highlighted the Trilogy concept as "especially interesting", pointing out that "it will certainly benefit from the technological fallout from LISA". This statement is however highly dependent on which measurement strategy is used for Trilogy (section 2.2), since the interferometric links planned for LISA are significantly different than the ranging links classically employed for ILR (subsection 3.1.1, subsection 3.3.2). Another positive assessment on the Trilogy concept is given by Fienga and Minazzoli (2024), according to whom "the outcome of these measurements would indeed impact the global accuracy of the ephemerides, improve significantly the Bepi-Colombo results but also allow for better constraints on the distribution of mass in the solar system".

2.2. Summary of proposed mission architectures

The core idea of Trilogy is to place ranging transceivers in three different planetary bodies to form a closed triangle of measurements, yet this requirement alone still allows for many different branches in the tree of mission architecture alternatives. One of the key decision variables is the locations of the three vertices, which can be placed in different combinations of planets or other locations of the Solar System. If rocky planets are chosen, each station can be either in orbit or on the surface. This is especially true for Earth, in which a solid ground station infrastructure already exists. The different architectures proposed by the studies up to date are summarized in Table 2.1.

Table 2.1: Trilogy mission configurations suggested by the different published studies. The specification of orbiter or lander is only given for those studies which explicitly state it.

	Station 1	**Station 2**	**Station 3**
Smith et al. (2018)	Moon orbiter	Venus orbiter	Mars orbiter
Cascioli et al. (2019)	Earth station	Mercury orbiter/lander	Mars orbiter/lander
	Earth station	Mercury orbit/lander	Jupiter orbiter
	Earth station	Venus orbiter/lander	Mars orbiter/lander
Bills and Skillman (2022)	Earth orbiter	Venus orbiter	Mars orbiter
Bills and Gorski (2022)	Earth orbiter	Venus orbiter	Mars orbiter
Fienga (2023a)	Earth	Venus	Mars

The original proposal by Smith et al. (2018) suggested to locate the non-Earth-based transceivers in the inner planets because they experiment the signature of planetary orbit expansion more rapidly, and would not present laser link

[1] The presentation slides and recordings are available at https://grailteam.mit.edu/Trilateration

requirements as strict as longer distances would. As per the Earth vertex, an orbit around the Moon could potentially improve the understanding of the Earth-Moon system dynamics, although this is subject to the trade-off of having a worse orbit determination around the Moon—unlike on Earth, where GNSS can be used—and it is unclear if the expected return would justify the additional cost.

In fact, just as Cascioli et al. (2019) suggested, it might well be a reasonable alternative to use Earth ground stations rather than an orbiting spacecraft. Placing laser transceivers in Earth's orbit to mitigate the atmospheric impact on the laser links was already suggested by Hurd et al. (2006), although according to Dirkx (2015, p. 82) it would likely have limited value for tracking, since "the problem of atmospheric propagation [...] would now be placed on the orbit determination of this relay satellite, propagating onto the error of the interplanetary target". However, Dirkx (2015) also acknowledges that a ground-based laser ranging measurement campaign will present more complicated scheduling due to the long time until target acquisition (p. 73), together with the fact that the prominence of existing stations in mid latitudes might introduce a seasonal signature in the accuracy of ILR measurements (p. 81), which would be mitigated by the use of a space-based station. For the purpose of Trilogy, however, no exact figures to firmly support one of the alternatives have been calculated.

For the other two vertices, the ground-based alternative is also mentioned by Smith et al. (2018). It would nevertheless imply the the need to correct for planetary rotation and tidal effects, together with a greater occultation time, and the additional costs of a lander. In the ILTN workshop, Mazarico (2023b) pointed the former out as weaknesses of this alternative, given the greater uncertainty of these parameters in other bodies, although it was also acknowledged that, if observations of enough quality are available, these unknowns could also be estimated to increase the scientific output related to the host planets. This is aligned with the view on ILR lander options by Dirkx et al. (2019), according to whom "depending on the target body [...] the uncertainty may be limited and accounted for by the addition of a number of estimated parameters".

If an orbiter is chosen instead, there are in turn several alternatives regarding its orbital configuration. Smith et al. (2018) support high-altitude orbits, so that they are "unperturbed by the planet's atmosphere [...] and the higher harmonics of the gravity field to provide the highest accuracy determination of the spacecraft orbit". These would be able to "monitor the time-variable, long-wavelength gravity field (less than spherical harmonic degree and order 4) and the orientation of the planet", hence also providing valuable planetary science output. If the planetary orbits were set low, apart from the increased influence of drag and higher-order gravity terms, the increased number of occultations would reduce the number of measurements possible, and the more frequent eclipses would make the thermal management more complicated (Mazarico, 2023a). On the other hand, having the orbiters in free heliocentric orbits would increase the impact of SRP (Bills & Gorski, 2022), as well as third-body perturbations. These can be difficult to model if the influence of asteroids with unknown mass is significant, although this might again be an opportunity to estimate them (section 5.2). In the end, a balance between being subject to the influence of parameters to estimate but not so much as to have too many unknowns for too little observations will need to be found with more rigorous numerical assessments.

Note that these are general considerations, but not all of them are applicable to all the candidate hosting bodies. For instance, Mercury has such a thin atmosphere that concerns on drag and laser link effects might be irrelevant, whereas that

Table 2.2: Alternatives for the location of the non-Earth-based transceivers for Trilogy. Summarized from Bills and Gorski (2022), Bills and Skillman (2022), Mazarico (2023a, 2023b), and Smith et al. (2018)

	Heliocentric flyer	**Planetary high orbit**	**Planetary low orbit**	**Lander**
Atmosphere (if applicable)	No drag effects	Very low drag effects	Higher drag effects	Atmospheric effects on the laser link
Impact of SRP	High effects	Mid-low effects	Low effects	No effects
Effects of unknown planetary parameters	No effects of high-order, unknown gravity coefficients	Low effects of high-order, unknown gravity coefficients	Higher effects of high-order, unknown gravity coefficients	Higher effects of the uncertainty in the 3D surface location, tidal deformations and rotation
Occultation and eclipse time	Virtually null	Low	High	High
Mission longevity	High	High	Mid-high	Presumably lower
Planetary science output	Very low	Mid-high	Very high	Very high

of Venus is so thick that the lander option might well be completely unfeasible. The general pros and cons of the possible transceiver location alternatives is summarized in Table 2.2. Cost considerations are not included because assessing how the delta-V requirements for different planets cause significant differences is beyond the reach of this qualitative assessment. Based on the information displayed, it looks clear how a planetary high orbit seems the most suitable option.

Regarding orbital inclination, Smith et al. (2018) declare that it "is less constrained, provided it does not restrict observations of the other host planets". True polar or sun-synchronous orbits are not advised, due to the fact that they are "geometrically frozen in inertial or solar orientation". Bills and Skillman (2022) also mention the possibility of placing a fourth sensor in a significantly inclined heliocentric orbit to gain more sensitivity on the third dimension, although "it is not yet clear that the advantage [...] would justify the additional cost".

The final mission architecture will greatly depend on whether the transceivers are individual payloads or secondary payloads onboard of other planetary missions. In the second case, the spacecraft will be launched based on the calendar needs of each particular mission, hence reducing the time of common operation of all three spacecraft. Otherwise, Trilogy will have the liberty of aiming for the architecture most suitable for its needs, potentially employing a single launcher to bring all three spacecraft to their respective orbits.

In this regard, Smith et al. (2018) detail that a single launch vehicle is viable, with "payloads of at least 120 kg [that] could be deployed into stable orbits at both Venus and Mars with a total travel time of order 2+ years". This is based on the available interplanetary impulse from the Atlas V-401 rocket, although no further details on the overall payload-to-mass ratio or the need for course and insertion delta-V are given. No studies have been made public regarding the launch architecture studies of other possible configurations (e.g., to Mercury or Jupiter).

The science output from Trilogy will be determined by three factors: the quality of the measurements, the number of measurements per unit of time and the total mission duration. While the latter will mostly depend on the chosen architecture, the former two will depend on the specifications of the available measurement subsystem. Table 2.3 summarizes the options proposed by the conducted studies up to date.

Table 2.3: Trilogy mission configurations suggested by the different published studies.

	Link type	**Accuracy**	**Sampling cadence**	**Mission duration**
Smith et al. (2018)	Laser	Few cm		Several years
Cascioli et al. (2019)	Radio	20 cm	10 hours	2 years
	Radio	2 cm	8 hours	1.5 years
Bills and Skillman (2022)	Laser	10 cm		
Bills and Gorski (2022)	Laser	1 cm	1 second	
Fienga (2023a)	Laser	0.1 mm	24 hours	1 year
	Laser	0.1 mm	24 hours	2.5 years
	Laser	0.1 mm	24 hours	5 years
	Laser	1×10^{-3} mm	24 hours	1 year
	Laser	1×10^{-3} mm	24 hours	2.5 years
	Laser	1×10^{-3} mm	24 hours	5 years

Most of the studies (Bills & Gorski, 2022; Bills & Skillman, 2022; Cascioli et al., 2019; Smith et al., 2018) assume a ranging accuracy in the order of a few centimeters. This has been proven to be achievable with laser-based instruments at interplanetary distances (section 3.3), yet it is also feasible with the new generation of radio-based transmitters such as the ones on-board of BepiColombo (Cascioli et al., 2019; Dirkx et al., 2019). Other than for the sake of measurement quality, Smith et al. (2018) defend laser transponders over microwave systems because of their narrow beam divergence and because there is no requirement for large spacecraft-mounted antennae.

Fienga (2023a), on the other hand, assumes ranging measurements several orders of magnitude more accurate. This is likely to require interferometric laser measurements (subsection 3.1.1), just as the Laser Interferometry Space Antenna (LISA) mission, and which is in contrast with the asynchronous transponder suggested by Smith et al. (2018) and the nonexistent need of coherent phase-link described by Bills and Skillman (2022). Based on the technological state of the art for ILR (section 3.3), this accuracy range seems overly optimistic.

Mission duration also plays a determining role in the final confidence of the science output. This is because estimation methods typically include all measurements throughout a mission time span and fit them into a single dynamical model, and the longer the period through which these measurements have been acquired, the more dynamical effects will be incorporated in the fit. The exact methods of orbit estimation are detailed in section 4.2, but as an illustrative example: if

there are accurate range measurements to Mars for a period of a tenth of its orbit only, there might be different model solutions that yield to virtually equal dynamic evolutions of Mars during this time but which would diverge in the future. Hence, incorporating the measurements from longer in the future helps narrowing the set of possible solutions.

According to Cascioli et al. (2019), a duration of 1.5 years with measurement specifications comparable to BepiColombo would "lead to unprecedented improvements in the knowledge of fundamental physics", with an expected reduction in the uncertainty of certain solar and relativistic parameters of several orders of magnitude with respect to current knowledge (section 5.5). However, after assessing the expected impact of longer durations, they conclude "a further enhancement of these results has to be obtained through a better measurement system rather than with a longer mission". Fienga (2023a) found that even with an accuracy of 0.1 mm and a mission duration of one year—the worst of the architectures considered in her study—the performance in the estimation of ephemerides and other solar system parameters increases by two orders of magnitude relative to the expected improvement from BepiColombo range measurements. Longer durations and higher accuracies yield to even better improvements of planetary parameters, although not of the solar parameters such as its mass and its oblateness. The challenge of getting accurate estimates of such parameters is developed in section 5.5.

3

Laser ranging

The aim of this chapter is to introduce all the necessary principles in which laser ranging simulations will be based. Mainly, these include the formulation of the measurement equations (section 3.2), both in their error-free and error-affected forms, together with a thorough description of the sources and their corresponding magnitudes both in random and systematic forms. The basic concepts needed for this are introduced in the initial overview (section 3.1), and finally the technology evolution up to the present day, including past working tests, and the constraints to be taken into account in the simulations are described in section 3.3.

3.1. Overview

3.1.1. Types of laser ranging

Light-based length measurements can be classified into two general categories: the first is based on the detection and timing of incoherent light pulses to infer the distance from their measured time-of-flight, whereas the second, based on wavelength interferometry, takes advantage of optical coherence to enhance the resolution (Ye, 2004). The two approaches are briefly described below in this section.

Time-tagged laser ranging

The fundamental principle of time-tagged laser ranging is based on timing the sending and receiving instants of laser pulses fired between two stations, and then calculating the distance traveled by each pulse from the computed time of flight. This is one typical method presently used in the tracking of planetary missions, together with Doppler range-rate measurements and very long-base interferometry (VLBI) (Dirkx, 2015, Sec. 2.1.1). Depending on the setup used and its regime of operation, Birnbaum et al. (2010) describe four possible approaches:

- **Passive two-way**: a single laser pulse is fired from the measuring station and it is reflected by a retroreflector located in the station to which distance is measured. The reflected pulse is then received by the same station where it originated, in which the time difference between sending and receiving the pulse is measured. This is how satellite laser ranging (SLR) and lunar laser ranging (LLR) work nowadays.
- **One-way**: a single laser pulse is fired from the measuring to the measured station, equipped with a detector and a timer. The time of reception must then be estimated or transmitted to the measuring station by a different means.
- **Echo two-way**: a laser pulse is fired from the measuring station, and it is then acknowledged by the measured station, which sends back another laser pulse in response after a calibrated processing time δt.
- **Asynchronous two-way**: both ends of the range to be measured send laser pulses to each other at defined, and not necessarily dependent intervals. This approach is named "paired one-way" by Birnbaum et al. (2010), but the term "two-way asynchronous" is more consistent with the literature (Degnan, 2002; Dirkx, 2015). The advantage of the asynchronous approach is to get rid of a main drawback of the echo approach, which is that in a low signal-to-noise environment such as ILR measurements, noise can mistakenly fire response pulses frequently.

A schematic of the pulse exchange setup for all four approaches is displayed in Figure 3.1. It must be noted that all these approaches but the passive two-way can also be used in non-laser-based systems. Retrorreflectors can only with pulses with wavelengths smaller than their characteristic lengths (in practice, near the optical spectrum), but the other approaches

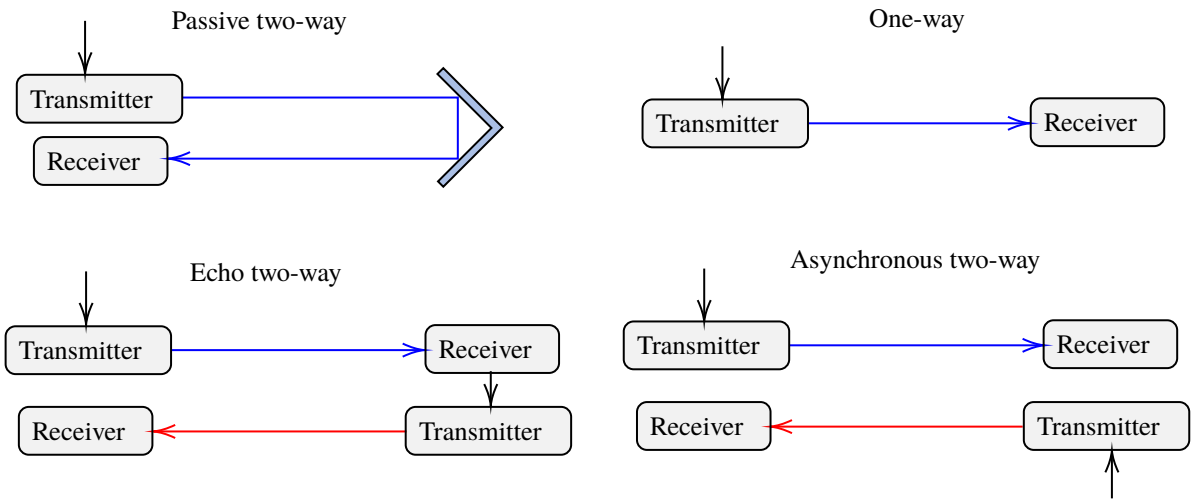

Figure 3.1: Sketch of laser pulse exchange for the four described approaches. Black lines represent signals to trigger the transmission of a pulse. Adapted from Birnbaum et al. (2010, Fig. 1) and Dirkx (2015, Fig 3.1).

only employ emitting and/or receiving transponders, which can also work for radio or microwave signals. In case passive two-way ranging is conducted with radio, the wavelength is large enough that the whole target object can reflect the incoming pulse. This is essentially a radar system.

Interferometric laser ranging

The fundamental principle of interferometry is the measurement of the interference pattern caused by two different beams of electromagnetic waves. As explained by Hariharan and Hariharan (2007), "since the wavelength of visible light is quite small [...], very small changes in the optical path difference produce measurable changes in the intensity of an interference pattern". This, together with the availability of monochromatic lasers, allows for measurements of sub-wavelength precision.

Although this basic measurement principle only contains information on the relative offset between two laser beams and not their true travel distance, several techniques exist to get highly accurate ranges from interferometric measurements: Lee et al. (2010) mention synthetic wavelength interferometry, coherence interferometry, dispersive interferometry and multi-heterodyne interferometry. Although the details of each of the methods are out of the scope of this description, it is worth mentioning that space missions using or planning to use interferometric links between two spacecraft are based on a working principle known as "transponder laser interferometry", which can be described as follows (Ming et al., 2020): one spacecraft, called the "master", fires a laser beam to the other spacecraft, named "slave". There, another laser is sent back to the master after its phase has been locked to the same as in the received beam. The phase meter onboard the master spacecraft then measures the phase difference between the emitted and the received laser pulses, which, thanks to the phase lock introduced by the slave, is only due to the relative distance between the two spacecraft. This basic setup is illustrated in Figure 3.2. The phase meter of the slave spacecraft is only employed for the sake of phase locking.

As described in subsection 3.3.2, despite the promising status of interferometric laser ranging for space applications, time-tagged laser ranging is currently the technique with best-established working principles and successful technology demonstrations at interplanetary distances. As seen in section 2.2, this is also what (Bills & Skillman, 2022; Cascioli et al., 2019; Smith et al., 2018) suggest for Trilogy. With this in mind, the core of this chapter (including the necessary hardware, the measurement principles and the error sources) is dedicated to the latter.

3.1.2. Laser ranging hardware

Although an accurate description of the hardware used for laser ranging is not within the scope of this work, it is important to name the main elements that play a role when describing the sources of error (subsection 3.2.2). The essential element that allows laser pulses to be fired and/or received is commonly named "transponder", a schematic of which is shown in Figure 3.3. Note how this simplified model neglects physical elements such as light filters and the telescope servo-controls, shown in other sketches found in literature (e.g., Combrinck, 2010).

The emitted and received laser pulses are sensed by two detectors, which send a signal to the event timer to get the time stamps of each event. This event timer is dependent on a high-accuracy clock, which provides the frequency standard thanks to which the event timer counts the elapsed time. Since the speed of light is $\sim 3 \times 10^8$ m/s, a precision of few mm

in a two-way measurement (see section 3.2) requires a timer precision of at least 20 ps (Combrinck, 2010).

A transponder with the capacity of both emitting and receiving laser pulses can also be referred as "transceiver", from the combination of transmitter and receiver. Among the four approaches displayed in Figure 3.1, one-way ranging is the only one that does not necessarily require one or more transceiver but just a transmitter at one and a receiver at the other. Passive two-way requires only one transceiver, whereas echo and asynchronous two-way methods require one transceiver at each of the two ends.

In the case of passive one-way laser ranging, a retroreflector is needed to make sure the emitted laser pulse is reflected back to the same station. The term "retroreflector" is used to refer to any type of reflector with the property of reflecting any beam of light with its original direction of incidence. The most simple and typical example of such reflector is the corner cube reflector (CCR), which consists of three perpendicular planes of reflecting surface. Multiple CCRs can be arranged in an array to form a larger retroreflector, such as the ones installed on the Moon by the Apollo missions 11, 14 and 15 (Faller et al., 1971).

Even after five decades of widespread use of CCRs for SLR and LLR, the geometry of retroreflectors is still an active topic of research. Kucharski et al. (2011) presented a novel type, making use of the Luneburg lens concept instead of CCRs, which erase the errors caused by their signature in the laser pulses (see subsection 3.2.2). On the other hand, Turyshev et al. (2013) introduced a new design for a lunar retroreflector, based on a single CCR. This results in a lower mass, and eliminates the error caused by CCR arrays due to the fact that each of the cubes in the array is at a slightly different location.

3.2. Measurement principles

Figure 3.4 and Figure 3.5 show space-time diagrams of the four possible time-tagged laser ranging approaches described above (subsection 3.1.1). These show the exchange of pulses between a measuring station A and a station B at the opposite end. Note that the diagrams are centered to A's worldline, with respect to which B moves arbitrarily. The space coordinate is defined by x, yet this can represent any of the three spatial coordinates or the set of all of them.

3.2.1. Error-free formulation

Measurements of a physical system by ranging require two main mathematical expressions to work with. On the one hand, the measurement equation that computes the range based on the values registered by the hardware—in this case, a set of transmission/reception times. On the other hand, the range observable equation, which relates the physical model parameters to be estimated—in the most simple case, the position vectors of both ends—with the expected value of the measured range. The formulation of these equations, in the ideal case where all the measurements are perfect, is detailed below for the four possible approaches.

Table 3.1 summarizes the measurement and observable equations for the methods displayed in Figure 3.4. In the case of passive two-way ranging, the measuring station will record a transmission time t_1 and a reception time t_3, which are, respectively, the start and end time of the two-way travel followed by light. In one-way ranging, on the other hand, the recorded reception time is t_2 and it bounds the one-way light travel. Hence, the range observable consists of the sum of the norm of the two travel segments in the former case and a single norm in the latter.

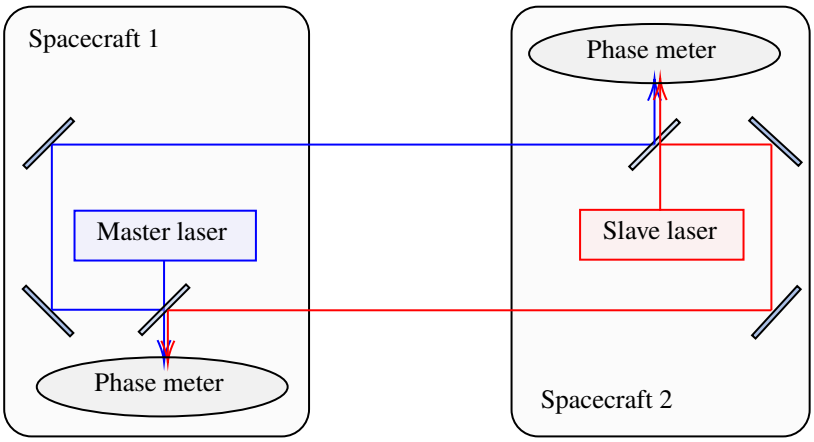

Figure 3.2: Sketch of interferometric laser pulse exchange between two spacecraft. Adapted from Ming et al. (2020, Fig. 1) and Sheard et al. (2012, Fig. 1).

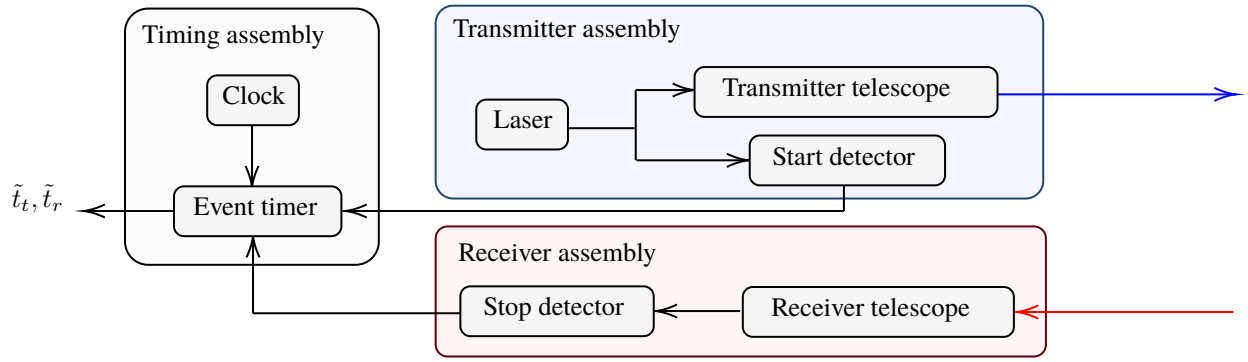

Figure 3.3: Transponder subsystems relevant for the time tagging of laser pulses. Adapted from Dirkx (2015, Fig. 3.8).

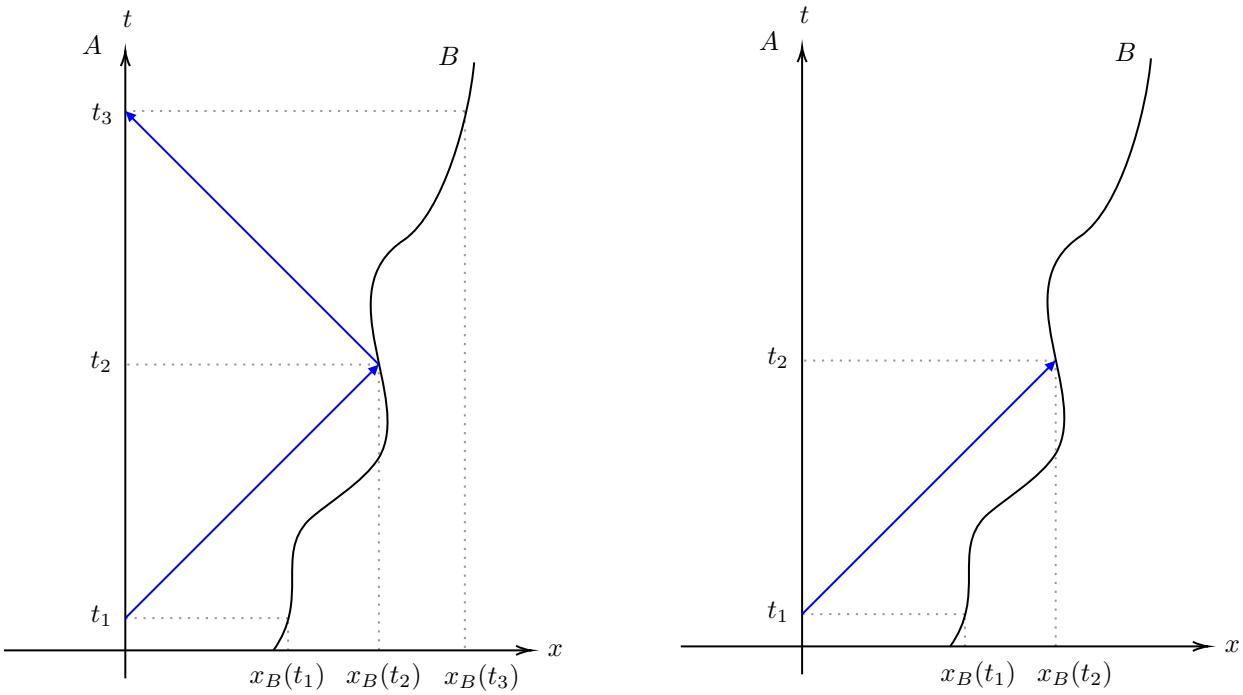

Figure 3.4: Space-time diagram of a laser ranging pulse in a passive two-way setup (left) and an unpaired one-way setup (right)

Table 3.1: Measurement and range observable equations for the ranging methods requiring a single transmitter

	Passive two-way	**One-way**
Measurement equation	$s = c\,(t_3 - t_1)$	$s = c\,(t_2 - t_1)$
Range observable equation	$s = \|\mathbf{r}_B(t_2) - \mathbf{r}_A(t_1)\| + \|\mathbf{r}_A(t_3) - \mathbf{r}_B(t_2)\|$	$s = \|\mathbf{r}_B(t_2) - \mathbf{r}_A(t_1)\|$

Synchronous and asynchronous two way ranging work essentially the same, with the only difference being in the relative timing of pulse exchanges. In the former, all pulses from B to A are sent just a fraction of time δt after a pulse from A is received by B, hence all the exchanged pulses throughout a longer time period can be, in the ideal case, perfectly matched. In the latter, all pulses are sent independently to one another. In Figure 3.5 (right) this is illustrated with the fact that the pulse from B to A is sent before the one from A reaches B, but this could also happen afterwards, with any arbitrary time separation between the two events.

Table 3.2 details the measurement and observable equations for both methods, whose space-time diagrams are represented in Figure 3.5. Note that each pair of exchanged pulses gives two separate one-way ranges, unlike in the cases where a single of the two terminals is actively transmitting. Following the formulation from Dirkx et al. (2015), a one-way range resulting of a pulse emitted from terminal A and received at terminal B is denoted $s^{(1)}_{BA}$. Two-way measurements are

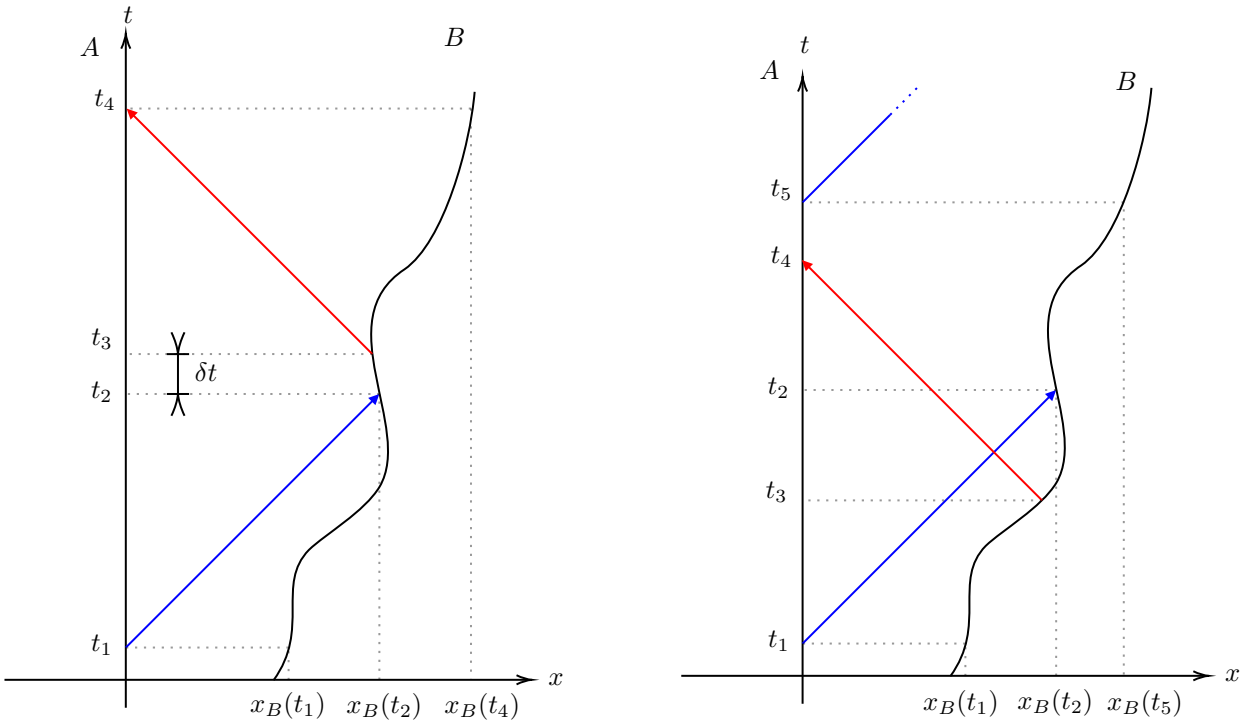

Figure 3.5: Space-time diagram of a pair of laser ranging pulses in a two-way synchronous setup (left) and a two-way asynchronous setup (right)

then obtained by pairing different one-way measurements at each station.

Table 3.2: Measurement and range observable equations for the ranging methods requiring two transceivers

	One-way ranges	**Two-way ranges**
Measurement equation	$s^{(1)}_{BA} = c\,(t_2 - t_1)$ $s^{(1)}_{AB} = c\,(t_4 - t_3)$	$s^{(2)}_{BA} = c\,(t_4 - t_1)$
Range observable equation	$s^{(1)}_{BA} = \lVert \mathbf{r}_B(t_2) - \mathbf{r}_A(t_1) \rVert$ $s^{(1)}_{AB} = \lVert \mathbf{r}_A(t_4) - \mathbf{r}_B(t_3) \rVert$	$s^{(2)}_{BA} = \lVert \mathbf{r}_B(t_2) - \mathbf{r}_A(t_1) \rVert + \lVert \mathbf{r}_A(t_4) - \mathbf{r}_B(t_3) \rVert + c\delta t_B$

One can observe how all range equations in Table 3.1 and Table 3.2 obey a general form

$$s = c\,(t_r - t_t)\,, \tag{3.1}$$

where t_t is the time of transmission, t_r is the time of reception, and c is the speed of light in vacuum. It is important to note that, the way the measurement and range equations are defined, the measured distance is not the actual distance at a given time t between A and B, but rather the distance between the point in space where one of the two terminals is at instant t_r and the point where the other terminal is at instant t_t. This does make a difference given the movement of the two terminals during the light travel time.

The definitions above are aligned with that from Dirkx (2015), but different formulations can be found in literature. Birnbaum et al. (2010) define the range measurements so that each measured s is indeed the true range between A and B at the same instant t. For this, the range measurement must include a term to account for the distance traveled by the receiving terminal during the time of light travel. If such movement causes the range to vary through time at a constant rate v, this term takes the form $-v\,(t_r - t_t)$. If this velocity is unknown, enough observations can allow for it to be solved. This is however a simplistic approach: in reality, not only the rate of separation between the two terminals is not constant but Special Relativity does not allow for a true simultaneous instant at which to measure this range to even exist (e.g., Arthur, 2019). This is why it is preferrable to use the formulation from Table 3.1 and Table 3.2, in which the relative motion of the two ends is embedded. Since Figure 3.4 and Figure 3.5 are centered in A's worldline, all times in Table 3.1 and Table 3.2 are those viewed from A's perspective.

3.2.2. Introducing error sources

Measurement and range observable equations

Following the notation from Dirkx (2015) and Dirkx et al. (2019), the recorded t_t and t_r times will be measured, respectively, with some error Δt_t and Δt_r, yielding to imperfect time values $\tilde{t}_t = t_t + \Delta t_t$ and $\tilde{t}_r = t_r + \Delta t_r$. Hence, the measured range will also be an imperfect value $\tilde{s}$, transforming the measurement equation (3.1) into

$$\tilde{s} = c\left(\tilde{t}_r - \tilde{t}_t\right). \tag{3.2}$$

The error sources contributing to Δt_t and Δt_r are summarized in Table 3.3 and described below. Their knowledge and modeling allows for an estimate of the range error $\hat{\epsilon}$ to be computed and introduced in equation (3.2) in order to get an estimation $\hat{s}$ of the true range s:

$$\hat{s} = c\left(\tilde{t}_r - \tilde{t}_t\right) - \hat{\epsilon}. \tag{3.3}$$

As per the range observable equations, imperfections introduce the need to account for range errors, denoted Δs, and the difference of time measured by the two stations. Continuing with the definition of the time tags of the exchanged laser pulses from Figure 3.4 and Figure 3.5, the updated formulation is as follows for each of the ranging methods:

- **One-way**: time t_2 is recorded at the receiving station, and hence it could be transmitted to station A. However, the way to do so in a precise enough way to effectively get the true clock offset between A and B, so that it can be included in Δs, is to perform laser time transfer (LTT) (subsection 3.3.1), hence effectively making a two-way laser range measurement. Therefore, if a truly one-way laser link only is available, Dirkx et al. (2015) define the proper approach to be based on t_1 only:

$$s^{(1)}_{BA} = \left\| \mathbf{r}_B\left(t_1 + \frac{s^{(1)}_{BA}}{c}\right) - \mathbf{r}_A(t_1) \right\| + \Delta s^{(1)}_{BA}. \tag{3.4}$$

- **Two-way**: Again, if the range to B is computed from A, with only times t_1 and t_4 known, the times of reception and sending at B are better estimated from the range itself. Dirkx et al. (2015) define two possible approaches to compute the two-way range: $s^{(2)}_{BA_t}$, referenced at the transmission time, and $s^{(2)}_{BA_r}$, referenced at the reception time.

$$s^{(2)}_{BA_t} = s^{(1)}_{BA_t} + s^{(1)}_{AB_t} + c\delta t_B \tag{3.5a}$$

$$s^{(1)}_{BA_t} = \left\| \mathbf{r}_B\left(t_1 + \frac{s^{(1)}_{BA_t}}{c}\right) - \mathbf{r}_A(t_1) \right\| + \Delta s^{(1)}_{BA} \tag{3.5b}$$

$$s^{(1)}_{AB_t} = \left\| \mathbf{r}_A\left(t_1 + \frac{s^{(1)}_{BA_t}}{c} + \delta t_B + \frac{s^{(1)}_{AB_t}}{c}\right) - \mathbf{r}_B\left(t_1 + \frac{s^{(1)}_{BA_t}}{c} + \delta t_B\right) \right\| + \Delta s^{(1)}_{AB} \tag{3.5c}$$

$$s^{(2)}_{BA_r} = s^{(1)}_{BA_r} + s^{(1)}_{AB_r} + c\delta t_B \tag{3.6a}$$

$$s^{(1)}_{BA_r} = \left\| \mathbf{r}_B\left(t_4 - \frac{s^{(1)}_{AB_r}}{c} - \delta t_B\right) - \mathbf{r}_A\left(t_4 - \frac{s^{(1)}_{AB_r}}{c} - \delta t_B - \frac{s^{(1)}_{BA_r}}{c}\right) \right\| + \Delta s^{(1)}_{BA} \tag{3.6b}$$

$$s^{(1)}_{AB_r} = \left\| \mathbf{r}_A(t_4) - \mathbf{r}_B\left(t_4 - \frac{s^{(1)}_{AB_r}}{c}\right) \right\| + \Delta s^{(1)}_{AB} \tag{3.6c}$$

The formulation above is valid for all passive, echo and two-way laser ranging. The only difference is the value of δt_B: in the passive setup, $\delta t_B = 0$; in the echo setup it is a small (sub-second) positive value; whereas in asynchronous two-way ranging it is an arbitrary value, either positive or negative.

Note how $s^{(1)}_{BA}$ in one-way ranging (equation 3.4) is equivalent to $s^{(1)}_{BA_t}$ (equation **??**) in two-way ranging. This evinces how two-way ranges are simply pairs of one way ranges. In the two-way case, however, the two different formulations account for the two possible reference times: since the measuring end (in this case, A) has recorded both t_1 and t_4 with its clock, each of the two is equally valid to reference a range observable.

Table 3.3: Summary of error sources affecting laser range measurements. Top half: instrument-related; bottom half: environment-related.

Error source	Magnitude	Type	Reference(s)	Context
Laser pulse measurement	4-5 mm	Random	Exertier et al. (2006)	SLR
	1.3-13 mm	Random	Dirkx et al. (2019)	ILR
	2 mm	Systematic	Schreiber et al. (2018)	SLR
Multi-photon signals	Several mm	Systematic	Dirkx, Noomen, et al. (2014)	ILR
		Systematic	Wilkinson et al. (2019)	SLR
Detector precision	3-6 mm	Random	Exertier et al. (2006)	SLR
	0-12 mm	Systematic	Schreiber et al. (2018)	SLR
	3 mm	Random	Dirkx et al. (2019)	ILR
	2 mm	Random	Schreiber et al. (2018)	SLR
Detector dark counts		Random	Degnan (2002)	ILR
		Random	Dirkx (2015, p. 67)	ILR
Timer	2-3 mm	Random	Exertier et al. (2006)	SLR
	Negligible	Systematic	Dirkx et al. (2019)	ILR
		Systematic	Wilkinson et al. (2019)	SLR
Clock		Random	Degnan (2002)	ILR
	1 mm	Random	Exertier et al. (2006)	SLR
	subm-mm	Random	Dirkx et al. (2019)	ILR
	Negligible	Systematic	Schreiber et al. (2018)	SLR
Other hardware errors	1-4 mm	Systematic	Exertier et al. (2006)	SLR
		Systematic	Dirkx (2015)	ILR
Atmosphere	1-3 mm	Systematic	Degnan (1993)	SLR
	4-6 mm	Systematic	Exertier et al. (2006)	SLR
	3 mm	Systematic	Schreiber et al. (2018)	SLR
	0.2-0.8 mm	Random	Kral et al. (2005)	SLR
	3-5 mm	Random	Exertier et al. (2006)	SLR
	1 mm	Random	Dirkx, Noomen, et al. (2014)	ILR
	<0.5 mm	Random	Dirkx et al. (2019)	ILR
Planetary albedo		Random	Degnan (2002)	ILR
		Random	Dirkx (2015)	ILR
Atmospheric-scattered sunlight		Random	Degnan (2002)	ILR
Planetary blackbody radiation		Random	Dirkx (2015)	ILR
Stellar background	Comparatively small	Random	Degnan (2002)	ILR
Sun light			Degnan (2002)	ILR
Stray light		Random	Dirkx (2015)	ILR
Target depth/signature	1-5 mm	Random	Exertier et al. (2006)	SLR
	1-50 mm	Random	Exertier et al. (2006)	LLR
	1-4 mm	Systematic	Exertier et al. (2006)	SLR
	3 mm	Systematic	Schreiber et al. (2018)	SLR
	25 mm	Systematic	Schreiber et al. (2018)	LLR

Systematic errors and random errors

The first consideration to be made when describing the sources of error in range measurements is the distinction between systematic and random errors. Systematic errors are caused by a bias in the measuring instrument, which results in a constant offset between the measured magnitudes and their true values. Many systematic errors can be accounted for through calibration, yet an imperfect calibration will result in a persisting bias. This bias is said to result in a loss of accuracy. Moreover, if this bias is not constant through time, calibration becomes more challenging and greater biases can

arise. The magnitude that defines how small the time variability of systematic errors is is the stability (Dirkx, 2015).

Random errors, on the other hand, are caused by unpredictable effects—also known as "noise"—that have an impact in the values measured by the instrumentation. Their stochastic nature makes them essentially a measurement uncertainty, hence they cannot be corrected for but can only be understood with proper statistical analysis. A higher level of random errors is said to cause a loss of precision.

Description of the sources of error in laser ranging measurements

The list of error sources in laser ranging given in Table 3.3 is split into two categories: caused by the instrumentation and caused by the environment. The former are mainly related to the measurement of the exact time of signal reception, whereas the latter are related to the distortion of the laser pulse throughout its travel and the existence of natural sources that can be misinterpreted as laser pulses by the instrumentation.

The first aspect that causes an error is the nature of the laser pulse itself. Exertier et al. (2006) stated that pulse lengths at the moment were between 35 and 1000 ps long; Dirkx, Vermeersen, et al. (2014) updated this figure to the 10 to 1000 ps range. Today, pulses of less than 15 ps are "routinely achieved by several SLR systems" (Schreiber et al., 2018). According to Lee et al. (2012), such pulses cannot be further narrowed to the femtosecond domain because "the bandwidth of photo-detection electronics is limited to the picosecond range".

The beam of photons in a laser pulse has a Gaussian profile through time and space (T. Murphy, 2001), hence if a single photon is detected there is a statistical uncertainty (random error) related to its position in the original pulse (e.g., Dirkx, Noomen, et al., 2014, Fig. 1). On the other hand, if more than one photon is detected, then the detector is more likely to be triggered by the front photons, hence yielding to a certain bias (systematic error). This error has still a random nature, but the bias arises from the fact that its expectancy (mean value) is no longer zero (e.g., Dirkx, Noomen, et al., 2014, Fig. 2), unlike in the single-photon case. On top of this, a non-Gaussian signal distribution in actuality can be the source of an extra systematic error (Schreiber et al., 2018).

Besides the random nature of the photon beams, the detector itself also constrains the quality of the measurements. Due to the non-instantaneous electronics and its finite temporal resolution, the detection signals will be sent to the timer with a certain offset. Although this signal rise and processing time can be calibrated to very high accuracy (Dirkx, 2015, p. 77), instabilities will be the source of a random error. Such instabilities can also cause the actual energy threshold value at which the detector is activated to be subject to a certain jitter (Schreiber et al., 2018). Exertier et al. (2006) quantify this overall random error to a magnitude of a few millimeters, with a greater contribution of the detector of the received pulses than that of the emitted ones. Additionally, Schreiber et al. (2018) give a slightly greater figure for a potential systematic error, which can be present in case calibration does not account for differences in received signal intensity or it is performed with a non-reciprocal setup.

Degnan (2002) and Dirkx (2015, p. 67) also mention dark counts (i.e., false signals in the detector due to quantum fluctuations, proportional to temperature) as a potential source of random error. However, Degnan (2001) details them to be "relatively low compared to the solar background", and states that they "can often be ignored".

The next hardware component that can introduce a measurement error is the event timer. Exertier et al. (2006) described a few mm uncertainty due to the finite resolution of event timers at the moment, and detailed the requirement of event timers more accurate than 5 ps as future development. Today, "the smallest division of modern event timing devices is just below of 3 ps" (Schreiber et al., 2018). Dirkx et al. (2019) describe new timers to have "sub-ps precision and a stability of several fs over a period of minutes to hours", which allows to neglect the contribution of this error source to the range error budget. As an example of such performance of new technologies, Wilkinson et al. (2019) highlight the timer presented by Panek et al. (2010), with a precision of less than 700 fs and a stability better than 30 fs over up to hours.

Next, the clock that provides the frequency standard to the timer can also be subject to instabilities that introduce deviations from the true range in the final measurements. Exertier et al. (2006) detailed such range errors to be of a few millimeters in the SLR network back then, and stated that clocks with a frequency accuracy of 10^{-16} should be able to provide "an absolute range at the 1 meter level and to reach the sub-centimetre level in measuring relative distances over several days of integration", referring to future ILR measurements. According to Dirkx et al. (2019), "a stability of about 10^{-15} over a typical ILR light time of 1000 s will result in 1 ps timing error (0.3-mm one-way range error)". Such stability is feasible with some of today's hydrogen masers used for Global Navigation Satellite System (GNSS) (e.g., Batori et al., 2021, Fig. 1), hence this error source is not expected to play a significant role. In the case of SLR, Schreiber et al. (2018) describe clock instabilities as "not concerning", since the level of stability in use today does not introduce significant errors anymore.

Finally, the electronic components other than those displayed in Figure 3.3 can also introduce systematic errors that need to be calibrated for. Again, imperfect calibration will introduce a source of bias, listed under "other hardware errors" in Table 3.3.

When it comes to environment-originated error sources, atmospheric effects are one of the largest contributors in case

at least one of the two range ends is ground-based in a celestial body with atmosphere (e.g., Earth's ground stations). According to Dirkx (2015, p. 64), "the influence of the atmosphere on the laser pulse can be divided into a deterministic contribution and a stochastic contribution". The deterministic one is caused by the refraction of the laser beam through the atmosphere, which effectively forces it through a longer path. The stochastic one, on the other hand, is caused by atmospheric turbulence, which acts as a series of random lenses through the atmosphere that introduce an extra refraction effect to the laser pulse.

The refraction effect can cause a light travel path between 2 and more than 10 meters longer, depending on the elevation of the pointing from ground (Combrinck, 2010, Fig. 9.3). However, it is currently understood and corrected for, through a series of models that compute the expected atmospheric delay in the post-processing of ranging measurements. The model by Mendes and Pavlis (2004), adopted by the Analysis Working Group of the International Laser Ranging Service (ILRS) in 2006 (Combrinck, 2010) and by International Earth Rotation Service (IERS) in its most recent conventions document (Luzum & Petit, 2012), achieves sub-millimeter accuracy for wavelengths between 355 nm and 1064 nm. As Schreiber et al. (2018) detail, the remaining bias is due to systematic errors in the measurement of the pressure, temperature and humidity conditions that need to be applied in the model.

The stochastic contribution caused by atmospheric turbulence was first measured by Kral et al. (2005), who identified "path fluctuations [...] in the range of units of picoseconds" in SLR. Dirkx, Noomen, et al. (2014), on the other hand, simulated the effect of Earth's atmospheric turbulence in laser ranging measurements to Mars, concluding that turbulence "could be a significant contributor to an ILR error budget", namely, a 1 mm increase to a turbulence-free error budget of 5.6 mm. The same study states that the Gaussian shape of the beam of photons "is not significantly influenced by atmospheric turbulence [...], except for pulse lengths on the order of picoseconds or shorter". As seen above, however, current SLR signals already have a duration of this order.

Next, environmental sources of noise must also be considered. Degnan (2002) analyzed the contributions of planetary albedo and local atmospheric scattering of solar light in an Earth-Mars laser link, and concluded that in a ground-based Martian transceiver, the noise from Earth's albedo "dominates local solar scattering in the Martian atmosphere", whereas the opposite is not true by a difference of several orders of magnitude. Dirkx (2015, p. 68) also mentions the planetary black body radiation as a source of noise together with its albedo. The noise from stellar background, on the other hand, is assessed by Degnan (2002) to be "relatively small compared to those induced by planetary reflections or emissions".

Direct sun light is also to be avoided from pointing at the receiver, since "the range of operating wavelengths (typical values are 532 and 1064 nm) coincides with the peak of the Sun's radiation output (883 nm)" (Dirkx, 2015, p. 67). Even if the receiver is not directly pointed towards the Sun, reflections in the optical system can lead to undesirable stray lights that also act as a source of noise. Degnan (2002) suggests physical means to avoid that, such as "the use of light baffling in the telescope, internal light tubes, and an enclosed detector box".

Finally, in case of passive two-way laser ranging, the laser pulse gets distorted with a signature by the surface it was reflected to. Although this is commonly a purpose-built retro-reflector (subsection 3.1.2), it can also be considered an environmental source of noise if the ranging is performed without it. For instance, it is possible to conduct laser ranging to space debris with no retro-reflectors (Wilkinson et al., 2019).

Summary of error budget in ILR

According to Dirkx et al. (2019), the sources of error for ILR will be essentially the same as they are today for SLR. This is due to the fact that the technology used in the emission and detection of laser pulses is essentially interchangeable, with the only difference that ILR is expected to use active, two-way ranging and thus there will not be any target signature errors related to the retrorreflectors.

The total budget of random errors, when adding all magnitudes listed in Table 3.3, gives a range of 7 to 28 mm. The upper limit of this range comes however from the older studies (e.g., Exertier et al., 2006), which were based on a technology that yielded greater errors than today (e.g., Dirkx et al., 2019). Additionally, random errors, if properly understood and characterized as such, can be mitigated by averaging several consecutive measurements. According to Dirkx et al. (2019), "1.0-4.3 mm precision averaged over 10 measurements (for 10–100 ps pulse length) may be achieved". When averaging over a greater number of single-photon detections, they state that "a limiting precision (but not accuracy) <0.1 mm" is possible.

Accuracy, on the other hand, depends on the remaining systematic errors. From Table 3.3, neglecting atmospheric effects, the most constraining magnitudes are the 0 to 12 mm bias caused by the detector according to Schreiber et al. (2018) and the several mm bias caused by multi-photon signals according to Dirkx, Noomen, et al. (2014). For the former, it is assumable that biases close to zero can be obtained if the best available hardware is used. For the latter, the full statistical development is presented by Dirkx, Noomen, et al. (2014) and it highly depends on the nature of the laser pulses used and the number of photons detected. In the particular case where the number of received photons is a uniformly distributed random variable between 1 and 4, they get an expected bias of 8 mm. This can be expected to get lower if

single-photon detections are more common, and in the limit where there are no multi-photon detections at all the resulting bias is zero. Thus, the only remaining source of bias is due to the calibration errors. Considering the 1-4 mm range given by Exertier et al. (2006), it is reasonable to assume a lower limit for the total bias of 2 mm, which can account for them together with sporadic multi-photon detections. This is consistent with the systematic error reported by Schreiber et al. (2018) due to the measurement of the laser pulses. The final consideration to be made, if at least one of the transceivers is ground-based, is to expect at least an extra 1 mm of bias due to atmospheric calibration errors (Dirkx, Noomen, et al., 2014).

3.3. Interplanetary Laser Ranging

3.3.1. Applications of interplanetary lasers

Although ranging distances is the main focus of this work among all possible interplanetary laser applications, it is worth contextualizing it within the other possibilities to better understand the corresponding technological evolution. Apart from ILR, laser technologies in interplanetary missions have been used for the following:

- **Communications**: since the frequency of light in the optical spectrum is considerably higher than that of the radio or microwave spectrum, laser pulses can be used to exchange information at higher data rates. The first space test of this technology was conducted by the lunar orbiter Lunar Atmosphere and Dust Environment Explorer (LADEE), which was able to operate at up to 622 Mbps (Boroson et al., 2014). Given the fact that this technology also requires the exchange of laser pulses that can be timed, high-accuracy ranging was also achieved "as a by-product of the lasercom links". In particular, the accuracy achieved was of 200 ps, which corresponds to 6 cm of two-way ranging. More recently, the Deep Space Optical Communications (DSOC) payload onboard NASA's Psyche spacecraft tested, for the first time, a laser communications link from beyond the Moon. Early results presented by Biswas et al. (2024) show how the spacecraft was able to send downlink data at a rate of 267 Mbps from a distance of 55 million km. According to the authors, "expanded functionality to include ranging and light science are anticipated".

  Despite the technological similarities between the technologies for laser communications and laser ranging, Dirkx (2015, p. 89) points out some fundamental differences: unlike in laser ranging setups, single-photon detection is not desirable for communications, and this also has the effect of pointing requirements being much more stringent. The amounts of information to be sent can also make communications systems work at much higher frequencies than ranging systems. This makes communications laser systems generally adaptable to give ranging results as a collateral output, whereas it does not happen the other way around. In any case, since this does not mean the two applications are incompatible, this opens the door for instrumentation conceived for the two purposes simultaneously: for instance, Hemmati et al. (2009) proposed a transponder design that could achieve both 1-mm resolution in ranging and up to 500 Mbps of downlink data rate.
- **Laser Time Transfer** (LTT): this is the technique by which two clocks can be accurately synchronized by sending each other precisely timed laser pulses. This procedure is not implicitly embedded in laser ranging, but it can be also performed with the same setup: as described by Dirkx (2015, p. 92), "time-transfer data can be extracted from a two-way link by using the up- and/or downlinks separately in addition to the full two-way observable" (equations 3.6 and 3.5). LTT can be approached by introducing the difference in proper time between the two ends of a range link in the parameter estimation process, although as shown by Dirkx et al. (2016) this can degrade the final formal uncertainties of the estimated parameters. LTT has been conducted multiple times in different ground-based and space-based experiments, although never at interplanetary distances (see Exertier et al., 2019 for a review).
- **Altimetry**: this is the procedure by which laser pulses are fired from a spacecraft orbiting a celestial body towards its surface, and from the detected reflected pulse one can infer information on the surface albedo, roughness and distance from it. This was first carried out by the Apollo missions around the Moon (Sjogren & Wollenhaupt, 1973), and has been applied in numerous occasions around other celestial bodies since (see Zhou et al., 2017 for a review). The technology required for this is the same as for ILR in terms of laser emitter and detector, timer and clock. This is the reason why some of the past tests of ILR (see subsection 3.3.2) have been performed using an altimeter on the receiving end instead of a dedicated transponder. This can be inconvenient, however, since it requires either the limitation of fully ILR operations or the introduction of hardware complications (Dirkx, 2015, p. 93).

3.3.2. Tehcnology evolution and current status

Although SLR and LLR had been a reality since the sixties, it was not until 1992 where a laser transmission was tried from Earth to a trans-lunar distance. It was with the Galileo Optical Experiment (GOPEX) experiment (Wilson & Lesh, 1993), onboard the Galileo spacecraft, when it was on its way to Saturn. Although it was not properly a laser ranging

experiment because the pulses were not time-tagged, it was useful to prove how the existing laser systems could be pointed at and received by spacecraft at distances of millions of kilometers. This was nevertheless a one-directional transmission, since the space instrument was not equipped with a transponder.

Following this, Degnan (1996) started discussing the feasibility of space-based laser transponders for ranging purposes, and presented a preliminary design shortly after (Degnan et al., 1998). The full theory of two-way interplanetary laser ranging with asynchronous transponders was presented by Degnan (2002), concluding that an Earth-Mars link was "within the SLR state-of-the-art", and supporting that "precise range measurements to the inner planets, or to spacecraft in orbit about the Sun, would certainly result in [...] important scientific results in the fields of planetary science, solar physics, fundamental physics, and general relativity".

Three years later, the technology was tested in two NASA missions: Mercury Surface, Space Environment, Geochemistry and Ranging (MESSENGER), equipped with the Mercury Laser Altimeter (MLA), on its way to Mercury; and the Mars Global Surveyor (MGS), equipped with the Mars Orbiter Laser Altimeter (MOLA), in orbit around Mars. Both experiments were laser altimeters, which had been designed to receive and send laser pulses to Earth as their secondary purpose. Although the latter failed in the sending, the reception of the laser pulses from Earth still allowed the determination of the clock offset within 10 ms (Dirkx, 2015, p. 84). MLA, on the other hand, worked successfully and achieved a range measurement with 20 cm precision (Smith et al., 2006). Both experiments are considered to have "demonstrated the possibility of interplanetary communication and precise ranging using modest power" (Neumann et al., 2006).

In 2015, the light detection and ranging (LIDAR) instrument onboard the Hayabusa 2 asteroid sample return mission exchanged laser pulses with the Earth with the aim of demonstrating "synchronous two-way laser ranging at planetary distances", together with testing new LTT techniques and checking the alignment of the instrument, which was to be used later when the spacecraft reached its target. In the end, the downlink signal was not established, hence two-way ranging and instrument alignment were not possible. Moreover, the received pulses were not well time-tagged and therefore one-way ranging was not sucessful either (Noda et al., 2017). Hence, this test was unable to provide figures on range measurement accuracy. Nevertheless, the authors claim that "the clock frequency of the LIDAR was adjusted successfully" as part of a LTT experiment.

The summary of all past ILR tests to date is presented in Table 3.4. As Dirkx et al. (2019) point out, "none of the demonstrations of ILR have been performed with dedicated hardware, and the attainable measurement accuracy has not yet been pushed to the limit of state of the art". In fact, the only operational laser ranging to a spacecraft further than those commonly tracked by SLR was conducted on the Lunar Reconaissance Orbiter (LRO), which is technically not ILR because it was within the Earth-Moon system. The aim of this one-way laser link was to provide ranging measurements and perform LTT (Bauer et al., 2017) by sending laser pulses from the Earth SLR infrastructure to LRO's Lunar Observer Laser Altimeter (LOLA) instrument. Although range data with a precision of about 10 cm was obtained, "complications in the analysis of the removal of clock noise from the one-way data [...] combined with the unexpectedly high quality of the (radio) Doppler data, resulted in laser ranging not being included in the operational orbit determination of LRO" (Dirkx, 2015, p. 84).

Table 3.4: Past experiments involving interplanetary laser ranging up to 2024

Year	Experiment	Mission	Link to be tested	Distance	Reference
1992	GOPEX	Galileo	Non-time-tagged, one-way	6 million km	Wilson and Lesh (1993)
2005	MLA	MESSENGER	Time-tagged two-way asynchronous	24 million km	Smith et al. (2006)
2005	MOLA	MGS	Time-tagged, one-way	80 million km	Abshire et al. (2006)
2015	LIDAR	Hayabusa 2	Time-tagged, two-way synchronous	6.6 million km	Noda et al. (2017)

None of the interplanetary laser events described above has used interferometric measurements. The first mission that has successfully carried out inter-spacecraft interferometric ranging is the GRACE Follow-On mission, which introduced the Laser Ranging Interferometer (LRI) instrument with respect to the microwave-only ranging instrument in the previous GRACE mission (Abich et al., 2019). These measurements were taken between two satellites separated by 220 ± 50 km, and the authors reported a noise level of 1 $\mathrm{nm}/\sqrt{\mathrm{Hz}}$ at frequencies above 100 mHz. Other than that, the LISA Pathfinder mission, which had the aim of proving the technology for space-based detection of GWs, reported "a displacement readout noise of $(3.48 \pm 0.3)\mathrm{fm}/\sqrt{\mathrm{Hz}}$ (Armano et al., 2016).

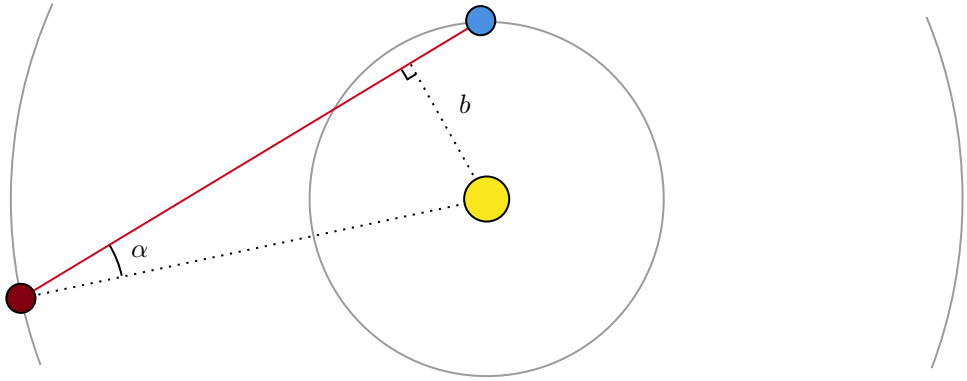

Figure 3.6: Schematic of the solar separation angle α and corresponding impact parameter b.

The future prospects for space-based interferometric ranging at greater distances are precisely in the context of the detection of GWs (subsection 5.5.4). The LISA mission is the one in a most advanced stage today, and its planned interferometric system is "similar" to the LRI instrument onboard GRACE Follow-On (GRACE-FO). There are, nevertheless, some key differences: LISA performs interferometry between two, non-parallel laser beams. While in ground-based detectors these have known lengths, in space the fact that the exact inter-spacecraft distance is unknown complicates the detection of nanometric range deformations due to space-time ripples. However, the designed approach does not require to fully determine the range with this precision: thanks to the procedure of "time-delay interferometry", measurements will be converted to be processed as if they were taken by a ground-based detector with fixed length, and the required inter-spacecraft range accuracy to do so is in the order of 1 m (Thorpe, 2010). Although recent calculations by Reinhardt et al. (2024) suggested that the proper precessing of LISA range data can achieve

3.3.3. Operational constraints

The main point of ILR is to have continuous, precise range observations, yet a full continuity without any interruption is impossible even with the most dedicated infrastructure. The different contraints of ILR operations are summarized below:

- **Occultation**: a laser link between two celestial bodies can be blocked by a third celestial body that happens to be in between. These events are rare, and can only be predicted through accurate ephemerides-based computations.
- **Planetary rotation**: in the case of ground-based transceivers, the link to a different celestial body is not available if the rotation of the host planet brings the transceiver to its far side from the perspective of the other end. On Earth, this can be overcome by the alternate usage of different stations around the globe, yet if a transceiver is sent to a different celestial body in a lander, it will likely be the only available link end there, hence ILR operations will only be able to happen during visibility windows.
- **Elevation angle**: in the case of a ground-based transceiver in a celestial body with atmosphere, even if there is direct visual contact between the two ends of the laser link, such link must be above a certain minimum elevation angle $\delta_{\text{min}} > 0$. This is because if the link is too close to the horizon, the tropospheric affectations will be too large to be corrected with the available atmospheric models.
- **Solar separation angle**: If the laser link points too close to the Sun, the solar plasma can interfere with it and turn the ranging measurement invalid. The solar separation angle of a laser link from Mars to the Earth is represented in Figure 3.6. The value of minimum solar separation angle so that ILR links work is not consistent through literature: Dirkx, Vermeersen, et al. (2014) consider it to be 5º; Fienga (2023a), on the other hand, consider a "very conservative limit" of 30º; whereas Cascioli et al. (2019) consider the limit to be determined by an impact parameter b of 7 solar radii, which viewed from Earth is equivalent to only 0.27º—this is consistent with the fact that they assumed radio ranging, which is able to achieve these small separations if the proper bands (X+Ka) are used.

  The constraint of the solar separation angle is more and more significant the smaller the heliocentric distance of the receiving end of the laser link is with respect to that of the emitting end. As seen in Figure 3.7, Venus is hardly ever seen from Mars with a solar separation angle of more than 30 degrees, whereas the inverse link happens most time well above this limit.

  The relative position of the Sun must also be taken into account together with the angle limit. For instance, in Figure 2.1 (left), the solar separation angle of Venus viewed from Mars is small and hence the mars transceiver is likely unable to receive correct laser pulses from Venus. However, since Venus is between Mars and the Sun and not

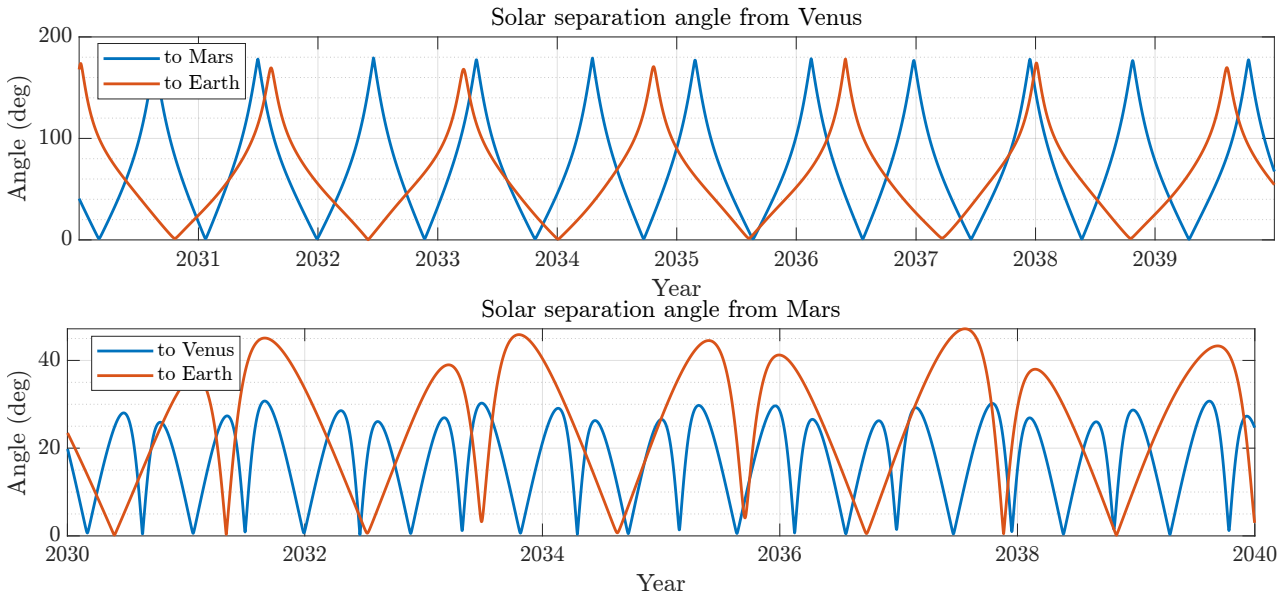

Figure 3.7: Solar separation angle from Venus and Mars throughout the decade of the 30's

on the other side, Venus will likely be perfectly able to keep receiving laser pulses from Mars. Hence, depending on the position of the Sun, ILR links under the limit solar separation angle will be either completely blocked or limited to one-way ranging.

3.3.4. Comparison with other tracking types

Traditionally, the tracking of interplanetary orbiters has been based on range-rate observations (Algorithm 4.2.2). These encode the rate of change of range measurements, i.e., the projection of the spacecraft velocities to the line of sight to the tracking station. The measurement of this magnitude is conducted by counting phase cycles of the received range (radio) signal, which is mathematically equivalent to measuring its Doppler effect. This is why range-rate observations are often called Doppler observations (e.g., Dirkx et al., 2019).

The observable equation of a Doppler observation is the numerical derivative of two consecutive range measurements over a defined integration time Δt_i (Dirkx, 2015): if $s^{(1)}_{BA_t}(t_1)$ and $s^{(1)}_{BA_t}(t_3)$ are two one-way range measurements referenced at their respective transmission times t_1 and t_3, then $\Delta t_i = t_3 - t_1$ and the one-way Doppler observation is described as

$$\dot{s}^{(1)}_{BA_t}(t_3) = \frac{s^{(1)}_{BA_t}(t_3) - s^{(1)}_{BA_t}(t_1)}{t_3 - t_1}. \tag{3.7}$$

Equivalent formulations can be defined for two-way Doppler observations, and both one- and two-way can be referenced at the reception times instead of the transmission times. In this work, however, we stick to the usage of one-way Doppler referenced at the transmission time.

4

Simulation strategies

The core of this work will be conducted by means of numerical simulations of the spacecrafts' trajectories, together with the planetary bodies of interest. The aim of this chapter is to provide the theoretical foundations upon these simulations will be based. Since the `Tudat`[1] software will be the main tool used, the following exposition is limited to the options it has available.

4.1. Orbit propagation

4.1.1. Equations of motion

The differential equation that describes the motion of a body in space can be generally stated as

$$\dot{\mathbf{x}} = f(\mathbf{x}, s, \mathbf{p}, \mathbf{u}), \tag{4.1}$$

where $\mathbf{x}$ is the state vector of the body to be propagated and $\dot{\mathbf{x}}$ is its time derivative. s is an independent variable (usually time), $\mathbf{p}$ is the set of environmental parameters, and $\mathbf{u}$ is the set of control parameters (e.g., thrust sources) of the propagated body. The exact definition of the state vector $\mathbf{x}$ depends on the chosen formulation of the equations of motion.

Cowell formulation

In the Cowell formulation, the state consists of the position and velocity vectors of the body, $\mathbf{r}$ and $\dot{\mathbf{r}}$, in an inertial, Cartesian reference frame. Its time derivative therefore includes the acceleration, which is the sum of all acceleration sources $\mathbf{a}_i$ acting on the body. Acceleration sources are a function of either the position $\mathbf{r}$ of the body, its velocity $\dot{\mathbf{r}}$, time t, environment $\mathbf{p}$ or control $\mathbf{u}$, or a combination of them.

$$\mathbf{x} = \begin{bmatrix} \mathbf{r} \\ \dot{\mathbf{r}} \end{bmatrix}; \tag{4.2}$$

$$\dot{\mathbf{x}} = \begin{bmatrix} \dot{\mathbf{r}} \\ \ddot{\mathbf{r}} \end{bmatrix} = \begin{bmatrix} \dot{\mathbf{r}} \\ \sum_i \mathbf{a}_i(\mathbf{r}, \dot{\mathbf{r}}, t, \mathbf{p}, \mathbf{u}) \end{bmatrix}. \tag{4.3}$$

Although this is the most common formulation of the equations of orbital motion due to its simplicity, it comes with the disadvantages of the need to calculate large and largely-varying values for the state derivative, which can compromise the accuracy of the result when using a numerical integrator (Dirkx & Mooij, 2019).

Encke formulation

The Encke formulation is suitable for situations in which the propagated body is subject to one main source of attraction (e.g., planet around which it orbits), so that all other acceleration sources can be interpreted as orbit perturbations that deviate it from the ideal trajectory, resulting of considering the main source a point-mass. This approach makes sense because the two-body problem of a massless body orbiting a point-mass has a closed analytical form, i.e., the Keplerian orbit solution.

Hence, in the Encke formulation, the state vector does not include absolute position and velocity but just their deviations from the Keplerian trajectory corresponding to its initial conditions. If such Keplerian trajectory were described by a

[1] Documentation is available at https://docs.tudat.space/en/latest/

position vector $\boldsymbol{\rho}$ and its corresponding velocity $\dot{\boldsymbol{\rho}}$, deviations in position and velocity from this trajectory are, respectively, $\Delta\mathbf{r} = \mathbf{r} - \boldsymbol{\rho}$ and $\Delta\dot{\mathbf{r}} = \dot{\mathbf{r}} - \dot{\boldsymbol{\rho}}$. As Wakker (2015, p. 551) shows, the state vector $\mathbf{x}$ and its derivative $\dot{\mathbf{x}}$ then become

$$\mathbf{x} = \begin{bmatrix} \Delta\mathbf{r} \\ \Delta\dot{\mathbf{r}} \end{bmatrix} \tag{4.4}$$

$$\dot{\mathbf{x}} = \begin{bmatrix} \Delta\dot{\mathbf{r}} \\ \frac{\mu}{\rho^3}\left(\mathbf{r}\mathcal{F}(q) - \Delta\mathbf{r}\right) + \sum_i \mathbf{a}_{p_i}(\mathbf{r}, \dot{\mathbf{r}}, t, \mathbf{p}, \mathbf{u}) \end{bmatrix}, \tag{4.5}$$

where μ is the gravitational parameter of the main body, $\rho = \|\boldsymbol{\rho}\|$, $\mathbf{a}_{p_i}$ is the i-th perturbation acceleration (i.e., not including the point-mass contribution of the main body), and

$$\mathcal{F}(q) = \frac{2q}{1+2q}\left(1 + \frac{1}{1+2q+\sqrt{1+2q}}\right); \tag{4.6}$$

$$q = \frac{1}{2}\left(\frac{r^2}{\rho^2} - 1\right), \tag{4.7}$$

with $r = \|\mathbf{r}\|$. This formulation gets rid of the problems caused by the computation of large state derivatives in the numerical integration, yet it has its own drawbacks: the final state will require a Keplerian trajectory to be also computed, and this can be the source of an additional error on top of the one arising from numerical integration (Dirkx & Mooij, 2019).

Gauss' planetary equations

The planetary equations describe the evolution of the orbital elements themselves with the influence of a perturbing acceleration $\mathbf{F}$. The Keplerian orbital elements are the semimajor axis a, eccentricity e, inclination i, argument of perigee ω, right ascension of the ascending node Ω, and true anomaly θ or mean anomaly M (e.g., Vallado, 2013, sec. 2.4.1), hence the state vector is

$$\mathbf{x} = \begin{bmatrix} a & e & i & \omega & \Omega & M \end{bmatrix}^\top, \tag{4.8}$$

which can be converted to Cartesian coordinates by means of known transformations (e.g., Vallado, 2013, sec. 2.6). In an orbit around a mass with gravitational parameter μ, and given a perturbation acceleration, again resulting from the sum of all perturbation sources p_i, i.e.,

$$\mathbf{F} = \boldsymbol{R}^{(RSW/I)} \begin{bmatrix} F_R \\ F_S \\ F_W \end{bmatrix} = \sum_i \mathbf{a}_{p_i}(\mathbf{x}, \dot{\mathbf{x}}, t, \mathbf{p}, \mathbf{u}), \tag{4.9}$$

expressed in the RSW frame (Vallado, 2013, Fig. 3-15), the Gauss planetary equations read (Dirkx & Mooij, 2019)

$$\frac{\mathrm{d}a}{\mathrm{d}t} = \frac{2ah}{\mu\left(1-e^2\right)}\left[e\sin(\theta)F_R + (1+e\cos(\theta))F_S\right] \tag{4.10a}$$

$$\frac{\mathrm{d}e}{\mathrm{d}t} = \frac{h}{\mu}\left[\sin(\theta)F_R + (\cos(\theta)+\cos E)F_S\right], \tag{4.10b}$$

$$\frac{\mathrm{d}i}{\mathrm{d}t} = \frac{\cos(\omega+\theta)r}{h}F_W, \tag{4.10c}$$

$$\frac{\mathrm{d}\omega}{\mathrm{d}t} = -\frac{h}{\mu}\frac{1}{e}\left[\cos(\theta)F_R - \left(\frac{2+e\cos(\theta)}{1+e\cos\theta}\right)\sin(\theta)F_S\right] - \frac{\cos(i)\sin(\omega+\theta)r}{h\sin(i)}F_W \tag{4.10d}$$

$$\frac{\mathrm{d}\Omega}{\mathrm{d}t} = \frac{\sin(\omega+\theta)r}{h\sin(i)}F_W \tag{4.10e}$$

$$\frac{\mathrm{d}M}{\mathrm{d}t} = n + \frac{h}{\mu}\frac{\sqrt{1-e^2}}{e}\left[\left(\cos(\theta) - \frac{2e}{1-e^2}\frac{r}{a}\right)F_R - \left(1+\frac{1}{1-e^2}\frac{r}{a}\right)\sin(\theta)F_S\right], \tag{4.10f}$$

where h is the angular momentum $h = \sqrt{\mu a\left(1-e^2\right)}$, n is the mean motion $n = \sqrt{\mu/a^3}$, and E is the eccentric anomaly, related to the mean anomaly M through the Kepler equation: $M = E - e\sin(E)$.

The disadvantage of this formulation is mainly the fact that it presents singularities for the cases when $e = 0$, $e = 1$, $\sin(i) = 0$ and $h = 0$. The latter happens if the velocity vector is perfectly aligned with the point mass. To overcome some of these singularities, Walker et al. (1985) introduced the Modified Equinoctial Elements:

$$p = \begin{cases} a\left(1-e^2\right) & (e \neq 1) \\ 2a & (e = 1) \end{cases}; \tag{4.11a}$$

$$f = e\cos(\omega + I\Omega); \tag{4.11b}$$
$$g = e\sin(\omega + I\Omega); \tag{4.11c}$$
$$h = \tan^I\left(\frac{i}{2}\right)\sin(\Omega); \tag{4.11d}$$
$$k = \tan^I\left(\frac{i}{2}\right)\cos(\Omega); \tag{4.11e}$$
$$L = \omega + I\Omega + \theta, \tag{4.11f}$$

where I is a seventh parameter set to either 1 or -1 to avoid the singularities at every instant. In `Tudat`, I must be manually set at the beginning of the propagation, but it is also possible to set it as a seventh state element with a defined changing routine (Dirkx & Mooij, 2019).

The re-formulation of the Gaussian planetary equations using the Modified Equinoctial Elements then reads (Walker et al., 1985, Eq. 9, with corrections by Walker, 1986):

$$\frac{\mathrm{d}p}{\mathrm{d}t} = \frac{2pF_S}{w}\sqrt{\frac{p}{\mu}}; \tag{4.12a}$$
$$\frac{\mathrm{d}f}{\mathrm{d}t} = \sqrt{\frac{p}{\mu}}\left[F_R\sin(L) + \frac{(w+1)\cos(L)+f}{w}F_S - \frac{g(h\sin(L)-k\cos(L))}{w}F_W\right]; \tag{4.12b}$$
$$\frac{\mathrm{d}g}{\mathrm{d}t} = \sqrt{\frac{p}{\mu}}\left[-F_R\cos(L) + \frac{(w+1)\sin(L)+g}{w}F_S + \frac{f(h\sin(L)-k\cos(L))}{w}F_W\right]; \tag{4.12c}$$
$$\frac{\mathrm{d}h}{\mathrm{d}t} = \sqrt{\frac{p}{\mu}}\frac{s^2F_W}{2w}\cos(L); \tag{4.12d}$$
$$\frac{\mathrm{d}k}{\mathrm{d}t} = \sqrt{\frac{p}{\mu}}\frac{s^2F_W}{2w}\sin(L); \tag{4.12e}$$
$$\frac{\mathrm{d}L}{\mathrm{d}t} = \sqrt{\mu p}\left(\frac{w}{p}\right)^2 + \sqrt{\frac{p}{\mu}}\frac{h\sin(L)-k\cos(L)}{w}F_W, \tag{4.12f}$$

where $s^2 = 1 + h^2 + k^2$ and $w = 1 + f\cos(L) + g\sin(L)$. This formulation gets rid of most of the singularities from the original formulation with Keplerian elements, but they still remain for $i = 0°$ when $I = -1$ and $i = 180°$ when $I = 1$ (Dirkx & Mooij, 2019).

Unified State Model

A suitable formulation of the equations of motion with no singularities, stable over long propagations and with few fast-varying variables is the Unified State Model (USM). Three variations of the formulation exist, including the one describing the 3D orientation with quaternions, the one doing so with Modified Rodrigues Parameters, and a more elaborate one named USM, introduced by Vittaldev et al. (2012). The equations of the three variations of the model are not reproduced here for the sake of compactness. Moreover, although the three have been tested in the integrator analyses presented in Appendix A, they have not played any significant role in the present research.

4.1.2. Sources of acceleration

In the equations of motion presented above, the orbiting body has been said to be influenced by either a series of acceleration sources (equation 4.3) or a main point-mass with gravitational parameter μ and a series of extra accelerations acting as perturbations (equations 4.5 and 4.9). The most common sources of acceleration influencing such perturbations are listed below.

Gravity of a non-spherical body

Let B be a body with mass M and gravitational parameter $\mu_B = GM$ located at a position $\mathbf{r}_B$. The acceleration caused to a different, point-mass body A, located at a position $\mathbf{r}_A$, is equal to the gradient of the gravity potential U_B at the location $\mathbf{r}_A$:

$$\ddot{\mathbf{r}}_A = \nabla U_B(\mathbf{r}_A). \tag{4.13}$$

Body B can be considered the same as a point-mass with the same μ if such body is perfectly spherical and has radially symmetric density (e.g., Curtis, 2014, app. E). In this case, the potential gravity field U_B at any arbitrary point $\mathbf{r}$ is

$$U_B = \frac{\mu_B}{r}, \tag{4.14}$$

where $r = \|\mathbf{r} - \mathbf{r}_B\|$, and therefore applying equation (4.13)

$$\ddot{\mathbf{r}}_A = -\frac{\mu_B}{r^3}\left(\mathbf{r}_A - \mathbf{r}_B\right). \tag{4.15}$$

In real life, however, bodies do not have a perfectly spherical shape nor uniform density, and thus the gravity field U can take an arbitrary spheroid shape. This can be described by means of the spherical harmonic series, which reads (e.g., Vallado, 2013, sec. 8.6.1)

$$U_B\left(\mathbf{r}\right) = \frac{\mu}{r}\sum_{l=0}^{\infty}\sum_{m=0}^{l}\left(\frac{R}{r}\right)^l P_{lm}(\sin(\phi))\left(C_{lm}\cos(m\theta) + S_{lm}\sin(m\theta)\right). \tag{4.16}$$

In this expression, $\mathbf{r}$ is the position of an arbitrary point with respect to the center of mass of body B, and $r = \|\mathbf{r}\|$. R is the reference radius of body B (typically equatorial), and ϕ and θ are, respectively, the latitude and longitude of the $\mathbf{r}$ position as seen from body B. P_{lm} are the Legendre polynomials of degree l and order m, while C_{lm} and S_{lm} are the spherical harmonic coefficients. The notation presented in equation (4.16) has unnormalized coefficients—in the normalized case, one would find $\bar{P}_{lm}$, $\bar{C}_{lm}$ and $\bar{S}_{lm}$ instead of P_{lm}, C_{lm} and S_{lm} (Dirkx & Cowan, 2023). In `Tudat`, the normalized formulation is used. Since the infinite terms cannot be computed by a finite computational power, terms in the harmonic expansion are only computed up to a user-defined maximum order l_{max}.

Relativistic influence

Note to the reader: the final implementation has neglected all types of relativistic influence, as described in section 3.3.1 of Part IV.

Equation (4.13) represents the Newtonian understanding of gravity, but since Einstein (1915) published his General Theory of Relativity, this classical conception is known to be incomplete. Although Einstein described a completely different model, in which gravity is not a force but a deformation of the space-time reference frame, in practice this can be translated as a series of correction terms (i.e., perturbations) to the Newtonian model.

The Einstein–Infeld–Hoffmann equations (Einstein et al., 1938) give the expansion of terms that approximate the effect of General relativity to a body A influenced by N point-masses. The first term of such expression is the known Newtonian expression for gravity, i.e., equation (4.15). For N bodies, each of them causes its own separate influence following this expression, and the total effect over body A is the linear combination of all. According to the Einstein–Infeld–Hoffmann equations, however, this acceleration is also affected by higher-order terms, which are a nonlinear contribution of all N bodies, causing a total extra effect over A that responds to

$$\begin{aligned}\Delta\ddot{\mathbf{r}}_A = -\frac{1}{c^2}\sum_{B\neq A}\frac{\mu_B}{r_{BA}^3}\left(\mathbf{r}_A - \mathbf{r}_B\right)\Bigg[\|\dot{\mathbf{r}}_A\|^2 + 2\|\dot{\mathbf{r}}_B\|^2 - 4\left(\dot{\mathbf{r}}_A\cdot\dot{\mathbf{r}}_B\right) - \frac{3}{2}\left(\frac{\mathbf{r}_A - \mathbf{r}_B}{r_{BA}}\cdot\dot{\mathbf{r}}_B\right)^2 - \\ -4\sum_{C\neq A}\frac{\mu_C}{r_{CA}} - \sum_{C\neq B}\frac{\mu_C}{r_{CB}} + \frac{1}{2}\left(\left(\mathbf{r}_B\cdot\mathbf{r}_A\right)\cdot\ddot{\mathbf{r}}_B\right)\Bigg] + \\ + \frac{1}{c^2}\sum_{B\neq A}\frac{\mu_B}{r_{BA}^3}\left[\left(\mathbf{r}_A - \mathbf{r}_B\right)\cdot\left(4\dot{\mathbf{r}}_A - 3\dot{\mathbf{r}}_B\right)\right]\left(\dot{\mathbf{r}}_A - \dot{\mathbf{r}}_B\right) + \frac{7}{2c^2}\sum_{B\neq A}\frac{\mu_B}{r_{BA}}\ddot{\mathbf{r}}_B + \mathcal{O}(c^{-4}),\end{aligned} \tag{4.17}$$

where $r_{XY} = \|\mathbf{r}_X - \mathbf{r}_Y\|$. In the case of two-body motion affetced by GR around a massive body B with $\mathbf{r}_B = \dot{\mathbf{r}}_B = \ddot{\mathbf{r}}_B = 0$, the Einstein–Infeld–Hoffmann equation (4.17) reduces to the correction term known as the Schwarzschild term (Dirkx & Mooij, 2020):

$$\Delta\ddot{\mathbf{r}}_A = -\frac{1}{c^2}\frac{\mu_B}{r_{BA}^3}\mathbf{r}_A\left(\|\dot{\mathbf{r}}_A\|^2 - 4\frac{\mu_B}{r_A}\right) + \frac{1}{c^2}\frac{\mu_B}{r_A^3}\left(\mathbf{r}_A\cdot 4\dot{\mathbf{r}}_A\right)\dot{\mathbf{r}}_A. \tag{4.18}$$

Moreover, if the massive body B has a non-negligible angular momentum $\mathbf{J}$ associated with its rotation, an additional effect known as the Lense-Thirring (LT) correction must be also taken into account. This is caused by the rotational dragging of the space-time fabric:

$$\Delta\ddot{\mathbf{r}} = 2\frac{\mu}{c^2 r^3}\left[\frac{3}{r^2}(\mathbf{r}\times\dot{\mathbf{r}})(\mathbf{r}\cdot\mathbf{J}) + (\dot{\mathbf{r}}\times\mathbf{J})\right] \tag{4.19}$$

Finally, if the reference frame in which the equations are solved has a non-null angular rate $\dot{\mathbf{R}}$, a relativistic correction must be added besides all the classical velocity transformation terms. This is known as the De Sitter correction:

$$\Delta\ddot{\mathbf{r}} = 3\left[\dot{\mathbf{R}}\times\left(\frac{-\mu\mathbf{R}}{c^2R^3}\right)\right]\times\dot{\mathbf{r}} \tag{4.20}$$

Aerodynamic acceleration

Note to the reader: in the final implemented simulations, spacecraft orbits have been selected to be high enough as to neglect the effect of any aerodynamic acceleration.

In the environment of a planetary atmosphere, the air molecules that impact the orbiting body will cause a non-conservative force that needs to be accounted for. Just as in classical fluid mechanics, this force is said to be proportional to the air density ρ, the cross-sectional surface S of the body and its velocity squared with respect to air, with a proportionality constant equal to the aerodynamic coefficient.

The general model for aerodynamic influence on an orbiting body is generally (e.g., Vallado, 2013, p. 551) described as drag-only, which means that the resulting acceleration is in the exact opposite sense as the velocity vector, and hence there is need for a single aerodynamic coefficient, named drag coefficient C_D. However, this does not take into account possible non-symmetries in the orbiting body, which can deviate the resulting force from being purely drag. A more general formulation can be expressed as (Dirkx & Mooij, 2020)

$$\Delta\ddot{\mathbf{r}} = -\frac{\rho(\mathbf{r},t)S}{m}\|\mathbf{v}_{\text{rel}}\|^2 \boldsymbol{R}^{(I/B)}\boldsymbol{R}^{(B/Aero)}\begin{bmatrix} C_D \\ C_S \\ C_L \end{bmatrix}, \tag{4.21}$$

where m is the mass of the orbiting body, $\mathbf{v}_{\text{rel}}$ is its relative velocity with respect to the atmosphere, and C_D, C_S and C_L are, respectively, the coefficients of drag, side force and lift. Since these coefficients are defined in the aerodynamic frame, the rotation matrices $\boldsymbol{R}^{(B/Aero)}$ (from aerodynamic to body frame) and $\boldsymbol{R}^{(I/B)}$ (from body to inertial frame) need to be introduced. As per the relative velocity, if the atmosphere rotates mutually with its host body, which rotates at an angular speed $\boldsymbol{\omega}$, then

$$\mathbf{v}_{\text{rel}} = \dot{\mathbf{r}} - \boldsymbol{\omega} \times \mathbf{r}. \tag{4.22}$$

Of course, the presence of winds modifies this relative velocity, but wind models are typically used in atmospheric (e.g., entry) maneuvers rather than fully orbital propagation. In `Tudat`, any custom wind model depending on position and time can be set up by the user.

This model relies on two different quantities that must be known in order to compute the aerodynamic acceleration: the air density and the aerodynamic coefficients. Several models for both magnitudes exist today, although they come with their limitaions:

- **Atmospheric density models**: air properties strongly depend on the altitude from ground, although other position and time-dependent parameters can also play a role.
  - Standard atmospheric models are a function of altitude h only, and they have the lowest computational cost. The most simple one is the exponential atmosphere, which reads

    $$\rho(h) = \rho_0 e^{-\frac{h}{H_s}}, \tag{4.23}$$

    where the reference density ρ_0 and scale height H_s are the two parameters, generally empirically estimated, that define the density curve. On Earth, the two most widespread of such models are the *U.S. Standard Atmosphere* (1976) and the International *Standard Atmosphere* (1975), which consist of different layers of exponential atmospheres.
  - Reference atmospheric models depend on the full position vector (i.e., taking into account differences in latitude and longitude) as well as time (i.e., solar cycle and night/day cycle). On Earth, these variations can lead to density oscillations of up to five orders of magnitude at a 400 km altitude (Doornbos, 2012, Fig. 2.1). Several of such models exist (e.g., Vallado, 2013, Fig. 8-16), and they are usually empirical, i.e., based on a series of parameters estimated experimentally, generally from satellite observations. This makes them considerably more accurate than standard models, although also much more computationally expensive. One of the most common in use today is the NRLMSISE-00 (Picone et al., 2002), which was updated by Emmert et al. (2021) to the NRLMSISE-2.0 version. Among all other reference atmospheric models available today, Ding et al. (2023) found that NRLMSISE-00 is the best performing in orbits around 485 km when multi-station satellite tracking is conducted.

  In `Tudat`, USSA76 and NRLMSISE-00 are available for the Earth atmosphere. For other system bodies, an exponential atmosphere (equation 4.23) can be set with any input values of reference density and scale height.
- **Aerodynamic coefficient models**: although "it has been a common practice to assume a constant C_D equal to 2.2 for low earth orbit flying satellites, it is [nowadays] widely accepted that the drag coefficient is not constant and can present very different values depending on the spacecraft shape and the atmospheric temperature and composition

at the flying altitude" (Prieto et al., 2014). In reality, the aerodynamic coefficients for orbital flight are simply an attempt to characterize in a simple manner the behavior of individual particles from a rarefied flow impacting the surfaces of the satellite. Livadiotti et al. (2020) review different lower-level methods to model such behavior, and conclude that "an easy-to-implement model applicable to different scattering regimes and to different gas-solid systems is still to be defined".

In `Tudat`, any desired set of C_L, C_S and C_D coefficients can be set, and equation (4.21) is applied automatically if aerodynamic effects are turned on and the proper atmospheric environments are set up.

Radiation pressure

It is well known that photons, despite being massles, do carry momentum that is transferred when impacting a solid body. This has the effect of introducing an extra acceleration due to radiation pressure, which, if the body is uniformly radiating, obeys (e.g., Vallado, 2013, Eq. 8-43)

$$\Delta\ddot{\mathbf{r}} = \frac{P}{4\pi c}\frac{C_r A}{m}\frac{\mathbf{r}}{\|\mathbf{r}\|^3}, \tag{4.24}$$

where P is the total radiative power of the emitting source, c is the speed of light in vacuum, $\mathbf{r}$ is the vector from the emitting source to the orbiting body, C_r is the radiation pressure coefficient, A is the cross-sectional area of the body as viewed from the radiating source, and m is its mass. The source of radiation is usually the Sun, which causes the perturbation known as solar radiation pressure (SRP), yet in applications requiring very high accuracy it can also be due to other celestial bodies: for instance, when analyzing Global Positioning System (GPS) and Galileo satellites, Svehla (2018) found that Earth's planetary radiation contributes approximately "-14.6 mm to the constant bias in the radial direction".

The modeling of SRP based on equation (4.24) mainly depends on the knowledge of the spacecraft's cross-sectional area A and radiation pressure coefficient C_r. In `Tudat`, the latter can be defined by the user whereas the former depends on the model of spacecraft. If a cannonball model is used, the value of A is constant regardless of the attitude, whereas if a paneled model is defined, the rotational dynamics of the spacecraft will also need to be propagated. For translational-only propagations, therefore, a cannonball SRP model is the most suitable. Finally, the exact value of the SRP acceleration will also depend on the exact power irradiated by the Sun at every instant.

There are several established models for SRP that take these factors into account, and their inaccuracies are evinced by the differences caused by chosing one or another. Analyzing the orbits of GPS satellites, Duan and Hugentobler (2021, Tab. 9) found that the final RMS of orbit determination fits can vary up to 3 cm for non-eclipsed orbits and 20 cm for eclipsed orbits.

Finally, another very slight perturbation caused by radiation pressure is the antenna thrust, caused by the reaction momentum inflected by the photons beamed from the spacecraft antennae. In Galileo satellites, this was found to cause a constant bias in the orbit determination of approximately 5 cm (Zajdel et al., 2017, Fig. 8). Whether or not similar effects will be observable due to the emission of highly energetic laser beams in ILR missions is still unclear.

Third-body influence

Let A still be an orbiting body around body B. The extra acceleration induced by a point-mass body C to the two-body motion of A around B is (e.g., Wakker, 2015, Eq. 21.31)

$$\Delta\ddot{\mathbf{r}}_A = \mu_C\left(\frac{\mathbf{r}_C - \mathbf{r}_A}{\|\mathbf{r}_C - \mathbf{r}_A\|^3} - \frac{\mathbf{r}_C - \mathbf{r}_B}{\|\mathbf{r}_C - \mathbf{r}_B\|^3}\right). \tag{4.25}$$

This expression evinces how the third-body accelerations do not necessarily point towards those third bodies, but to a direction which is the result of subtracting, from a vector pointing to body C from body A, a vector pointing to body C from body B. Hence, the closer B and A are, the less dissimilar those vectors will be and hence the smaller the result of the subtraction. In the limit of body A being at the same point where body B is, the third-body perturbations do not have any impact. This is the reason why low planetary orbits are less affected by third-body perturbations, as described in **??**.

4.1.3. Integration methods

The description hereinabove addresses the formulation and computation of the derivatives in the equations of motion, but the next step is to integrate them by means of a numerical algorithm. The details of such methods are out of the scope of this report, but with the aim of summarizing the available tools to carry out the simulations, the list of implemented integrators in `Tudat` is given below:

- **Multi-stage** integrators, ranging from the classical fixed step size Runge-Kutta of 4th order to variable step size formulations of higher order such as the Runge-Kutta Dormand-Prince of order 8(7), the Runge–Kutta–Fehlber of

order 12(10), or Feagin's integrator of order 14(12). According to the `Tudat` documentation, in many typical cases, the Dormand-Prince variation of order 8(7) or the Fehlber variation of order 7(8) "provide a good trade-off between accuracy, runtime, robustness and output density".

- **Extrapolation** integrators based on the Bulirsch-Stoer method with both fixed or variable step sizes, and different number of evaluations to be made at each step. According to the `Tudat` documentation, these give "generally good trade-off between computational efficiency and solution quality".
- **Multi-step** integrators of variable step size based on the Adams-Bashforth-Moulton formulation. According to the `Tudat` documentation, this results in typically short time steps, hence it is suitable in cases where output density is a strong constraint.

Each particular application of astrodynamics simulations has its own optimal trade-off between accuracy of the results and computational cost. The suitable choice of problem formulation and integrator to be used in the present study will be assessed in later stages.

4.2. Orbit determination and estimation

Theory of orbit determination encompasses mainly two possible approaches: full estimation and covariance analyses. These are developed below, respectively, in subsection 4.2.2 and subsection 4.2.3. Before these, a set of mathematical definitions essential for both approaches is detailed in subsection 4.2.1.

4.2.1. Introductory definitions

State and extended state

Just as in subsection 4.1.1, let $\mathbf{x}_i$ be a 6×1 vector with the state of an orbiting body, consisting of its Cartesian position and velocity:

$$\mathbf{x}^{(i)} = \begin{bmatrix} x & y & z & \dot{x} & \dot{y} & \dot{z} \end{bmatrix}^\top . \tag{4.26}$$

During the propagation of multiple bodies, it is common practice to define a single state vector $\mathbf{x}^{(i)}$ containing the state vectors of each body i, which is therefore sized $6 \times n_b$, where n_b is the number of bodies:

$$\mathbf{x} = \begin{bmatrix} \left(\mathbf{x}^{(1)}\right)^\top & \dots & \left(\mathbf{x}^{(n_b)}\right)^\top \end{bmatrix}^\top . \tag{4.27}$$

In addition, let $\mathbf{p}$ be the vector of parameters of the physical model to be estimated, sized $n_p \times 1$:

$$\mathbf{p} = \begin{bmatrix} p_1 & p_2 & \cdots & p_{n_p} \end{bmatrix}^\top . \tag{4.28}$$

Examples of p_i are the aerodynamic coefficients of a spacecraft or the gravitational parameter and/or spherical harmonic coefficients of a celestial body. Any of the control parameters, denoted $\mathbf{u}$ in equation (4.1), can also be included in $\mathbf{p}$—the separation is hereinafter removed for the sake of simplicity. The fundamental distinction between $\mathbf{x}$ and $\mathbf{p}$ is that the former contains trajectory parameters only, whereas the latter contains all other parameters to be estimated. Another important remark si that while in equation (4.1) $\mathbf{p}$ referred to the whole set of environmental parameters that affect the orbit propagation, here and from now on $\mathbf{p}$ only refers to the selection of such environmental parameters to be estimated.

Vectors $\mathbf{x}$ and $\mathbf{p}$ can be grouped into a single vector $\mathbf{y}$, sized $(6 + n_p) \times 1 = n \times 1$, which allows to unify the estimation of the trajectory and the model parameters (Montenbruck & Gill, 2001, p. 259):

$$\mathbf{y} = \begin{bmatrix} \mathbf{x} \\ \mathbf{p} \end{bmatrix} . \tag{4.29}$$

Observations and design matrix

A state $\mathbf{x}$ and a set of model parameters $\mathbf{p}$ will lead to a closed value for an expected range observation z, or set $\mathbf{z} = \begin{bmatrix} z_1 & \cdots & z_m \end{bmatrix}^\top$ if m observation stations are available. This relationship can be compactly expressed as

$$\mathbf{z} = \mathbf{h}(\mathbf{y}), \tag{4.30}$$

where in the case of time-tagged laser ranging observables, function h has the form of equation (3.5) or (3.6). Let $\boldsymbol{H}$ be the $m \times 6$ Jacobian matrix of the observable function $\mathbf{h}$ with respect to the state $\mathbf{x}$, named the "design matrix":

$$\boldsymbol{H} = \frac{\partial \mathbf{h}(\mathbf{y})}{\partial \mathbf{x}} = \begin{bmatrix} \frac{\partial z_1}{\partial x_1} & \cdots & \frac{\partial z_1}{\partial x_n} \\ \vdots & \ddots & \vdots \\ \frac{\partial z_m}{\partial x_1} & \cdots & \frac{\partial z_m}{\partial x_n} \end{bmatrix}. \tag{4.31}$$

It is worth noting that notation for matrix $\boldsymbol{H}$ is not consistent through literature: Montenbruck and Gill (2001) name it $\boldsymbol{G}$, whereas Tapley et al. (2004) name it $\tilde{\boldsymbol{H}}$. Here the notation $\boldsymbol{H}$ is preserved for consistency with Siemes (2023)[2].

Covariance matrices

If $\mathbf{y}$ were known to perfect accuracy, its associated uncertainty would be zero. This is however impossible in real life: in actuality, any value of $\mathbf{y}$ will be the result of an estimation $\hat{\mathbf{y}}$, which will deviate from the true $\mathbf{y}$ by $\Delta\mathbf{y} = \hat{\mathbf{y}} - \mathbf{y}$. In this case, the state resulting from the estimation will have an associated covariance matrix (Tapley et al., 2004, eq. 4.16.5)

$$\boldsymbol{P}_{\mathbf{y}} = E\left[\Delta\mathbf{y}\Delta\mathbf{y}^{\top}\right] = \begin{bmatrix} E\left[(\hat{y}_1 - y_1)(\hat{y}_1 - y_1)\right] & \cdots & E\left[(\hat{y}_1 - y_1)(\hat{y}_n - y_n)\right] \\ \vdots & \ddots & \vdots \\ E\left[(\hat{y}_n - y_n)(\hat{y}_1 - y_1)\right] & \cdots & E\left[(\hat{y}_n - y_n)(\hat{y}_n - y_n)\right] \end{bmatrix}. \tag{4.32}$$

Similarly, an observation vector $\mathbf{z}$ will contain measurements $\hat{z}_i$ subject to a measurement error, that make them differ from the true z_i. Their covariance matrix can thus be written as

$$\boldsymbol{P}_{\mathbf{z}} = E\left[\Delta\mathbf{z}\Delta\mathbf{z}^{\top}\right] = \begin{bmatrix} E\left[(\hat{z}_1 - z_1)(\hat{z}_1 - z_1)\right] & \cdots & E\left[(\hat{z}_1 - z_1)(\hat{z}_m - z_m)\right] \\ \vdots & \ddots & \vdots \\ E\left[(\hat{z}_m - z_m)(\hat{z}_m - z_m)\right] & \cdots & E\left[(\hat{z}_m - z_m)(\hat{z}_m - z_m)\right] \end{bmatrix}. \tag{4.33}$$

Each quantity $E\left[(\hat{x}_1 - x_1)(\hat{x}_2 - x_2)\right]$ is known as the covariance between variables x_1 and x_2. Equations (4.32) and (4.33) cannot be applied straightforwardly, precisely because the true, errorless values of each variable are unknown. The common approach in statistics (e.g., Montenbruck and Gill, 2001, p. 263), if M samples of both x_1 and x_2 are available, is to compute their averages $\bar{x}_1$ and $\bar{x}_2$ and calculate their covariance as

$$\mathrm{Cov}(x_1, x_2) = \sigma_{x_1}\sigma_{x_2} \approx \frac{1}{M}\sum_{k}^{M}\left[(x_{1,k} - \bar{x}_1)(x_{2,k} - \bar{x}_2)\right], \tag{4.34}$$

where $x_{i,k}$ represents the k-th realization of variable x_i. This assumes that the average is an effective way to estimate the mathematical expectancy, and the expectancy is only the true value if only random errors, and not systematic ones, come into play. Hence, the resulting covariances will indicate the expected variation in different realizations of the same measurement due to random errors.

In the context of orbit determination, however, the observations vector $\mathbf{z}$ contains all observations from different sources at an instant t_i, hence each individual observation z_j is at a specific instant with a specific source and therefore cannot get multiple realizations to apply equation (4.34)—doing so would mean getting observations at different times, hence their expected value would not be the same due to the relative motion of the two range ends. Therefore, matrix $\mathbf{P}_{\mathbf{z}}$ is commonly filled by the expected variance due to random errors of the instrumentation. Different measurement stations are generally uncorrelated, hence $\sigma_{z_i}\sigma_{z_j} = 0\ \forall i \neq j$, and the resulting covariance matrix of the observations becomes

$$\boldsymbol{P}_{\mathbf{z}} = \begin{bmatrix} \sigma_{z_1}^2 & & \\ & \ddots & \\ & & \sigma_{z_m}^2 \end{bmatrix}, \tag{4.35}$$

where each $\sigma_{z_j}^2$ is the variance of observations from station j due to random errors. Nonzero off-diagonal terms would imply that the observations are not independent, and their uncertainty levels depend on each other with to the extent described by such values. The covariance matrix of the state, $\boldsymbol{P}_{\mathbf{y}}$, on the other hand, must be computed as part of the state estimation process (subsection 4.2.3).

[2] In Part IV, we switch to the more typical notation of $\boldsymbol{H} = \partial\mathbf{h}/\partial\mathbf{x}_0$.

The probability ellipsoid

Matrix $\boldsymbol{P}_{\mathbf{y}}$ is associated to a key concept of orbit estimation: the probability ellipsoid. If state $\mathbf{y}$ only contains the three components of position $\mathbf{r}$, then the equation (Tapley et al., 2004, eq. 4.16.6)

$$\mathbf{y}^{\top}\boldsymbol{P}_{\mathbf{y}}^{-1}\mathbf{y} = l^2 \tag{4.36}$$

gives the three-dimensional ellipsoid that limits the contour where the state is truly located with a confidence of l-σ. Since the state $\mathbf{y} = \mathbf{r}$ consists of three components only, the confidence value must be taken from the cumulative distribution function of the three-dimensional Gaussian distribution: e.g., 0.971 for $l = 3$. More generally, the confidence level for a given l and a covariance matrix of a vector $\mathbf{y}$ sized n is given by the χ^2 distribution of n degrees fo freedom evaluated at l^2. This follows from the fact that the left-hand side of equation (4.36) is a Mahalanobis Distance, known to follow such χ^2 distribution (e.g., Cano et al., 2023). If $\mathbf{y}$ has $n > 3$ components (recall from equation 4.29 that typically $n > 6$), then equation (4.36) gives a hyper-ellipsoid in the whole parameter space. The diagonalization of matrix $\boldsymbol{P}_{\mathbf{z}}$ gives the basis that defines the orientation of the ellipsoids' axes, which have a semi-length equal to each of the corresponding eigenvalues squared.

Consider parameters

The covariance matrix is an efficient way to assess the uncertainty of a certain set of parameters, but it is "often found to be too optimistic in the presence of systematic force and measurement model errors" (Montenbruck & Gill, 2001, p. 265). This is especially true regarding environmental parameters: they can be estimated (hence included in vector $\mathbf{p}$), or neglected if there are not enough observations to accurately solve for them in the estimation. However, if this is the case, the uncertainty due to imperfect knowledge or model simplification in the constant value of such parameters set in the simulations will introduce an extra source of error in the final estimation. This is why some of these parameters should not be neither estimated nor neglected but "considered" (Tapley et al., 2004, p. 389).

If this is the case, one can define a covariance matrix $\boldsymbol{C}$ which describes the uncertainty of the considered parameters: following the formulation of equations (4.32) and (4.33), if $\mathbf{c}$ is the $n_c \times 1$ vector containing all the values assigned to each of the n_c considered parameters and $\Delta\mathbf{c}$ is the vector of differences between the assigned and true values, the consider parameters covariance matrix is then

$$\boldsymbol{C} = E\left[\Delta\mathbf{c}\Delta\mathbf{c}^{\top}\right] = \begin{bmatrix} E\left[(\hat{c}_1 - c_1)(\hat{c}_1 - c_1)\right] & \cdots & E\left[(\hat{c}_1 - c_1)(\hat{c}_{n_c} - c_{n_c})\right] \\ \vdots & \ddots & \vdots \\ E\left[(\hat{c}_{n_c} - c_{n_c})(\hat{c}_1 - c_1)\right] & \cdots & E\left[(\hat{c}_{n_c} - c_{n_c})(\hat{c}_{n_c} - c_{n_c})\right] \end{bmatrix}. \tag{4.37}$$

Similarly, the matrix of covariances between the full parameter vector $\mathbf{y}$ and the consider parameters is

$$\boldsymbol{P}_{\mathbf{yc}} = E\left[\Delta\mathbf{y}\Delta\mathbf{c}^{\top}\right] = \begin{bmatrix} E\left[(\hat{y}_1 - c_1)(\hat{c}_1 - c_1)\right] & \cdots & E\left[(\hat{y}_1 - y_1)(\hat{c}_{n_c} - c_{n_c})\right] \\ \vdots & \ddots & \vdots \\ E\left[(\hat{y}_n - y_n)(\hat{c}_1 - c_1)\right] & \cdots & E\left[(\hat{y}_n - y_n)(\hat{c}_{n_c} - c_{n_c})\right] \end{bmatrix}. \tag{4.38}$$

In addition, the matrix of partial derivatives of the observation function h with respect to the consider parameters $\mathbf{c}$ is defined as

$$\boldsymbol{H}_{\mathbf{c}} = \frac{\partial \mathbf{h}(\mathbf{y})}{\partial \mathbf{c}} = \begin{bmatrix} \dfrac{\partial z_1}{\partial c_1} & \cdots & \dfrac{\partial z_1}{\partial c_{n_c}} \\ \vdots & \ddots & \vdots \\ \dfrac{\partial z_m}{\partial c_1} & \cdots & \dfrac{\partial z_m}{\partial c_{n_c}} \end{bmatrix}. \tag{4.39}$$

As stated by Montenbruck and Gill (2001, p. 266), "typical examples of consider parameters are measurement biases, station location errors or uncertainties in the drag and radiation pressure model". Matrix $\boldsymbol{C}$ must be estimated based on the confidence in the knowledge of the environment, non-estimated parameters used in the simulations. This plays an important role in the consider covariance analysis, described in subsection 4.2.3.

Variational equations

Let $\mathbf{\Phi}(t, t_0)$ be a matrix sized 6×6, named "state transition matrix", which relates the state at t with the state at t_0 (Montenbruck & Gill, 2001, eq. 7.1):

$$\mathbf{\Phi}(t, t_0) = \frac{\partial \mathbf{x}(t)}{\partial \mathbf{x}(t_0)} = \begin{bmatrix} \frac{\partial x(t)}{\partial x(t_0)} & \cdots & \frac{\partial x(t)}{\partial \dot{z}(t_0)} \\ \vdots & \ddots & \vdots \\ \frac{\partial \dot{z}(t)}{\partial x(t_0)} & \cdots & \frac{\partial \dot{z}(t)}{\partial \dot{z}(t_0)} \end{bmatrix}, \tag{4.40}$$

so that $\mathbf{x}(t) = \mathbf{\Phi}(t, t_0)\mathbf{x}(t_0)$. Similarly, let $\boldsymbol{S}$ be a matrix sized $6 \times n_p$, named "sensitivity matrix", that relates changes in the model parameters $\mathbf{p}$ with changes in the state $\mathbf{x}$ (Montenbruck & Gill, 2001, eq. 7.2):

$$\boldsymbol{S}(t) = \frac{\partial \mathbf{x}(t)}{\partial \mathbf{p}} = \begin{bmatrix} \frac{\partial x(t)}{\partial p_1} & \cdots & \frac{\partial x(t)}{\partial p_{n_p}} \\ \vdots & \ddots & \vdots \\ \frac{\partial \dot{z}(t)}{\partial p_1} & \cdots & \frac{\partial \dot{z}(t)}{\partial p_{n_p}} \end{bmatrix}. \tag{4.41}$$

During an estimation process, however, equations (4.40) and (4.41) cannot be applied straightforward, precisely, because $\mathbf{x}(t)$ and $\mathbf{p}$ are the unknowns to be estimated. Instead, Montenbruck and Gill (2001, sec. 7.2.1) describe the differential equations, named "variational equations", through which $\mathbf{\Phi}(t, t_0)$ and $\boldsymbol{S}(t)$ can be integrated:

$$\frac{\mathrm{d}}{\mathrm{d}t}\mathbf{\Phi}(t, t_0) = \frac{\partial \dot{\mathbf{x}}}{\partial \mathbf{x}}\mathbf{\Phi}(t, t_0); \tag{4.42a}$$

$$\frac{\mathrm{d}}{\mathrm{d}t}\boldsymbol{S}(t) = \frac{\partial \dot{\mathbf{x}}}{\partial \mathbf{x}}\boldsymbol{S}(t) + \frac{\partial \dot{\mathbf{x}}}{\partial \mathbf{p}}, \tag{4.42b}$$

with initial conditions

$$\mathbf{\Phi}(t_0, t_0) = \boldsymbol{I}_{6\times 6}; \tag{4.43a}$$

$$\boldsymbol{S}(t_0) = \mathbf{0}_{6\times n_p}, \tag{4.43b}$$

and where the derivative $\partial\dot{\mathbf{x}}/\partial\mathbf{x}$ is computed from the acceleration model $\dot{\mathbf{x}} = f(\mathbf{x}, t, \mathbf{p})$ (equation 4.1):

$$\frac{\partial \dot{\mathbf{x}}}{\partial \mathbf{x}} = \begin{bmatrix} \frac{\partial f(\mathbf{x}, t, \mathbf{p})_{(1)}}{\partial x} & \cdots & \frac{\partial f(\mathbf{x}, t, \mathbf{p})_{(1)}}{\partial \dot{z}} \\ \vdots & \ddots & \vdots \\ \frac{\partial f(\mathbf{x}, t, \mathbf{p})_{(6)}}{\partial x} & \cdots & \frac{\partial f(\mathbf{x}, t, \mathbf{p})_{(6)}}{\partial \dot{z}} \end{bmatrix}, \tag{4.44}$$

where subindices (i) refer to the i-th component of the result of $f(\mathbf{x}, t, \mathbf{p})$. Analogously,

$$\frac{\partial \dot{\mathbf{x}}}{\partial \mathbf{p}} = \begin{bmatrix} \frac{\partial f(\mathbf{x}, t, \mathbf{p})_{(1)}}{\partial p_1} & \cdots & \frac{\partial f(\mathbf{x}, t, \mathbf{p})_{(1)}}{\partial p_{n_p}} \\ \vdots & \ddots & \vdots \\ \frac{\partial f(\mathbf{x}, t, \mathbf{p})_{(6)}}{\partial p_1} & \cdots & \frac{\partial f(\mathbf{x}, t, \mathbf{p})_{(6)}}{\partial p_{n_p}} \end{bmatrix}. \tag{4.45}$$

The horizontal concatenation of the state transition matrix $\mathbf{\Phi}$ and the sensitivity matrix $\boldsymbol{S}$ gives a $6 \times n$ matrix, which we denote $\mathbf{\Psi}$ for convenience:

$$\mathbf{\Psi}(t, t_o) = \begin{bmatrix} \mathbf{\Phi}(t, t_0) & \boldsymbol{S}(t) \end{bmatrix}. \tag{4.46}$$

This Ψ matrix is relevant because it is what allows to propagate a covariance matrix $\boldsymbol{P}_{\mathbf{y}}$ to a later instant than the reference epoch t_0 of its associated extended state $\mathbf{y}$:

$$\boldsymbol{P}_{\mathbf{x}}(t) = \mathbf{\Psi}(t, t_o)\boldsymbol{P}_{\mathbf{y}}(t_0)\mathbf{\Psi}(t, t_o)^{\top}. \tag{4.47}$$

Note that this covariance propagation outputs the covariance matrix corresponding to the state $\mathbf{x}$ only. If the full $\boldsymbol{P}_{\mathbf{y}}$ matrix needst o be propagated instead, equation (4.46) needs to be extended as shown in equation (10) of Part IV.

Least squares solutions

Before describing the batch estimation algorithm in section 4.2.2, the fundamentals of nonlinear least squares solutions must be outlined. Let a linear system of equations be $\mathbf{z} = \boldsymbol{A}\mathbf{y}$, defined by the $m \times 1$ vector $\mathbf{z}$, the $m \times n$ matrix $\boldsymbol{A}$ and the $n \times 1$ vector of unknowns $\mathbf{y}$. If Rank($\boldsymbol{A}$)$> n$, then the system is overdetermined and an exact solution does not exist. However, a "best-fit" solution for $\mathbf{y}$ can be found by minimizing the L_2 norm (denoted $\|.\|_2$) of the difference between $\mathbf{z}$ and $\boldsymbol{A}\mathbf{x}$. Simple linear algebra then yields to

$$\hat{\mathbf{y}} = \underset{\mathbf{y}}{\operatorname{argmin}} \|\mathbf{z} - \boldsymbol{A}\mathbf{y}\|_2^2 = \left(\boldsymbol{A}^\top \boldsymbol{A}\right)^{-1} \boldsymbol{A}^\top \mathbf{z}, \tag{4.48}$$

where the hat notation stands for "estimated". This is also commonly known as the solution to the "normal equations" of a system. If, instead, the weighted norm $\|.\|_{\boldsymbol{W}}$ is used (defined as $\|\mathbf{x}\|_{\boldsymbol{W}} = \sqrt{\mathbf{x}^\top \boldsymbol{W}\mathbf{x}}$, where $\boldsymbol{W}$ is a matrix of weights), then equation (4.48) becomes

$$\hat{\mathbf{y}} = \underset{\mathbf{y}}{\operatorname{argmin}} \|\mathbf{z} - \boldsymbol{A}\mathbf{y}\|_{\boldsymbol{W}}^2 = \left(\boldsymbol{A}^\top \boldsymbol{W}\boldsymbol{A}\right)^{-1} \boldsymbol{A}^\top \boldsymbol{W}\mathbf{z}. \tag{4.49}$$

As seen next in subsection 4.2.2, the inverse of the obersvation covariance (equation 4.33) is commonly taken as weights matrix in the context of orbit estimation. It is important to note that the term $(\boldsymbol{A}^\top \boldsymbol{A})^{-1}$ (or its equivalent in the weighted form) is the covariance matrix of the estimated solution (see Tapley et al., 2004, Eqs. 4.4.8-4.4.18 for a proof). Hence, if the solution estimates the state of a spacecraft, this result will be the one representing the associated uncertainty of each estimated component and their correlations.

4.2.2. Full estimation

Let $F_{i,0}$ be the function that integrates a state from its value at t_0, $\mathbf{x}_0$, to a later instant t_i, and $h(\mathbf{y})$ the function that outputs a set of observations $\mathbf{z}$ given a full state $\mathbf{y}$ (equation 4.30)[3]. If a set of observations $\mathbf{z}_i = \mathbf{z}(t_i)$ is available, the estimation problem can be formulated as: find the full state $\mathbf{y}_0 = \mathbf{y}(t_0)$, consisting of the initial state $\mathbf{x}_0$ and the set of constant environmental parameters $\mathbf{p}$, so that the propagated state $\mathbf{x}_i = \mathbf{x}(t_i)$ gives observations as close as possible to the observed set $\mathbf{z}_i$. If this similarity is expressed in terms of the weighted norm ($\|.\|_{\boldsymbol{W}}$) of the difference between the simulated and the observed observations, this can be mathematically formulated as

$$\hat{\mathbf{y}}_0 = \underset{\mathbf{y}_0}{\operatorname{argmin}} \|\mathbf{z}_i - \mathbf{h}(F_{i,0}(\mathbf{y}_0)\|_{\boldsymbol{P}_{\mathbf{z}_i}^{-1}}^2, \tag{4.50}$$

where the hat notation stands for "estimated" and the inverse of the observation covariance matrix $\boldsymbol{P}_{\mathbf{z}}$ (equation 4.33) is used as a weighting matrix in order to give less weight to the less reliable observations. Given the nonlinear nature of functions h and F, the problem must be solved iteratively by updating an initial guess of $\hat{\mathbf{y}}_0$ as

$$\hat{\mathbf{y}}_0 \leftarrow \hat{\mathbf{y}}_0 + \underset{\mathbf{y}_0}{\operatorname{argmin}} \left\| \Delta\mathbf{z}_i - \frac{\partial \mathbf{h}}{\partial \mathbf{y}_i} \frac{\partial \mathbf{y}_i}{\partial \mathbf{y}_0} \mathbf{y}_0 \right\|_{\boldsymbol{P}_{\mathbf{z}_i}^{-1}}^2, \tag{4.51}$$

where $\Delta\mathbf{z}_i = \mathbf{z}_i - \mathbf{h}(F_{i,0}(\hat{\mathbf{y}}_0))$, the matrix $\partial h/\partial \mathbf{y}_i$ is computed with equation (4.31), and the matrix $\partial \mathbf{y}_i/\partial \mathbf{y}_0$ is given by equation (4.46). The result of the argmin operator is denoted $\Delta\hat{\mathbf{y}}_0$, and the linearized nature of its interior yields the well-known least squares solution (equation 4.49).

The above is valid when estimating the initial state $\mathbf{x}_0$ and set of parameters $\mathbf{p}$ given a single observation set $\mathbf{z}_i$. If multiple observations are available at multiple instants t_i, with $i = 1, \ldots, m$, then there are multiple alternatives to proceed. The main categories in which these are encompassed are two: the batch estimation and the sequential estimation. These are developed below.

Batch estimation algorithm

The batch estimation algorithm is designed with the aim of computing $\mathbf{y}_0 = \mathbf{y}(t_0)$ given a batch of m observations $\mathbf{z}(t_i)$, with $i \geq 0$. Since the difference between computed and observed observations is not minimized in a single set of observations but a whole batch, equation (4.50) is therefore

$$\hat{\mathbf{y}}_0 = \underset{\mathbf{y}_0}{\operatorname{argmin}} \left(\sum_i^m \|\mathbf{z}_i - h(F_{i,0}(\mathbf{y}_0))\|_{\boldsymbol{P}_{\mathbf{z}_i}^{-1}}^2 \right). \tag{4.52}$$

[3] In Part IV we switch to the more common approach of defining the $\mathbf{h}$ function as the one that directly maps an extended initial state $\mathbf{y}_0$ to the full set of expected observations $\mathbf{z}$ at different instants. The separation between $\mathbf{h}$ and $F_{i,0}$ is maintained here with the aim of giving a deeper insight, although we acknowledge that this formulation is not suitable, for instance, when different observations happen at common instants.

Moreover, if an initial *a priori* estimate $\bar{\mathbf{y}}_0$, with its associated covariance $\bar{\boldsymbol{P}}_0$ are available, they can be introduced into the minimization problem (e.g., Tapley et al., 2004, Eq. 4.3.24) so that the solution will also be taken closer to $\bar{\mathbf{y}}_0$, which makes equation (4.52) turn to

$$\hat{\mathbf{y}}_0 = \underset{\mathbf{y}_0}{\operatorname{argmin}} \left(\sum_i^m \|\mathbf{z}_i - h(F_{i,0}(\mathbf{y}_0))\|^2_{\boldsymbol{P}_{\mathbf{z}_i}^{-1}} + \|\bar{\mathbf{y}}_0 - \mathbf{y}_0\|^2_{\bar{\boldsymbol{P}}_0^{-1}} \right). \tag{4.53}$$

When following the same procedure as to arrive at the classical least squares solution (4.49) but with equation (4.53), one gets an equivalent form of the normal equations but in which the corresponding matrix and vector are accumulated throughout the whole set of observations. The complete procedure is detailed in Algorithm 1.

Algorithm 1 Batch estimation algorithm. Based on Tapley et al. (2004, p. 196-197) with adapted notation.

Require: An initial estimate of $\mathbf{y}_0 = \mathbf{y}(t_0)$. If available, also an *a priori* estimate $\bar{\mathbf{y}}_0$, with its associated covariance $\bar{\boldsymbol{P}}_0$.
  Set convergence criteria δ and initialize $\Delta\mathbf{y}$
  while $\|\Delta\mathbf{y}\|/n > \delta$ **do**
    Initialize $i = 1$, $\boldsymbol{\Lambda} = \mathbf{0}, \mathbf{N} = \mathbf{0}$
    for all observations $\mathbf{z}_i = \mathbf{z}(t_i)$ **do**
      Read observation $\mathbf{z}_i$ and its associated covariance matrix $\boldsymbol{P}_{\mathbf{z}}$
      Integrate equation (4.1) together with equations (4.43) from t_0 to t_i to get $\mathbf{x}_i = \mathbf{x}(t_i)$, $\boldsymbol{\Phi}(t_i, t_0)$ and $\boldsymbol{S}(t_i)$;
      Compute $\boldsymbol{\Psi}(t_i, t_0)$ with equation (4.46);
      Compute $\boldsymbol{H}|_{\mathbf{x}_i}$, evaluating equation (4.31) at $\mathbf{x}_i$
      Compute $\Delta\mathbf{z} = \mathbf{z}_i - h(\mathbf{x}_i, \mathbf{p})$
      Compute the auxiliary matrix $\boldsymbol{A} = \boldsymbol{H}|_{\mathbf{x}_i} \boldsymbol{\Psi}(t_i, t_0)$
      Update matrix $\boldsymbol{\Lambda} \leftarrow \boldsymbol{\Lambda} + \boldsymbol{A}^\top \boldsymbol{P}_{\mathbf{z}}^{-1} \boldsymbol{A}$
      Update vector $\mathbf{N} \leftarrow \mathbf{N} + \boldsymbol{A}^\top \boldsymbol{P}_{\mathbf{z}}^{-1} \Delta\mathbf{z}$
    end for
    Solve $\Delta\mathbf{y} = \left(\boldsymbol{\Lambda} + \bar{\boldsymbol{P}}_0^{-1}\right)^{-1} (\mathbf{N} + \bar{\mathbf{y}}_0)$
    Update $\mathbf{y}_0 \leftarrow \mathbf{y}_0 + \Delta\mathbf{y}$
  end while
  The estimated initial full state is $\mathbf{y}_0 = \begin{bmatrix} \mathbf{x}_0^\top & \mathbf{p}^\top \end{bmatrix}^\top$, and its corresponding covariance is $\boldsymbol{P}_{\mathbf{y}} = \left(\boldsymbol{\Lambda} + \bar{\boldsymbol{P}}_0^{-1}\right)^{-1}$.

The batch estimation can be performed either in a single arc comprising all observations or in a multi-arc fashion, given different sets of observations clustered in different, short spans of time. The distinction between the two approaches is illustrated in Figure 4.1. In it, each of the three fits (single-arc and two multi-arc) are third-degree polynomials, representing the constraints of a certain physical model, which is the same regardless of the estimation process applied. Note how the effect of a multi-arc estimation is that each of the individual arcs fits the observations better than the multi-arc. This is because the latter has the exact same flexibility but it has to be consistent with a larger set of not-necessarily-aligned observations.

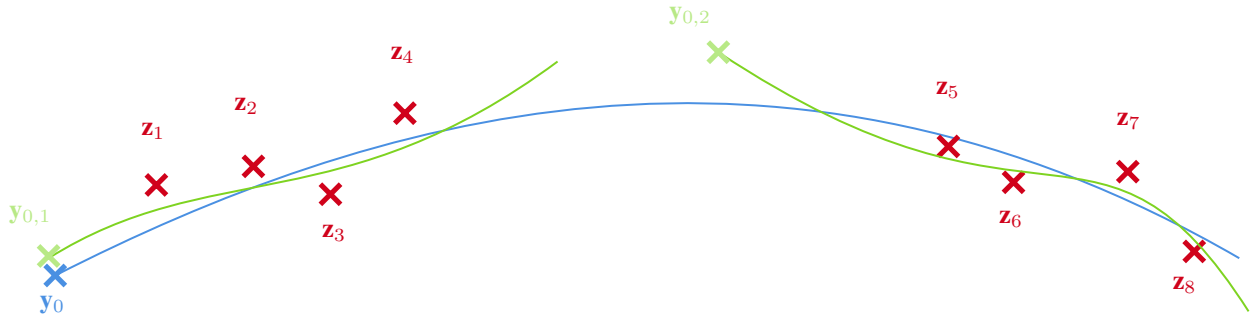

Figure 4.1: Representation of single- (blue) vs multi-arc (green) batch solutions for the initial state of an orbiting body given a set of observations

Sequential estimation algorithm

Note to the reader: the final selected approach has been based on batch estimations only, hence this subsection is only relevant to the present study to the extent that it has been useful to discard sequential estimation as a possibility.

In the sequential approach, the state is estimated at every instant an observation is available, based on the propagated covariance from the last estimation and the covariance of the observation itself. The mathematical formulation of the problem to solve is (Tapley et al., 2004, Eq. 4.7.3)

$$\hat{\mathbf{x}}_i = \underset{\mathbf{x}_i}{\operatorname{argmin}} \left(\|\mathbf{z}_i - h(\mathbf{x}_i)\|^2_{\boldsymbol{P}^{-1}_{\mathbf{z}_i}} + \|\bar{\mathbf{x}}_i - \mathbf{x}_i\|^2_{\bar{\boldsymbol{P}}^{-1}_{\mathbf{x},i}} \right). \tag{4.54}$$

Note how in equation (4.54) the only nonlinear function that intervenes and thus requires to be linearized is h (equation 4.31). However, the linearization of the $F_{i,j}$ function in equations (4.52) and (4.53), which is equal to matrix $\Phi(t_i, t_j)$, still intervenes in this problem because it is what allows for the *a priori* state $\bar{\mathbf{x}}_i$ and covariance $\bar{\boldsymbol{P}}_{\mathbf{x},i}$ to be calculated.

Depending on whether the variational equations and the linearization of h is evaluated at a "reference" state or at the "nominal" state, based on the last estimation, the sequential estimation algorithm is said to be "linearized" or "extended", respectively. The two approaches are represented in Figure 4.2.

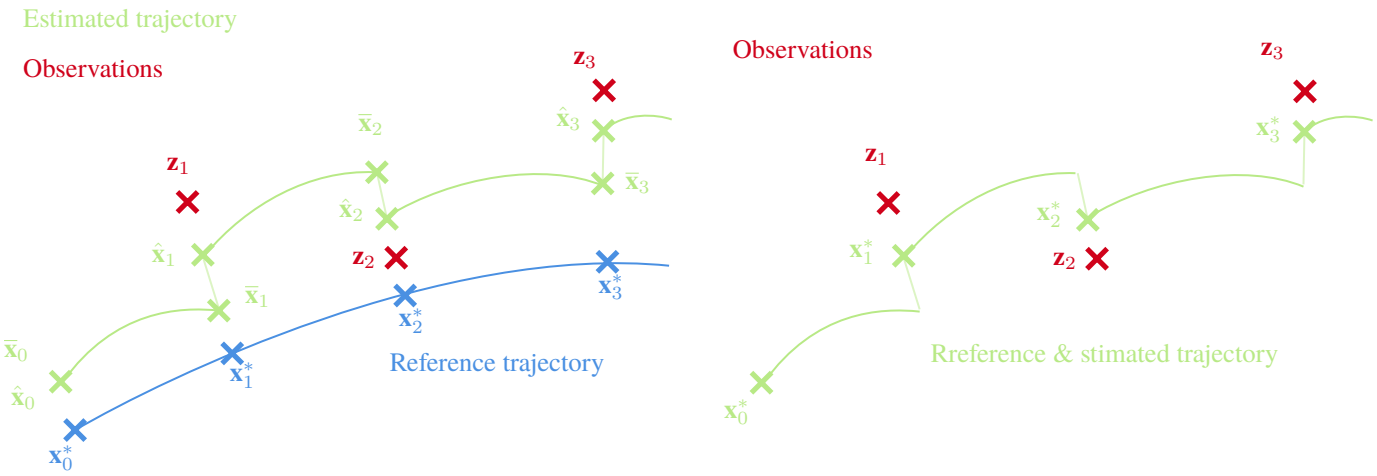

Figure 4.2: Representation of the linearized sequential estimation (left) and the extended sequential estimation (right). Based on Montenbruck and Gill (2001, Figs. 8.7 & 8.8).

The algorithm for the linearized sequential approach is presented in Algorithm 2. The formulation requires the computation of certain matrices named "Kalman gain matrices", also needed for the extended approach. This is why the sequential estimation is also commonly known as "Kalman filter". See Tapley et al. (2004, Sec. 4.7) for the derivation of the linearlized approach.

Algorithm 2 Sequential estimation algorithm. Based on Tapley et al. (2004, p. 203-204) with adapted notation.

Require: An initial *a priori* estimate $\bar{\mathbf{x}}_0$, with its associated covariance $\bar{\boldsymbol{P}}_0$, and a reference state $\mathbf{x}^*_0$.
  Initialize $\hat{\mathbf{x}}_0 = \bar{\mathbf{x}}_0$, $\boldsymbol{P}_{\mathbf{x},0} = \bar{\boldsymbol{P}}_0$ and $i = 1$.
  for all observations $\mathbf{z}_i = \mathbf{z}(t_i)$ **do**
    Read observation $\mathbf{z}_i$ and its associated covariance matrix $\boldsymbol{P}_{\mathbf{z}}$
    Integrate equation (4.1) together with equations (4.43) from t_{i-1} to t_i to get $\mathbf{x}^*_i = \mathbf{x}^*(t_i)$, $\boldsymbol{\Phi}(t_i, t_{i-1})$ and $\boldsymbol{S}(t_i)$;
    Compute the design matrix $\boldsymbol{H}|_{\mathbf{x}^*_i}$, evaluating equation (4.31) at $\mathbf{x}^*_i$
    Compute the *a priori* state $\bar{\mathbf{x}}_i = \boldsymbol{\Phi}(t_i, t_{i-1})\hat{\mathbf{x}}_{i-1}$
    Compute the *a priori* covariance matrix $\bar{\boldsymbol{P}}_{\mathbf{x},i} = \boldsymbol{\Phi}(t_i, t_{i-1})\boldsymbol{P}_{\mathbf{x},i-1}\boldsymbol{\Phi}^\top(t_i, t_{i-1})$
    Compute $\Delta\mathbf{z} = \mathbf{z}_i - h(\mathbf{x}_i, \mathbf{p})$
    Compute the Kalman gain matrix $\boldsymbol{K}_i = \bar{\boldsymbol{P}}_{\mathbf{x},i}\boldsymbol{H}^\top \left(\boldsymbol{H}_i \bar{\boldsymbol{P}}_{\mathbf{x},i} \boldsymbol{H}_i^\top + \boldsymbol{P}_{\mathbf{z}} \right)^{-1}$
    Compute the estimated state at t_i: $\hat{\mathbf{x}}_i = \bar{\mathbf{x}}_i + \boldsymbol{K}_i \left(\mathbf{z}_i - \boldsymbol{H}_i \bar{\mathbf{x}}_i \right)$
    Compute the corresponding covariance matrix $\boldsymbol{P}_{\mathbf{x},i} = \left(\boldsymbol{I} - \boldsymbol{K}_i \boldsymbol{H}_i \right) \bar{\boldsymbol{P}}_{\mathbf{x},i}$
    $i \leftarrow i + 1$
  end for

On the other hand, the extended sequential agorithm is detailed in Algorithm 3. The development of the mathematical formulations used is described by Tapley et al. (2004, Sec. 4.7.2).

Algorithm 3 Extended sequential estimation algorithm. Based on Tapley et al. (2004, p. 212) with adapted notation.

Require: An initial *a priori* covariance $\bar{\boldsymbol{P}}_0$, and a reference state $\mathbf{x}_0^*$.
  Initialize $\boldsymbol{P}_{\mathbf{x},0} = \bar{\boldsymbol{P}}_0$ and $i = 1$.
  for all observations $\mathbf{z}_i = \mathbf{z}(t_i)$ **do**
    Read observation $\mathbf{z}_i$ and its associated covariance matrix $\boldsymbol{P}_{\mathbf{z}}$
    Integrate equation (4.1) together with equations (4.43) from t_{i-1} to t_i to get $\mathbf{x}_i^* = \mathbf{x}^*(t_i)$ and $\boldsymbol{\Phi}(t_i, t_{i-1})$
    Compute the *a priori* covariance matrix $\bar{\boldsymbol{P}}_{\mathbf{x},i} = \boldsymbol{\Phi}(t_i, t_{i-1})\boldsymbol{P}_{\mathbf{x},i-1}\boldsymbol{\Phi}^\top(t_i, t_{i-1})$
    Compute $\Delta\mathbf{z} = \mathbf{z}_i - h(\mathbf{x}_i^*, \mathbf{p})$
    Compute the design matrix $\boldsymbol{H}|_{\mathbf{x}_i^*}$, evaluating equation (4.31) at $\mathbf{x}_i^*$
    Compute the Kalman gain matrix $\boldsymbol{K}_i = \bar{\boldsymbol{P}}_{\mathbf{x},i}\boldsymbol{H}^\top \left(\boldsymbol{H}_i\bar{\boldsymbol{P}}_{\mathbf{x},i}\boldsymbol{H}_i^\top + \boldsymbol{P}_{\mathbf{z}}\right)^{-1}$
    Update the reference state at t_i: $\mathbf{x}_i^* \leftarrow \mathbf{x}_i^* + \boldsymbol{K}_i\mathbf{z}_i$
    Compute the corresponding covariance matrix $\boldsymbol{P}_{\mathbf{x},i} = (\boldsymbol{I} - \boldsymbol{K}_i\boldsymbol{H}_i)\,\bar{\boldsymbol{P}}_{\mathbf{x},i}$
    $i \leftarrow i + 1$
  end for

Strategies used in present research

The two main orbit estimation presented above are the batch and sequential estimations. Nowadays, the latter is the most common in the monitoring of Earth-orbiting satellites, which get updated observations by an extended network of ground stations all around the globe and therefore new states can be estimated by continuously applying either Algorithm 2 or Algorithm 3. The orbits of deep space spacecraft, on the other hand, which are not as continuously monitored as Earth satellites, are usually estimated by grouping different batches of tracking data and estimating their initial state as described in Algorithm 1.

This can nevertheless change in the future, if a deep-space tracking infrastructure is available and the uncertainty of interplanetary spacecraft needs to be continuously narrowed for certain applications. On Earth, this is essential, for instance, for collision avoidance, but so far there have not been requirements as stringent for any mission out of cislunar space. With an eye on the future, Petricca and Genova (2022) proposed a sequential estimation method for interplanetary spacecraft based on spacecraft-to-spacecraft Doppler measurements. Sequential estimation is however expected to be more relevant in the context of autonomous navigation, and for a mission like Trilogy, where data can be downloaded to the ground, batch estimations are still deemed preferable (Genova, 2024, priv. comm.).

Batch estimations themselves can be performed in a single- or multi-arc fashion, and trackers of interplanetary spacecraft opt for the latter. This is because spacecraft in orbit around other planets are subject to rapid dynamics (e.g., thousands of orbits in a mission of one year in Mars orbit) highly affected by complex effects than can yield to remaining model errors (e.g., high-order and/or time-varying gravity fields, atmospheric drag). Therefore, these errors will accumulate up to a point where the flexibility of a single arc in the defined dynamical model will not be enough to fit all the observations properly. With the multi-arc approach, the trajectory is only fitted during different short-time windows, and therefore they are not corrupted by unmodelled dynamical effects during previous observation batches. This results in a higher overall accuracy in the spacecraft orbit determination, although as pointed out by Lari et al. (2022), it has the weakness "that it gets rid of the accumulated information contained in the global orbit of the spacecraft". A suitable alternative is the "constrained multi-arc approach", developed by Alessi et al. (2012) for the tracking of Bepi-Colombo. In it, continuity between arcs is not enforced—this would effectively make it a single-arc approach—but the jumps in between are also introduced in the optimization process as parameters to minimize.

When it comes to estimating planetary ephemerides instead of spacecraft orbits, the common approach is to use a single, multi-arc estimation with all observations available throughout a time span of several years. Normal points of planetary distances are taken from spacecraft ranges, but after their orbits have been estimated, generally using Doppler data only, "planetary ephemerides are then estimated using range/VLBI data (without adjusting the spacecraft orbit)" (Dirkx et al., 2019). This is said to be a decoupled approach.

The alternative is to perform a coupled estimation, where the orbits of both the spacecraft and the celestial body are computed in a single estimation process. Genova et al. (2018) did so for the first time with the orbit of Mercury based on MESSENGER data, and stated that this "mitigates the systematic errors related to the spacecraft position and velocity". Fayolle et al. (2022) formulated coupled and decoupled estimation approaches to be applied to Jupiter Icy Moons Explorer (JUICE) and the Galilean moons, and found that their ephemerides were computed with slightly greater formal errors in their tangential positions but more than one order of magnitude less uncertainty in their radial positions when using the coupled approach.

The advantage of using Doppler observations for the orbit determination of the spacecraft alone in the decoupled

approach is that they are less sensitive than range observations to errors in planetary positions given by ephemerides models. In the case of ILR, Dirkx et al. (2019) predict that the "laser data will have significant and useful information on the dynamics of both natural and artificial bodies, requiring the coupling to be incorporated". The most suitable approach for the Trilogy concept will only be determined based on results of numerical simulations. In their conclusions, Dirkx et al. (2019) also state that the tracking of interplanetary orbiters "will continue to require Doppler data", following the classical approach, and "ILR will start to be competitive for determining signatures of >1.5–2 h".

4.2.3. Covariance analysis

Given the computational cost of applying full estimation algorithms, a simplified alternative is instead to simply perform a covariance analysis. Given the fact that, when solving the normal equations (4.48, 4.49), the inverse of the left-hand side is the covariance matrix of the solution, the covariance analysis approach is to compute this matrix only instead of the full solution. The result will therefore assess the expected uncertainty at the end of an estimation process, but without actually carrying it out.

The covariance matrix of the solution after applying the batch estimation algorithm, as described in Algorithm 1, is the inverse of matrix $\boldsymbol{\Lambda}$ plus the *a priori* covariance matrix $\bar{\boldsymbol{P}}_0$, i.e.,

$$\boldsymbol{P}_{\mathbf{y}_0} = \left(\sum_i^m \boldsymbol{\Psi}_{i,0}^\top \, \boldsymbol{H}|_{\mathbf{x}_i}^\top \, \boldsymbol{P}_{\mathbf{z}_i}^{-1} \, \boldsymbol{H}|_{\mathbf{x}_i} \, \boldsymbol{\Psi}_{i,0} + \bar{\boldsymbol{P}}_0^{-1} \right)^{-1} . \tag{4.55}$$

Just as in the case of applying the full algorithm the state must be propagated together with the variational equations in order to compute matrix $\boldsymbol{\Psi}_{i,0} = \boldsymbol{\Psi}(t_i, t_0)$ and evaluate the design matrix $\boldsymbol{H}$ at each time step t_i where observations are available. However, these can be evaluated with a single propagation, and there is no need to loop it until convergence like in the full estimation.

Consider covariance analysis

If the uncertainty of the non-estimated (but considered) environmental parameters is given by matrix $\boldsymbol{C}$ (equation 4.37), then the resulting covariance matrix $\boldsymbol{P}_{\mathbf{y}_0}$ from equation (4.55) gets an extra contribution $\boldsymbol{P}_{\mathbf{y}_0}^{(\mathbf{c})}$ of the form (Tapley et al., 2004, Eqs. 6.3.56-6.3.67)

$$\boldsymbol{P}_{\mathbf{y}_0}^{(\mathbf{c})} = \boldsymbol{P}_{\mathbf{yc}} \boldsymbol{C}^{-1} \boldsymbol{P}_{\mathbf{yc}}^\top ; \tag{4.56a}$$

$$\boldsymbol{P}_{\mathbf{yc}} = -\boldsymbol{P}_{\mathbf{y}_0} \boldsymbol{M}_{\mathbf{yc}} \boldsymbol{C} ; \tag{4.56b}$$

$$\boldsymbol{M}_{\mathbf{yc}} = \sum_i^m \left(\boldsymbol{\Psi}_{i,0}^\top \, \boldsymbol{H}|_{\mathbf{x}_i}^\top \, \boldsymbol{P}_{\mathbf{z}_i}^{-1} \, \boldsymbol{H}_{\mathbf{c}}|_{\mathbf{x}_i} \right) + \bar{\boldsymbol{M}}_{\mathbf{yc}} ; \tag{4.56c}$$

$$\bar{\boldsymbol{M}}_{\mathbf{yc}} = -\left(\bar{\boldsymbol{P}}_0 - \boldsymbol{P}_{\mathbf{yc}} \boldsymbol{C}^{-1} \boldsymbol{P}_{\mathbf{yc}}^\top \right)^{-1} \boldsymbol{P}_{\mathbf{yc}} \boldsymbol{C}^{-1} , \tag{4.56d}$$

where matrices $\boldsymbol{C}$ and $\boldsymbol{P}_{\mathbf{yc}}$ (equations 4.37 and 4.38) are, respectively, the covariance matrix of the consider parameters $\mathbf{c}$ and that of the relationship between the full set of estimated parameters $\mathbf{y}$ and the considered parameters $\mathbf{c}$; matrix $\boldsymbol{P}_{\mathbf{y}_0}$ is the result of equation (4.55); matrix $\boldsymbol{\Psi}_{i,0}$ is computed with equation (4.46) after integration of the variational equations; $\boldsymbol{H}$ is the design matrix (equation 4.31), and $\boldsymbol{H}_{\mathbf{c}}$ is the equivalent matrix for the considered parameters (equation 4.39). As noted in equation (4.56c), both $\boldsymbol{H}$ and $\boldsymbol{H}_{\mathbf{c}}$ are evaluated at the integrated state $\mathbf{x}$ at instant t_i. The final expected covariance after an estimation will be therefore

$$\boldsymbol{P} = \boldsymbol{P}_{\mathbf{y}_0} + \boldsymbol{P}_{\mathbf{y}_0}^{(\mathbf{c})} . \tag{4.57}$$

In the particular case of a single observation ($m = 1$) and no correlation between the estimated parameters $\mathbf{y}$ and the considered parameters $\mathbf{c}$ (hence, $\boldsymbol{P}_{\mathbf{yc}} = \mathbf{0}_{m \times n_c}$), then equation (4.56) becomes

$$\boldsymbol{P}_{\mathbf{y}_0}^{(\mathbf{c})} = \boldsymbol{P}_{\mathbf{y}_0} \boldsymbol{\Psi}^\top(t, t_0) \, \boldsymbol{H}|_{\mathbf{x}}^\top \, \boldsymbol{P}_{\mathbf{z}}^{-1} \, \boldsymbol{H}_{\mathbf{c}}|_{\mathbf{x}} \boldsymbol{C} \boldsymbol{C}^{-1} \boldsymbol{C}^\top \, \boldsymbol{H}_{\mathbf{c}}|_{\mathbf{x}}^\top \left(\boldsymbol{P}_{\mathbf{z}}^{-1} \right)^\top \, \boldsymbol{H}|_{\mathbf{x}} \, \boldsymbol{\Psi}(t, t_0) \boldsymbol{P}_{\mathbf{y}_0} , \tag{4.58}$$

which is equivalent to the consider covariance expression given by Montenbruck and Gill (2001, Eq. 8.42) if the inverse of the observation covariance matrix $\boldsymbol{P}_{\mathbf{z}}$ is taken as the weights matrix. This can be however a too simplistic approach, since it neglects the correlations between the estimated parameters and any other non-estimated ones. For instance, as seen in section 5.5, the relativistic parameters α and β are strongly correlated, and they are in turn correlated with the solar gravitational oblateness J_2. Hence, if only some of these parameters are esitmated but the others still play a role in the dynamical model, their correlations will not be null in matrix $\boldsymbol{P}_{\mathbf{yc}}$.

5

Solar System Situational Awareness

The term Space Situational Awareness (SSA) is commonly used to refer to the "knowledge of our near-space environment", both in its natural an man-made components (Kennewell & Vo, 2013). Typically, SSA research has been focused on Earth's orbit, and not on any objects further away than the Moon . It is reasonable to define an equivalent term that includes the awareness of all bodies in the Solar System (namely, their existence, location and properties), which is also an active research topic, as discussed in this chapter. In this work, we coin the term Solar System Situational Awareness (SSSA), to refer to this field with a clear separation of the typical, Earth-orbit-focused concept of SSA.

5.1. Planetary ephemerides

Ephemerides are models that describe the locations and velocities of known Solar System bodies as a function of time. These are commonly calculated by fitting (see batch estimation in subsection 4.2.2) numerically integrated orbits to range and/or angular observations from both Earth- and space-based instruments. Currently, they are given by three main institutions that work on their own models independently:

- The Celestial Mechanics and Ephemerides Calculations Institute (IMCEE) in France periodically releases the INPOP ephemerides, with their last release being INPOP-21a, published by Fienga et al. (2021). They are calculated by fitting 401 parameters, which mainly contain the position and velocity of the different Solar System bodies, but not other physical parameters such as the gravitational parameter of the major bodies (Fienga, 2023b)
- The Jet Propulsion Laboratory (JPL) in California is in charge of the DE, with its last version being DE440 and DE441, published by Park et al. (2021). It consists of the fit of the position of the Sun, the barycenter of the eight planets, the Moon and Pluto, 343 asteroids, and Kuiper Belt Objects (KBOs) consisting of 30 individual objects plus a circular ring of 30 objects of equal mass. The gravitational parameters of the Moon and the Sun are also estimated in DE400.
- The Institute for Applied Astronomy (IAA) of the Russian Academy of Sciences in Russia develops the Ephemerides of the Planets and the Moon (EPM), with their latest release being the EPM2021, published by Pitjeva et al. (2019). This model includes the fitting of several physical parameters such as the solar gravitational parameter $\mu_\odot$ and oblateness J_2, the lunar moments of inertia and the masses of 379 asteroids and 30 TNOs.

Table 5.1 summarizes the proportion of each observation source used in the fitting of the INPOP and DE ephemerides models. Although the equivalent data for the EPM is not available, it is clear how range measurements to deep-space spacecraft is, by far, the category that contributes the most to the full set of data in which these models are based. Some of these spacecraft are in stable orbits around their host planets (e.g., as detailed by Fienga et al., 2021, the Mars Reconaissance Orbiter (MRO) provided 20985 range measurements between 2002 and 2014), yet others approached other planets in only flyby maneuvers (e.g, Park et al., 2021 only list one spacecraft range measurement to Uranus and Neptune, performed during the Voyager 2 approaches).

Besides ranging to spacecraft, Table 5.1 also lists other obervation methods: angular observations are given by both Earth-based and space-based (e.g., Gaia Collaboration, 2016) telescopes, and direct ranging includes ground-based radar observations to Venus conducted between 1965 and 1990 (Fienga et al., 2021). VLBI can also be used to directly range planets, but it is becoming a more and more common technology to complement radio-based ranging of spacecraft. Duev et al. (2012) obtained VLBI measurements to the Venus Express spacecraft, and Jones et al. (2014) did the same

Table 5.1: Relative number of observations used to fit the INPOP and DE ephemerides models, separated by observation type. Information from Fienga (2023b) and Park et al. (2021).

	INPOP21a	DE440/441
LLR		31.8%
Ranges to spacecraft	64.7%	34.4%
Optical angular observations	34.7%	33.3%
Direct ranging	0.8%	
VLBI to spacecraft	0.2%	0.5%

with the Cassini spacecraft around Saturn. Gurvits et al. (2013) and Gurvits et al. (2023) introduced the Planetary Radio Interferometry and Doppler Experiment (PRIDE) to perform joint measurements of VLBI and Doppler ranging to the JUICE spacecraft, with the potential of significantly improving the understanding of the Jovian System dynamics. According to Dirkx et al. (2017), these measurements are expected to make "the uncertainty in the ephemerides less dependent on the error in the orbit determination of the JUICE spacecraft itself".

The different methods listed in Table 5.1 have significantly different accuracies: Fienga et al. (2021) assume direct planetary ranges to Venus to have a prior accuracy of 1400m, whereas angular optical observations are considered to be accuracte below the arcsecond level, and VLBI is in turn three orders of magnitude more accurate. For instance, an angular accuracy of 0.6 mas obtained by VLBI to the Cassini spacecraft corresponds to a distance of a few kilometers. This is to be improved by the joint usage of Doppler and VLBI in the PRIDE experiment.

The intercomparison of the three models can be used to estimate their true errors (Dirkx, 2015, p. 39). Comparing the releases previous to the most current, Wenxiao et al. (2021) found that "the deviation levels [...] range from hundred meters to kilometers, and the differences between EPM2017 and the other two are large". Fienga et al. (2021) plot the discrepancy between INPOP21a and DE440 for the few decades around present day, showing how the discrepancy is in the order of tens of meters for the inner planets—these figures are reproduced in section B.1—a few hundreds of meters for Jupiter and Saturn, and several hundreds of kilometers for uranus and Neptune. Newer releases of JPL and INPOP ephemerides "seem to be converging", which indicates there are no fundamental discrepancies in their independent methods (Fienga, 2023b). Even so, the current level of true errors will only be improved when new (and more accurate) observations are introduced.

5.2. Determination of asteroid masses

Nowadays, more than one million asteroids are known to be orbiting in the Main Belt[1]. Their detailed characterization is a crucial research area due to its multiple implications: first, to better understand the formation and evolution of the Solar System (e.g., Shi et al., 2022); second, to better prepare any potentially needed planetary defense missions in the future (e.g., Rivkin et al., 2021); and lastly, to allow well-founded assessments for asteroid mining mission plans (e.g., Ferus et al., 2022).

Such characterization encompasses several aspects: for instance, Galache et al. (2015) emphasize the determination of their size, composition and rotation periods; Chesley et al. (2014) focus on the orbit and density of asteroid Bennu, and Goffin (2014) aim for calculating asteroid masses. Some properties like rotation period or spectral class can be directly inferred from observations of the objects alone, and hence they are listed in the existing catalogs. Masses, on the other hand, cannot be inferred from direct observations of the objects alone. Fienga, Avdellidou, and Hanuš (2020) group the possible methods for estimating asteroid masses in five categories:

- **From spacecraft motion around asteroids**: when a spacecraft flies near an asteroid, it is subject to its gravitational pull. The gravitational parameter of the asteroid, and thus its mass, can be inferred from the exact motion of the spacecraft, the range and range-rate to which are measured from Earth. This method was first applied with the Galileo spacecraft around asteroid 243 Ida (Belton et al., 1995), and has been repeated a small number of occasions since (see Fienga, Avdellidou, and Hanuš, 2020 for full list). It is "by far the most precise technique" (Carry, 2012).
- **From asteroid-asteroid perturbations**: this method is based on assessing the mutual interaction of two asteroids when flying near enough to each other so that the trajectory of the lighter is perturbed by the heavier. This was the technique used for the first-ever calculation of an asteroid mass, namely, that of 4 Vesta by Hertz (1966). The procedure has been replicated numerous times since, due to the high number of similar events (e.g., Hilton et al., 1996 found 460 asteroid encounters between the mid 50's and the early 2000's). This technique is also known

[1] An updated catalog can be found in https://www.spacereference.org/category/main-belt-asteroids.

as "astrometric method" (e.g., Galád and Gray, 2002), due to the fact that it is mostly based on ground-based astrometric observations.

Although historically being a very fruitful method, "these mass determinations often have large errors since the astrometric measurements of both bodies must be extremely accurate to properly model the interaction, [and] the influence of any other nearby bodies must be well known" (Murray, 2023). In this regard, the European Space Agency (ESA)'s Gaia mission (Gaia Collaboration, 2016) has been of significant impact in the last decade. Launched in 2013, it has provided astrometric measurements of the whole sky dome with unprecedented accuracy. Mouret et al. (2007, 2008) predicted several hundreds of asteroid masses to be potentially determinable thanks to the measurements of asteroid encounters. With the mission's data release (DR)2, however, Deram et al. (2022) and Murray (2023) found challenges associated with the systematic errors of the astrometric measurements, and aimed for the next data delivery, DR3. A first study with DR3 has already been published by Li et al. (2023), achieving to estimate masses of 10 asteroids with a precision better than 5% of the 20 asteroids analyzed.

- **From the motion of natural satellites around asteroids**, or binary asteroids: this is a straightforward method that only requires to know the orbital period of a smaller body around an asteroid to apply Kepler's third law and obtain the mass of the larger. It is "the most productive method of accurate mass determinations", "with currently more than 200 known binaries" (Carry, 2012). This method was first applied by Descamps et al. (2008) with asteroid (22) Kalliope, and has been replicated multiple times since (see Fienga, Avdellidou, and Hanuš, 2020 for a list).
- **From the Yarkovsky effect**, which introduces a non-gravitational acceleration to an asteroid due to the combined effect of its rotation and thermal emissions (e.g., Lissauer and de Pater, 2013, sec. 2.8.3). The measurement of this acceleration was first used by Chesley et al. (2003) to infer the bulk density of asteroid 6489 Golevka, and it was repeated by Chesley et al. (2014) with 101955 Bennu as part of the design of NASA's Origins, Spectral Interpretation, Resource Identification, and Security – Regolith Explorer (OSIRIS-REx) Mission (see Fienga, Avdellidou, and Hanuš, 2020 for a full list).
- **From asteroid-planet perturbations**: this method consists of analyzing the deviation of planetary orbits from an asteroid-less model to infer the masses of the asteroids causing the observed deviations. This was originally proposed by Williams (1984), who suggested to use the ranges to the Viking Mars landers, which was succesfully carried out by Standish and Hellings (1989), estimating the masses of 1 Ceres, 2 Pallas and 4 Vesta. Mars is especially sensitive to these perturbations, "because of the planet's proximity with the asteroid belt" (Kuchynka & Folkner, 2013).

  Currently, this method is applied in the fitting of the main planetary ephemerides models (section 5.1). Pitjeva et al. (2019) fit 379 masses in their dynamical model for EPM21, although 102 result in negative values and are thus discarded. Based on the fit of the INPOP19a ephemerides, Fienga, Avdellidou, and Hanuš (2020) give uncertainties better than 33 per cent for 103 asteroids.

In summary, there have been plenty of asteroid mass estimations carried out in the past decades. Conveniently, Kretlow (2020) grouped all of them into a single, open-acces catalog named SiMDA[2]. This currently lists all mass and diameter estimates for a total of 428 objects, for which both the individual and the average mass and diameter values, together with their resulting 1-σ error, are given. The distribution of these errors are shown in the vertical histogram of the figure, evincing how most masses are estimated with uncertainties that give rough ranges rather than accurate values. On top of this, it is worth noting that this simply represents a tiny portion of all known Solar System bodies: in the words of Fienga (2023b), "close to mars we have at least 250k objects with unknown mass".

5.3. Discovery of Trans-Neptunian Objects

Note to the reader: although TNO masses to be estimated have been included in the final implementation of this work (Part IV), the estimation of unknown massive objects has not been addressed. Still, this section details the state of the art on this matter.

5.3.1. The Kuiper Belt

During the 20th century, researchers proposed the existence of a belt of TNOs by extrapolating the mass distribution of the Solar System as a function of heliocentric distance (e.g., Edgeworth, 1949; Kuiper, 1951). This work is the reason why this group of objects, currently confirmed to exist, is commonly known as the "Kuiper Belt". Today, the discovery of unknown KBOs is still an active field of research. A better understanding of them and their distribution will have significant impact in different open research fields, including planetary migration dynamics, the evolution of star protoplanetary disks or

[2]Accessible at https://astro.kretlow.de/simda/catalog/

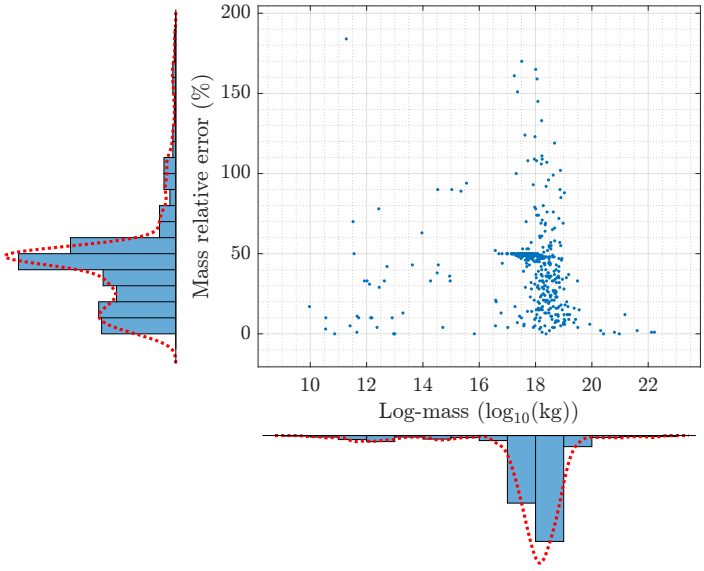

Figure 5.1: Distribution of all known asteroids with their mass and relative error, as of march 2024. Data extracted from the SiMDA catalog (Kretlow, 2020).

planetessimal formation models (Gladman & Volk, 2021). In fact, it is believed that "traces of the original protosolar cloud are likely to remain only at the periphery of the Solar System beyond the orbit of Neptune" (Pitjeva & Pitjev, 2012). Regarding planetary migrations, Siraj (2023) statistically concluded that it is expected that there be ~ 1.2 Mars-like planet in the outer Solar System, with an extrasolar origin but captured by gravitational interactions.

Today, the lack of knowledge of TNOs is a major source of uncertainty in the orbital ephemerides of the outer planets (section 5.1), where currently approximate solutions such a single-mass ring are fitted into the models. The results of such fits are a major contribution in the current research on TNOs, including the total mass of the Kuiper Belt and the distribution of objects. Pitjeva and Pitjev (2018), using the EPM model, estimate their total mass to add up to $(0.0197 \pm 0.0030)M_{\oplus}$ with 3σ confidence, stating that "the bulk of the KBOs are in the ring zone from 39.4 to 47.8 AU". di Ruscio et al. (2020), on the other hand, use the fit of INPOP ephemerides to arrive to the figure of $(0.0243 \pm 0.003)M_{\oplus}$, and state that it is not fully comparable to that from Pitjeva and Pitjev (2018) due to "the different mass distribution considered in the two models, and the degeneracy between the mass of the ring and its distance to the solar system barycentre".

These two studies agree on the fact that the aggregate mass of all TNOs is around two orders of magnitude smaller than that of Earth, but this conclusion has opposing views. Lykawka and Mukai (2008) proposed the existence of a planet of a few tenths of an Earth mass, currently in a stable orbit at > 100 AU. This theory was aligned with the century-old "Planet X" suggested by Lowell (1915), who had predicted a massive body causing perturbations to the orbits of Uranus and Neptune—although such claims were later shown to be based on spurious observations (Standish, 1993). Lykawka and Mukai (2008), however, affirmed that their suggested body would explain the high number of detached TNOs (i.e., those who "do not encounter Neptune"), the existing highly inclined objects and certain observed resonances. With more advanced simulations, Lykawka and Ito (2023) defined their predicted planet to be between 1.5 and 3 Earth masses, and in an orbit of 250 to 500 AU in its semimajor axis and an inclination of 30 degrees. This mass and orbital distances are more similar to another candidate of massive, currently unknown TNO, theorized during the last decade: Planet Nine. This is developed below.

5.3.2. The Planet Nine hypothesis

Batygin and Brown (2016) published the results of numerical simulations suggesting that a distant planet of several Earth masses could explain several aspects of the orbits of KBOs, which are clustered "not only in argument of perihelion, but also in physical space", together with the existence of high-perihelion objects, "as well as the known collection of high semimajor axis objects with inclinations between 60° and 150°, whose origin was previously unclear". This study had significant impact in the community, and further analysis and observation campaigns have followed since. Table 5.2 summarizes the different theorized Planet 9 parameters up to date, including its mass M, semimajor axis a, eccentricity e, inclination i, current true anomaly θ and current heliocentric distance r.

Brown and Batygin (2016) complemented the study with new simulations reaching very similar conclusions. Fienga et al. (2016) tested their proposed Planet 9 configuration in the fit of INPOP ephemerides, specially focusing on the recent

Table 5.2: Theoretical estimates for the mass and orbital parameters of Planet 9

	M ($M_\oplus$)	a (AU)	e ()	i (deg)	θ (deg)	r (AU)
Batygin and Brown (2016)	10	700	0.6			
Fienga et al. (2016)					117.8^{+11}_{-10}	
Brown and Batygin (2016)	5-20	380-980		30		
Batygin et al. (2019)	5-10	400-800	0.2-0.5	15-25		
Fienga, Ruscio, et al. (2020)	5					> 500
	10					> 650
Brown and Batygin (2021)	$6.2^{+2.2}_{-1.3}$	380^{+140}_{-80}		16 ± 5		
Brown et al. (2024)	$6.6^{+2.6}_{-1.7}$	500^{+170}_{-120}				550^{+250}_{-180}

accurate ranges to Saturn made possible by the Cassini spacecraft. Their findings showed how, if the Planet 9 described by Batygin and Brown (2016) were to be today in a particular range of true anomalies, the residuals of the Cassini ranges after fit would significantly reduce. Concurrently, Gomes et al. (2016) argued that a planet in this orbital configuration could explain the inclination of the ecliptic with respect to the solar equator.

One of the main challenges to the Planet 9 hypothesis is whether the observed clustering of TNOs' orbits that yield to the theory can be due to observational bias. Brown (2017) concluded that "the probability of detecting these two independent clusterings [spatial and in argument of perihelion] in a randomly distributed sample is 0.025%". Brown and Batygin (2019) corrected this figure to 0.2%, extending the method with an "explicit calculation of the bias in pole position". Batygin et al. (2019) seconded this idea, defending that "the distant KBO are thus distinctly clustered at the 99.8% confidence level".

However, this view is still far from undoubted. Lawler et al. (2016) replicated simulations of the Kuiper Belt with an extra planet, finding inconsistencies in the currently observed scattering and detached populations, and stating that no evidence for clustering of orbital angles was found in their simulations. Moreover, Shankman et al. (2017) studied the "striking and non-intuitive biases that exist for the detection of TNOs with large semimajor axes", concluding that the current orbital distribution from the Outer Solar System Origins Survey (OSSOS) is actually "consistent with being detected from a uniform underlying angular distribution". Batygin et al. (2019) replied that the associated likelihood of this bias being real is less than 1%, and insisted on the fact that "multiple lines of evidence all point to the same Planet Nine model".

When it comes to observations, all efforts have been unsuccesful so far. Holman and Payne (2016) looked at astrometric observations of Pluto and other TNOs, fitting different sources of gravitational perturbations and concluding that the planet should be "either more massive or closer than argued for by Batygin and Brown (2016) or Fienga et al. (2016)". Naess et al. (2021) presented the results of a Planet 9 survey with the Atacama Cosmology Telescope, reporting "no statistically significant detections", which effectively eliminated "roughly 17% and 9% of the parameter space for a 5 and 10 Earth-mass Planet 9, respectively". Additionally, Belyakov et al. (2022) ruled out an additional 5% of the parameter space from Brown and Batygin (2021) that would have already been detected by the Dark Energy Survey.

The lack of observational evidence is currently the factor that casts most doubt on the Planet 9 hypothesis. The most recent update, based on the Panoramic Survey Telescope and Rapid Response System (Pan-STARRS) survey and published in a preprint by Brown et al. (2024), states that 78% of the parameter space defined by Brown and Batygin (2019) is already ruled out. In addition, Fienga, Ruscio, et al. (2020) repeated the analysis based on the residuals of the INPOP ephemerides fit when introducing the alledged Planet 9, this time with the addition of Juno range data, and concluded that the addition of Planet 9 "does not improve the planetary residuals regardless of the configurations that are considered". As a still existing possibility, only some regions in the parameter space where the fit is not significantly degraded were given.

If a massive body is indeed perturbing the Kuiper Belt, one possible explanation for the lack of visible evidence is suggested by Scholtz and Unwin (2020): that it is not a planet but a primordial black hole (PBH). This could still be detectable through its Hawking radiation (Siraj & Loeb, 2020), and would offer a privileged fundamental physics laboratory in the backyard of the Solar System.

During the course of this work, a new study was published by Batygin et al. (2024), claiming to show evidence robust to 5-σ of observed TNO distribution consistent with the Planet Nine hypothesis. Despite the lack of results from the visual surveys and the inconclusive result by Fienga, Ruscio, et al. (2020), the authors defend that "if anything, today we are more confident than we were 5 years ago" (Batygin, 2024, priv. comm.).

5.4. Solar System rotation and inertial reference frames

Note to the reader: this topic has not been addressed in the final objectives of this work.

In one of the few studies following the publication of the original Trilogy paper by Smith et al. (2018), Bills and Skillman (2022) studied the implications of considering the Trilogy arrangement as a solar-system-scale gyroscope. The reasoning behind is that the proposed setup will be able to take advantage of the Sagnac effect (Sagnac, 1913), just as current laser gyroscopes do.

The Sagnac effect describes how, for a given planet distribution, light will cover the Earth-Venus-Mars laser links in different times depending on whether those are prograde (in the same rotation sense as the planets) or retrograde (in the opposite sense). Due to the finite speed of light and the fact that planets move during the light travel time, retrograde loops will take less time than prograde loops. More specifically, this time difference will be equal to

$$\Delta t = \frac{4}{c^2}\mathbf{\Omega} \cdot \mathbf{A}, \tag{5.1}$$

where c is the speed of light in vacuum, $\mathbf{\Omega}$ is the rotation rate of the triangle with respect to inertial space, and $\mathbf{A}$ is the normal area vector. Hence, the measured time deviation, together with the value of the closed area, can lead to the determination of the rotation rate of the triangle (and thus, of the Solar System) with respect to inertial frame (Bills, 2023). This can also be computed by existing VLBI, but according to preliminary calculations by Eubanks (2023), ILTN could achieve in a few thousand seconds the accuracy VLBI achieves in one year.

Increasing the accuracy of the monitorisation of the Solar System rotation has a twofold impact: on the one hand, it would increase the precision of reference frames such as the International Celestial Reference Frame (ICRF), on which global navigation systems like GPS are dependent. On the other hand, it would reduce the uncertainty on the total angular momentum of the Solar System, which could theoretically help in the determination of the currently unknown masses and even the discovery of currently unknown objects. The need for an accuracy increase in the definition of the ICRF is nevertheless unclear: Liu et al. (2023) state that "the orientation of current planetary ephemeris frames is as accurate as at least 0.4 mas, and the nonrotation is better than 5μas per year". The accurate justification for an improvement with respect to the current figures is still to be defined.

5.5. Heliophysics and astrophysics

Note to the reader: although these topics have not been addressed in the final formulation of the research questions of this work, the research summarized below supported the decision of assuming GR to be true and focusing on ephemerides and asteroid masses instead.

5.5.1. Expansion of the Solar System

The motion of Solar System bodies is mainly described by the Sun's gravitational parameter $\mu_\odot = GM_\odot$, where G is the universal gravitational constant and $M_\odot$ is the solar mass. Their product $\mu_\odot$ is commonly taken as constant, and currently known to be (Pitjeva, 2015)

$$\mu_\odot = 132\,712\,440\,042 \pm 10 \text{ km}^3/\text{s}^2.$$

However, it is known that in actuality $\mu_\odot$ varies through time. One reason for this is the change of mass of the Sun, but it is possible that a non-constant G also contributes to this variation.

As the gravitational pull of the Sun gets reduced, the orbits of all bodies orbiting around it increase their semimajor axes: as shown by Pitjeva and Pitjev (2012),

$$\frac{\dot{\mu}}{\mu} = -\frac{\dot{a}}{a}. \tag{5.2}$$

An accurate time measuring of the rate of increase of the orbit semimajor axis of Solar System bodies would therefore give valuable insight on the real behavior of $\dot{\mu}_\odot$ over time. In fact, this was the main purpose of the Trilogy Mission when presented by Smith et al. (2018). This would however only measure the change of the product of G and $M_\odot$— measuring the two quantities separately is a challenging problem, discussed below.

Solar mass burn rate

It is well known that our Sun continuously loses mass: as hydrogen is fused into helium, 2.9% of a proton mass is transformed to energy in the reaction (Sackmann et al., 1993). Solar wind, coronal mass ejections and in-falling material also play a role in the mass variation of the Sun, and it is still to be fully understood how these magnitudes are affected by the cycle of solar activity. A full understanding of this behavior would provide valuable insight on the physics of the Solar interior (e.g., Christensen-Dalsgaard, 2021). Figure 5.2 shows the recent estimates of the rate of change of the solar mass.

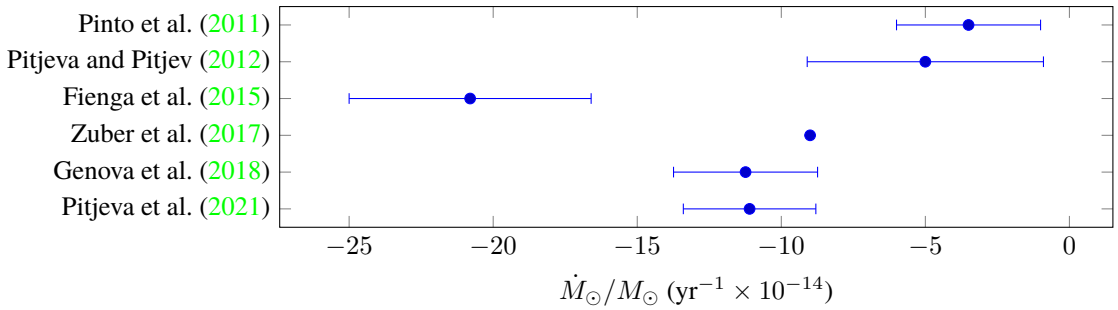

Figure 5.2: Solar mass burn rate according to the existing estimates.

Using theoretical knowledge on solar physics to estimate its mass loss due to fusion, wind and ejections, Pinto et al. (2011, Fig. 8) show a curve oscillating between a maximum and a minimum value as the solar cycle progresses. Zuber et al. (2017) estimate the same figures based on simple calculations, getting a single value without error range. On the other hand, the most common method to estimate the solar mass burn rate is through the fit of planetary ephemerides.

Pitjeva and Pitjev (2012) fitted $\dot{\mu}_\odot/\mu_\odot$ into the computation of the EPM model, and separated the values of $\dot{M}_\odot/M_\odot$ and $\dot{G}/G$ by making an educated guess of the upper and lower limits of solar mass change through time. Pitjeva et al. (2021) refined the same methodology with the most recent version of the EPM ephemerides, including new range data such as that from MESSENGER and Juno. An equivalent approach, but enforcing $\dot{G} = 0$, is followed by Fienga et al. (2015)—Figure 5.2 shows the value reported after full estimation, although the paper lists other results with "limited" approaches. As they note, there is an "important increase of the uncertainties when more asteroid masses are included in the fit". Finally, a similar methodology was followed by Genova et al. (2018), using ranges from MESSENGER to fit both the orbits of mercury and the spacecraft, calculating a series of other parameters—inculding $\dot{\mu}_\odot/\mu_\odot$—and improving in the process the accuracy of the estimation of Mercury's ephemerides with respect to those of the DE model.

Pitjeva and Pitjev (2012) claimed that "the modern level of observational accuracy does not allow one to reveal any definite change in astronomical unit (AU)", since the change in semimajor axis of the of the orbit of the Earth cannot be fitted into the parameter estimation and get a formal error smaller than the fitted value itself. This is presumably applicable to all other Solar System bodies, especially those which lack an accurate series of measurements in a large time span. Pitjeva et al. (2021) insist on the fact that "direct search for a resizing of orbits due to the time evolution of the value of GM for the central body [...] is ineffective because over a time interval of several tens or hundreds of years, the effect is too small". However, the change in orbital period associated with the change in semimajor axis does be measurable, and this is why "using long-range observations allows us to find the change over time $\dot{\mu}_\odot$".

Non-constant gravitational constant

The gravitational constant G was introduced by Newton as the proportionality constant of his law of gravitation, and it is still a fundamental constant in Einstein's GR equation (e.g., Carroll, 2004, eq. 1.5). Its value is known to be

$$G = 6.67 \times 10^{-11}\ \mathrm{m}^3/(\mathrm{kg\,s}^2).$$

The decimal figures after the 7 already show discrepancies between the results of different experiments (Tiesinga et al., 2021, Tab. XXIX), and in fact "increasing the accuracy of G measurements [...] comprises one of the central problems of modern physics and metrology" (Bronnikov et al., 2022). The measurement of G alone is challenging, for instance due to its coupling with the required measurement of any mass used in the experiment. As an example of such challenges, Anderson et al. (2015) suggested that the Earth's changes in magnetic field and moments of inertia affect the measurement of G in ground-based experiments.

Despite GR predicts G to be a truly fundamental constant, the fact that it is not a definitive theory leaves room for speculating other options. Although GR has passed all experimental tests so far (e.g., Will, 2014), some nuanced or alternative theories might answer some of the greatest unknowns such as the actual nature of dark matter. One possibility, for instance, is that G is not constant but it is time-varying or space-varying. If it were time-varying, a nonzero value of $\dot{G}/G$ should be measurable. The most precise estimates today, however, are all consistent with an actual value of $\dot{G} = 0$. A summary of recent estimates is shown in Figure 5.3.

One method for the calculation of $\dot{G}/G$ is the same as introduced above for the computation of $\dot{M}_\odot/M_\odot$: the value of $\dot{\mu}_\odot/\mu_\odot$ is fitted into the dynamical model of planetary ephemerides, and the value of $\dot{G}/G$ is decoupled from it based on other estimates for the solar mass burn rate. This is the approach followed by Fienga et al. (2015), Pitjeva and Pitjev (2012, 2013), and Pitjeva et al. (2021). Genova et al. (2018) follow a very similar method, but with Mercury's orbit only.

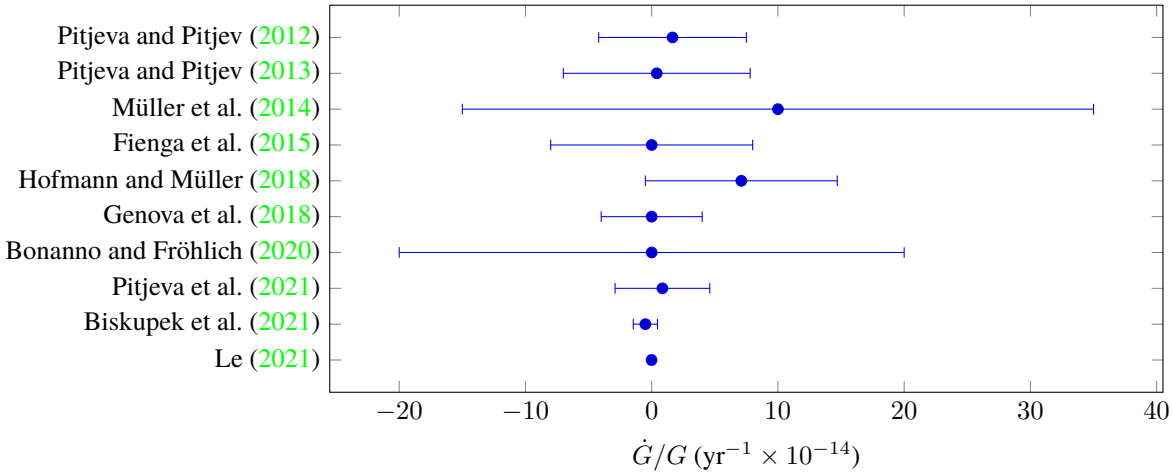

Figure 5.3: Possible time variation of the gravitational constant according to recent estimates. Extended from Pitjeva et al. (2021).

Another approach is to use the accurate observations of LLR, which allow to directly get a decoupled estimate of $\dot{G}$. This is because, unlike with the Sun, the mass of other celestial bodies can be considered constant, hence the measured change in gravitational parameter is directly proportional to the change in G (Fienga & Minazzoli, 2024, Eq. 137). This is the methodology followed by Biskupek et al. (2021), Hofmann and Müller (2018), and Müller et al. (2014).

Other methods to directly measure $\dot{G}/G$ are based on pulsar timing (W. W. Zhu et al., 2018, 2015), or astroseismology of low-mass stars (Bellinger & Christensen-Dalsgaard, 2019). These approaches are not reported in Figure 5.3 because they give uncertainty ranges in the order of 10^{-12}. Finally, Le (2021) estimates $\dot{G}$ based on spectral observations of a White Dwarf, getting the most narrow uncertainty range up to date with just $\pm 0.2449 \times 10^{-14}$.

On the other hand, it is possible that a space variation of G were detectable. Fischbach et al. (1986) suggested, based on certain discrepancies in laboratory-measured values of G, that the well known Newtonian potential U_N caused by a point mass be corrected as

$$U(r) = U_N \left(1 + \alpha e^{-\frac{r}{\lambda}}\right), \tag{5.3}$$

where α and λ are two different fundamental constants, and r is still the radial distance to a point mass. This was acknowledged by the community as the "fifth-force formalism", and one possible interpretation is that the only deviation from classical theory is due to a spatially-damped G (Fischbach & Talmadge, 1999, Eq. 2.1.10):

$$G(r) = G_\infty \left[1 + \alpha e^{-\frac{r}{\lambda}} \left(1 + \frac{r}{\lambda}\right)\right]. \tag{5.4}$$

Investigating the validity of such formulation was suggested by Peron (2023) in the ILTN workshop as one possible scientific objective of Trilogy.

5.5.2. Other solar parameters

The precession of Mercury's perihelion detected in the late 19th century evinced how there was something still to be understood with planetary dynamics. This was firstly attempted to be explained by introducing an non-spherical gravity field of the Sun, although in pre-GR times this lead to inferred values that were "not possible, even with a rapidly rotating solar core" (Rozelot & Damiani, 2011). Today, "it is admitted [...] that GR can account for almost all the observed perihelion advance but not all" (Damiani et al., 2011)—in particular, "the solar gravitational oblateness J_2 and the angular momentum $\mathbf{S}_\odot$ are responsible for additional precession rates of 0.029" per Julian century and 0.002" per Julian century, respectively" (Genova et al., 2018). The ongoing work to estimate these two parameters is described below.

Gravitational oblateness

The first important point to notice is that the internal dynamics of the Sun make its physical—or photospheric—oblateness not as straightforwardly related to its gravitational oblateness—described by its gravitational moments J_n—as in a solid body. Rozelot and Fazel (2014) describe how the "photospheric oblateness is [...] sensitive to the interior rotation rate", and encourage work to model it accurately in order to "provide constraints on the rotation of the core" and study "the impact on the solar gravitational moments". This relationship can be illustrated by the simplified expression given by Meftah et al. (2016, eq. 1), which relates the photospheric oblateness with the J_2 coefficient and the exterior rotation

raten of the Sun, although ackowledging that it is an "ill-posed problem". It is intuitive to see how this is the case if a single equation relates three unknown quantities, i.e., the photospheric and gravitational oblatenesses and the rotation rate.

Traditionally, studies of the Sun's gravitational oblateness had been theoretical and based on helioseismology. For instance, Mecheri et al. (2004) and Paterno et al. (1996) agreed to a high extent in a J_2 value between 2.20×10^{-7} and 2.23×10^{-7}. Pijpers (1998) supported this value, although reporting a lower bound down to 2.12×10^{-7}. With the increasing availability of deep-space range measurements, the more modern approach is to fit the value of $J_{2,\odot}$ into planetary ephemerides models. Recent values obtained with this method are displayed in Figure 5.4.

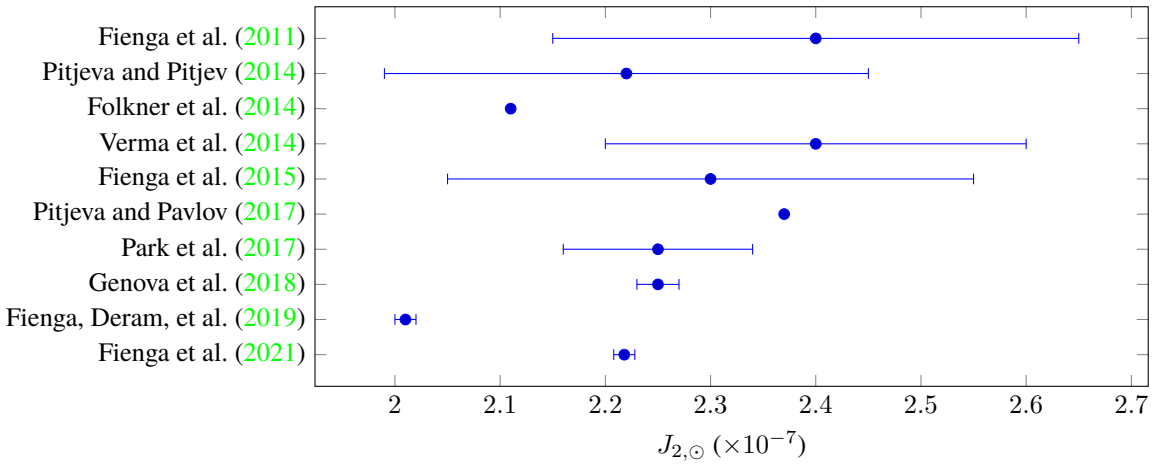

Figure 5.4: Recent estimates of the solar oblateness $J_{2,\odot}$. Based on van der Zwaard and Dirkx (2022, Tab. A1)

It is worth highlighting that the first half of reported values (Fienga et al., 2011, 2015; Folkner et al., 2014; Pitjeva & Pitjev, 2014; Verma et al., 2014) used dynamical models that did not account for the Lense-Thirring (LT) effect, unlike all posterior studies (Fienga, Deram, et al., 2019; Fienga et al., 2021; Genova et al., 2018; Park et al., 2017; Pitjeva & Pavlov, 2017). The values displayed in Figure 5.4 can suggest that the inclusion of this effect has made the upper bounds of ephemerides-estimated values differ less from the values estimated via helioseismology, supporting the claim by Fienga and Minazzoli (2024) that "the values obtained with LT [...] are indeed closer to the ones issued from helioseismologic surveys [...] than those obtained before the LT introduction".

The actual current value of J_2 is not the only open question regarding the Sun's oblateness: higher order coefficients are even harder to measure, and some past estimates put it between the same order of magnitude as J_2 and two orders of magnitude lower (see Rozelot and Damiani, 2011 for a full review). Today, according to Fienga and Minazzoli (2024), "only J_2 leads to a significant impact on the planetary ephemerides at the current level of accuracy".

The time variability of the solar oblateness has also been an open topic since more than a century ago, when Poor (1905) published correlations between the observed photospheric oblateness and the 11-year solar activity cycle monitored by the number of visible sunspots (e.g., Sakurai et al., 2023). This cyclic variation was supported by different observations during the 20th century (Damiani et al., 2011), but the behavior of the gravitational oblateness is not as clear. Antia et al. (2008) stated that "J_2 does not exhibit any significant temporal variation"—only some higher-order moments. On the other hand, Rozelot et al. (2009) opposed their interpretation, and suggested that both the physical and gravitational oblatenesses are time-dependent. Irbah et al. (2019) summarized the different measurements of photospherical oblateness, which were apparently inconsistent with a direct correlation with the 11-year solar activity cycle: "variations are observed in anti-phase with the solar activity during Cycle 24, whereas they were in phase with activity during Cycle 23". After confirming with past data how the trend suggested "in-phase variation during odd cycles and anti-phase variation during even cycles", they suggested that this variation followed the 22-year magnetic cycle of the Sun. Xu et al. (2017) showed how how a periodic variation of J_2 could have an effect "of nearly 0.8 per cent of the secular perihelion precession of Mercury", and concluded that "a better understanding of the solar oblateness is required", which could be "through observation in the solar orbits instead of on the Earth".

Angular momentum

Angular momentum is the magnitude responsible for the Lense-Thirring (LT) effect (equation 4.19), which, as described above, causes effects similar to those from the solar oblateness. Hence, the accurate knowledge on the solar angular momentum $\mathbf{S}_\odot$ is essential to make accurate interpretations of observations and simulation results.

Using helioseismology, Pijpers (1998) obtained $\mathbf{S}_\odot = (1.900 \pm 0.015) \times 10^{41}$ kg m^2/s. Other studies followed during the 2000's, all agreeing in a value between 1.63×10^{41} kg m^2/s and 2.05×10^{41} kg m^2/s (Iorio, 2012, Tab. 1). However,

when introducing the theoretical constraints of GR in a moment when ephemerides fits did not account for the LT effect and range observations of MESSENGER were starting to be available, Iorio (2012) found an upper value of $\mathbf{S}_\odot$ that decreased two-fold the average of the previous estimates. Although Iorio (2015) defended that this discrepancy "might, perhaps, hide something anomalous which deserves further investigations", the value given by Pijpers (1998) is still used in the modern ephemerides fits and estimation simulations mentioned above (Fienga et al., 2021; Genova et al., 2018; Park et al., 2017).

5.5.3. Alternative gravitational theories

The parametric Post-Newtonian formalism

Despite the solid experimental support for GR, research to find possible deviations from the theory as described by Einstein (1915) is still being conducted. The modern means by which this is formulated is the parametrized post-Newtonian (PPN) formalism. This formulation was pioneered by Eddington (1923) and it was extended and generalized further by several contributions throughout the 20th century (see Hohmann, 2021 for a summary). Today, the widely-used PPN formalism uses 10 different parameters (Will, 2014, Tab. 2). Hohmann (2021) describes them as follows:

- γ measures the amount of spatial curvature produced by unit rest mass;
- β measures the non-linearity in the gravitational superposition law;
- α_1, α_2 and , α_3 measure the violation of local Lorentz invariance, i.e., the presence of preferred-frame effects;
- ζ_1, ζ_2, ζ_3 and ζ_4, together with α_3, measure the violation of total energy-momentum conservation; and
- ξ measures the violating of local position invariance, i.e., the presence of preferred-location effects.

In addition, Nordtvedt Jr (1968a, 1968b) introduced the relationship

$$\eta = 4\beta - \gamma - 3 - \frac{10}{3}\xi - \alpha_1 + \frac{2}{3}\alpha_2 - \frac{2}{3}\zeta_1 - \frac{1}{3}\zeta_2, \tag{5.5}$$

currently known as the Nordtvedt parameter. This plays a relevant role in the equivalence principle, developed later in this section.

In GR, $\gamma = \beta = 1$ and all other parameters are equal to zero. In several theories of gravity, α_3 and all ζ_i are equal to zero—those in which they are not are "non-metric" (Will, 2014). Moyer (2005, Eq. 4-26) gives the expression for the acceleration of a body under the influence of a system of point masses in terms of γ and β:

$$\begin{aligned}\boldsymbol{a}_i = &\sum_{j\neq i} \frac{GM_j\left(\boldsymbol{r}_j - \boldsymbol{r}_i\right)}{r_{ij}^3}\left\{1 - \frac{2(\beta+\gamma)}{c^2}\times\sum_{k\neq i}\frac{GM_k}{r_{ik}} - \frac{2\beta-1}{c^2}\sum_{k\neq j}\frac{GM_k}{r_{jk}}\right.\\
&+\gamma\left(\frac{v_i}{c}\right)^2 + (1+\gamma)\left(\frac{v_j}{c}\right)^2 - \frac{2(1+\gamma)}{c^2}\boldsymbol{v}_i\cdot\boldsymbol{v}_j - \frac{3}{2c^2}\left[\frac{(\boldsymbol{r}_i-\boldsymbol{r}_j)\cdot\boldsymbol{v}_j}{r_{ij}}\right]^2 + \frac{1}{2c^2}(\boldsymbol{r}_j-\boldsymbol{r}_i)\cdot\boldsymbol{a}_j\left.\right\}\\
&+\frac{1}{c^2}\sum_{j\neq i}\frac{GM_j}{r_{ij}^3}\left\{[\boldsymbol{r}_i-\boldsymbol{r}_j]\cdot[(2+2\gamma)\boldsymbol{v}_i \ -(1+2\gamma)\boldsymbol{v}_j]\right\}(\boldsymbol{v}_i-\boldsymbol{v}_j) + \frac{(3+4\gamma)}{2c^2}\sum_{j\neq i}\frac{GM_j\boldsymbol{a}_j}{r_{ij}}.\end{aligned} \tag{5.6}$$

Note how, if $\gamma = \beta = 1$, equation (5.6) becomes equivalent to equation (4.17), which is the original Einstein-Infeld-Hohmann equation.

Equation (5.6) can be used in the fit of planetary ephemerides, which allows to solve for γ and β instead of keeping them fixed. However, these two parameters produce effects strongly correlated with those from the solar gravitational oblateness $J_{2,\odot}$. To overcome these effects, instead of fitting all three parametrers simultaneously (as Pitjeva and Pitjev, 2013; Verma et al., 2014 do), some authors opt for fixing some and estimating the others (Fienga, Bigot, et al., 2019; A. S. Konopliv et al., 2011; Park et al., 2017) or even exploring the whole parameter space through random walks (Fienga, Bigot, et al., 2019) or genetic algorithms (Fienga et al., 2015). Based on all the exisitng estimates for β and γ based on planetary ephemerides, Fienga and Minazzoli (2024) give their current known constraint

$$\begin{aligned}(\beta-1) &= (-0.45\pm1.75)\times10^{-5};\\ (\gamma-1) &= (0.55\pm1.35)\times10^{-5}.\end{aligned} \tag{5.7}$$

In order to compute the value of γ in a disentangled manner from β, another possibility is to take advantage of the Shapiro delay (Shapiro, 1964), which describes how light gets curved due to gravitational influence and which only depends on the value of γ (Fienga & Minazzoli, 2024, Eq. 97). This was successfully verified by Bertotti et al. (2003)

using ranges to the Cassini spacecraft, and obtained a value of $\gamma - 1 = (2.1 \pm 2.3) \times 10^{-5}$. In their words, "this agrees with the predictions of standard general relativity with a sensitivity that approaches the level at which, theoretically, deviations are expected in some cosmological models".

So far, planetary ephemerides tests have tried to fit γ and β only, and Fienga and Minazzoli (2024) state that "several studies still seem to be needed before being able to constrain the full PPN framework with planetary ephemerides". Imperi et al. (2018) expect an improvement of a factor 40 in the fitting of β and one order of magnitude in the fitting of γ thanks to future Bepi-Colombo data. De Marchi and Cascioli (2020) conducted a covariance analysis to assess how present and future Solar System missions could additionally constrain other PPN parameters α_1, α_2 or ζ_1, and found that the greatest improvement would come from Bepi-Colombo range data, agreeing with Imperi et al. (2018) in expecting the estimation of γ to be improved by one order of magnitude. The authors also point out how Cascioli et al. (2019) already showed how a Trilogy-like concept—or "a strategy based on the simultaneous data analysis of several missions"—might lead to a further reduction of the formal uncertainties of the estimated parameters "thanks to a reduction of their correlations".

Violations of the equivalence principle

The equivalence principle is a fundamental concept in both modern and classical physics. Today, it is commonly defined through two definitions: the weak and the strong equivalence principles:

- **The weak equivalence principle** states that, in a uniform gravity field, all bodies undergo the same acceleration regardless of their mass, composition or internal structure. As described by Will (2018a, p. 11), if Newton's second law is $\mathbf{F} = m_I \mathbf{a}$, where m_I stands for "inertial mass", and the gravitational force is $\mathbf{F} = m_P \mathbf{g}$, where m_P stands for "passive gravitational mass", then the weak equivalence principle states that, for any body, $m_I = m_P$. This was an assumption made by Newton, and it was later defined to be an intrinsic property of GR. Within GR, however, the equivalence principle can be extended as follows:
- **The strong equivalence principle** states that "a uniform gravitational field is locally indistinguishable from an accelerated reference frame" (Genova et al., 2018).

Genova et al. (2023) introduce the generalized formulation that relates gravitational and inertial masses without assuming the validity of neither of two principles:

$$m_G = m_I \left(1 + \delta + \eta \frac{\Omega}{m_I c^2}\right), \tag{5.8}$$

where δ accounts for violations of the weak equivalence principle and η, which is the Nordtvedt parameter defined in equation (5.5), accounts for violations of the strong equivalence principle. Ω is the gravitational self-energy, which is proportional to Gm_G^2/R, where R is the radial separation between the gravitational mass m_G and the source of the gravity field. As Genova et al. (2018) states, when proving the strong equivalence principle, "the test mass used in the experiment needs to be sufficiently large so that the self-gravitational force is not negligible", which makes planetary tests the most suitable. If the weak and strong equivalence principles are truly valid, δ and η must be, respectively, strictly equal to zero.

Both principles have passed all experimental tests so far (see Fienga and Minazzoli, 2024, p. 60 for a summary). Besides ground-based, laboratory tests, Touboul et al. (2022) used a space-based experiment and found "no [weak] EP violation at the level of 2.7×10^{-15}". Regarding the strong equivalence principle, most tests (e.g., Hofmann and Müller, 2018; Müller et al., 2014) have been performed through LLR. Viswanathan et al. (2018) approached the problem by fitting the solution of the INPOP17a model to the available LLR data set, and Genova et al. (2018) tackled the estimation of η by means of the Mercury orbit fit based on MESSENGER observations. The method described in the latter takes advantage of a theorized discrepancy in the computation of the Solar System barycenter (SSB), which coul only be observable if $\eta \neq 0$. The values obtained with each of the methods are displayed in Figure 5.5.

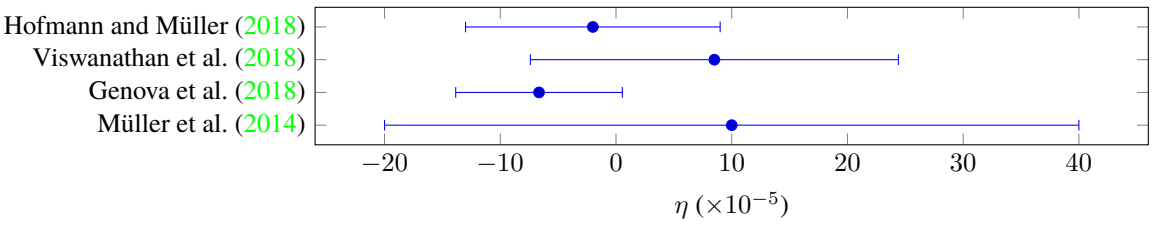

Figure 5.5: Constraints on the Nordtvedt parameter according to recent estimates.

Future experiments expect the results from the Bepi-Colombo spacecraft to further reduce the uncertainties of relativistic parameters. De Marchi et al. (2016) described a semianalytic model used to perform a covariance analysis on

the expected determination of the Nordtvedt parameter, and concluded it will be estimated with an uncertainty that is of the same order of magnitude as the recent values reported in Figure 5.5. In their words, "the uncertainties of the masses of Solar System bodies degrade the precision of the estimation of η by about 1 order of magnitude". Imperi et al. (2018), on the other hand, psuh this figure to an expected two orders of magnitude improvement. Regarding the Trilogy concept, Cascioli et al. (2019) found that the Venus-Earth-Mars configuration would yield to the most accurate determination of η, with a reported formal uncertainty of 6.7×10^{-6}.

Massive gravitons

The formulation of a space-decaying gravitational field (equation 5.4) is closely related to the theory of massive gravity. This is a sub-field inside quantum gravity, which aims to fit gravity within the framework of particle physics, postulating that the graviton would be the intermediary particle of gravity just as the photon is that of the electromagnetic force. Massive gravity is the formulation in which the graviton is alleged not to be massless, contradicting GR. Although there are multiple formulations of massive gravity (de Rham, 2014), in its simplest approximation, the observable effect of the existence of a massive graviton is given by the modification of the Newtonian gravitational potential U_N caused by a point mass as (Will, 2018b)

$$U = U_N e^{-\frac{r}{\lambda_g}}, \tag{5.9}$$

where λ_g is the Compton wavelength of the graviton. The Compton wavelength of a particle is a well established concept in quantum theory, and it is defined as the wavelength of a photon whose energy is equal to the rest mass energy of the particle (Compton, 1923). It is related to massive particles with the known relationship $\lambda = h/(mc)$, where h is Planck's constant, m is the mass of the particle and c is the speed of light in vacuum. Hence, if the mass of the graviton were $m_g = 0$, then $\lambda_g = \infty$.

The question remaining is of course whether or not a hypothetical finite value of λ_g, which would support the existence of massive gravitons, is measurable. Will (2018b) tackled the problem from the ephemerides approach, and claimed that "data on the perihelion advance of Mars obtained from MRO leads to a credible lower bound on λ_g between 1.2×10^{14} km and 2.2×10^{14} km". However, Fienga and Minazzoli (2024) reply that "because of the correlation between λ_g and other parameters, any modification induced by a non-null [non-infinite*] value of λ_g may—at least in part—be reabsorbed by the modification of other parameters of the ephemerides". This issue is acknowledged by Bernus et al. (2020), who fit all the ephemerides using the extra acceleration term resulting from (5.9) in their numerical integrator, yielding to the conclusion that "the residuals of Mars orbiters, Cassini, MESSENGER, and Juno, degrade significantly when $\lambda_g \leq 3.43 \times 10^{13}$ km". Finally, Mariani et al. (2023) addressed problem with a Markov chain Monte Carlo approach and the most recent version of the INPOP ephemerides, and found the bound for the graviton wavelength to be $\lambda_g \geq 1.225 \times 10^{15}$ km. This shows a clear increasing trend in the lower bound of the hypothetical wavelength of a massive graviton, which may perfectly suggest that there is actually no violation of GR in this regard.

5.5.4. Gravitational waves

General Relativity (GR) predicts the existence of GWs, which are deformations of space-time that propagate at the speed of light. Ground-based detectors such as the Laser Interferometer Gravitational-Wave Observatory (LIGO) are constrained by Earth scales and seismic noises, and this is why space-based detectors were starting to be suggested in the 20th century. The concept of the Laser Interferometry Space Antenna (LISA) mission was first proposed by Danzmann et al. (1993) and it is currently expected to be launched in 2037. Other missions with the same purpose have also been suggested: Taiji, which is essentially the same as LISA but with a slightly larger arm, TianQin and DECi-hertz Interferometer Gravitational wave Observatory (DECIGO), which would be placed in smaller geocentric orbits instead, and Astrodynamical Space Test of Relativity using Optical Devices optimized for Gravitational Waves (ASTROD-GW), which would essentially work as

Table 5.3: Space-based gravitational wave detector missions currently under development/discussion. Adapted from Ming et al. (2020).

Name	Arm length	Spacecraft locations	Reference
LISA	2.5 million km	Heliocentric orbits	Danzmann (2000)
ASTROD-GW	260 million km	Sun-Earth L3, L4 & L5	Ni (2013)
TianQin	170 thousand km	Geocentric orbits	Luo et al. (2016)
Taiji	3 million km	Heliocentric orbits	Hu and Wu (2017)
DECIGO	1000 km	Geocentric orbits	Kawamura et al. (2006)

if the Trilogy concept were set to be based on free heliocentric orbits and had interferometric measurements available. Table 5.3 presents a summary of the different proposals.

If Trilogy were equipped with the capability of conducting interferometric measurements, it might well be capable of detecting the signatures of GWs. Preliminary calculations presented by Eubanks (2023) suggested that it would be sensitive to GWs caused by more massive objects than LISA, although it wouldn't reach sensitivity to amplitudes as small as LISA will. The conclusions presented in the Workshop stated that numerical simulations of Kerr super-massive black hole mergers and the corresponding detectable signatures from the Trilogy mission are strongly needed.

Part III

Implementation

6

Planetary simulation only

6.1. Description

Describe the ephemerides models, the asteroid masses, the planetary covariances and the true vs estimation models. Covariance inconsistency to be developed here.

6.1.1. Simulation settings

Ephemerides models

The implemented simulations make use of the default ephemerides settings for the Solar System main bodies, which consist of the set of states computed for the INPOP19a model (Fienga, Deram, et al., 2019). These are loaded through the spice kernel `inpop19a_TDB_m100_p100_spice.bsp`, which is included in the Tudat bundle and can be accessed through the official site[1]. In the implemented simulation, these are assigned to the main Solar System bodies during each simulation setup through the function `get_standard_body_settings()`.

Regarding asteroid ephemerides, the default file included in Tudat is `codes_300ast_20100725.bsp`, which lists the states of the 300 heaviest asteroids and which is directly provided by NASA's Navigation and Ancilliary Information Facility (NAIF)[2]. With the aim of overcoming this 300 asteroids limitation and being able to generate ephemerides for all the 415 objects included in the SiMDA catalog (section 5.2), the implemented simulation makes use of JPL's Horizons database[3] instead, which includes ephemerides of 1,422,855 asteroids. To avoid storing a file with such a large amount of information, Tudat offers the `HorizonsQuery` module, which can be used to retrieve information regarding an individual object from the Horizons database. The implemented simulation creates an asteroid dictionary with the desired asteroids at the beginning and stores the ephemerides of each of them by means of the `get_true_asteroid_ephem()` function, which internally makes use of `HorizonsQuery`.

Asteroid masses

Information of asteroid masses is included in the spice kernel `inpop19a_TDB_m100_p100_spice.tpc`, which is included by default in Tudat. This, however, only lists the masses estimated during the fit of the INPOP19a ephemerides, which results in estimated masses that can be significantly different to the results of other mass estimation methods (section 5.2). In order to get a more representative depiction of reality, the nominal mass values assigned to each asteroid i have been set to be the mass averages $\bar{M}_i$ provided in the SiMDA catalog (section 5.2). These are the result of combining all individual mass estimates of each asteroids with the Expected Value Method (EVM), which is described by Birch and Singh (2014).

Similarly, all mass uncertainties $\sigma_{\bar{M}_i}$ reported in the catalog, also computed with the EVM, are taken as representative estimates of the 1-σ true uncertainties in our asteroid mass knowledge. In the implemented simulation, when the dictionary of asteroids to be included in the system of bodies is created by means of the `create_true_asteroids_dict_from_names()` function, each mass is assigned by caling the subroutine `get_true_simulation_mass()`. This can be called with `error_mode='None'`, which assigns to each asteroid mass M_i the mean mass value reported in the SiMDA catalog, i.e., $M_i \leftarrow \bar{M}_i$; or with `error_mode='gaussian_one_sigma'`, which assigns a randomly generated mass from a Gaussian distribution defined by the mean and 1-σ uncertainty reported in the SiMDA catalog, i.e., $M_i \leftarrow \tilde{M}_i$ with

[1] https://www.imcce.fr/recherche/equipes/asd/inpop/download19a
[2] https://naif.jpl.nasa.gov/pub/naif/generic_kernels/spk/asteroids/
[3] https://ssd.jpl.nasa.gov/horizons/

$M_i \sim \mathcal{N}\left(\bar{M}_i, \sigma_{\bar{M}_i}\right)$. Statistically, this is equivalent to assuming the vector of asteroid masses $\mathbf{M} = \begin{bmatrix} M_1 & \dots M_N \end{bmatrix}^\top$ to have an associated covariance matrix

$$\boldsymbol{P}_{\mathbf{M}} = \begin{bmatrix} \sigma_{\bar{M}_1} & & \\ & \ddots & \\ & & \sigma_{\bar{M}_N} \end{bmatrix}. \tag{6.1}$$

Implicitly, this carries the assumption that all asteroid mass uncertainties are independent from each other. This is not fully true, since a significant portion of available estimations (i.e., the ones coming from the fitting of ephemerides and astrometric observations; section 5.2), have been conducted by computing several different masses in a joint estimation, and the resulting post-fit covariance matrix is unlikely to result diagonal. The published results, however, rarely include full covariance matrices but a list of formal uncertainties (i.e., diagonal terms) only. This is why, given the lack of any extra information, Kretlow (2020) assumed independent errors when elaborating the SiMDA catalog and we follow the same assumption. Notably, the fact that this catalog combines different estimations that are truly independent (i.e., carried out with different methods and different teams), does support the assumed independence of the resulting uncertainties. This mass covariance matrix is therefore also used to generate the *a priori* matrix during the estimation of planetary states and asteroid masses.

Covariances of planetary states

In the implemented simulations, the states of Venus, the EMB and Mars are not taken from the ephemerides but propagated and subsequently estimated. Similarly as with the asteroid mass uncertainties, it is required to use a covariance matrix that describes the current uncertainty levels of such ephemerides, both in order to be used as *a priori* in the simulation and to compare it against the post-fit covariance from using Trilogy observations, to assess how much the mission would improve current planetary uncertainties. Unlike with the asteroid masses, however, it is not possible to assign a diagonal matrix for the uncertainties of planetary states because depending on the settings of the dynamical model used, it might diverge over time. A representative estimate for the true covariances of the planetary ephemerides should instead remain approximately constant over time, and mimic the expected levels of true errors in planetary states. The method followed to generate such planetary covariances is based on Zenk et al. (2023), which is in turn based on typical approaches to tackle similar problems (e.g., Lainey, V. et al., 2007). This can be summarized as detailed in algorithm 4, which has been implemented in the `Lainey_covariance_oop.py` file.

Algorithm 4 Obtention of covariances for planetary states

Require: Desired covariance levels for the planetary states in radial (R), along-track (S) and cross-track(W) positions.
Generate cartesian position observations of the bodies of interest during the desired time period
Apply a batch estimation (algorithm 1) with an identity weight matrix ($\boldsymbol{P}_{\mathbf{z}} = \boldsymbol{I}$) to find the initial states $\mathbf{x}_0$ that lead to a propagation that best matches the tabulated ephemerides with the dynamical model at use.
Initialize discrepancy metric ζ and desired discrepancy level ζ_0
while $\zeta > \zeta_0$ **do**
  Tune the weights matrix $\boldsymbol{W}$;
  Re-compute the post-fit covariance $\boldsymbol{P}_0$ with equation (4.55)
  Propagate the post-fit covariance with equation (4.47) to get $\boldsymbol{P}_0(t)$.
  Assess the discrepancy ζ between the resulting propagated formal error levels and the desired RSW uncertainty levels
end while

Although it is impossible, by definition, to know the true errors of planetary ephemerides models, the intercomparison between different models can be used as an estimation. As detailed in depth in Appendix B.1, the planetary positions in the RSW frame have been retrieved from both the INPOP21a (Fienga et al., 2021) and the DE440 (Park et al., 2021) models, and their component-wise RMS between 2010 and 2040 have been taken as desired error levels for each planet's R, S and W position. This results in error levels of ≈ 100 meters for the alogn-track and cross-track positions of the three planets, while radial positions agree within 1-2 meters for Venus and the EMB and ≈ 20 meters for Mars (Figure B.5)

The "discrepancy metric" ζ detailed in algorithm 4 allows to formalize the assessment of the disagreement between the propagated formal errors and the desired covariance levels, but in the implemented simulation it has not been defined as any particular numeric figure of merit. Instead, at each iteration of the while loop, the propagated formal errors have been visually compared to the desired RSW error levels until the resulting curves (appendix B.2) were found not to match any better with further refining of the weights matrix.

Another important remark is that this weight matrix can only be set as diagonal in Tudat. This means that the cartesian position observations (i.e., in inertial XYZ components) can be weighted differently in the X, Y and Z direction, but not in the R, S and W directions, since this would require to apply the $\boldsymbol{R}^{RSW/I}$ rotation matrix to each set of weights $\text{diag}(W_X\, W_Y\, W_Z)$ and would therefore result in non-diagonal weight matrix blocks. Since assigning different weights in X and Y directions therefore does not replicate the effect of doing so in the R and S directions, the modification of the weight matrix at each iteration of algorithm 4 has thus consisted of setting, for each planet, separate weight values $W_X = W_Y$ and W_Z.

Simulation initial states

A key idea in which algorithm 4 is based is that the dynamical model at use needs to employ an initial state that makes the whole propagation as close as possible to the known planetary ephemerides, and this is why the fit of the best initial state $\mathbf{x}_0$ is conducted before finding the best weights $\boldsymbol{W}$ to get the desired formal error propagation. For the sake of consistency, planetary initial states should be assigned this best-fit $\mathbf{x}_0$ in all subsequent simulations.

The implementation, however, was completed with the inconsistency of retrieving all initial states from the ephemerides (function `get_system_initial_state()`), which therefore does not enforce such a good similarity between the propagation and the expected real dynamics and makes the validity of the found covariance $\boldsymbol{P}_0$ more dubious. In order to check the impact of this inconsistency, the same covariance matrix $\boldsymbol{P}_0$ can be propagated with the variational equations resulting from starting at the initial state given by the ephemerides instead of the found best-fit $\mathbf{x}_0$—the result of doing so is presented in Figure 6.1. It can be clearly observed how the propagated formal errors are essentially identical to the

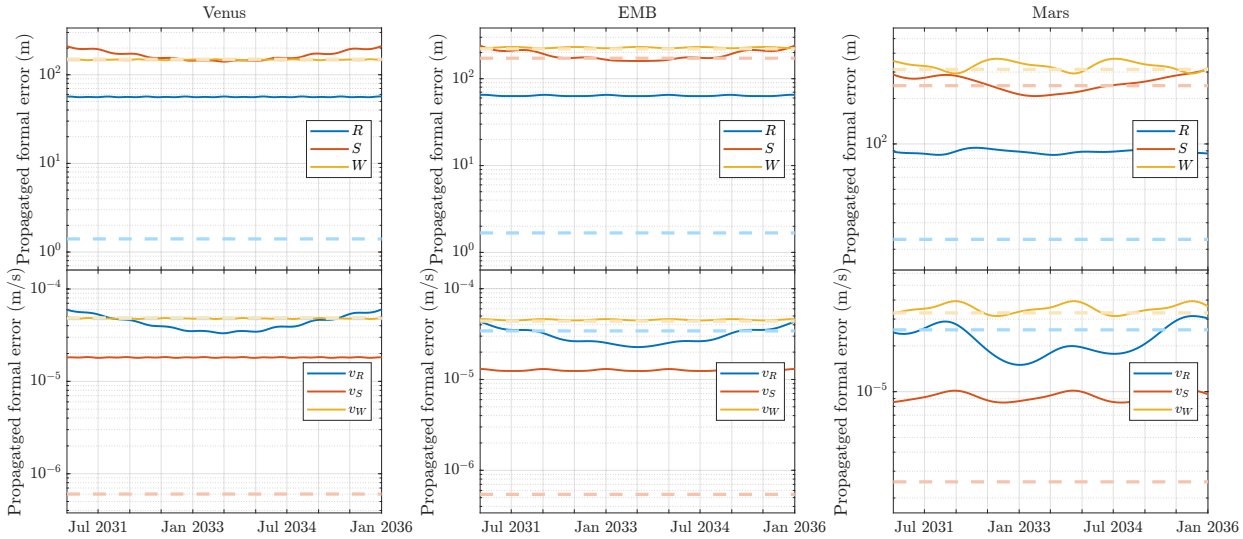

Figure 6.1: Formal error propagation under the usage of the found optimal weights $\boldsymbol{W}$ found in algorithm 4 but when starting from the ephemerides $\mathbf{x}_0$ instead of the found best-fit $\mathbf{x}_0$. Dashed lines indicate the error levels presented in Figure B.5.

results shown in Figure B.11, hence supporting the usage of this covariance matrix even with the inconsistent initial state. This, together with the reasonably close match between the dynamical model and the ephemerides even before finding the best-fit $\mathbf{x}_0$ (section 6.3.1), has led to giving validity to the results obtained from using the initial states given by the ephemerides instead of the best-fit $\mathbf{x}_0$.

The starting date of the simulated Trilogy mission has been set to January 1st 2031 at 12:00:00 UTC. Although the mission concept is still in a very preliminary phase and no particular dates are being considered (chapter 2), this follows our judgment of a mission of this kind to be very unlikely to fly this decade. From the INPOP19a ephemerides model used in this work (see Ephemerides Models earlier in this section), the planetary initial state is the one listed in Table 6.1. This initial state is with respect to the Sun, which is a requirement of the chosen Encke propagator (section A.1). As detailed in section 4.1.1, this propagates the difference between the true trajectory and the initial osculating orbit. The Keplerian orbit therefore needs to be computed, and this requires a finite mass of the central body so that the Keplerian orbital period is fixed.

6.1.2. True and estimation simulation dynamical models

In real life, Trilogy measurements will arise from the true behavior of the Solar System planets, and the resulting observations will be used to constrain the state-of-the-art ephemerides models to be better adjusted to such real dynamics.

Table 6.1: Initial heliocentric states of the Trilogy planets, retrieved from the INPOP19a ephemerides on January 1st 2031 at 12:00:00.

Venus	X_0	86532732966.7914	m
	Y_0	-65893452417.6616	m
	Z_0	-5898764013.79623	m
	v_X	20997.233021226	m/s
	v_Y	27726.2038991526	m/s
	v_Z	-830.243854245838	m/s
EMB	X_0	-26630900076.0844	m
	Y_0	144669714579.773	m
	Z_0	-9984390.91359078	m
	v_X	-29781.6480510734	m/s
	v_Y	-5505.08112574243	m/s
	v_Z	0.552932511209	m/s
Mars	X_0	-242261118382.045	m
	Y_0	56146016331.3576	m
	Z_0	7115530373.26066	m
	v_X	-4567.77846394081	m/s
	v_Y	-21532.5236921280	m/s
	v_Z	-339.319581071984	m/s

In order to assess the performance of this operation (chapter 7), the implemented simulation needs to account for two different "true" and "nominal" dynamical models, whose discrepancy mimics the expected difference between ephemerides and real life. These have been defined as follows:

- **Nominal model**: all simulation settings are set according to the above description, i.e., the planetary initial states are the ones described in Table 6.1 and the asteroid masses are the mean $\bar{M}_i$ values reported in the SiMDA catalog (section 5.2). The dynamical model includes the point-mass influence of the Sun, the eight planets and the 415 asteroids included in the SiMDA catalog.
- **True model**: with the same system of bodies as in the nominal model, planetary initial states are perturbed from the one in Table 6.1 according to the multivariate normal distribution defined by the covariance matrix $\boldsymbol{P}_0$ found in algorithm 4, and asteroid masses are perturbed according to the covariance $\boldsymbol{P}_{\mathbf{M}}$ (equation 6.1).

6.2. Sensitivity of Trilogy vertices to third-body perturbations

Before running any estimation of asteroid masses based on range measurements obtained by Trilogy, it is worth assessing how much such masses are expected to perturb the interplanetary ranges. The more perturbed these ranges are, the more information content is expected to be encoded in the range measurements and thus the better the masses are expected to be estimable. On the other hand, if a certain mass is expected to cause negligible perturbations to the interplanetary distances, its value is not expected to be possibly reconstructed from the information of interplanetary ranges alone. As a first approximation, the hard limit below which such perturbations can be considered negligible is the minimum expected error level of ILR. As described in detail in section 3.2.2, this has both a random and a systematic component, both of different strengths depending on the exact system employed. The order of magnitude of this measurement quality limit, however, is overall expected to be below 1 cm and hardly below 1 mm.

In order to assess how many of the cataloged asteroid masses are expected to cause strong enough signatures to the interplanetary ranges as to be estimated, their individual pre-fit signatures have been computed and are presented in Figure 6.2 and Figure 6.3. Following the figures given by Smith et al. (2018) for the signature of solar mass loss, we compute such signals by generating, for every body i, a propagated history of interplanetary distances with setup where asteroid i perturbs the orbit of the planets, and then subtracting the equivalent interplanetary distance histories resulting from running an equivalent simulation but without asteroid i . The rationale behind this analysis is that if the impact of a certain asteroid on the interplanetary distance history is found negligible, then it is safe to assume the range measurements will not encode enough information to estimate its mass and therefore it does not need to be included in the fit. Alternatively, asteroids showing a great amplitude pre-fit signal are more likely to inflect a unique dynamical behavior to the measured ranges, from which its mass can be fitted with better confidence.

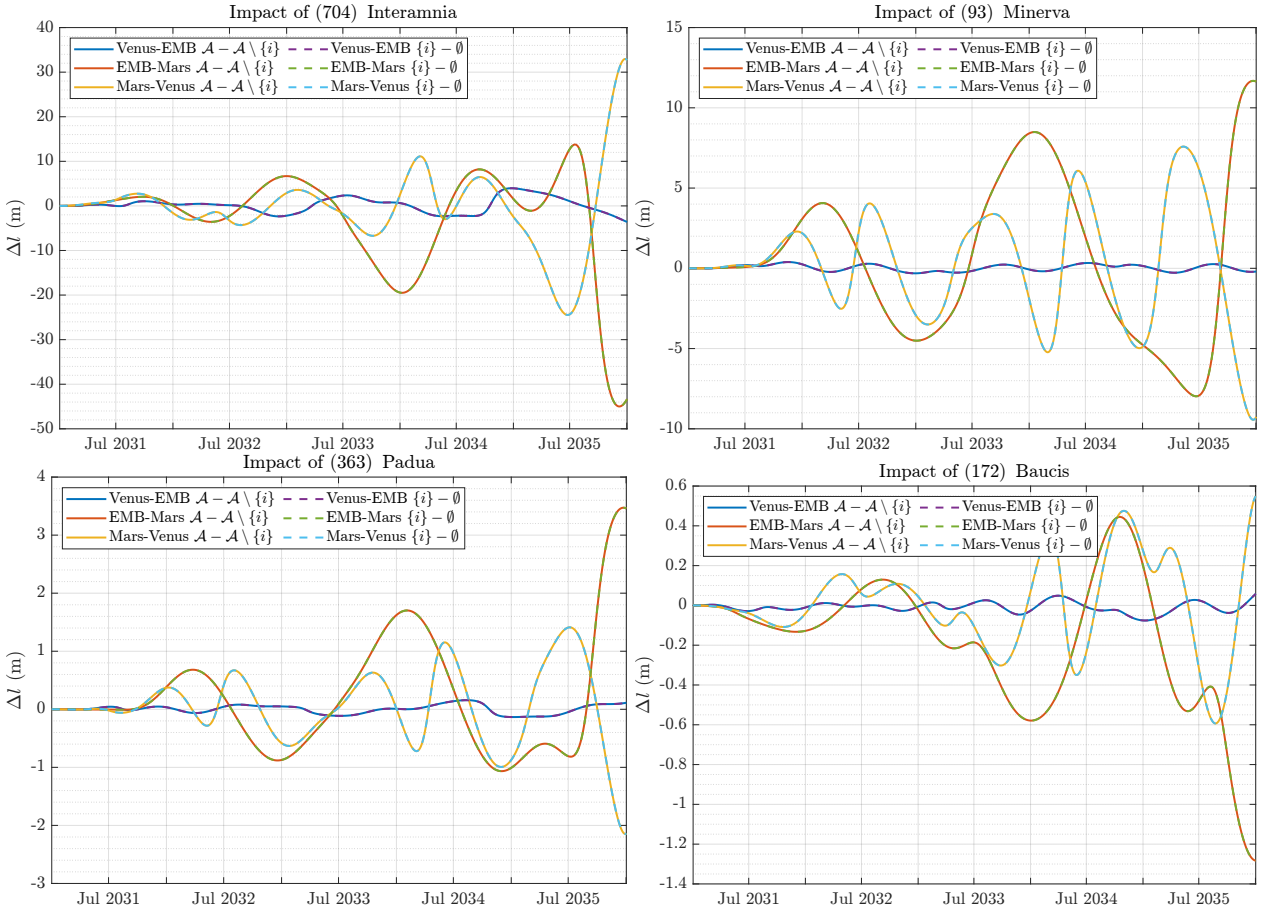

Figure 6.2: Pre-fit signals to the interplanetary distances of the Trilogy legs caused by four representative asteroids. $\mathcal{A}$: all asteroids included; $\mathcal{A} \setminus \{i\}$: all asteroids but i included; $\{i\}$: asteroid i only included; $\emptyset$: no asteroids included.

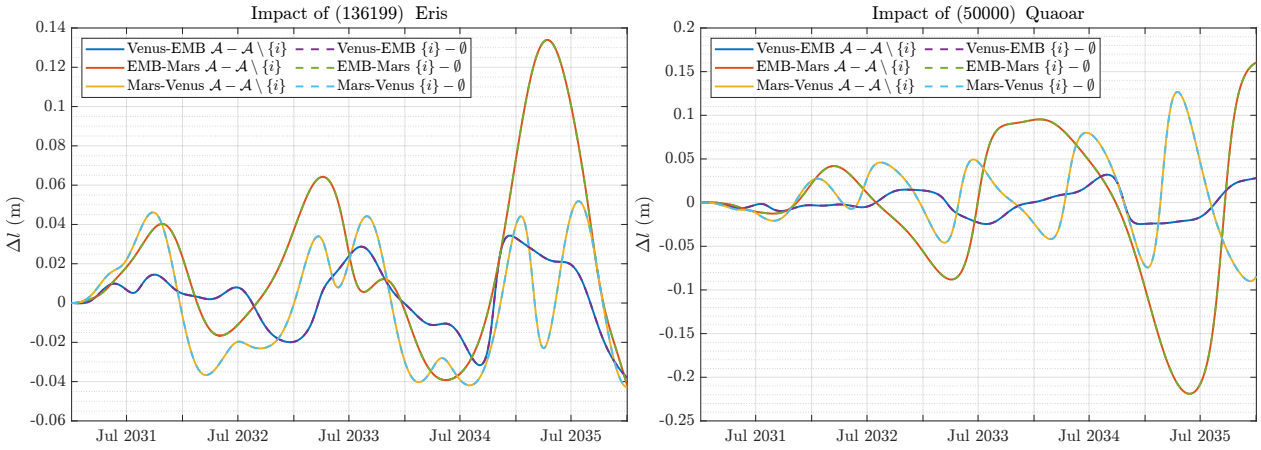

Figure 6.3: Pre-fit signals to the interplanetary distances of the Trilogy legs caused by two representative TNOs. $\mathcal{A}$: all asteroids included; $\mathcal{A} \setminus \{i\}$: all asteroids but i included; $\{i\}$: asteroid i only included; $\emptyset$: no asteroids included.

Such pre-fit signatures of each asteroid i can be computed two different ways: on the one hand, subtracting the interplanetary distance history resulting from propagating the dynamics including all asteroids except i from that resulting from propagating the dynamics including all asteroids. On the other hand, subtracting the interplanetary distance history resulting from propagating the dynamics including no asteroids at all from that resulting from propagating the dynamics including asteroid i only. The results for the two appropaches are marked with solid and dashed lines in Figure 6.2 and Figure 6.3. It can be immediately observed how both methods give virtually the same pre-fit signatures, which suggests that the expected impact of each individual asteroid to the interplanetary ranges is not affected by the nonlinearities

introduced by other third-body perturbations in any significant manner.

In order to confirm such claim for the whole set of analyzed asteroids, Figure 6.4 shows the scatter plot of the resulting maximum amplitude for all asteroids computed with both methods. As it can be observed, the equivalence is confirmed by a linear regression with a fitted slope that differs from 1 by $\mathcal{O}(10^{-7})$ and an R^2 that differs from 1 by $\mathcal{O}(10^{-11})$. This result suggests how the sensitivity of interplanetary ranges to asteroid masses can be assessed individually without any need to run costly simulations with all perturbations acting at once. This motivates the development of analytical methods to assess such sensitivity, which are developed in more detail in Appendix C.

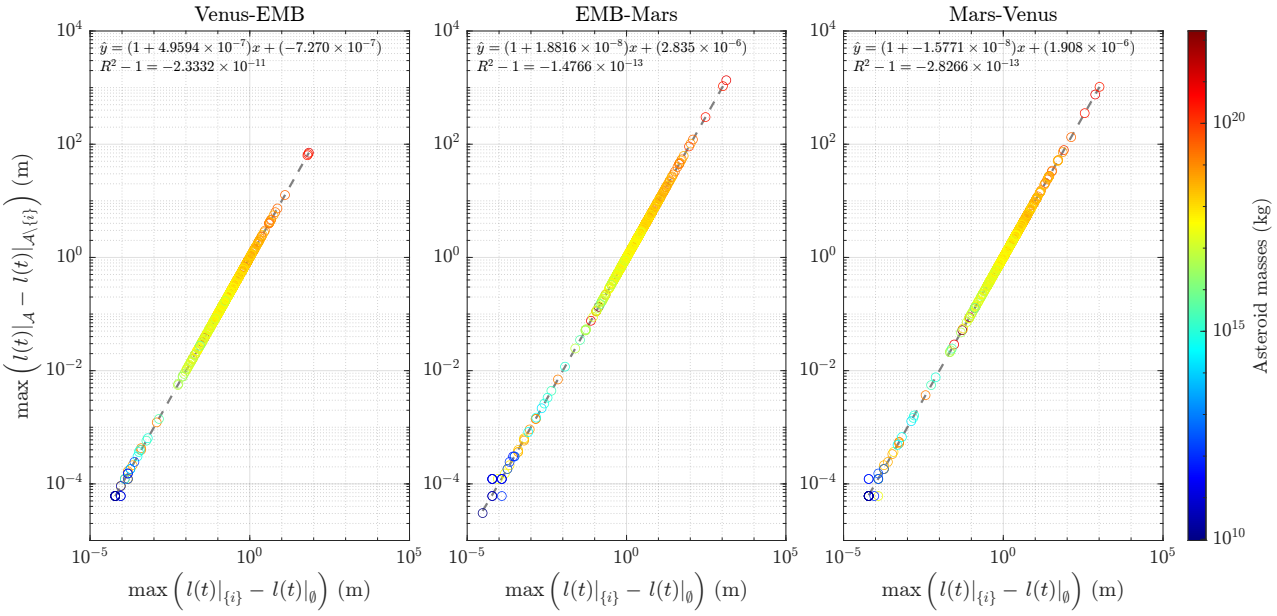

Figure 6.4: Maximum amplitude of individual pre-fit asteroid signals on the three Trilogy legs computed with the full dynamics (all asteroids vs. all asteroids except for i) vs. simplified dynamics (only asteroid i vs. no asteroids).

As a first order approximation, it could be expected that the main driver of such sensitivity is the mass of each asteroid. To assess this hypothesis, a similar figure to Figure 6.4 but plotted against asteroid mass is presented in Figure 6.5. It can be observed how, despite the direct proportionality is still evident, the possible different signature amplitudes for a given mass can vary in a range of one and a half orders of magnitude. For instance, asteroids of $GM \approx 0.1$ km^3/s^2 can cause an amplitude to the oscillation in the EMB-Mars distance between a few tens of centimeters and 10 meters. The points dispersed in an area of smaller amplitudes, significantly under the bulk where most asteroids are located, correspond to TNOs, and hence cause a much smaller perturbation for the same mass value. This evinces how orbital parameters are also a factor that plays a significant role in the expected signals introduced by asteroid masses to the interplanetary ranges.

Given the fact that masses alone are not found to be an accurate single predictor for the amplitude of the signals caused by individual asteroids to the interplanetary ranges, the amplitude results from the numerical simulation (Figure 6.4 or vertical axis of Figure 6.5) have been instead used to list the asteroids in order of priority to be estimated from Trilogy measurements. This is consistent with Somenzi et al. (2010), who used the same method to list the asteroids that cause "the highest variations of the relative interplanetary distance over the period considered". The difference is that their study estimated 15 asteroids and was based on Earth-Mars range measurements only. To cope with the usage of the triple ranging link, we compute the sum of the absolute value of the three temporal signatures of each asteroid caused to the three Trilogy links and we get its amplitude as its maximum. This procedure allows to order the 415 objects in the SiMDA catalog in descending order consistently with the expected signal caused to the Trilogy legs in a mission spanning from early 2031 to late 2035.

An extract of representative bodies in the resulting ordered list is presented in Table 6.2. It can be observed how around 300 objects are responsible for signals of between 10 cm and 1 m in the Trilogy legs, and even objetcs in the lower part (e.g., the TNO Eris) are responsible for individual amplitudes above the order of 1 cm, to which ILR is theoretically sensitive enough. The few tens of objects causing a smallest signal are several orders of magnitude smaller in mass, and mainly consist of near-Earth asteroids (NEAs) whose mass estimates have been conducted with methods other than ephemerides or astrometric fits, mainly observations of binaries or individual radar tracking (Neish et al., 2003; Pravec et al., 2006; Scheirich & Pravec, 2009). As seen in Figure 6.5, the signal of order 0.1 mm these bodies appear to break the linearity pattern, which is due to the fact that the results are affected by numerical noise. This is consistent with the level

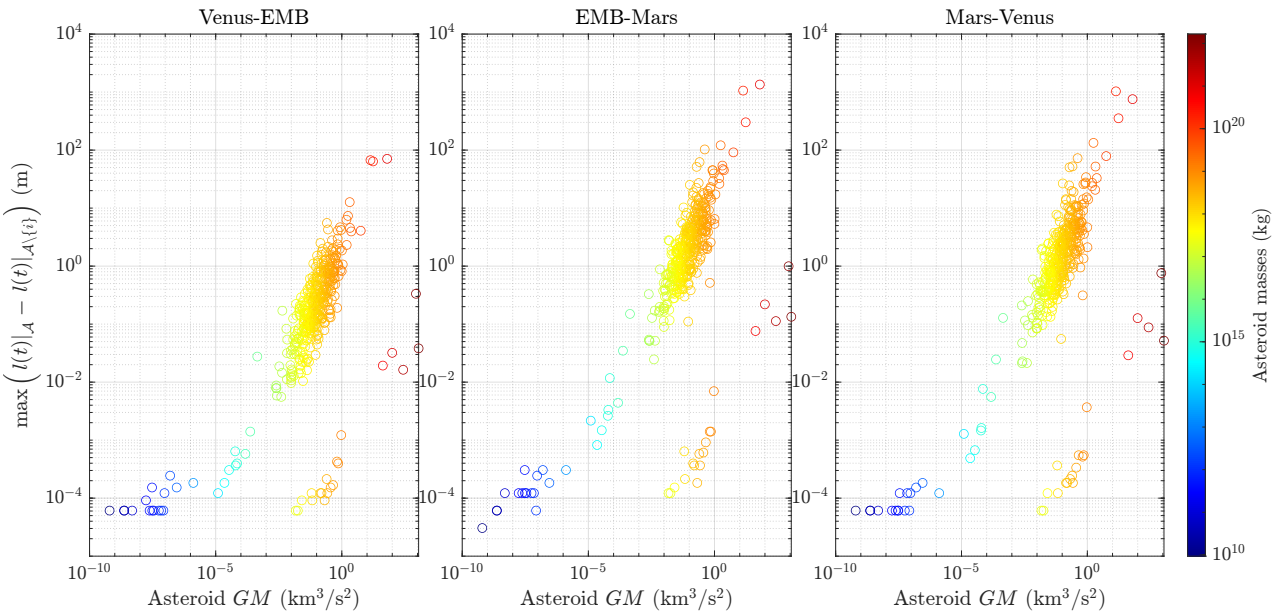

Figure 6.5: Maximum amplitude of individual pre-fit asteroid signals on the three Trilogy legs vs. asteroid mass.

of rounding error reported to affect the simulations at play (appendix A.1).

These results evince how the fundamental limit in ranging accuracy and precision set by ILR technology (i.e., 1 mm - 1 cm) is theoretically able to capture not only signals caused by most of the main belt asteroids for which mass estimates already exist but also to many more corresponding to other bodies for which they do not. This can be clearly observed in Figure 6.5: for the two ranging legs that have Mars as one end, there is a significant gap of data points between the main bulk of existing estimates and the limit of 1 to 10 mm. This gap exists because asteroids in this mass range are not massive enough as to have measured their masses with current methods (section 5.2) and available technology. For the Venus-Earth leg, on the other hand, asteroids lighter than the visible bulk cause smaller signals in comparison, being mostly under the cm level. This is consistent with the other legs being the most sensitive ones to asteroid perturbations, as seen in Figure 6.2 and Figure 6.3, which is due to the greater proximity (and thus sensitivity) of Mars to the Main Asteroid Belt (MAB) (Kuchynka & Folkner, 2013).

From this result, a remark to be made is that if the purpose of a Trilogy-like mission is to allow asteroid mass estimations, placing one of the vertices at Venus is potentially less useful than placing it closer to the MAB (e.g., a triangle formed by the Earth, Mars and one asteroid will presumably encode more useful information for asteroid mass calculations). Smith et al. (2018) suggested the usage of a Venus vertex due to its closer proximity to the Sun, which makes it more sensitive to the signature of solar mass loss. However, their study also evinced how the orbit of Mercury is reasonably more sensitive to this signal than those of the other planets, which is translated in greater pre-fit signatures of solar mass loss in interplanetary distances with Mercury as one of the two ends. The Venus-Earth-Mars configuration can be deemed as a reasonable trade-off that can allow for both estimations of solar mass loss and asteroid masses, but it is only through further study and simulations that a final conclusion will be made in this regard.

As a closing remark, it is important to note that all these results are based on the figures given by the pre-fit effect of each individual asteroid, i.e., they describe the impact of turning the asteroid on at t_0 without having estimated the planetary initial states that best describe the perturbations observed by the interplanetary ranges. Therefore, although it is a useful metric to set the initial picture of approximately how many asteroids can potentially be estimated, it only serves the role of a rule of thumb that needs to be confirmed by the corresponding estimations.

6.3. Verification

6.3.1. Consistency of planetary dynamics

The first check that needs to be conducted to verify the simulation to be well implemented is to assess how well the propagation results obtained with the simulation settings at use match the expected planetary motion. A good metric for this is found in Appendix B, when presenting the results of algorithm 4 to obtain a representative covariance of planetary states. The first step of the procedure consists of finding a best-fit initial state for the planets that matches the

Table 6.2: Extract of the resulting list of individual asteroid/TNO pre-fit signal amplitudes to the Trilogy ranging legs in descending order.

				Signal amplitudes (m)			
	IAU #	**Name**	GM (km^3/s^2)	Venus-EMB	EMB-Mars	Mars-Venus	Aggregate
1	2	Pallas	13.674	66.985	1060.791	1030.413	2123.050
2	1	Ceres	62.565	70.751	1349.784	754.937	2118.066
3	4	Vesta	17.275	63.792	301.308	353.573	574.803
4	3	Juno	1.754	7.334	120.973	133.176	253.032
5	41	Daphne	0.410	2.787	102.628	72.595	174.863
50	40	Harmonia	0.223	1.087	8.271	8.891	17.025
100	56	Melete	0.305	0.921	4.200	4.773	8.282
200	505	Cava	0.093	0.472	2.000	1.163	3.224
281	134340	Pluto	867.1	0.333	0.995	0.757	1.367
300	449	Hamburga	0.012	0.125	0.699	0.292	1.113
370	136199	Eris	1107.2	0.038	0.134	0.052	0.179
400	35107	1991 VH	9.34×10^{-8}	<0.001	<0.001	<0.001	<0.001

tabulated ephemerides. In the figures showing the observation residuals during such procedure (Figure B.8, Figure B.9, Figure B.10), it is evident how the pre-fit discrepancy (iteration 1) does not overpass the level of a few hundred kilometers after the complete five-years period. This discrepancy is an order of magnitude smaller than the diameters of these planets. Given the fact that the observations are direct cartesian positions retreived from the ephemerides, these residuals directly measure the discrepancy between them and the results of the implemented propagator. It is therefore safe to assume that the implemented dynamics mimic the expected planetary motion to accurate levels, even before finding the best-fit $\mathbf{x}_0$ by means of algorithm 4.

6.3.2. Estimation performance

In order to make sure the simulation of asteroid mass estimations has been set up properly, a simplified test case can be verified to converge to the expected solution. Figure 6.7 presents the mass estimation results (pre- vs. post-fit) of a simulation case with a total of 30 asteroids in the dynamical model, all of which get their masses estimated. The two-way range observations, presented in Figure 6.6 are generated once per day, with a random error of 10 mm and no bias. In

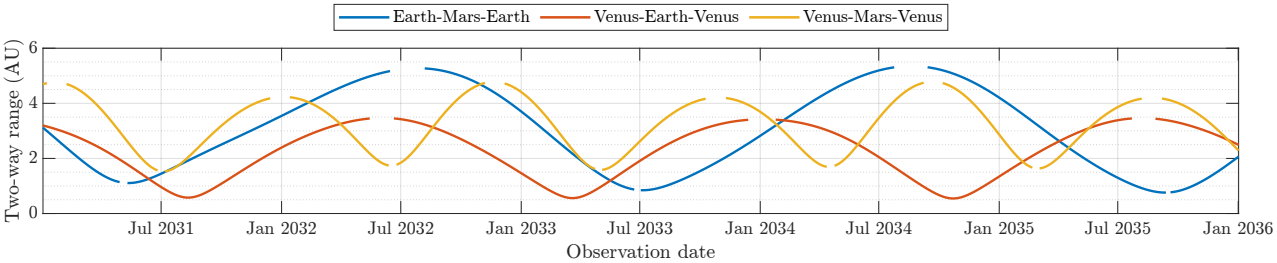

Figure 6.6: Two-way range observations obtained by Trilogy between January 1st 2031 and December 31st 2035. Solar separation angle: 5°.

the "truth" dynamical model used to generate the observations, all asteroid masses are perturbed from their nominal values according to their covariance (equation 6.1). The estimation then takes as *a priori* the dynamical model that has all asteroid masses set to their nominal values (i.e., the mean masses $\bar{M}_i$ from the SiMDA catalog; section 6.1.1), and it is expected to converge to the true mass values with the batch algorithm (1). This procedure also estimates the initial states of the Trilogy vertices, which in this simple test case have not been modified in the true dynamical model from the nominal dynamical model. The estimator has been run with the *a priori* covariance

$$\bar{\boldsymbol{P}}_0 = \begin{bmatrix} \bar{\boldsymbol{P}}_{\mathbf{x}_0} & \\ & \bar{\boldsymbol{P}}_{\mathbf{M}} \end{bmatrix}, \tag{6.2}$$

where $\bar{\boldsymbol{P}}_{\mathbf{x}_0}$ is the covariance of planetary initial states, obtained with algorithm 4, and $\bar{\boldsymbol{P}}_{\mathbf{M}}$ is the covariance of asteroid masses detailed in equation (6.1). The inclusion of this *a priori* matrix to the batch estimator is intended to prevent the estimator from diverging from the true solution, thanks to the extra penalty term in the cost function (equation 4.53).

The aim of this analysis is not to draw any conclusions from the expected performance of Trilogy, but simply to verify how the asteroid mass estimation performs as expected in a favorable case. In other words, if this case does perform well but more complicated cases (e.g., more asteroids, non-perfect *a priori* planetary initial states, worse observations) do not, the results of this simple case should support the conclusion that the cause of such poorer performance is not a fundamental error in the implementation. The comparison between the pre- and post-fit asteroid masses after following this procedure is displayed in Figure 6.7.

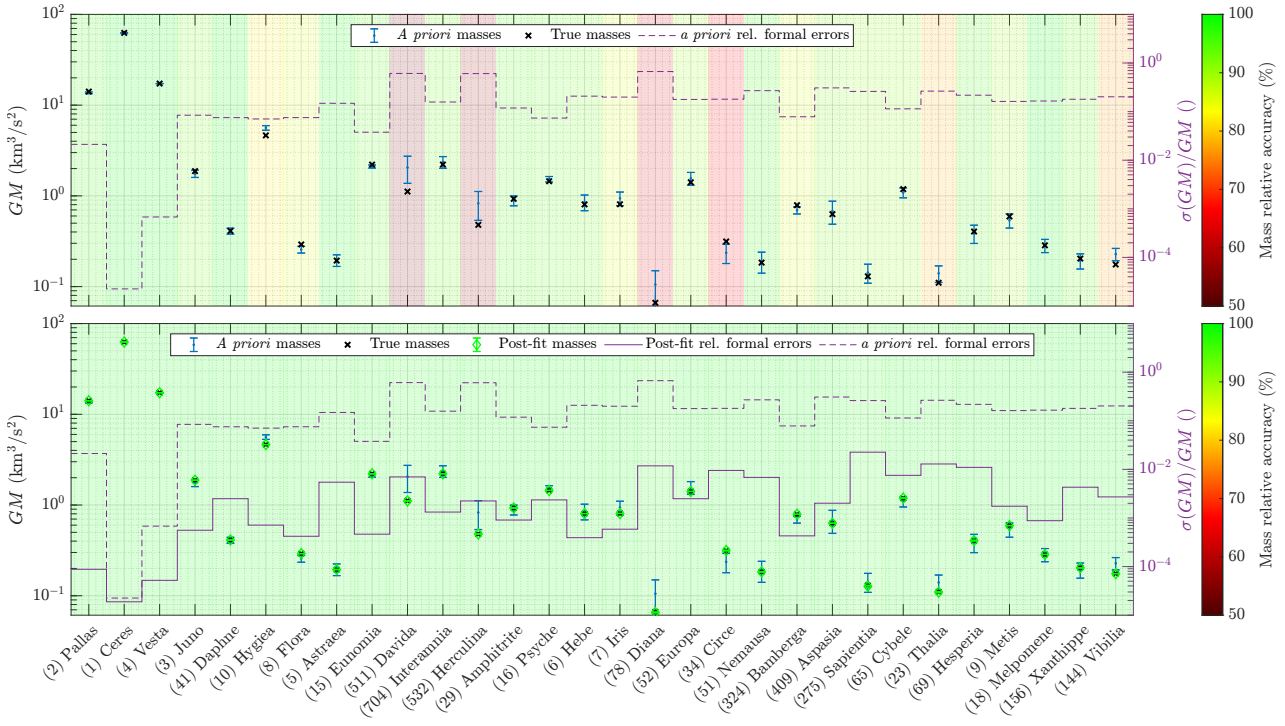

Figure 6.7: Pre-fit (top) and post-fit asteroid mass errors in an estimation scenario with the first 30 asteroids and no perturbation of the planetary initial states. Absolute GM values correspond to the left axes, relative formal errors to the right axes, and relative true errors to the color shading.

Figure 6.7 clearly evinces how all asteroid masses do converge to their true values as a result of applying the batch estimation filter. The correct performance of the estimation is also supported by the post-fit residuals seen in Figure 6.8, which are normally distributed with a standard deviation equal to 1 cm, which coincides with the observation noise level used. Finally, the distribution of true-to-formal error ratios presented in Figure 6.9 is supposed to be consistent with a standard normal distribution. Although the low number of data points is not enough to make the histogram truly reveal the shape of the underlying statistical distribution, the fact that the standard deviation is of order of magnitude ≈ 1 allows us to assume that the estimation has performed as expected from the statistical standpoint.

This correct estimation behavior is however tested with a single data point in the full space of possible simulation scenarios. In order to verify the numerical stability of the solution for different cases, the estimation simulation of 30 asteroids has been re-run for different configurations of observation noise and frequency. Initial states have also been perturbed in the true dynamical model, from which observations are generated, with respect to the *a priori* dynamical model. The performance of the estimation is assessed by two metrics: the behavior of the final formal errors as given by the post-fit covariance matrix (equation 4.55), and the standard deviation of the true-to-formal error ratios after a full estimation (e.g. Figure 6.9). The former are expected to be directly proportional to the observation noise σ_{obs} and inversely proportional to the square root of the number of observations used N, while the latter is expected to be ≈ 1 independently of the estimation settings. This expected behavior of the true-to-formal error ratios is a consequence of the fact that, under the lack of any dynamical mismodeling, the post-fit covariance is expected to be the true statistical distribution from where the resulting true errors are realized.

For the sake of compactness, the results are presented for two of the 48 estimated parameters (18 initial state components + 30 asteroid masses), selected to be the masses of (5) Astraea and (704) Interamnia. Their resulting formal error as a

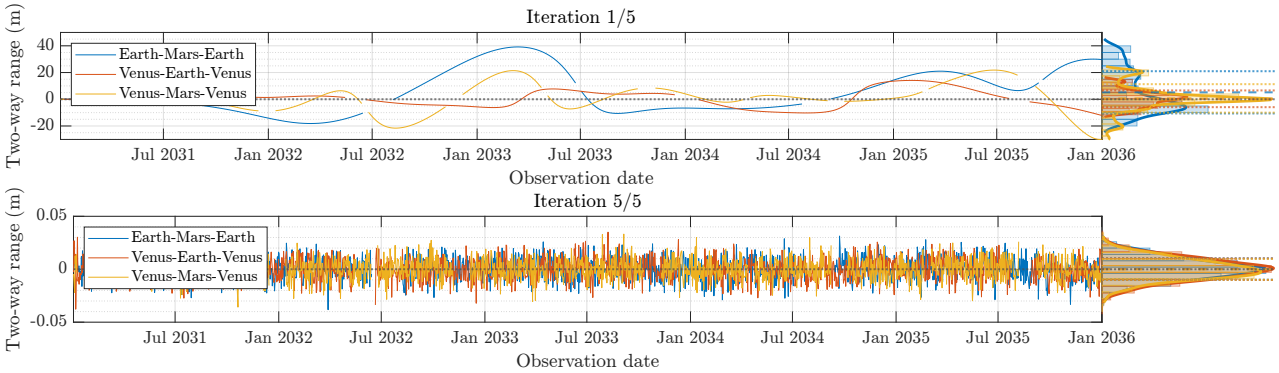

Figure 6.8: Pre- and post-fit observation residuals in the test case of 30 asteroid mass estimations.

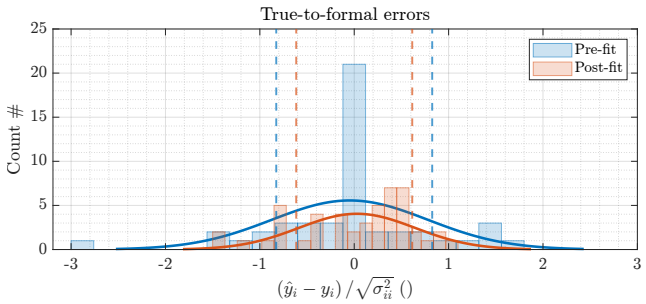

Figure 6.9: Distribution of true-to-formal error ratios in the test case of 30 asteroid mass estimations.

function of the observation cadence and noise are presented in Figure 6.10, whereas the standard deviation of the resulting true-to-formal error ratios along the same parameter space are shown in Figure 6.11. The dashed blue contours display the geometric loci of the observation configurations that yield each post-fit formal error to be equal to the corresponding *a priori* of each asteroid mass.

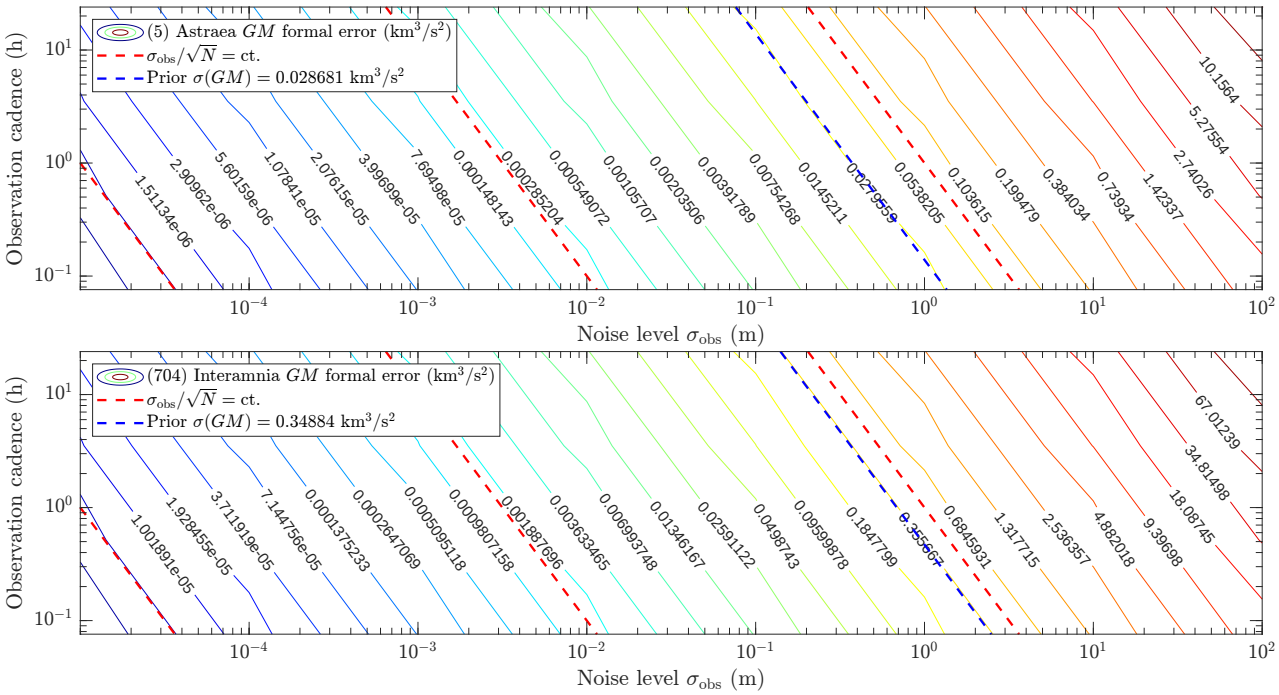

Figure 6.10: Formal errors corresponding to the estimated mass of (5) Astraea (top) and (704) Interamnia (bottom) as a function of the observation cadence and observation noise level.

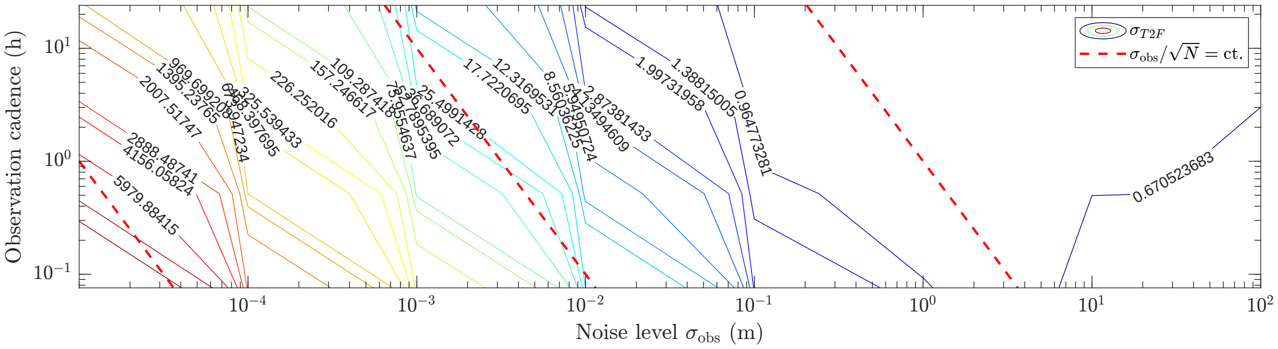

Figure 6.11: Standard deviation of the resulting true-to-formal error ratios of all 48 estimated parameters (18 initial state components + 30 asteroid masses) as a function of observation noise and observation frequency.

It is clear to observe how the formal errors do behave as expected for the whole tested domain: their proportionality to the observation noise and the inverse of the square root of the number of observations is evinced by the fact that the contour lines are parallel to the $\sigma_{\mathrm{obs}}/\sqrt{N} = \mathrm{ct.}$ curves. Observing the bottom plots, however, it becomes evident how many of these configurations do not allow the batch filter converge with good numerical stability—instead of the expected ≈ 1 standard deviation of the true-to-formal error ratios for all configurations, high observation frequencies and low observation noises (i.e., configurations that result in lower formal errors) result in a clear divergence, i.e., true errors much higher than expected by the formal errors).

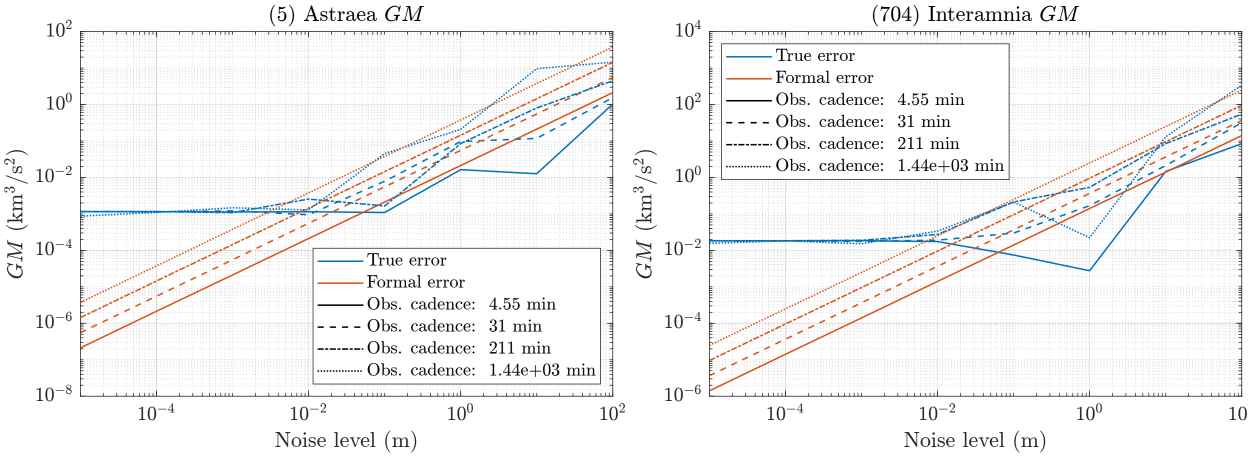

Figure 6.12: Convergence of true and formal errors for the estimated masses of Astraea and Interamnia as a function of noise level for different observation frequencies.

The reason behind this behavior can be understood looking at Figure 6.12, which shows the resulting true and formal errors as a function of the observation noise level for different observation frequencies. As observed, while formal errors show the expected geometric reduction (i.e., linear behavior in the logarithmic plot), true errors saturate at a certain level, under which they do not keep converging as the formal errors do. The reason behind this discrepancy lies in the mathematical nature of the differential correction step (Algorithm 1), i.e.,

$$\Delta\mathbf{y} = \left(\boldsymbol{H}^{\top}\boldsymbol{W}\boldsymbol{H} + \bar{\boldsymbol{P}}_0^{-1}\right)^{-1}\left(\boldsymbol{H}^{\top}\boldsymbol{W}\Delta\mathbf{z} + \Delta\bar{\mathbf{y}}\right), \tag{6.3}$$

and can be the result of multiple potential causes. Different possibilities are listed below:

- With too high observation weights $\boldsymbol{W}$ as a result of very low observation noise, the *a priori* term $\bar{\boldsymbol{P}}_0^{-1}$ might vanish when added to $\boldsymbol{H}^{\top}\boldsymbol{W}\boldsymbol{H}$ due to the finite double precision. This might result in the failure to contain the final solution close to the *a priori* value and hence divergence during the application of the batch filter.
- The vector of observation residuals $\Delta\mathbf{z}$ might be subject to numerical errors arising from
  - the integration error, or

  - the interpolation error when generating the observations from the tabulated state history,

  which get significantly enlarged when mapped to the estimated parameter space.
- The condition number of the normal equations (6.3), which is found to be $\mathcal{O}(10^{14})$ as a result of mixing parameters of several different orders of magnitude (e.g., velocities and GM's) in the vector of estimable parameters $\mathbf{p}$, might cause the numerical inversion of the system to be unstable.

A thorough investigation to confirm or refuse these hypotheses has not been finalized at the time of writing this manuscript. Instead, the conclusion that has been drawn is that the estimation results given by the final implemented solution (section 7.2) must take this into account and confirm the solution found with the particular settings at play to fulfill statistical consistency and numerical stability by means of a distribution of true-to-formal errors that has a standard deviation ≈ 1. Another key take from these results is that an analysis of the performance of Trilogy for asteroid mass estimations under different observation configurations cannot be confidently run across the whole domain seen in figures 6.10 and 6.11, other than based on covariance analysis results only. The limitation this entails is that, without simulating full estimations, it is impossible to assess the level from which further reducing formal errors by means of higher observation cadences or lower measurement noise becomes irrelevant due to other limiting factors such as high correlations between different parameters or dynamical mismodeling not allowing the batch estimator converge to the true solution.

7

Final simulation including spacecraft

The aim of this thesis has been, from the beginning, to make a step forward in the assessment of the potential scientific output of Trilogy by means of numerical simulations of higher fidelity than the existing studies up to date. A key aspect that remains to be addressed in the studies by Cascioli et al. (2019), Fienga (2023a), and Smith et al. (2018) is the impact of imperfect orbit determination of the three transceivers, which can degrade the resulting planet-to-planet ranges. Finding the most suitable approach to assess it has been a major challenge in this work, and different alternatives were consideredbefore a decision was made on the final implemented solution. The failed and discarded alternatives are detailed in section section 7.1, while the description of the final implemented approach is detailed in section 7.2.

7.1. Discussion on the considered solutions

7.1.1. Consider covariance analysis

Addition of consider parameters to planet-to-planet ranges

The first approach that was discussed was the usage of consider parameters (ref missing) with the aim of assessing how much model errors are expected to map into the final formal errors of the estimated planetary parameters (i.e., initial states and asteroid masses). As discussed in Equation 4.2.1, consider parameters are usually used to assess the effect of the uncertainties in parameters that are assumed constant during orbit estimation but which are subject to uncertainty due to imperfect knowledge or model errors. In orbit estimation around the Earth, observation range biases are sometimes introduced as consider parameters to "represent possible errors in the measurements model and calibration process" (Cano et al., 2023). In a comparable fashion, we can think that conducting the same planetary estimation as in section 6.3.2 but adding range biases as consider parameters, which can account for the extra model errors due to imperfect spacecraft orbit determination, can help determine its impact on the final estimated values of planetary parameters.

Figure 7.1 shows the pre- and post-fit relative formal errors in asteroid masses computed with the same settings as in Figure 6.7, but with the addition of the formal errors arising from the consider contribution (orange). This contribution results from applying equation (4.56) with a consider parameter matrix $\boldsymbol{C}$ that represents the uncertainty in the parameters to be considered. If such considered parameters are the observation biases of the Trilogy ranges, it takes the form

$$\boldsymbol{C} = \begin{bmatrix} \sigma_{b,1} & & \\ & \sigma_{b,2} & \\ & & \sigma_{b,3} \end{bmatrix}, \tag{7.1}$$

where $\sigma_{b,i}$ is the uncertainty of each Trilogy leg i measurement due to model or calibration error. If this is expected to model the impact of the imperfect orbit determination of the spacecraft, the suitable choice is to interpret it as model error and then assign it an order of magnitude of around one meter. The result of considering $\sigma_{b,1} = \sigma_{b,2} = \sigma_{b,3} = 1$ m is presented in Figure 7.1 right, whereas Figure 7.1 left presents the result of assuming $\sigma_{b,1} = \sigma_{b,2} = \sigma_{b,3} = 0.01$ m instead, which would be more consistent with a pessimistic scenario of systematic error in the ILR system (section 3.2.2).

The significantly different formal error contributions resulting from the two cases evince how impactful unmodeled measurement biases can be to the post-fit formal errors of the estimated parameters, but these results alone allow for little conclusions to be drawn. First and foremost, because the level of formal errors given by a covariance analysis does not truly represent the estimation capability of the problem under study—whether or not the batch estimation will actually converge to the true solution with a confidence consistent with such formal errors depends on the amount of

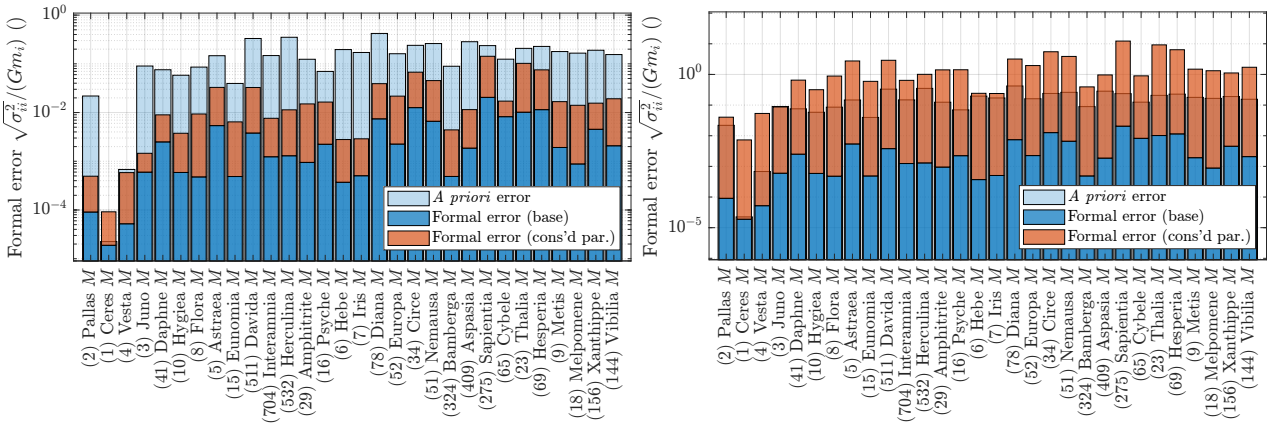

Figure 7.1: Asteroid formal errors with the consider contribution after assuming a diagonal observation bias consider covariance of 1 cm (left) and 1 m (right).

significant correlations and the impact of any unmodeled planetary dynamics. Moreover, the usage of the consider covariance as defined in equation (7.1) carries the assumption that such bias errors are Gaussian with a constant standard deviation σ_b through the whole observations period. Spacecraft orbit determination errors are however expected to be a function of time, and modeling their time variability is challenging with he consider parameter formulation, which are "assumed to be constant throughout a single orbit determination" (Montenbruck & Gill, 2001, p. 266). In Tudat, a possible workaround would be to set different, independent bias parameters in different (short) propagation arcs by means of the `arcwise_absolute_observation_bias()` function, but this was discarded in favor of other approaches expected to take into account the time variability of the spacecraft position error more faithfully (section 7.1.2).

It should also be noted that the assumption of uncorrelated observation biases (equation 7.1) is hardly realistic, given the shared measurement ends in the Trilogy setup. For example, if the Earth-to-Mars and Venus-to-Mars links are close to parallel, the error in the orbit determination of the Mars spacecraft will likely affect both measurements in a correlated manner. Computing an accurate representation of the $\boldsymbol{C}$ matrix that accounts for such correlations depending on the geometry of the Trilogy links would require a more elaborate process, that was not deemed worth attempting given the aforementioned drawbacks of this approach.

Addition of consider parameters to spacecraft-to-spacecraft ranges

With the aim of using all the information available from the spacecraft-to-spacecraft measurements while also taking into account the impact of their imperfect orbit determination, the following approach was considered: the post-fit covariance of the estimation of planetary initial states and asteroid masses is computed with high-frequency spacecraft to-spacecraft measurements, while assuming the orbits of the spacecraft to be fully known. Then, an extra contribution is added to such resulting covariance mapping the effect of uncertainties in spacecraft state errors to the estimated parameters. Again, the consider covariance formulation might be seen as a suitable alternative to apply this method.

This approach was implemented in script `decoupled_sc_to_sc.py`, without satisfactory results. The first drawback found was related to the internal behavior of Tudat: if measurements are taken from spacecraft to spacecraft but such spacecraft are not propagated but fixed around their host bodies (which are propagated during batch estimation) with a set of given ephemerides, then Tudat sets the partials of the observations with respect to the state components of the host planets to zero instead of taking into account the dependence through the spacecraft states. For this reason, the implemented simulation had to propagate both spacecraft and planets concurrently during estimation, which means that the set of estimated initial states includes those of both.

In summary, the implemented procedure consisted of: 1) propagate both spacecraft and planets concurrently; 2) generate inter-spacecraft measurements 3) compute the covariance of all estimated parameters (i.e., spacecraft initial states, planetary states and asteroid masses) based on such observations (equation 4.55); 4) Remove the covariance matrix elements corresponding to the spacecraft initial states to get the remaining $\boldsymbol{P}_0$; 5) Get the rows of the design matrix corresponding to the derivatives of the observations with respect to the spacecraft initial states to form $\boldsymbol{H}_\mathbf{c}$, and keep the remaining design matrix as $\boldsymbol{H}_\mathbf{x}$ 6) compute the consider covariance contribution caused by the uncertainty in spacecraft initial states with the consider covariance contribution equation (4.56), namely

$$\boldsymbol{P}_\mathbf{c} = \left(\boldsymbol{P}_0 \boldsymbol{H}_\mathbf{x}^\top \boldsymbol{W}_\mathbf{x} \boldsymbol{H}_\mathbf{c}\right) \boldsymbol{C} \left(\boldsymbol{P}_0 \boldsymbol{H}_\mathbf{x}^\top \boldsymbol{W}_\mathbf{x} \boldsymbol{H}_\mathbf{c}\right)^\top, \tag{7.2}$$

where $\boldsymbol{W}_{\mathbf{x}}$ is the weight matrix corresponding to the remaining $\boldsymbol{H}_{\mathbf{x}}$ and $\boldsymbol{C}$ is the consider covariance matrix, containing the uncertainty of each spacecraft position components.

This evinces the other drawback of this approach: again, the consider covariance matrix $\boldsymbol{C}$ is constant, but the behavior of the spacecraft orbit determination uncertainty is time-dependent. The workaround of setting different $\boldsymbol{C}$ matrices for different spacecraft arcs, in this case, comes with a greater inconvenient, which is that the resulting design matrices computed by Tudat become significantly larger due to the increased number of initial states to estimate. Although different arcs can be assumed to be independent, Tudat is not sparse-matrix-friendly and thus the resulting computational cost increases dramatically. For this reason, this multi-arc workaround was not addressed.

Before giving this option up, one could wonder if using a constant $\boldsymbol{C}$ that accounts for the order of magnitude of the expected spacecraft state uncertainties matrix might still give acceptable results. Figure 7.2 shows the results on the resulting formal errors of the Martian initial states, after following the procedure described above in a simulation scenario with one Trilogy measurement per minute during a total time of six months. The constant $\boldsymbol{C}$ matrix used has been set to

$$\boldsymbol{C} = \begin{bmatrix} \boldsymbol{P}_{\mathbf{x}_{\mathrm{S/C}}} & & \\ & \boldsymbol{P}_{\mathbf{x}_{\mathrm{S/C}}} & \\ & & \boldsymbol{P}_{\mathbf{x}_{\mathrm{S/C}}} \end{bmatrix}; \qquad \boldsymbol{P}_{\mathbf{x}_{\mathrm{S/C}}} = \begin{bmatrix} \sigma(r_X^{\mathrm{S/C}}) & & & & & & \\ & \sigma(r_Y^{\mathrm{S/C}}) & & & & & \\ & & \sigma(r_Z^{\mathrm{S/C}}) & & & & \\ & & & \sigma(v_X^{\mathrm{S/C}}) & & & \\ & & & & \sigma(v_Y^{\mathrm{S/C}}) & & \\ & & & & & \sigma(v_Z^{\mathrm{S/C}}) \end{bmatrix}, \tag{7.3}$$

hence assigning the same diagonal covariance to each spacecraft position. The exact values of the error levels have been varied to produce Figure 7.2, where the vertical axes of each subplot show the post-fit formal errors of each component of the initial state of Mars, whereas horizontal axes represent the uncertainty level in the spacecraft position components $\sigma(r_I^{\mathrm{S/C}})$ and the different curves represent uncertainty level in spacecraft velocity components $\sigma(v_I^{\mathrm{S/C}})$.

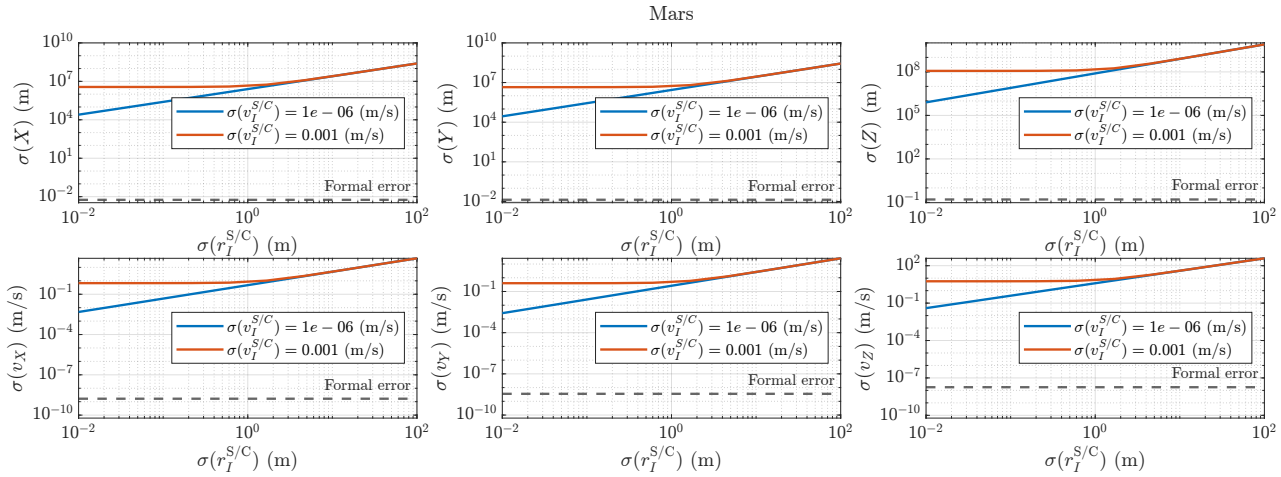

Figure 7.2: Formal errors in the estimated initial state components of Mars and consider contributions for different spacecraft position errors added as consider parameters. Horizontal dashed lines indicate post-fit formal errors without consider covariance contributions.

It can be observed how even truly optimistic spacecraft state uncertainties (e.g., 1 cm in position and 0.001 mm/s in velocity) make the final formal error of the estimated initial states of Mars increase by a factor of 10^6 with respect to the post-fit formal errors given by the covariance matrix $\boldsymbol{P}_0$ without any consider contribution. The results corresponding to the initial states of the EMB and Venus are not reproduced here for the sake of efficiency, but they present an equivalent behavior. These results are clearly not trustworthy, which is likely due to the assumption of a constant spacecraft covariance given by equation (7.3) not being applicable in this case. Given the aforementioned efficiency drawbacks of applying different arc-wise $\boldsymbol{C}$ matrices, together with the limitations of a covariance analysis alone stated earlier in this section, this approach was discarded in favor of the options detailed in section 7.1.2.

7.1.2. Addition of spacecraft orbit determination error to interplanetary ranges

Temporally-dependent random error approach

Despite real mission operations require the orbit determination of the interplanetary spacecraft to be conducted in order to consequently generate the planet-to-planet range measurements to be used in planetary estimation step, preliminary

mission analyses (Dirkx et al., 2017; van der Zwaard & Dirkx, 2022) commonly simulate the performance of the estimation by generating planet-to-planet measurements directly, and assess the impact of the omitted spacecraft orbit determination step in a simplified manner. One common approach is to add an extra error source to the generated range measurements to account for orbit determination errors, besides the intrinsic random noise coming from the ranging system itself. This way, if $\sigma_{\rho_{S/C}}$ is the ILR one-sigma noise level on the range measurement and $\boldsymbol{\sigma}_{\mathbf{r}_{S/C}}$ are the components of the spacecraft position uncertainty with respect to its host body after orbit determination, then it is assumable that the uncertainty of the range measurement to the center of mass of the planet is

$$\sigma_\rho(t) = \sigma_{\rho_{S/C}} + \left|\hat{\boldsymbol{\rho}} \cdot \boldsymbol{\sigma}_{\mathbf{r}_{S/C}}\right|, \tag{7.4}$$

where $\hat{\boldsymbol{\rho}} = \hat{\boldsymbol{\rho}}(t)$ is the unit vector in the direction of the ILR link to the spacecraft. It is therefore enough with having an estimate for the uncertainty position vector of the spacecraft $\boldsymbol{\sigma}_{\mathbf{r}_{S/C}}$, either constant or time-varying, to get the total range measurement uncertainty σ_ρ. From here, range measurements can be sampled from planet to planet directly, with the noise function given by $\sigma_\rho(t)$ instead of simply the ranging system noise level $\sigma_{\rho_{S/C}}$. $\boldsymbol{\sigma}_{\mathbf{r}_{S/C}}$ can be estimated with a covariance analysis alone, removing the need to simulate full spacecraft orbit estimations, which is a key advantage of this method. For the problem under study, the pros and cons of this approach are summarized in Table 7.1

Table 7.1: Pros and cons of the approach consisting of adding an extra error source to the noise level of the range measurements to account for the spacecraft orbit determination errors.

Advantages	Disadvantages
• Low computational cost. • Primarily, full spacecraft orbit determination of the spacecraft not required (covariance analysis to get $\boldsymbol{\sigma}_{\mathbf{r}_{S/C}}$ suffices).	• Getting $\boldsymbol{\sigma}_{\mathbf{r}_{S/C}}$ from a covariance analysis including ILR measurements is expected to be too optimistic by yielding uncertainties below model capabilities, but doing so with Doppler measurements only does not assess the benefit of supporting orbit determination with laser ranging. • The usage of $\boldsymbol{\sigma}_{\mathbf{r}_{S/C}}$ as a vector containing the diagonal terms of the spacecraft position covariance $\boldsymbol{P}_{S/C}$ omits the effect of any significant correlations. • Sampling interplanetary ranges at low frequency when making use of equation (7.4) can introduce aliasing effects, depending on the exact combination of measurement cadence and the nature of $\boldsymbol{\sigma}_{\mathbf{r}_{S/C}}(t)$. • When ILR is used, $\boldsymbol{\sigma}_{\mathbf{r}_{S/C}} \gg \sigma_{\rho_{S/C}}$, potentially making the results insensitive to the usage of high-precision laser ranging instead of traditional radio ranging.

This approach is followed by Dirkx et al. (2017) and van der Zwaard and Dirkx (2022) when studying, respectively, the JUICE and MESSENGER/BepiColombo missions. A key difference with respect to this study, however, is that they assumed the noise levels of the ranging system, i.e., $\sigma_{\rho_{S/C}}$, to be between tens of centimeters and few meters, following the traditional radio-based ranging system to be used in such missions. In the case of ILR, on the other hand, the term $\sigma_{\rho_{S/C}}$ can be $\sim$100 times smaller, and the potential scientific advantage of this improvement may become invisible if in equation (7.4) it is still added to a completely dominant spacecraft position error term of order one meter. Such spacecraft position uncertainty can be reduced if ILR measurements are used in orbit determination, yet assessing this improvement by means of a covariance analysis only can be highly misleading: unlike with radio-based measurements, the millimetric precision of laser ranging can result in formal covariances smaller than the dynamical mismodeling capabilities, and the impact of such mismodeling in a precise orbit determination process can only be reproduced by simulating the full estimation.

On top of this, it can also be argued that the estimation including highly precise ILR range measurements is not expected to be realistic unless the error in planetary positions is taken into account, since range measurements are highly sensitive to those—ILR errors are in the range of some mm (section 3.2.2), whereas the errors in planetary ephemerides are

several orders of magnitude greater (section B.1). The simulation of such full estimation including planetary mismodeling finally yields to the decided implemented approach, detailed in section 7.2.

Temporal error function approach

A close variation of the previous approach consists of adding a deterministic temporal error signature that accounts for the position error of the spacecraft after orbit determination, instead of taking it as an extra source of uncertainty to sample noise from. This can be formulated in terms of the modified one-way ranges resulting from adding the extra error source from each spacecraft's position error. For a one-way range from spacecraft A to spacecraft B (by a laser pulse that departs A at t_1 and arrives at B at t_2; section 3.2), the modified one-way range $\tilde{s}^{(1)}_{BA}$ becomes

$$\tilde{s}^{(1)}_{BA} = s^{(1)}_{BA} + \Delta s^{(1)}_{BA} + \hat{\boldsymbol{\rho}}(t_1) \cdot \Delta \mathbf{r}_A(t_1) + \hat{\boldsymbol{\rho}}(t_2) \cdot \Delta \mathbf{r}_B(t_2), \tag{7.5}$$

where $\Delta s^{(1)}_{BA} \sim \mathcal{N}(b_\rho, \sigma_{\rho_{S/C}})$ is the random error contribution of the ranging system, centred at the range bias b_ρ; $\hat{\boldsymbol{\rho}}$ is the unit vector in the direction of the range measurement; and $\Delta \mathbf{r}_X(t)$ is the true error in the position vector of spacecraft X at instant t. With this approach, the planetary estimation can be conducted by generating planet-to-planet measurements directly and adding the error contributions of all terms of equation (7.5) instead of just the noise contribution. The pros and cons of this method applied to the problem under study are summarized in Table 7.2.

Table 7.2: Pros and cons of the approach consisting of adding an extra error temporal signature to the range measurements to account for the spacecraft orbit determination errors.

Advantages	Disadvantages
• Primarily, full spacecraft orbit determination of the spacecraft not required	• Getting $\boldsymbol{\sigma}_{\mathbf{r}_{S/C}}$ from a covariance analysis including ILR measurements is expected to be too optimistic by yielding uncertainties below model capabilities, but doing so with Doppler measurements only does not assess the benefit of supporting orbit determination with laser ranging. • The required high sampling rate of range observations makes the design matrix significantly heavier and the simulation significantly slower. • Using a weight matrix defined by the observation noise (equation 4.33) of ILR makes the observations overly optimistic during estimation, potentially leading to wrong convergence.

Unlike with the previous method, this requires a deterministic error function $\Delta \mathbf{r}_X(t)$ for the position of each spacecraft X to be defined. This can be obtained by means of a full estimation, or by propagating an initial spacecraft state deviated from its true solution in accordance with the covariance matrix resulting from a covariance analysis and comparing it to the true trajectory. Getting the values of propagated formal errors directly as $\Delta \mathbf{r}_X(t)$ would not be correct, due to the strict positivity of the formal errors being in contrast with true error signatures, in which each of the orbital elements can oscillate between negative and positive throughout an orbit.

The first downside of this method is essentially the same as in the previous approach: a covariance analysis only can result too optimistic with the inclusion of ILR, whereas not adding it does not assess its benefits for spacecraft orbit determination. Assuming a full estimation of the spacecraft orbits needs to be conducted, the correct settings to take into account both spacecraft and planetary model errors lead to the final implemented approach (section section 7.2).

The idea behind this method is that using a high enough number of range measurements might end up mitigating the spacecraft error signature, leading to the fundamental limit of the intrinsic ranging system error (section 3.2.2) being the only dominant source of error affecting the planetary estimation. This can only be expected to happen if a high enough number of range measurements is used, presumably at a higher cadence than the spacecraft orbital period (i.e., order of minutes) to ensure proper averaging without any expected aliasing effects. The arising drawback is that the planetary estimation therefore needs to be conducted with range measurements generated at a high sampling rate, which significantly enlarges the design matrix (equation 4.31) and makes the estimation process much slower.

Finally, this requires to carefully assess the weighting of the observations to be used in the planetary estimation step. Classical weighting following the observation random error (equation (4.33)) might lead to the estimator not converging to the true solution, since the observations would be weighted according to uncertainty levels of order mm while potentially being off from the solution by several meters. If a weights matrix consistent with observation errors of order one meter is used instead, then the whole procedure would be consistent (both regarding true observation errors and weight matrix used in the batch filter) with the usage of classical radio-based ranging rather than highly accurate ILR.

This method was in fact implemented, applying equation (7.5) by means of generating the observations between the bodies of interest after calling a method named `add_sc_errors_to_state_hist_and_save_new_system_of_bodies()`. As its name indicates, it adds the temporal error of each spacecraft to the propagated state history of their corresponding planets, and stores the updated state history as the new ephemerides for the planets from which observations are subsequently generated. After assessing all of the above-described drawbacks at play, however, it was decided to move on with the final approach (section 7.2) instead, as it is assessed to more rigorously assess the impact of using ILR and it is not affected by such drawbacks.

7.2. Description of the implemented approach

The final implemented approach that has allowed to obtain the results presented in Part IV is based on the classical procedure for normal point generation from spacecraft orbit determination in real interplanetary missions (di Ruscio et al., 2020; A. Konopliv et al., 2020; Park et al., 2017). In particular, the study by di Ruscio et al. (2020) addressing Cassini orbit determination to improve the emphemerides of Saturn has been the main reference when reconstructing the full algorithm to be applied. This method allows to compute precise planet-to-planet ranges to be subsequently used in a planetary estimation where the spacecraft dynamics are ignored.

The main idea is to compute the multi-arc orbit estimation of the interplanetary orbiters including both Doppler and range observations, and then use the observed range discrepancies between expected and observed ranges to correct the virtual planet-to-planet observations generated from the *a priori* planetary model. The mathematically rigorous way to do so is by means of estimating a constant bias parameter for every range link at each orbit determination arc, and then add this bias to the virtual planet-to-planet range measurements. The main novelty of this work is to apply this method not with a single Earth-to-planet link but with three ranging and two Doppler links simultaneously. The addition of the Venus-Mars ranging link makes the orbit determination of the two interplanetary spacecraft not independent anymore, and by conducting this simulation it is possible to assess how much potential this has for improving such orbit determination and, ultimately, the generation of normal points for planetary estimation.

7.2.1. Planetary and spacecraft ephemerides

In order to proceed with the simulation, the "true" and "nominal" planetary ephemerides must be generated (section 6.1.2), together with the state history of each Trilogy spacecraft. The integration of the two is nuanced by the assumptions regarding the Earth-Moon system, as detailed below.

Just as in chapter 6, the planetary simulation of the Trilogy setup does not consider the dynamics of the Earth-Moon system around the EMB. Otherwise, the estimation could include the dynamics of the Earth and/or Moon around the EMB, yet it would be needed to assess whether or not this would indeed allow any better constraint than the currently introduced by LLR and lunar spacecraft such as LRO. Since adding these features was considered out of the scope of the current work due to the increased complexity, the dynamics of the Earth and Moon around the EMB have been neglected and only the state of the EMB is estimated (section 6.3.2). This is equivalent to assuming that Trilogy would not be capable of providing any better constraints than the other systems providing measurements of the Earth-Moon dynamics, which is in fact expected given the millimeter-level accuracy already achievable by LLR (T. W. Murphy, 2013). Analyses assessing the potential of combining both Trilogy and LLR/lunar-orbiter range measurements seeking better constraints of the Earth-Moon system are left for future work.

A problem arises when following this approach while considering spacecraft: the Trilogy vertex corresponding to the EMB is based on a single spacecraft orbiting either the Earth or the Moon (section 2.2), but the planetary estimation step considers a single body located at the EMB with the masses of the Earth and the Moon combined. With the aim of dealing with this inconsistency, the implemented algorithm for the generation of planetary and spacecraft ephemerides, which can be found in file `full_SC_ephemerides_generation.py`, is as follows:

1. The planetary ephemerides of Venus, the EMB and Mars are generated in accordance with the dynamical model described in section 6.1.1. This step is conducted twice: one for the "nominal" model and the other for the "true" model (section 6.1.2). These are labeled, respectively, $\bar{\mathbf{x}}_V$, $\bar{\mathbf{x}}_{EMB}$ and $\bar{\mathbf{x}}_M$; and $\mathbf{x}_V$, $\mathbf{x}_{EMB}$ and $\mathbf{x}_M$
2. Before proceeding with the generation of the spacecraft trajectories, new ephemerides of the Earth and Moon are

generated by setting their respective locations with respect to the EMB barycenter as given by the spice kernels (section 6.1.1) around the "true" state history of the EMB generated in step 1.

3. The trajectories of the Venus and Mars spacecraft, labeled $\mathbf{x}_{S/C_V}$ and $\mathbf{x}_{S/C_M}$, are generated with the two placed around their host planets, each following their corresponding ephemerides generated in step 1. The trajectory of the Earth spacecraft is propagated around the Earth, which is set to follow the ephemerides generated in step 2.

This procedure is summarized in Figure 7.3. These ephemerdies are then used in the full algorithm to simulate the spacecraft-to-spacecraft observations (section 7.2.2).

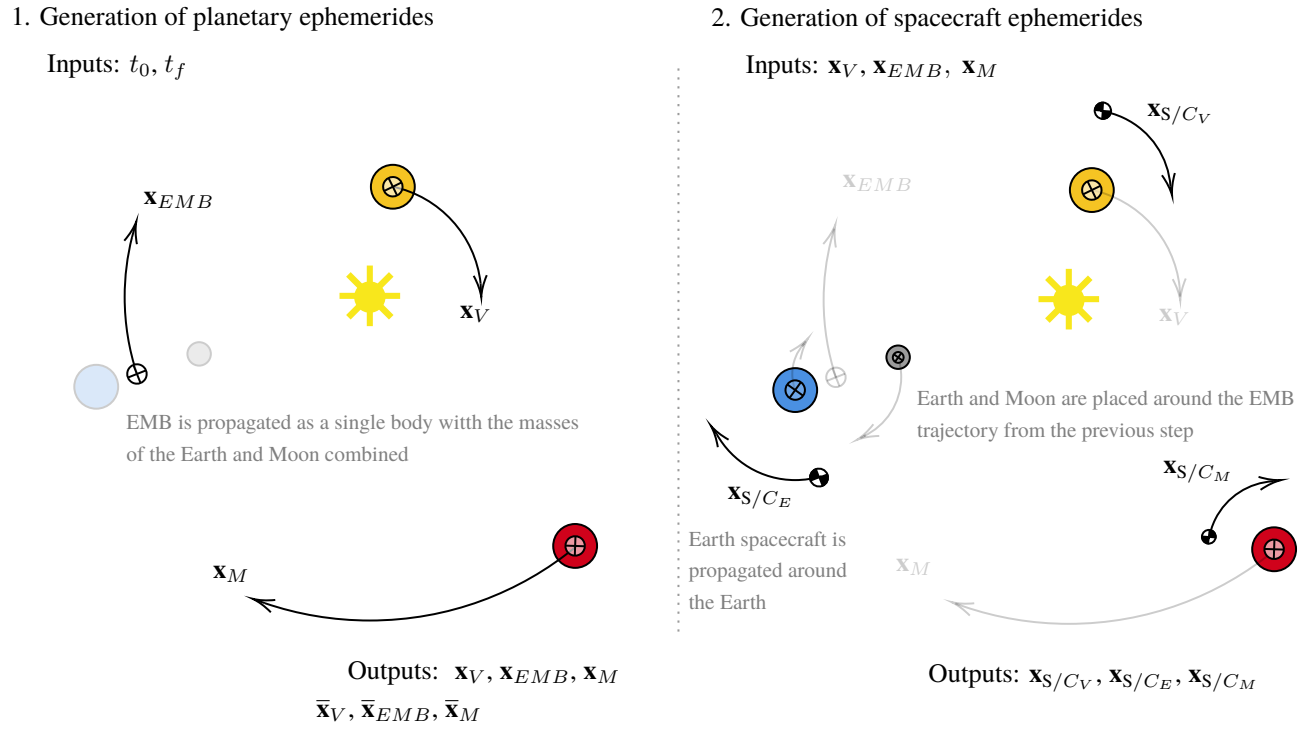

Figure 7.3: Two steps of the ephemerides generation procedure: generation of planetary ephemerides (left) and spacecraft ephemerides (right)

7.2.2. Full algorithm

The description of the implemented estimation approach can be found in section 3.2 of Part IV, yet with the extension constraints of the format of a scientific paper. In this section, the algorithm and the mathematical principles used are described in more depth.

Generation of observations

The set of observations used consists of ILR measurements between the three Trilogy spacecraft and Doppler measurements from Earth to the two interplanetary orbiters. As detailed in section 4.2.2, Doppler measurements are most suitable to capture fast (spacecraft) dynamics, whereas range measurements best capture slow (planetary) dynamics. Although the implemented simulation does not account for the estimation of high-order gravity field terms, which would clearly fall into the set of fast dynamics, both types of measurements are still used with the aim of simulating the availability of the two kinds of observables (hence, potentially more information) in a real operational scenario.

As detailed above, Trilogy ranges are used to estimate the location of the EMB only while considering the orbits of the Earth and the Moon to be fully known around it. Additionally, we introduce the assumption of the Earth-orbiting spacecraft to have its orbit fully known around the Earth-Moon system. This follows the state of the art of satellite orbit determination on Earth, which is capable of achieving true errors at the cm/sub-cm level thanks to the availability of SLR and GNSS (Selvan et al., 2023).

Given that the planetary estimation of the Earth-Moon system only takes into account the EMB by placing a single body with the masses of Earth and the Moon combined, the generation of observations has been conducted by placing the trajectory of the Earth spacecraft around the EMB directly. This is because the implemented method is meant to get

planet-to-planet range measurements from the centers of mass of the two bodies being orbited by the two ILR ends of each link (see Estimation Algorithm later in this section). More realistically, since the Earth spacecraft is orbiting Earth, the resulting planet-to-planet ranges would be Earth-Venus and Earth-Mars, and the orbit of Earth around the EMB would then be used to solve the state of the EMB. However, given our previous assumption that the dynamics of the Earth/Moon are fully solved around the EMB (section 7.2.1), this approach is essentially equivalent to simply assuming the generated ranges to be EMB-Venus and EMB-Mars (hence, the Earth spacecraft is directly orbiting the EMB) from the information standpoint. The reason it is still important to generate the trajectory of the Earth spacecraft around the Earth as described in section 7.2.1 instead of the combined Earth+Moon body at the EMB is that doing so would make the spacecraft subject to a false orbital period as a result of the increased mass of its host body.

Finally, Doppler observations are also generated from Earth to the two interplanetary orbiters. To ensure consistency with the ILR measurements to be used in a joint manner, these have been generated with respect to the EMB instead of the actual Earth. Making Doppler measurements consistent with ground infrastructure limitations such as the locations of the available stations on a rotating Earth has not been considered in this work—instead, all Doppler measurements have been originated at the center of mass (hence, in this case, the EMB), and no observation viability related to ground stations has been considered. Although this leaves the assessment on how much more realistically limited Doppler observations might impact the final results for future work, it can also be interpreted as a representation of an optimistic scenario where the ground infrastructure prioritizes Trilogy.

The combination of both ILR and Doppler observations yields to the final set of available observations from which the final simulation of orbit estimation is conducted. The procedure for observation generation is summarized in algorithm 5 and Figure 7.5 left.

Algorithm 5 Generation of observation set $\mathbf{z}$

Require: True ephemerides for Venus, EMB and Mars: $\mathbf{x}_V$, $\mathbf{x}_{EMB}$ $\mathbf{x}_M$.
Require: True spacecraft ephemerides $\mathbf{x}_{\mathrm{S/C}_V}$, $\mathbf{x}_{\mathrm{S/C}_E}$ and $\mathbf{x}_{\mathrm{S/C}_M}$.
Set the ephemerides of the Venus and Mars spacecraft around Venus and Mars, respectively, and those of the Earth spacecraft around the EMB.
Set observation times for Trilogy and Doppler observations.
for All observation epochs t **do**
Generate the simulated observations $\mathbf{z}(t)$, consisting of
- inter-spacecraft Trilogy observations by applying equation (3.6); and/or
- EMB-centred range-rate (Doppler) measurements to the Venus and Mars spacecraft by applying equation (3.7)

end for

Orbit determination arcs

As detailed in section 4.2.2, orbit determination of interplanetary spacecraft is typically performed in a multi-arc fashion, and as explained in section 3.2 of Part IV, we follow this approach instead of the more sophisticated alternatives such as the constrained multi-arc (Alessi et al., 2012). Hence, in this simulation, each batch orbit determination of the interplanetary spacecraft is independently conducted during a fixed window of time.

The arc duration can be set differently depending on the mission needs, but it usually spans between a few days and a week (Yan et al., 2017). As detailed in section 3.3.3 of Part IV, the chosen arc lengths for the simulated Trilogy orbit determination have been 12 hours, following di Stefano et al. (2023) in the shorter arc duration with the aim of mitigating the effect of unmodeled dynamics. Together with the production of one normal point per day, following Fienga (2023a), and the method that produces one normal point for each orbit determination arc (section 7.2.2), this results in one 12-hour arc every calendar day for the whole mission duration.

A further nuance must be however stated, which is that Tudat is not robust to generating observations too close to the start or end epochs of a propagation arc. This is because the range observation simulator must run a convergence loop to solve the range with the emission and reception times that match the speed of light (equations 3.6, 3.5), and an error can arise if during this procedure a time at which no propagation history exists is attempted. Some trial and error led to finding a margin of two hours and a half to mitigate this problem for the whole range of dates attempted, hence it was decided to set all arc propagations to start and end 2.5 hours earlier and later, respectively, than the start and end times of the 12-hour period of generated observations. This means that the orbit propagation arcs are actually 17 hours, whereas observations are available over a window of 12.

In practical terms, this means that the epoch of the estimated initial state is earlier than the epoch of the first observation, as observed in the sketch presented in Figure 7.4. This is not expected to affect the results in a significant manner, since the convergence of the batch estimation (algorithm 1) is still solely based on the residuals of the observations that are

available. The only real effect of separating the estimated initial state from the first observation by a too long period is that the errors in the dynamical model can accumulate during this "blind time", increasing the true error of the estimated initial state. In this study, however, we do not assess true errors of the estimated initial states but rather in the complete propagated arc (section 7.2.3).

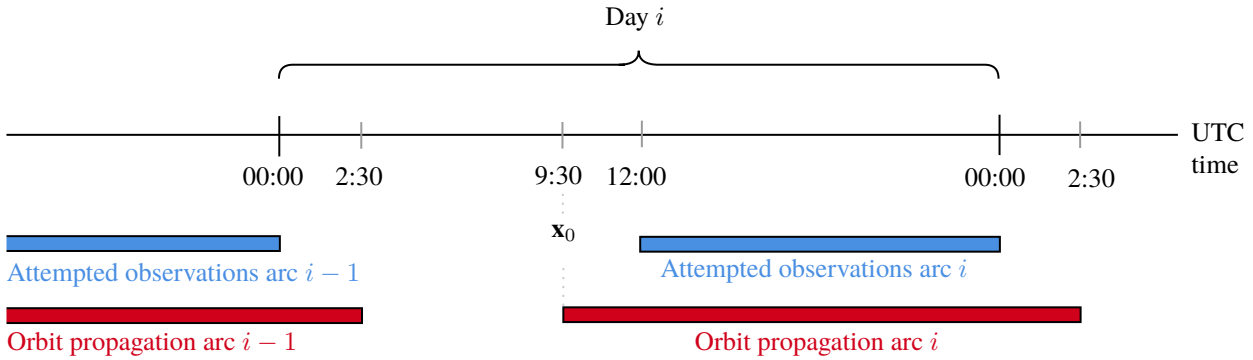

Figure 7.4: Representation of the definition of the individual orbit determination arcs. $\mathbf{x}_0$ corresponds to the initial state of arc i.

The orbit determination arcs set in real operations can typically contain several different observational windows (e.g., di Ruscio et al., 2020). Trilogy will be different because measurements will be nearly continuous, being only limited by the operational constraints of space-based ILR (i.e., planetary occultations and Sun avoidance; section 3.3.3) rather than the availability of ground infrastructure. Hence, orbit determination arcs can contain continuous ILR measurements rather than a few batches corresponding to particular measurement windows. Doppler observations, although expected to be less continuously available in real life, are treated equivalently to Trilogy regarding their availability during an orbit determination arc (see Generation of Observations earlier in this section). Hence, in summary, both Trilogy and Doppler observations are considered to be continuously attempted during the whole orbit determination arc, and they are only subject to the viability constraints given by planetary occultations and Sun avoidance angles.

Estimation algorithm

Since the orbit of the Earth spacecraft has been considered to be fully solved, the orbit determination arcs are only meant to estimate the states of the spacecraft around Venus and Mars. Hence, the estimated initial state is $\mathbf{x}_0 = \left[\mathbf{x}_{0_{\mathrm{S/C}_V}}^\top \quad \mathbf{x}_{0_{\mathrm{S/C}_M}}^\top\right]^\top$, where each $\mathbf{x}_{0_i}$ consists of the six cartesian components of the initial state, i.e.,

$$\mathbf{x}_{0_i} = \left[X_{0_i} \quad Y_{0_i} \quad Z_{0_i} \quad \dot{X}_{0_i} \quad \dot{Y}_{0_i} \quad \dot{Z}_{0_i}\right]^\top. \tag{7.6}$$

Additionally, constant range biases for each of the three ranging legs are introduced as estimable parameters with the aim of absorbing the difference between the nominal and the true planetary positions. As described in more detail below, these biases allow the generation of the planet-to-planet ranges to be used for planetary estimation. More rigorously, this is done by adding such constant biases to the range observable equation (3.5, 3.6) which then becomes

$$s_{BA}^{(2)} = s_{BA}^{(1)} + s_{AB}^{(1)} + c\delta t_B + b_{BA}, \tag{7.7}$$

where b_{BA} represents the bias of the $s_{BA}^{(2)}$ range measurement. The complete vector of estimated parameters $\mathbf{y}$ at every orbit determination arc therefore contains 15 scalar components, corresponding to the initial states of the Venus and Mars spacecraft and the three constant biases corresponding to the three Trilogy ranging legs:

$$\mathbf{y}_{\mathrm{S/C}} = \left[\mathbf{x}_{0_{\mathrm{S/C}_V}}^\top \quad \mathbf{x}_{0_{\mathrm{S/C}_M}}^\top \quad b_{EM} \quad b_{VE} \quad b_{VM}\right]^\top. \tag{7.8}$$

The *a priori* covariance matrix employed for the estimation of $\mathbf{y}_{\mathrm{S/C}}$ has been defined as

$$\boldsymbol{P}_{0_{\mathrm{S/C}}} = \begin{bmatrix} \boldsymbol{P}_{0_{\mathrm{S/C}_V}} & & & & \\ & \boldsymbol{P}_{0_{\mathrm{S/C}_M}} & & & \\ & & \sigma_b^2 & & \\ & & & \sigma_b^2 & \\ & & & & \sigma_b^2 \end{bmatrix}, \tag{7.9}$$

where $\boldsymbol{P}_{0_{S/C_X}}$ is the covariance associated to the initial state of spacecraft X and σ_b is the standard deviation associated to the biases to be estimated. The values of $\boldsymbol{P}_{0_{S/C_X}}$ should come from the post-fit results of a preliminary orbit determination (e.g., based on on-board navigation instruments) from which an *a priori* solution for the state $\bar{\mathbf{x}}_{S/C_X}$ is generated. In this work, however, this step is omitted and the $\boldsymbol{P}_{0_{S/C_X}}$ matrices are simply assumed to be diagonal with constant values in the RSW frame:

$$\boldsymbol{P}^{RSW}_{0_{S/C_V}} = \boldsymbol{P}^{RSW}_{0_{S/C_M}} = \begin{bmatrix} \sigma_R^2 & & & & & \\ & \sigma_S^2 & & & & \\ & & \sigma_W^2 & & & \\ & & & \sigma_{v_R}^2 & & \\ & & & & \sigma_{v_S}^2 & \\ & & & & & \sigma_{v_W}^2 \end{bmatrix}. \tag{7.10}$$

This covariance matrix is used to sample a perturbation from the true states $\mathbf{x}_{0_{S/C_X}}$ to generate, at every arc, an *a priori* state for the batch estimation (algorithm 1) as

$$\bar{\mathbf{x}}_{0_{S/C_X}} \sim \mathcal{N}\left(\mathbf{x}_{0_{S/C_X}}, \boldsymbol{P}_{0_{S/C_X}}\right), \tag{7.11}$$

from which the full *a priori* $\mathbf{y}_{S/C}$ is then set to

$$\bar{\mathbf{y}}_{S/C} = \begin{bmatrix} \bar{\mathbf{x}}^\top_{0_{S/C_V}} & \bar{\mathbf{x}}^\top_{0_{S/C_M}} & 0 & 0 & 0 \end{bmatrix}^\top. \tag{7.12}$$

Finally, the values of σ_b are set to several hundreds of meters with the aim of allowing the estimated solution to truly absorb the difference between true and nominal interplanetary distances, following di Ruscio et al. (2020).

The key of this method is that the values of the estimated biases at each orbit determination arc can be used to generate precise planet-to-planet ranges. This method is typically used when improving the ephemerides of planets based on range observations to interplanetary orbiters (A. Konopliv et al., 2020; Park et al., 2017), although the used formulation is based on the particular method description given by di Ruscio et al. (2020). The main idea is that once the bias b_{BA} is estimated, virtual planet-to-planet measurements can be computed with equation (7.7), using the nominal planet ephemerides (i.e., $\bar{\mathbf{x}}_V, \bar{\mathbf{x}}_{EMB}, \bar{\mathbf{x}}_M$) to compute the one-way ranges $s^{(1)}_{BA}$ and $s^{(1)}_{AB}$ (equations 3.5b, 3.5c, 3.6b, 3.6c), and setting the previously estimated bias to b_{BA}. This way, the bias estimated during the orbit determination corrects the planet-to-planet range expected from the nominal planetary dynamics, bringing it closer to the value resulting from the true dynamics. Following di Ruscio et al. (2020), the reference time at which this planet-to-planet range is generated is set to the mid epoch of the orbit determination arc at which the biases have been estimated.

The resulting planet-to-planet ranges are then used to run a batch estimation of the planetary parameters, which include the initial states of the Trilogy legs and the masses of the asteroids of interest. Namely, the vector of estimated parameters during this planetary estimation step is

$$\mathbf{y} = \begin{bmatrix} \mathbf{x}^\top_{0_V} & \mathbf{x}^\top_{0_{EMB}} & \mathbf{x}^\top_{0_M} & \mathbf{M}^\top \end{bmatrix}^\top, \tag{7.13}$$

where $\mathbf{x}_{0_X}$ is the state of body X at the simulation start epoch and vector $\mathbf{M}$ is the vector of asteroid masses. The *a priori* covariance matrix associated to vector $\mathbf{y}$ is the one given in equation (6.2). The resulting best-fit propagation is then taken as a new set of planetary ephemerides, and the whole procedure can be repeated until convergence is reached. The full algorithm is detailed in pseudocode format in algorithm 6.

The convergence criteria displayed in algorithm 6 is denoted ζ for the sake of readability, but similarly to algorithm 4 the convergence has been assessed visually: when the estimated planetary parameters do not show significant improvement with respect to their *a priori* values, convergence is assessed to be reached. The whole procedure has been implemented in two separate scripts: `sc_joint_multi_arc_estimation.py`, where the simultaneous spacecraft orbit determination is performed and the arc-wise observation biases are stored; and `main_only_planets_with_biases.py`, where the planetary estimation step is performed based on the stored biases. Each script can be set to run a different iteration (i.e., of the outermost while loop in algorithm 6), which then stores or retrieves the corresponding set of estimated biases.

7.2.3. Full results of the tested cases

The nominal configuration in which the simulation described above has been conducted is the one described in section 3.3 of Part IV. Additionally, different sub-cases with tweaked settings described in section 4.2 of Part IV have been also run to assess the sensitivity of the results to key design parameters. Although the description of the simulation configurations is not replicated here for the sake of compactness, the full set of figures omitted in Part IV due to space constraints is presented below.

Algorithm 6 Implemented solution

Require: Nominal ephemerides for Venus, EMB and Mars: $\overline{\mathbf{x}}_V$, $\overline{\mathbf{x}}_{EMB}$, $\overline{\mathbf{x}}_M$.
Require: Spacecraft ephemerides $\mathbf{x}_{\mathrm{S/C}_V}$ and $\mathbf{x}_{\mathrm{S/C}_M}$.
Require: Observation set $\mathbf{z}$
  Set observation times for Trilogy and Doppler observations
  Initialize convergence metric ζ and desired convergence level ζ_0
  Initialize the estimation *a priori* covariance $\overline{\boldsymbol{P}}_0$ as defined in equation (6.2).
  while $\zeta < \zeta_0$ **do**
    for All orbit arcs i **do**
      Take the observation subset $\mathbf{z}_i$ corresponding to the observations generated during the timespan of arc i.
      Use observations $\mathbf{z}_i$ to compute the batch estimation (algorithm 1) of the estimable parameters $\mathbf{y}$ (equation 7.8)
      Save the estimated biases $b_{EM}[i]$, $b_{EV}[i]$ and $b_{VM}[i]$.
    end for
    for All orbit arcs i **do**
      Compute the mid epoch of arc i, t_i
      Generate virtual two-way range measurements between the Trilogy vertices applying equation (3.6):
      $\overline{s}^{(2)}_{EM}(t_i) = s^{(1)}_{EM}\left(\overline{\mathbf{x}}_{EMB}, \overline{\mathbf{x}}_M; t_i\right) + s^{(1)}_{ME}\left(\overline{\mathbf{x}}_{EMB}, \overline{\mathbf{x}}_M; t_i\right) + c\delta t_M$
      $\overline{s}^{(2)}_{VE}(t_i) = s^{(1)}_{VE}\left(\overline{\mathbf{x}}_{EMB}, \overline{\mathbf{x}}_V; t_i\right) + s^{(1)}_{EV}\left(\overline{\mathbf{x}}_{EMB}, \overline{\mathbf{x}}_V; t_i\right) + c\delta t_E$
      $\overline{s}^{(2)}_{VM}(t_i) = s^{(1)}_{VM}\left(\overline{\mathbf{x}}_M, \overline{\mathbf{x}}_V; t_i\right) + s^{(1)}_{MV}\left(\overline{\mathbf{x}}_M, \overline{\mathbf{x}}_V; t_i\right) + c\delta t_M$
      Correct the three two-way ranges as
      $\hat{s}^{(2)}_{EM}(t_i) \leftarrow \overline{s}^{(2)}_{EM}(t_i) + b_{EM}[i]$
      $\hat{s}^{(2)}_{VE}(t_i) \leftarrow \overline{s}^{(2)}_{VE}(t_i) + b_{VE}[i]$
      $\hat{s}^{(2)}_{VM}(t_i) \leftarrow \overline{s}^{(2)}_{VM}(t_i) + b_{VM}[i]$
    end for
    Build the full planet-to-planet observation vector:
    $$\mathbf{z} = \left[\hat{s}^{(2)}_{EM}(t_0) \quad \hat{s}^{(2)}_{VE}(t_0) \quad \hat{s}^{(2)}_{VM}(t_0) \quad \dots \quad \hat{s}^{(2)}_{EM}(t_{n-1}) \quad \hat{s}^{(2)}_{VE}(t_{n-1}) \quad \hat{s}^{(2)}_{VM}(t_{n-1})\right]^\top.$$
    Use this observation vector $\mathbf{z}$ to run a batch estimation (algorithm 1) of the planetary parameters $\mathbf{y}$ (equation 7.13).
    Retrieve the best-fit propagation of Venus, the EMB and Mars ($\mathbf{x}_V$, $\mathbf{x}_{EMB}$ and $\mathbf{x}_M$) from the batch estimation.
    Retrieve the vector of estimated masses $\mathbf{M}$ from the batch filter results.
    Retrieve the post-fit covariance $\hat{\boldsymbol{P}}$ from the batch filter results.
    Update the nominal ephemerides models and asteroid masses as
    $\overline{\mathbf{x}}_V \leftarrow \mathbf{x}_V$
    $\overline{\mathbf{x}}_{EMB} \leftarrow \mathbf{x}_{EMB}$
    $\overline{\mathbf{x}}_M \leftarrow \mathbf{x}_M$
    $\overline{\mathbf{M}} \leftarrow \mathbf{M}$
    $\overline{\boldsymbol{P}}_0 \leftarrow \hat{\boldsymbol{P}}$
  end while

Nominal case (iterations 1-2)

Figures 5, 7 and 9 in Part IV correspond to the last iteration of Algorithm 6. For the sake of completeness, their equivalent results in iterations 1 and 2 are presented, respectively, in figures 7.7-7.9 and 7.10-7.12. Figures 6 and 8 in Part IV, presenting the relative geometry of the Trilogy links and the spacecraft orbital planes, are not replicated here. The reader shall refer there to verify the meaning of the dashed vertical lines in Figures 7.7 and 7.10.

One can verify how the figures corresponding to iteration 2 are essentially identical to those corresponding to iteration 3 presented in Part IV. This supports our claim that convergence of Algorithm 6 is reached after three iterations.

Modified subcase 1 (iteration 3)

The results of the last iteration of modified subcase 1, which is equivalent to the nominal except for a more pessimistic assumption on spacecraft dynamcial mismodeling (section 4.2 in Part IV), are presented in figures 7.13-7.15.

These results, which are not included in Part IV for the sake of compactness, evince how the more pessimistic spacecraft dynamical mismodeling does have a significant impact on the results: spacecraft orbit determination errors, although still significantly reduced with respect to the case of a single range constraint (as evinced in the shaded areas of Figure 7.13), is not reduced as much as in the nominal case (Figure 5 in Part IV) and it remains at the several tens of cm level. This

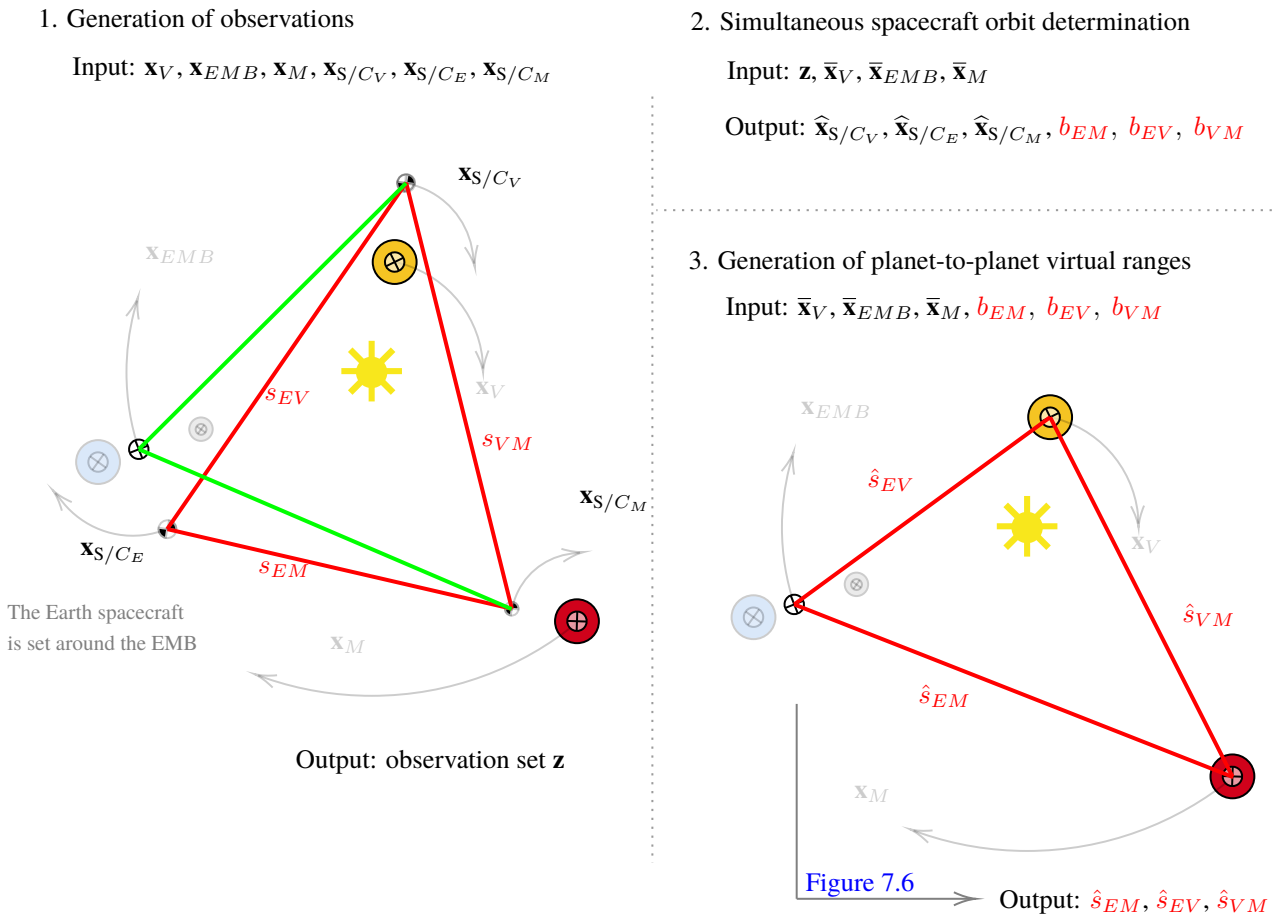

Figure 7.5: aaa

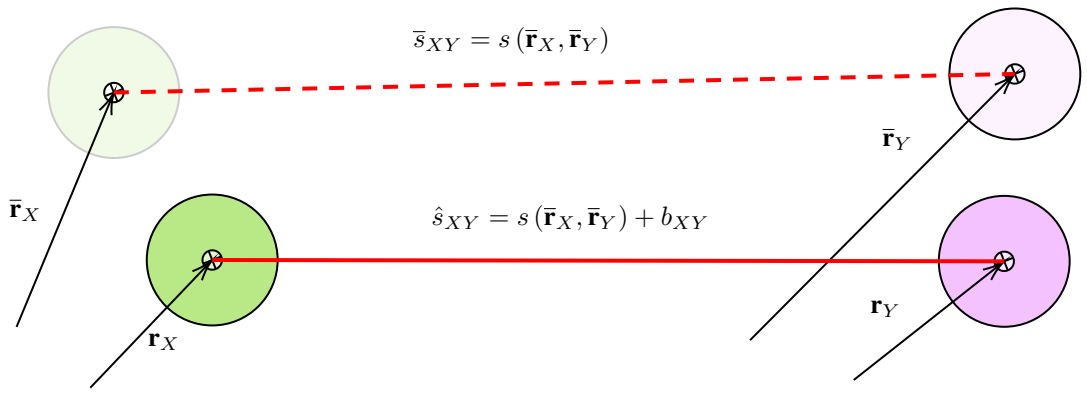

Figure 7.6: Generation of the (approximate) true planet-to-planet range between planets X and Y from the nominal (*a priori*) planet positions $\bar{\mathbf{r}}_X$ and $\bar{\mathbf{r}}_Y$ and the estimated bias b_{XY}.

degrades the quality of the produced normal points (Figure 7.14; Table 4 in Part IV), and as a result the discrepancy between their true errors and the formal errors of the fitted biases is much larger than in the nominal case (Figure 7.15 vs Figure 9 in Part IV). This supports our claim in section 4.2.1 of Part IV that the weighting of the observations for a planetary estimation assuming a true-to-formal error ratio of 50 is likely to be inaccurate and thus a strong candidate of causing the poor performance of asteroid mass estimations.

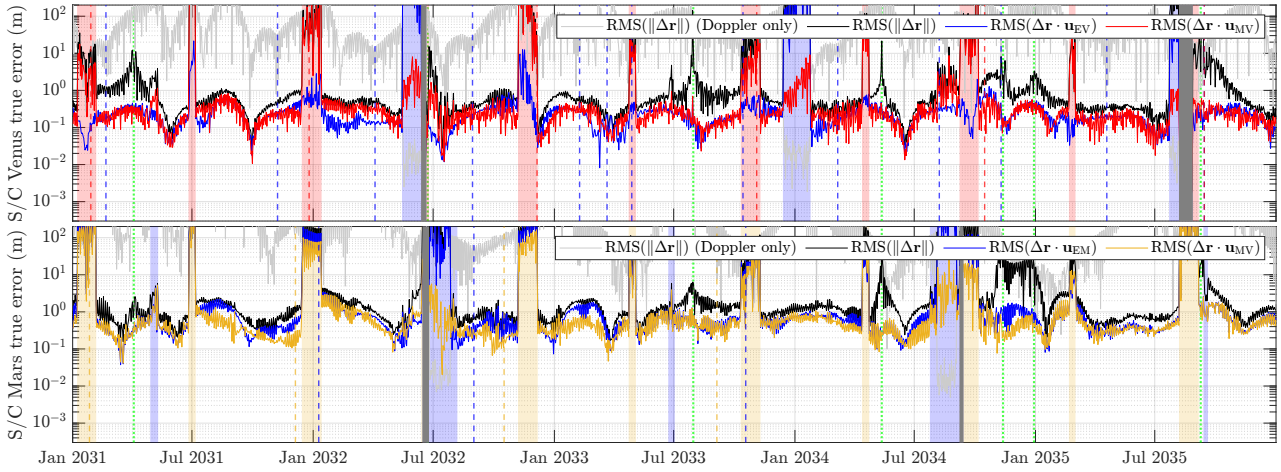

Figure 7.7: True errors of spacecraft orbit determination at the first iteration of Algorithm 6 for the nominal simulation settings.

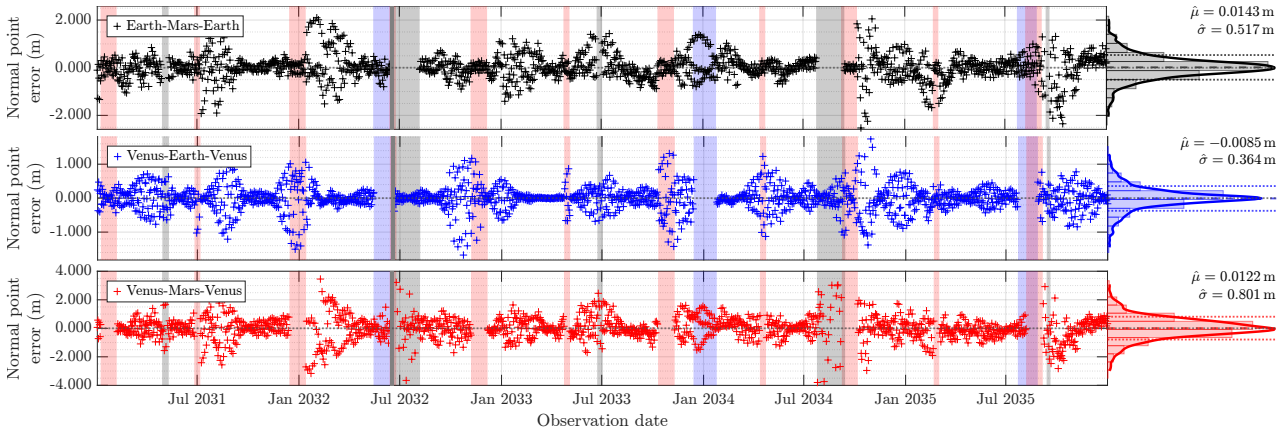

Figure 7.8: True errors in the planet-to-planet ranges generated at the first iteration of Algorithm 6 for the nominal simulation settings.

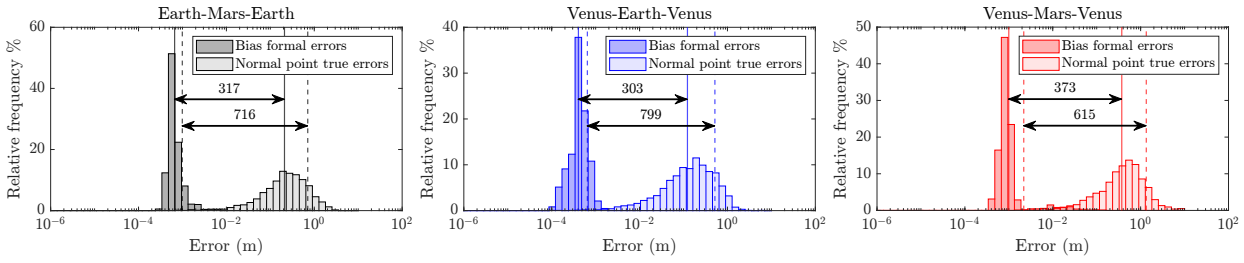

Figure 7.9: Distribution of true errors in the planet-to-planet ranges generated at the first iteration of Algorithm 6, compared to the formal errors of the fitted biases, for the nominal simulation settings.

Modified subcase 2 (iteration 3)

The results after the last iteration for subcase 2 of simulation settings (i.e., all spacecraft set to orbital periods of 12 hours) are presented in Figures 7.16-7.18. As discussed in section 4.2.2 of Part IV, this is the subcase that produces the most accurate planet-to-planet ranges (Figure 7.17), which we judge to be due to the optimal averaging of the spacecraft orbit determination errors over a full revolution.

These errors are presented in Figure 7.16, where it is evinced how they are not generally lower than in the nominal case (Figure 5 in Part IV). The fact that the three legs of planet-to-planet ranges do show a performance that pushes the limit of ILR technology (i.e., only a few mm in standard deviation of true errors, Figure 7.17) suggests that the averaging of the spacecraft orbit determination error over an entire orbit is indeed playing a significant role. One must also note that the resulting spacecraft orbit determination errors appear much more modulated in time (Figure 7.16) than in the nominal case (Figure 5 in Part IV). Although some peaks to appear aligned with the collinearity peaks (green dashed vertical lines,

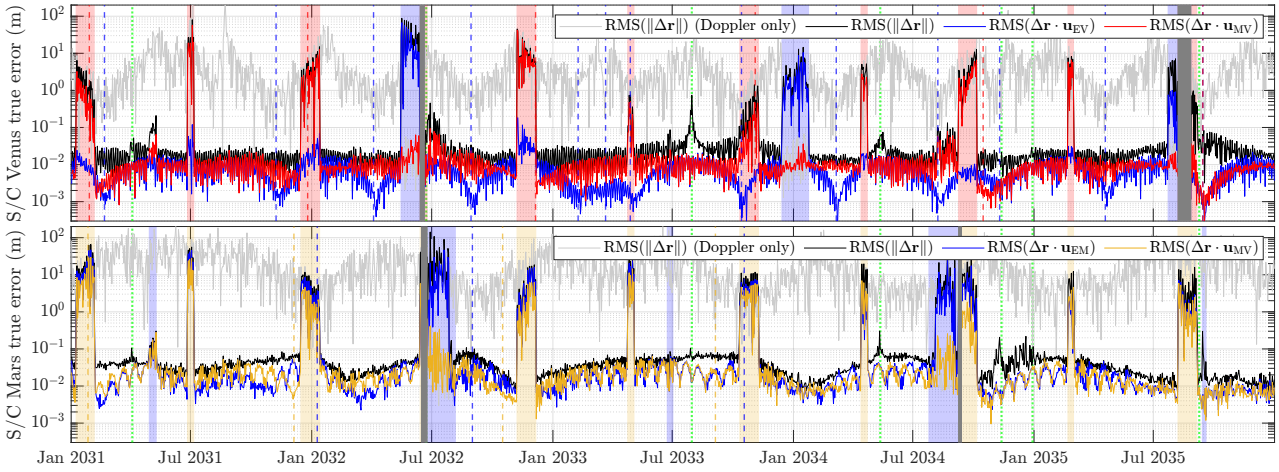

Figure 7.10: True errors of spacecraft orbit determination at the second iteration of Algorithm 6 for the nominal simulation settings.

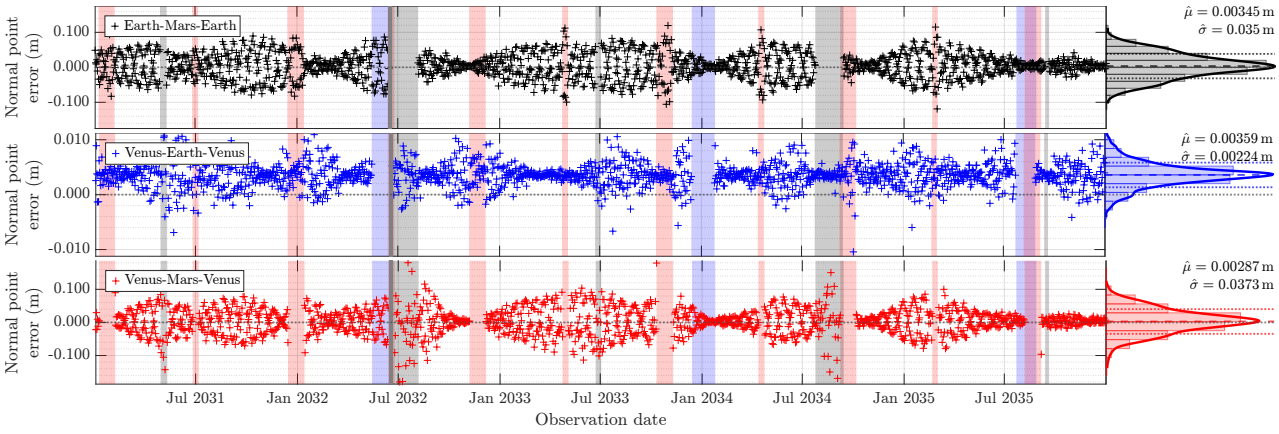

Figure 7.11: True errors in the planet-to-planet ranges generated at the second iteration of Algorithm 6 for the nominal simulation settings.

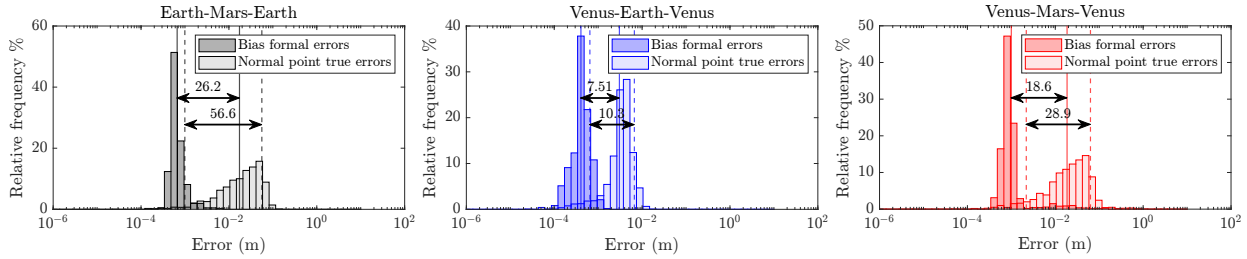

Figure 7.12: Distribution of true errors in the planet-to-planet ranges generated at the second iteration of Algorithm 6, compared to the formal errors of the fitted biases, for the nominal simulation settings.

see Figure 8 in Part IV), many of them remain of unclear cause at the time of ending this study.

The reader will notice that in Figure 7.17 all normal point errors present a mean shifted from zero, which is consistent with the constant bias introduced in the ILR observations, as explained in section 4.1.1 of Part IV. In this case, however, the used bias is not -3.6 mm as in the nominal case but 2.4 mm. This is not judged to have any significant impact because, as detailed in section 4.2.3 of Part IV, the constant systematic errors of the ILR measurements are not found to have any significant impact on the planetary estimation. This is due to the fact that the implementation of the algorithm assigns a different, randomly distributed ILR bias at every different run. This is sampled normally with a standard deviation of 2 mm, following an optimistic combination of systematic errors as described in subsection 3.2.2.

Modified subcase 3 (iteration 3)

As described in section 4.2 of Part IV, subcase 3 uses ILR observations with 3 cm random noise instead of 3 mm. The results are presented in figures 7.19-7.21.

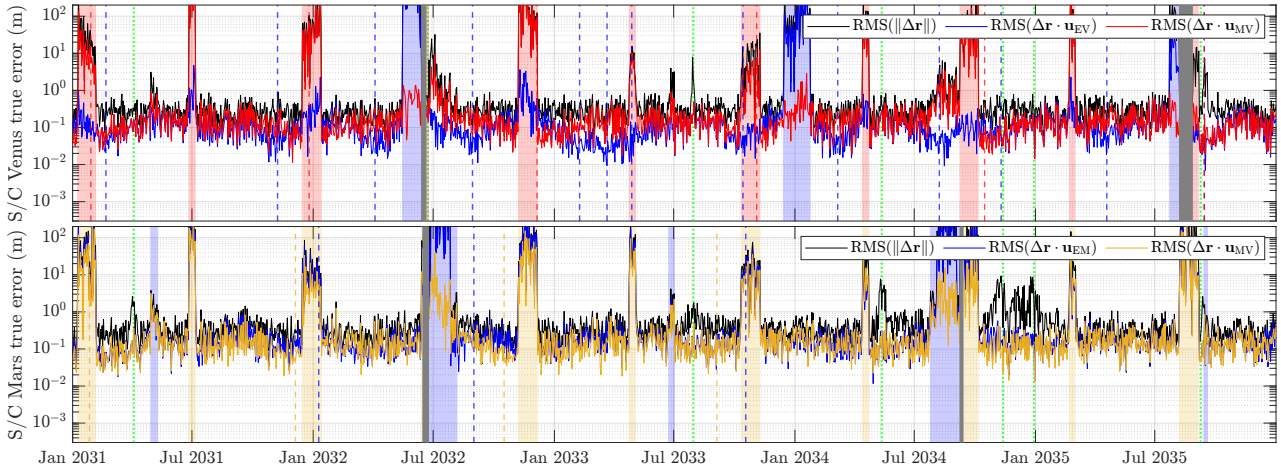

Figure 7.13: True errors of spacecraft orbit determination at the last iteration of Algorithm 6 for the simulation settings of subcase 1 (larger spacecraft dynamical mismodeling).

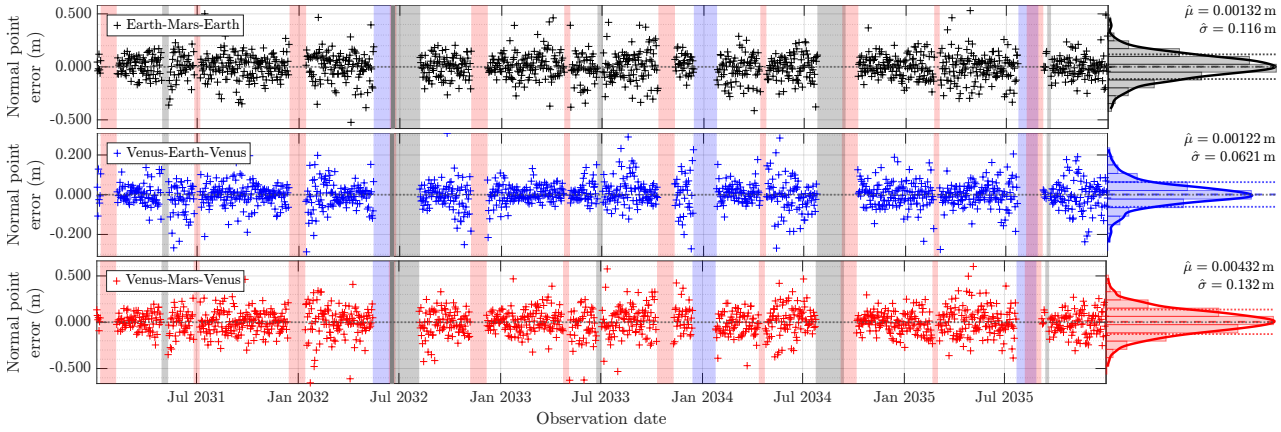

Figure 7.14: True errors in the planet-to-planet ranges generated at the last iteration of Algorithm 6 for the simulation settings of subcase 1 (larger spacecraft dynamical mismodeling).

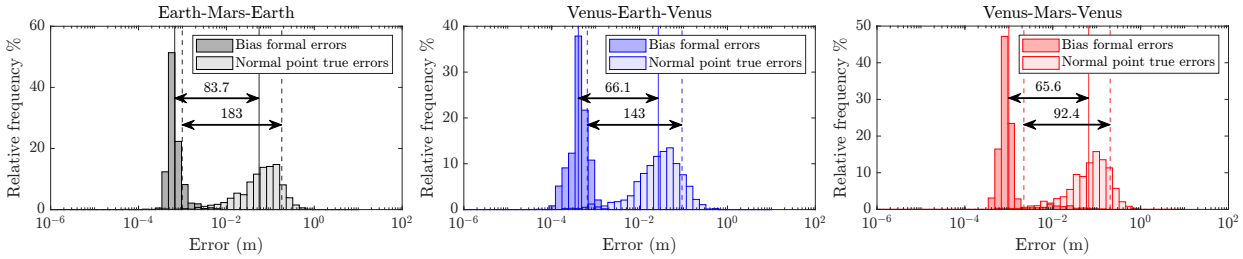

Figure 7.15: Distribution of true errors in the planet-to-planet ranges generated at the last iteration of Algorithm 6, compared to the formal errors of the fitted biases, for the simulation settings of subcase 1 (larger spacecraft dynamical mismodeling).

Figure 7.19 and Figure 7.20 look very similar to their counterparts in the nominal case (Figure 5 in Part IV). Closer inspection evinces how the dips in the projections of the orbit determination error of the Venusian spacecraft do not reach levels as low as in the nominal case, which shows how the usage of ILR can indeed improve the results with respect to more traditional ranging methods. It must still be acknowledged, however, that Figure 7.19 still shows how the significant factor in the reduction of spacecraft orbit determination is the presence of two range constraints from different directions, which causes the dramatic reduction in resulting error with respect to the periods where only one range constraint is available. In any case, the motivation to use ILR instead of radio ranging is still given not only by the observed slight improvement both in spacecraft orbit determination (Figure 7.19) and asteroid mass estimations (section 4.2.3 in Part IV) but also because of the need for large spacecraft antennae in the case of radio-based ranging (section 2.2).

Finally, one must also note how the normal point true-to-formal error ratios displayed in Figure 7.21 are much lower

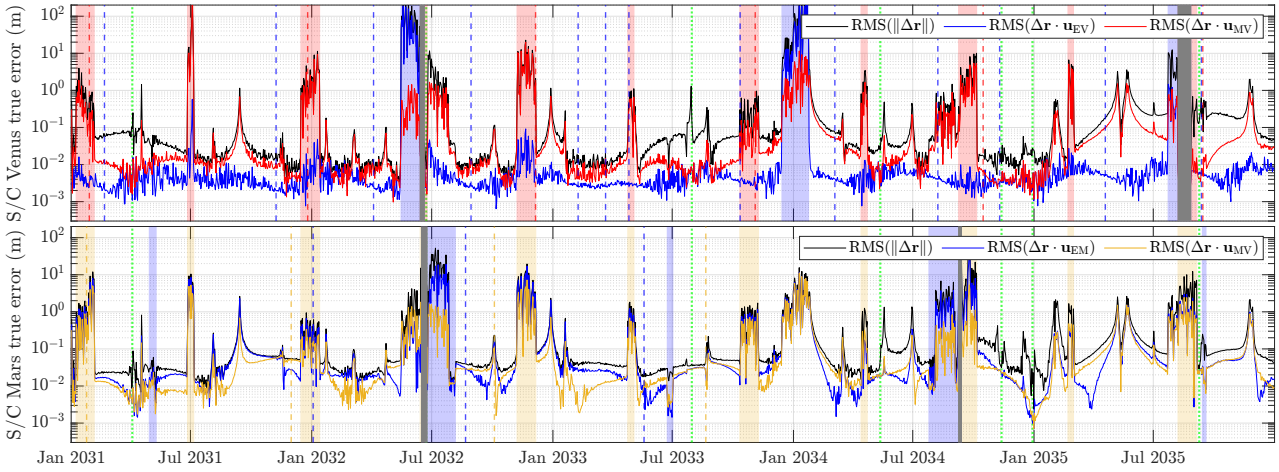

Figure 7.16: True errors of spacecraft orbit determination at the last iteration of Algorithm 6 for the simulation settings of subcase 2 (12-hour spacecraft periods).

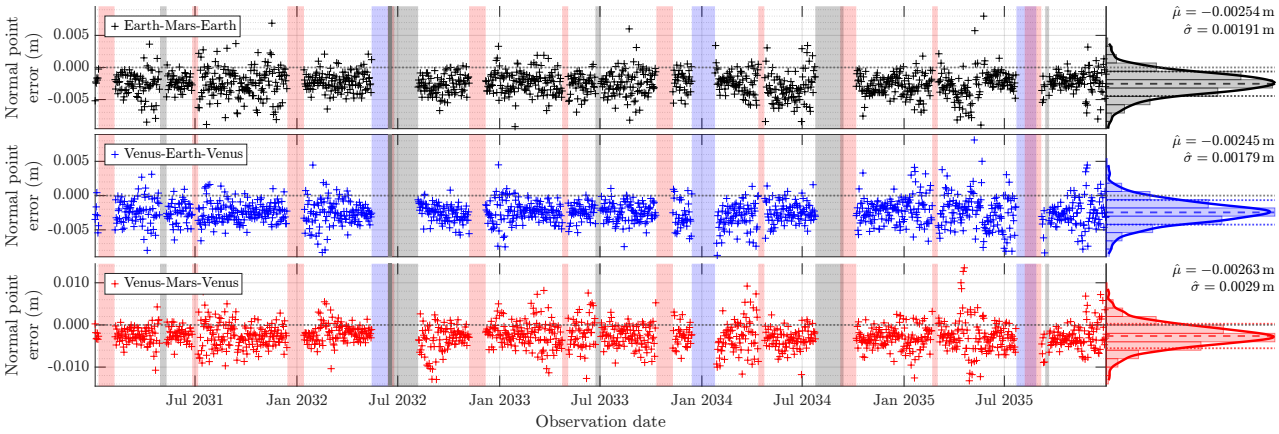

Figure 7.17: True errors in the planet-to-planet ranges generated at the last iteration of Algorithm 6 for the simulation settings of subcase 2 (12-hour spacecraft periods).

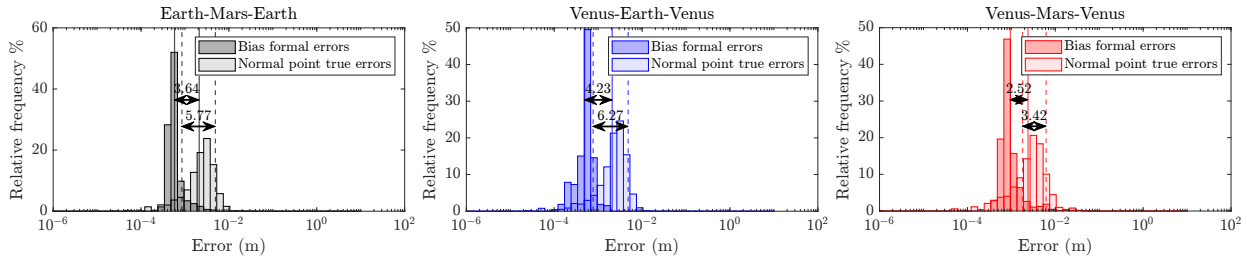

Figure 7.18: Distribution of true errors in the planet-to-planet ranges generated at the last iteration of Algorithm 6, compared to the formal errors of the fitted biases, for the simulation settings of subcase 2 (12-hour spacecraft periods).

than those in the nominal case (Figure 9 in Part IV). This is not due to true errors being lower, as seen in Figure 7.20, but due to the fact that the ILR observations in the orbit determination process have been weighted according to their noise level of 3 cm instead of 3 mm (equation 4.33), hence resulting in a greater post-fit covariane matrix and thus greater formal errors of the fitter biases.

Modified subcase 4 (iteration 3)

The fourth modified subcase in the sensitivity analysis (section 4.2 in Part IV) only differs from the nominal in the *a priori* covariance used for the spacecraft orbit determination, which is set to a 1 cm one-sigma level in each position component. The results arising from this configuration are presented in Figures 7.22-7.24.

Figure 7.22 is essentially equivalent to the nominal results (Figure 5 in Part IV), with the only difference that the

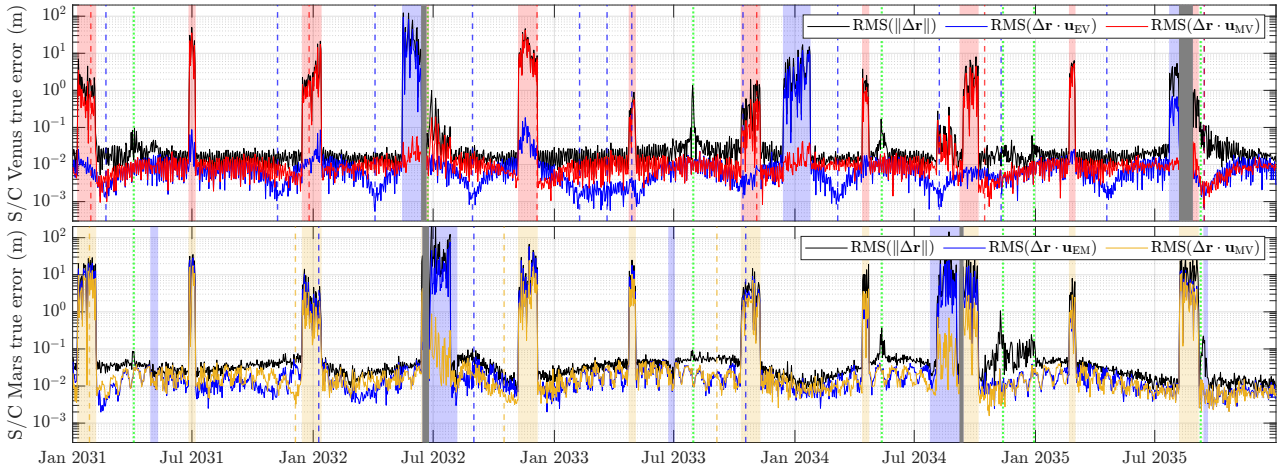

Figure 7.19: True errors of spacecraft orbit determination at the last iteration of Algorithm 6 for the simulation settings of subcase 3 (3 cm ILR random error).

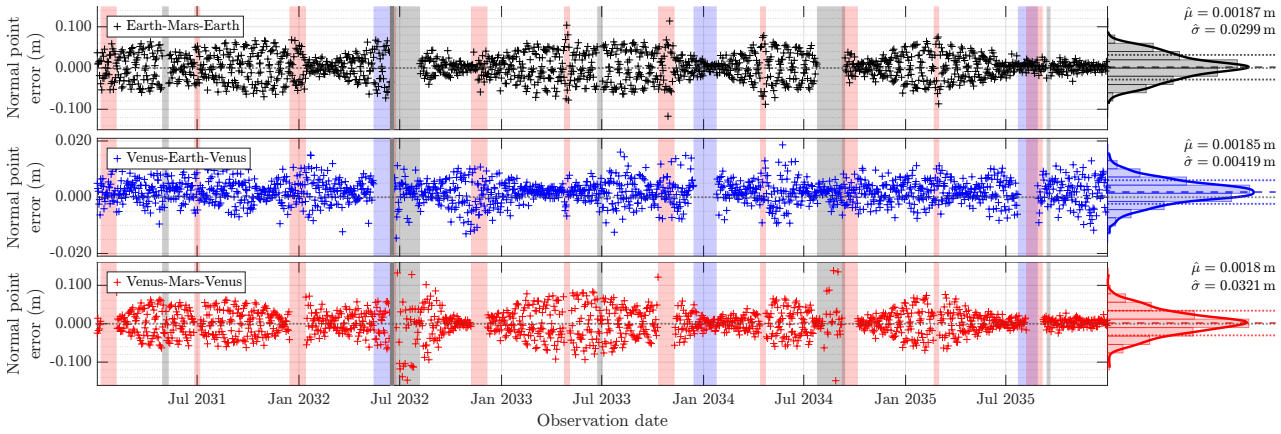

Figure 7.20: True errors in the planet-to-planet ranges generated at the last iteration of Algorithm 6 for the simulation settings of subcase 3 (3 cm ILR random error).

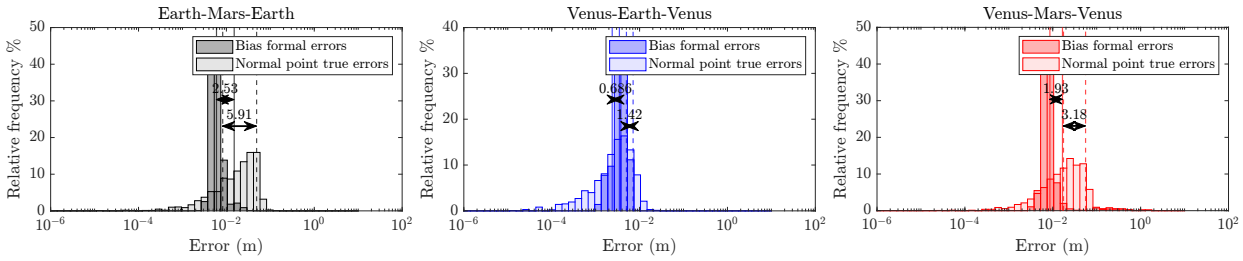

Figure 7.21: Distribution of true errors in the planet-to-planet ranges generated at the last iteration of Algorithm 6, compared to the formal errors of the fitted biases, for the simulation settings of subcase 3 (3 cm ILR random error).

spacecraft orbit determination error during episodes at which only one of the range constraints is available is contained to the cm level as a result of the *a priori*. This evinces both the correct behaviour of the *a priori* constraint in the batch filter (equation 4.53) and also how the true errors achieved by the two ranging links simultaneously do indeed outperform the results of a hypothetical orbit determination accurate to 1 cm in position components.

Again, one noticeable difference between this subcase and the nominal one is that the true errors of the normal points are seen to be centered at a different value: in this subcase, the systematic error of the ILR system has been set to 2.3 mm.

Modified subcase 5 (iteration 3)

Finally, the last of the modified subcases in the sensitivity analysis (section 4.2 in Part IV) consists of placing the Martian spacecraft closer to the surface of the planet with the aim of allowing orbit determination arcs to span at least one full

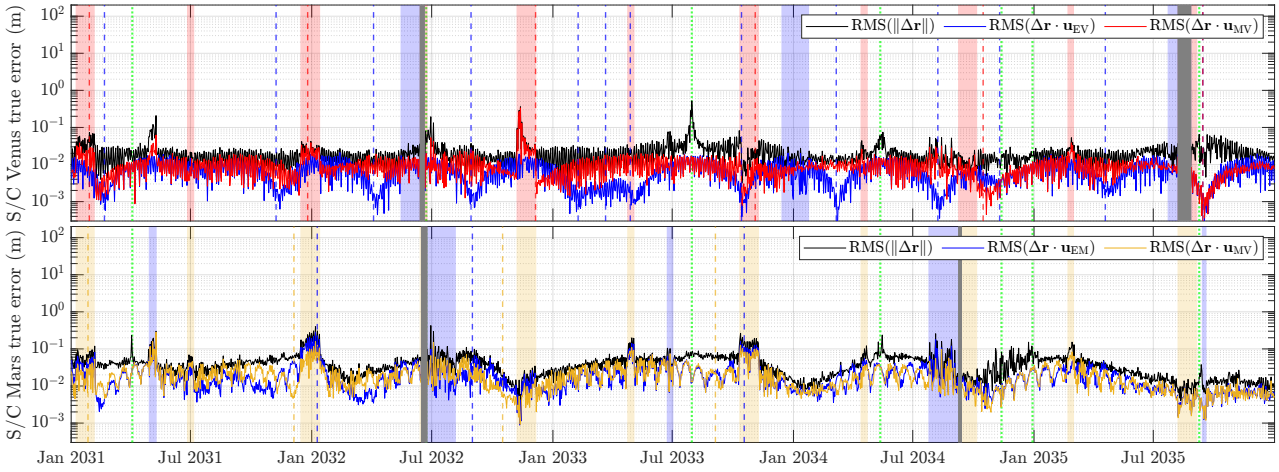

Figure 7.22: True errors of spacecraft orbit determination at the last iteration of Algorithm 6 for the simulation settings of subcase 4 (1 cm *a priori* spacecraft position uncertainty)

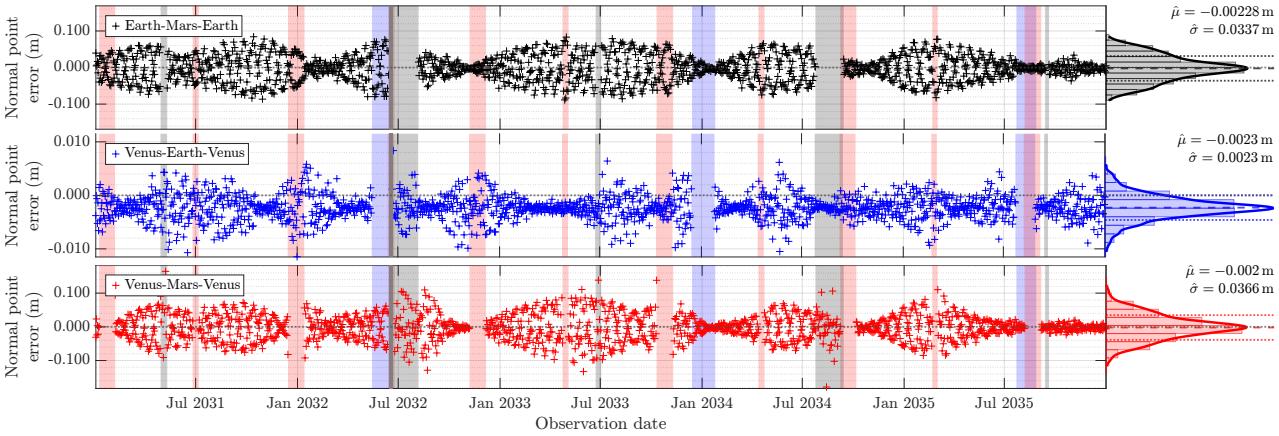

Figure 7.23: True errors in the planet-to-planet ranges generated at the last iteration of Algorithm 6 for the simulation settings of subcase 4 (1 cm *a priori* spacecraft position uncertainty).

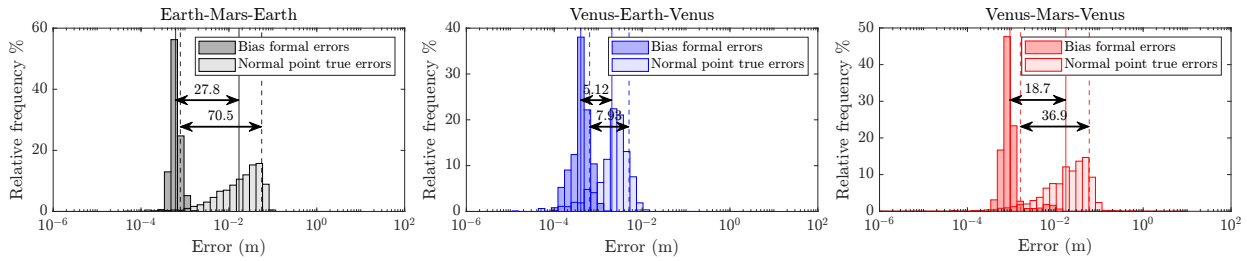

Figure 7.24: Distribution of true errors in the planet-to-planet ranges generated at the last iteration of Algorithm 6, compared to the formal errors of the fitted biases, for the simulation settings of subcase 4 (1 cm *a priori* spacecraft position uncertainty).

revolution. The corresponding results can be seen in Figures 7.25-7.27.

The results evince how the spacecraft orbit determination errors of the Martian spacecraft become more comparable to those of the Venusian one (Figure 7.25) than in the nominal case (Figure 5 in Part IV). As described in section 4.2.2 of Part IV, this has the effect of an overall improvement in the produced normal points (Figure 7.26), although not as much as in the case where all orbital periods are set to 12 hours. This evinces how making all orbital periods exactly match the length of the orbit determination arcs is beneficial, although the extent to which this is only due to our assumptions of unmodeled accelerations following the spacecraft orbital period remains to be tested. in this subcase, the constant bias added to the ILR observations has been set to 0.85 mm.

Perhaps more notably, the orbit determination errors of the Venusian spacecraft (Figure 7.25) are found to be worsened with respect to the nominal case (Figure 5 in Part IV), although its orbital configuration has not been modified in this

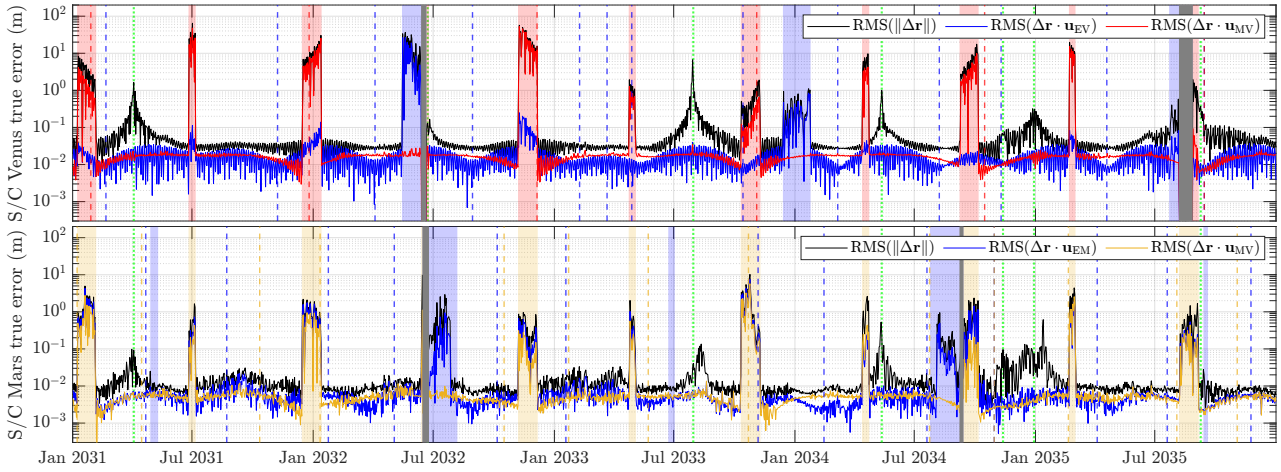

Figure 7.25: True errors of spacecraft orbit determination at the last iteration of Algorithm 6 for the simulation settings of subcase 5 (Mars spacecraft at lower altitude).

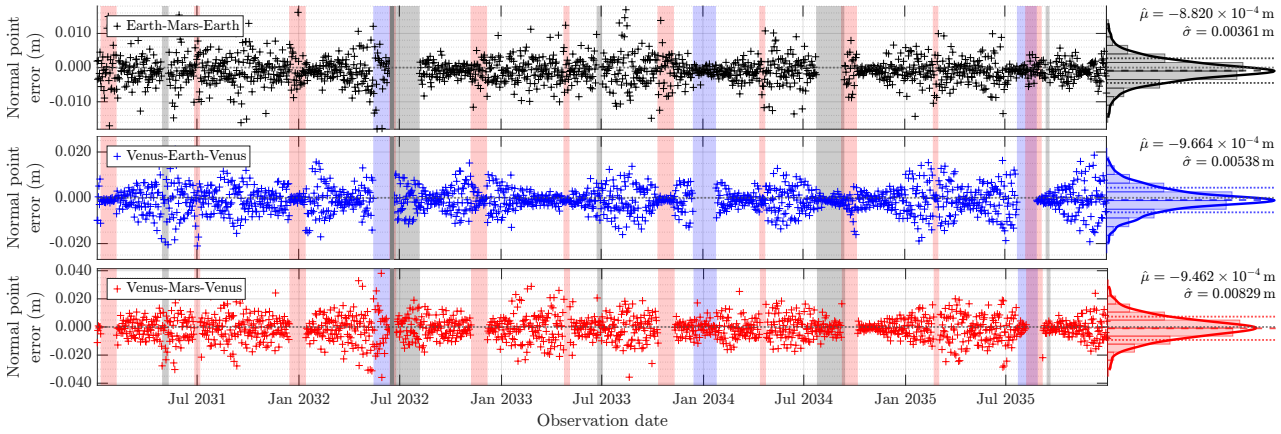

Figure 7.26: True errors in the planet-to-planet ranges generated at the last iteration of Algorithm 6 for the simulation settings of subcase 5 (Mars spacecraft at lower altitude).

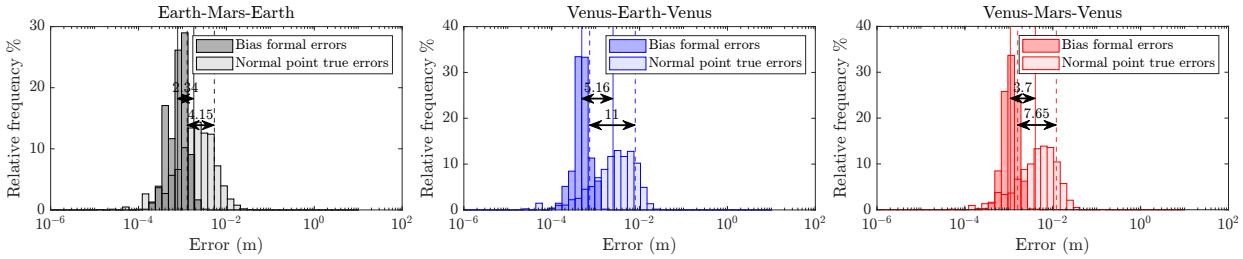

Figure 7.27: Distribution of true errors in the planet-to-planet ranges generated at the last iteration of Algorithm 6, compared to the formal errors of the fitted biases, for the simulation settings of subcase 5 (Mars spacecraft at lower altitude).

subcase. This evinces how the presence of the enclosed interplanetary links makes all orbit determinations dependent on each other, and the configurations that allow to maximize their potential must be searched in a joint rather than individual manner.

7.3. Verification

The implemented simulation makes use of the available propagation and estimation modules available in Tudat, which have been already verified and validated in the past. The verification step of this work has therefore consisted of checking the propagation to yield to the expected orbits and observation links, and assessing the results of a simplified spacecraft orbit estimation case using Doppler observations and no dynamical mismodeling. These are presented, respectively, in

sections 7.3.1 and 7.3.2.

7.3.1. Orbit geometry and interplanetary links

As a verification of the orbits resulting from the employed propagation settings, the interplanetary links used to generate ranging and Doppler observations have been plotted in Figure 7.28 and Figure 7.29. It is immediate to observe how

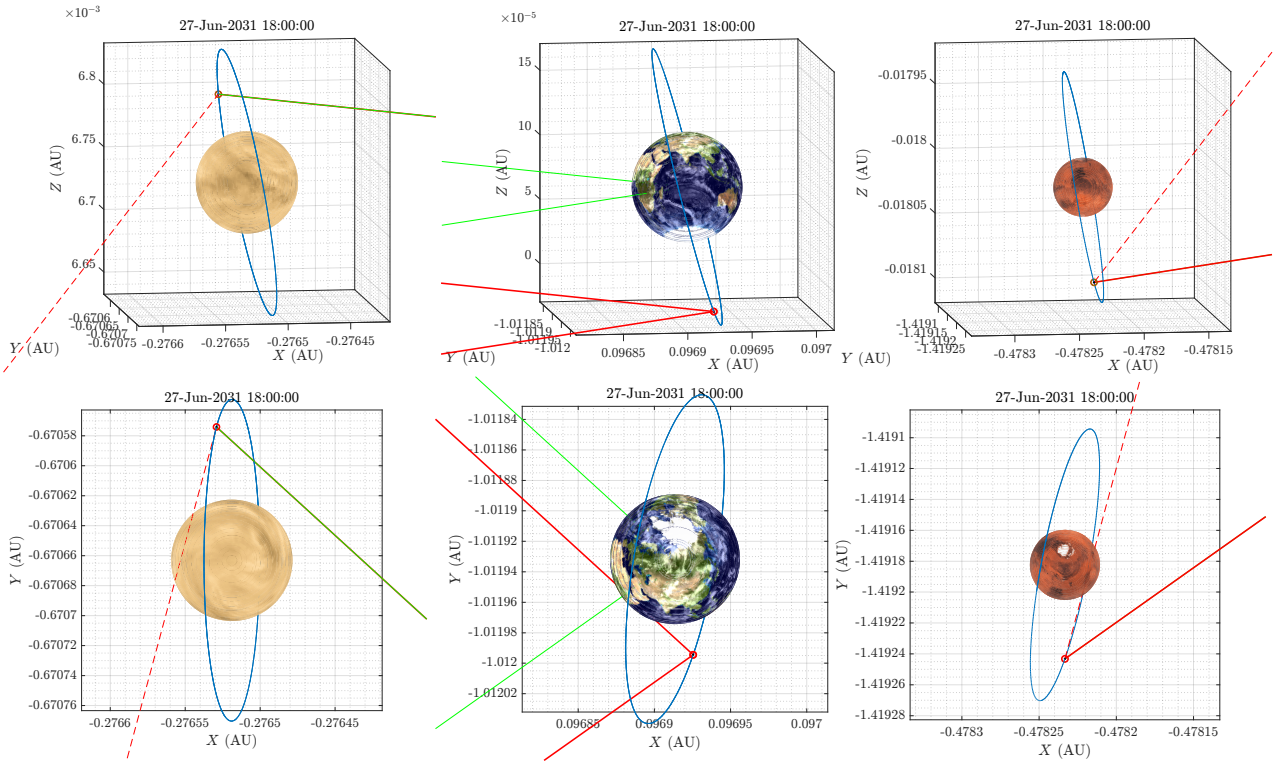

Figure 7.28: Geometry of the interplanetary links and spacecraft orbits on June 27th 2031 (Figure 2.1 left). Red: ILR links; Green: Doppler links.

the planetary positions in the XY plane coincide with those displayed in Figure 2.1. Given the fact that Figure 2.1 is generated from data given by MATLAB's `planetEphemeris` function, which is implemented independently from Tudat, this serves as a confirmation that the implemented simulation behaves as expected.

The orientations of the different interplanetary links are consistent with Figure 2.1, as evinced by the top views in Figure 7.28 and Figure 7.29. The ILR links are plotted in red from spacecraft to spacecraft, whereas Doppler links are plotted in green from the center of the Earth to the spacecraft. All links are plotted at the mid epoch of the corresponding orbit determination arcs, which span from noon to midnight every day. The function implemented to plot the observation links checks whether or not the assessed instant is between (or member of) consecutive observation times (i.e., observation times separated by the observation cadence only), and only plots a solid line if it is the case. As observed in Figure 7.28, the Venus-Mars link is marked with a dashed line, which means there are no observations happening around the analyzed epoch. This is consistent with the Venus-Mars-Sun angle being smaller than 5°, as clearly seen in Figure 2.1. This is also consistent with the observation gaps shown in Figure 6.6, which confirms that the Sun avoidance viability function works as expected.

Additionally, the animation of Figure 7.28 and Figure 7.29 throughout the entire orbit determination arcs allows to check the proper behavior of the function checking observation viability due to planetary occultation. This verification exercise allowed to find and patch a bug in the internal Tudat function applying this computation, as described in more detail in appendix D.1.

7.3.2. Spacecraft orbit estimation with Doppler

The main addition between the "planets-only" implementation (chapter 6) and the final implementation (section 7.2) is the set of Doppler measurements (subsection 3.3.4) to the two interplanetary orbiters, which not only support the orbit determination together with ILR but are capable to support such orbit determination on their own. To test the correct behavior of the implemented modules that introduce such observations, a full spacecraft orbit determination of

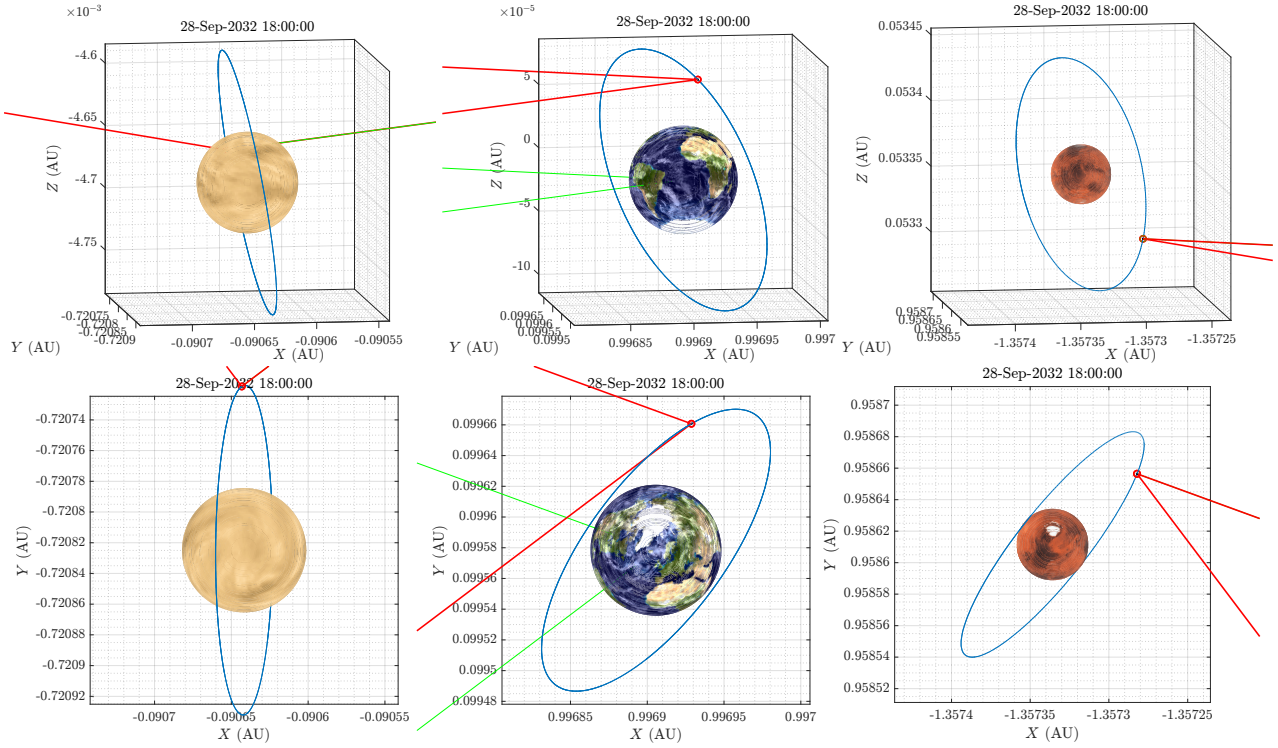

Figure 7.29: Geometry of the interplanetary links and spacecraft orbits on September 28th 2032 (Figure 2.1 right). Red: ILR links; Green: Doppler links.

the spacecraft around Venus and Mars is presented below. The simulation settings have been taken equal to those of the nominal simulation case (Table 2 in Part IV), except for the lack of ILR and the fact that no discrepancy between the true and estimation dynamical models has been introduced. This is implemented in the `sc_multi_arc_estimation.py` script, which just as the implementation of the main algorithm is also based on the `MainSimulationClass`.

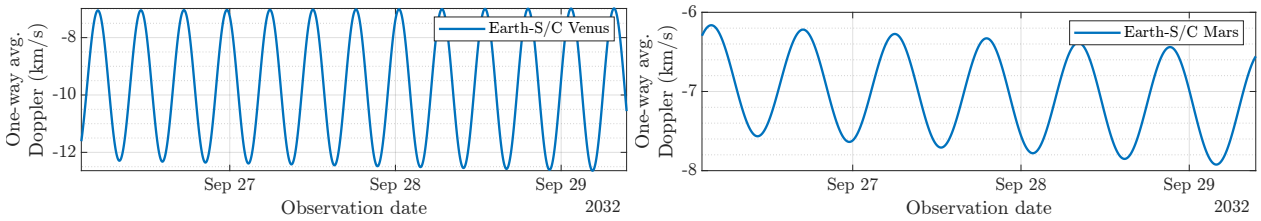

Figure 7.30: One-way averaged range-rate (Doppler) observations to the Venus (left) and Mars (right) spacecraft around September 28th 2032.

The range-rate observations to the Venus and Mars spacecraft obtained around September 28th 2032 (Figure 2.1 right; Figure 7.29) are shown in Figure 7.30. Each curve clearly shows the result of adding a fast oscillation that coincides with each spacecraft's orbital period on top of the much more slowly varying relative velocity between planets along their line of sight. These can be easily verified by assuming circular and coplanar orbits for the planets: the relative distance between, for instance, Earth and Venus, and its corresponding time derivative are

$$d_{\mathrm{EV}} = \sqrt{a_V^2 + a_E^2 - 2a_V a_E \cos(\theta)}, \tag{7.14}$$

$$\frac{\mathrm{d}d_{\mathrm{EV}}}{\mathrm{d}t} = \frac{a_V a_E \dot{\theta} \sin(\theta)}{\sqrt{a_V^2 + a_E^2 - 2a_V a_E \cos(\theta)}}, \tag{7.15}$$

where θ is the relative angle between their position vectors and a stands for their orbital semimajor axes. Since their relative angle is simply their difference in angular positions with respect to a common origin, its time derivative is simply

their difference in angular velocities or mean motions:

$$\dot{\theta} = n_E - n_V = \sqrt{\frac{\mu_\odot}{a_V^3}} - \sqrt{\frac{\mu_\odot}{a_E^3}}. \tag{7.16}$$

At the first epoch of the arc presented in Figure 7.30, the relative angle Earth-Sun-Venus is $\theta = 104.5°$ (see Figure 2.1 right). Taking $\mu_\odot = 1.327124 \times 10^{11}$ km^3/s^2, $a_V = 1.08210 \times 10^8$ km and $a_E = 1.49598 \times 10^8$ km[1],

$$\frac{\mathrm{d}d_{\mathrm{EV}}}{\mathrm{d}t} = \frac{a_V a_E}{\sqrt{a_V^2 + a_E^2 - 2a_V a_E \cos(\theta)}} \left(\sqrt{\frac{\mu_\odot}{a_V^3}} - \sqrt{\frac{\mu_\odot}{a_E^3}} \right) \sin(\theta) = -9.50\,\mathrm{km/s}, \tag{7.17}$$

which coincides with the average value of range rate during the early epochs of the arc (Figure 7.30 left). The high frequency oscillation is caused by the spacecraft orbit, which orbits at 10000 km above Venus' surface. Its velocity gets projected to the range-rate measurement from Earth with the cosine of the angle between its orbital plane and the Doppler observation link. At the first instant of the orbit arc displayed in Figure 7.30, this angle is 54.7°, as given by

$$\varphi = \arcsin\left(\frac{(\mathbf{r}_{\mathrm{S/C\,V}} \times \mathbf{v}_{\mathrm{S/C\,V}}) \cdot (\mathbf{r}_{\mathrm{V}} - \mathbf{r}_{\mathrm{E}})}{\|\mathbf{r}_{\mathrm{S/C\,V}} \times \mathbf{v}_{\mathrm{S/C\,V}}\| \|\mathbf{r}_{\mathrm{V}} - \mathbf{r}_{\mathrm{E}}\|} \right). \tag{7.18}$$

The expected velocity oscillation can be then computed from the orbital velocity of the spacecraft around Venus. Taking $\mu_V = 324860$ km^3/s^2 and $R_V = 6051.8$ km, together with the orbital altitude $h_{\mathrm{S/CV}} = 10000$ km, this results in

$$A = \sqrt{\frac{\mu_V}{R_V + h_{\mathrm{S/C\,V}}}} \cos(\varphi) = 2.60\,\mathrm{km/s}. \tag{7.19}$$

As seen in Figure 7.30, this coincides with the amplitude of the oscillation around -9.50 km/s (equation 7.17) at the initial instant of this particular orbit arc. It can therefore be safely concluded that the Doppler observations coincide with the expected values for the problem under study, which supports the correct implementation of the simulations employed.

These range-rate observations are thus used in a covariance analysis and full estimation of the spacecraft initial states. The propagation of the resulting covariance (equation 4.55) yields the formal errors through time displayed in Figure 7.31, whereas the correlations between the estimated parameters are shown in Figure 7.32.

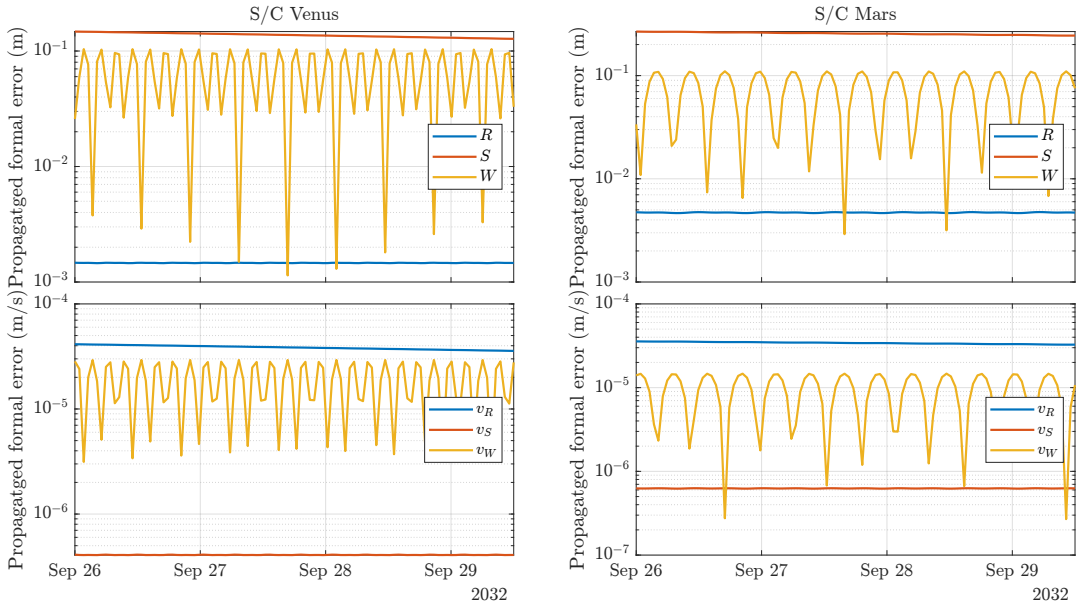

Figure 7.31: Propagated formal errors of the resulting orbit determination of the spacecraft around Venus (left) and Mars (right) during the orbit arc displayed in Figure 7.30.

The level of obtained formal errors can be verified against similar cases in published literature. If these simulations had been conducted through new implemented software, this verification should consist of reproducing the exact settings of a

[1] https://nssdc.gsfc.nasa.gov/planetary/factsheet/venusfact.html

reference case to be used as a benchmark. Instead, since the orbit estimation modules in Tudat have already been verified in the past, this is only used as a confirmation that the results are consistent with the expected order of magnitude and behaviour. Cappuccio et al. (2020, Fig. 7), for instance, present similar curves to Figure 7.31 for the orbit determination of JUICE around Ganymede, also obtained with Doppler measurements at 60 seconds of integration time and a gaussian noise of 0.012 m/s. Their reported uncertainties are written as 3-σ levels, and come from having used $\sim$10 times less observations due to shorter arc and ground station constraints. Hence, their results must be scaled by $1/(3\sqrt{10})$ to be comparable. Doing so, we get consistent values of few mm uncertainties for the radial (R) position, and $\sim$ 10 cm uncertainties for along-track (S) and cross-track (W) positions.

The behavior of the propagated formal errors through time is also consistent, showing that of the along-track direction flat above the other two and that of the cross-track direction presenting a clear oscillation with half the spacecraft orbital period. This means that the uncertainty ellipsoid remains roughly constant in the RS plane whereas it shrinks and grows twice every cycle in the W direction. Orbital mechanics are responsible for this behavior: an orbiting particle with a perturbation in the S direction of its initial state will remain ahead or behind its unperturbed counterpart until new perturbations come into play, whereas a perturbation in the W direction will cause a perturbed orbit with a different inclination that will still intersect the original one twice per revolution. A perturbation in the R direction will cause progressive separation in the S direction due to a difference in velocity, yet the effect is still insignificant at the level of formal error and arc length shown in Figure 7.31, hence its constant appearance.

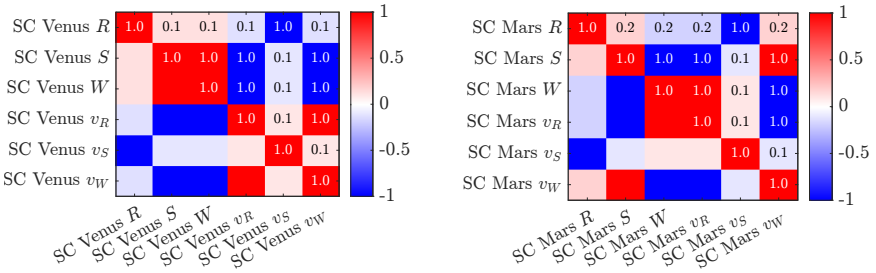

Figure 7.32: Correlation matrix of the estimated initial state of the spacecraft around Venus (left) and Mars (right) after the orbit determination arc displayed in Figure 7.30.

This behavior is also consistent with the resulting correlation matrices displayed in Figure 7.32: the direct relationship between along-track velocity v_S and radial position R is materialized in a high correlation coefficient between the two variables. Although the exact correlation mapping between the different components of the initial state can be sensitive to nuances such as the small eccentricity of the orbit or the gravity field perturbations introducing cross dependencies, a resulting correlations matrix showing high correlations between most initial state components is consistent with what can be found in literature (e.g., X. Zhu et al., 2021, Fig. 5), including a significantly less correlated radial component.

The observation residuals resulting of the orbit determination process with Doppler observations alone are presented in Figure 7.33 and Figure 7.34. It can be clearly observed how, after convergence, they present a Gaussian behaviour with a standard deviation corresponding to the 0.012 mm/s used as Doppler random noise, confirming that the estimator has converged to a solution that minimizes the cost function as expected from the observations used.

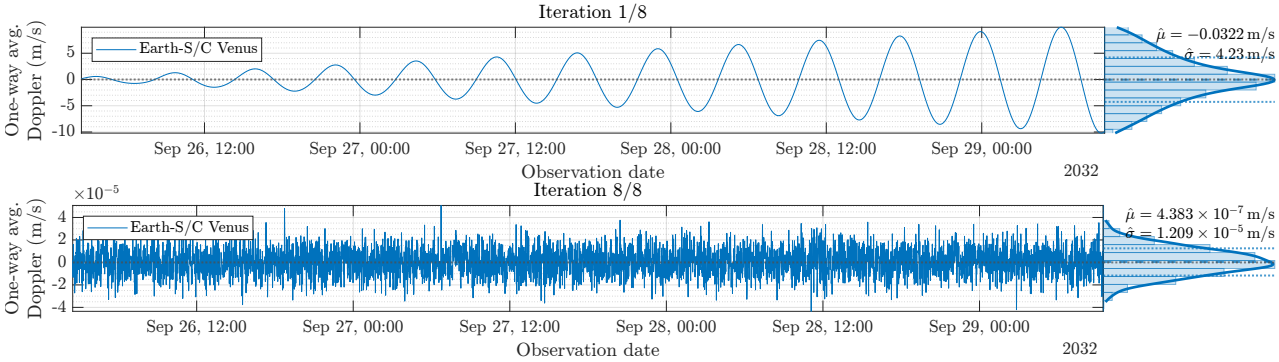

Figure 7.33: Pre- and post-fit estimation residuals corresponding to the initial state estimation of the spacecraft around Venus during the orbit arc displayed in Figure 7.30.

The batch filter estimator has been run for 8 iterations, although not all of them are required to reach the final solution.

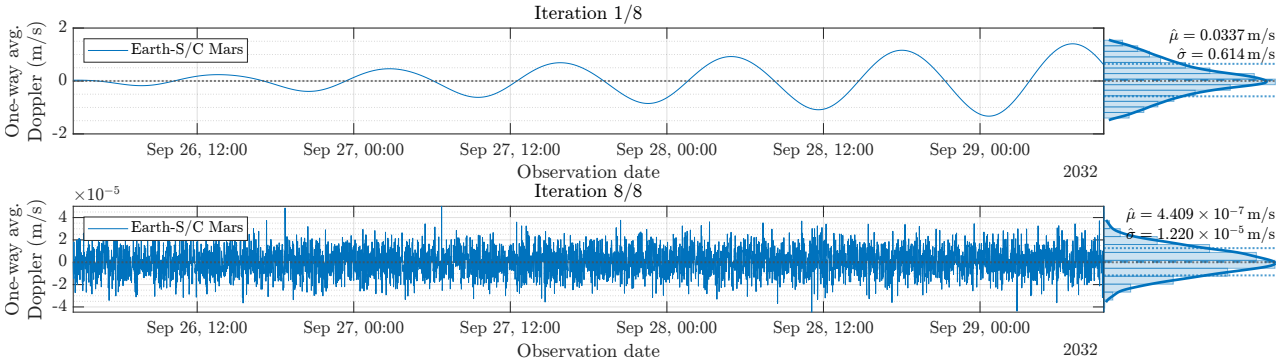

Figure 7.34: Pre- and post-fit estimation residuals corresponding to the initial state estimation of the spacecraft around Mars during the orbit arc displayed in Figure 7.30.

As the convergence curves for the individual components of the estimated intitial states evince in Figure 7.35, 3 iterations are enough to reach the final levels of true errors. Further iterations leave the solution essentially equal to the found value that minimizes the cost function, slightly off from the true solution due to the stochastic imperfections introduced by the measurement noise (Figures 7.34 and 7.33).

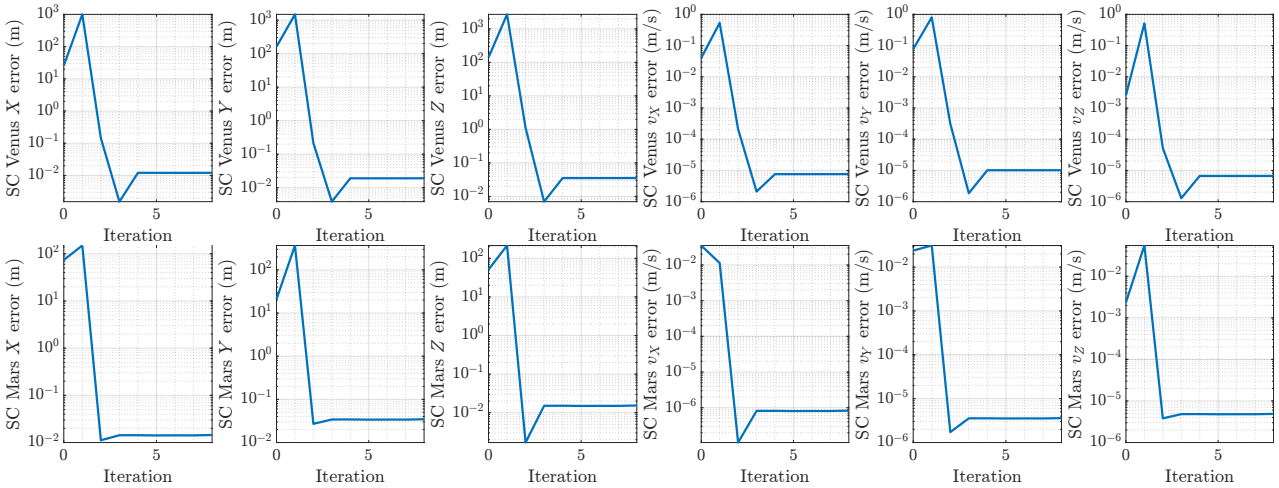

Figure 7.35: Convergence (error per iteration) during the application of the batch estimation algorithm (Algorithm 1) for the orbit estimation of the spacecraft around Venus (top) and Mars (bottom) for the orbit arc displayed in Figure 7.30.

The inherent uncertainty remaining in the estimated solution, caused by the observation noise and described by the post-fit covariance matrix and the corresponding formal errors (Figure 7.31), leads the estimated solution to be imperfect and cause a discrepancy between the true and the estimated trajectories. This is plotted in Figure 7.36. The behavior of the true error in the three position directions is consistent with the behavior described above for the formal errors, i.e., flat along-track error and cross-track error oscillating with half the spacecraft orbital period. The oscillation observed in the true errors of the radial direction are likely due to the fact that the frame conversion applied to generate Figure 7.36 has been performed with the RSW frame history given by the estimated solution, which is slightly rotated from the true one used in Figure 7.31.

In this simplified estimation scenario where the only source of estimation error is the random noise of the Doppler observations, which is properly modeled (equation 4.33) by means of the weight matrix used in the batch least squares filter (Algorithm 1), the formal errors are expected to be the true statistical distribution that defines individual realizations of true errors. To verify whether or not this is consistent with the observed behavior, the distribution of component-wise true-to-formal error ratios must be assessed to match a normal distribution of mean $\mu = 0$ and standard deviation $\sigma = 1$. Such distributions, combining the aggregate true-to-formal error ratios of all estimated orbit arcs, are displayed in Figure 7.37. Both the results for the Venus and Mars orbit determinations are consistent with standard normal distributions, hence we assess this test to confirm the correct behavior of the implemented simulation setup.

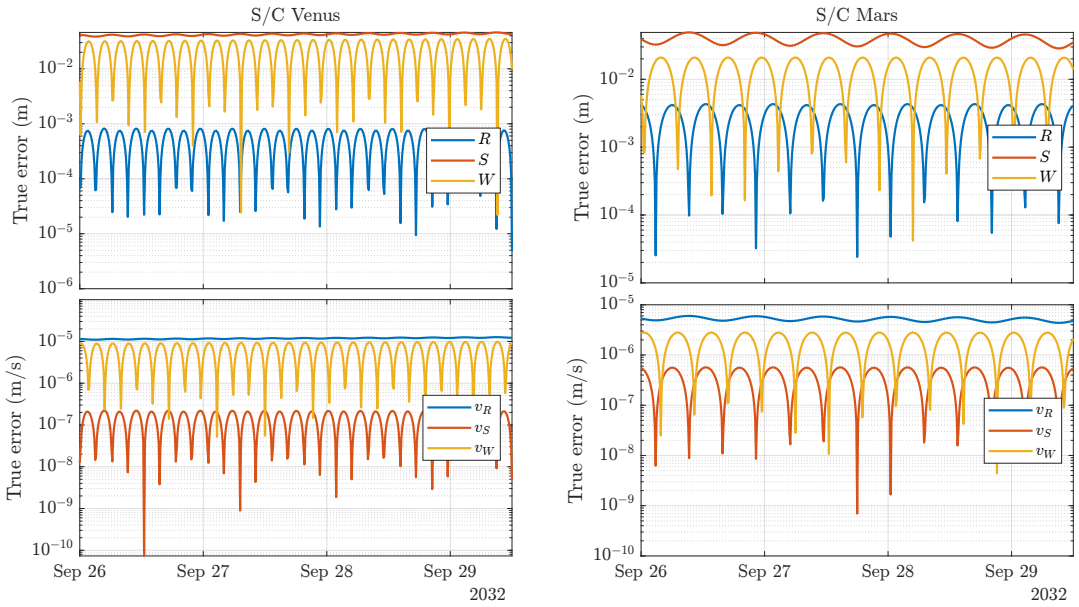

Figure 7.36: True errors of the estimated trajectory of the Venus (left) and Mars (right) spacecraft during the orbit arc from Figure 7.30.

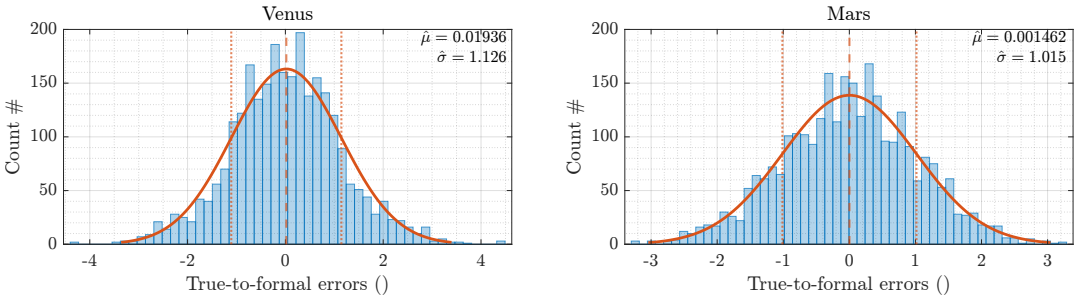

Figure 7.37: Distribution of all true-to-formal errors after estimating the initial states of 520 independent orbit arcs of the Venus and Mars spacecraft.

Part IV

Paper preprint

Improving planetary ephemerides and asteroid mass estimations with a triple-enclosed Interplanetary Laser Ranging system in the inner Solar System

L.R. Busquets[1,2]

[1] Department of Space Engineering, Faculty of Aerospace Engineering, TU Delft
Kluyverweg 1, 2629 HS Delft, Netherlands
[2] Colorado Center for Astrodynamics Research, Ann and H.J. Smead Aerospace Engineering Sciences, CU Boulder
3775 Discovery Dr, 80303 Boulder, CO

ABSTRACT

Context. Our current knowledge of Solar System dynamics is limited by a combination of unknowns, including the masses of most asteroids, the mass loss rate and oblateness of the Sun, and the potential presence of unknown trans-Neptunian objects. Interplanetary laser ranging has been suggested as a useful technology to address these uncertainties by enabling range measurements between planets at unprecedented accuracy, from which different dynamical phenomena can be reconstructed.
Aims. Following the mission proposal by the name of Trilogy, we simulate a triple interplanetary laser ranging setup obtaining frequent range measurements between space-based transceivers orbiting the Earth, Mars and Venus over five years. We simulate the generation of normal points from the orbit determination of the spacecraft and we use them to assess the extent to which the current uncertainties of planetary ephemerides and asteroid masses can be reduced.
Methods. Starting from reasoned assumptions on the true errors of current planetary ephemerides, we simulate the fitting of range biases during simultaneous spacecraft orbit determination that can account for such discrepancy. These biases allow the generation of precise planet-to-planet ranges, which are then used in a batch estimation of planetary ephemerides and asteroid gravitational parameters.
Results. We find that the presence of the range constraint from different directions can significantly reduce the orbit determination error of the interplanetary orbiters, containing them to the centimeter level and achieving to produce millimeter-accurate normal points as long as the orbit determination is averaged over at least one revolution and there are no significant force model errors corrupting the estimated spacecraft trajectories. The resulting planet-to-planet range measurements are found capable of estimating the radial positions of the three planets with millimetric true errors, whereas cross-track positions and asteroid masses are observed to improve more modestly, failing to reduce current uncertainty levels in a significant way. The number of asteroids found to get their true mass errors significantly reduced is found to be in the order of tens.
Conclusions. The usage of highly accurate range measurements to interplanetary spacecraft in different spatial directions has the potential of significantly improving interplanetary orbit determination and producing highly accurate planet-to-planet ranges. Although we confirm millimetric interplanetary ranges to be achievable, we find how the spacecraft orbit determination clearly limits their achievable precision under the tested approach, and we suggest that other mission architectures (e.g., including a highly inclined vertex) and/or more complex estimation methods (e.g., coupled, constrained multi-arc) shall be explored to maximize the scientific output of a Trilogy-like mission.

Key words. interplanetary laser ranging – ephemerides – normal points – asteroids – Solar System mass distribution

Contents

1. Introduction

Modern computations of planetary ephemerides typically include the estimation of several different unknowns besides the orbits of celestial bodies. Different examples related to active research fields include solar parameters such as the variation of its gravitational parameter $\dot{\mu}_\odot$ (Pitjeva et al. 2021; Fienga et al. 2015; Pitjeva & Pitjev 2012) or its gravitational oblateness $J_{2,\odot}$ (Fienga et al. 2019a; Genova et al. 2018; Park et al. 2017; Pitjeva 2015), dynamical perturbations caused by the mass distribution of Trans-Neptunian Objects (TNOs; di Ruscio et al. 2020; Fienga et al. 2020b; Pitjeva & Pitjev 2018) and asteroids (Pitjeva & Pitjev 2015; Liu et al. 2022), or relativistic parameters in search for violations of General Relativity (GR; Bernus et al. 2020; Mariani et al. 2023). A key contributor to the sets of observations that enable such calculations are range measurements to interplanetary spacecraft (section 2.1.1).

The Trilogy mission concept was proposed by Smith et al. (2018) with the aim of obtaining precise enough range measurements between Venus, the Earth and Mars to measure the expansion of the Solar System. This expansion is caused by the variation of the gravitational parameter of the Sun, $\dot{\mu}_\odot$, which causes planetary orbits to increase their semimajor axis (Pitjeva & Pitjev 2012). An accurate measurement of this magnitude would not only shed light to the currently poorly understood cycle of solar mass loss (Pinto et al. 2011; Pitjeva et al. 2021), which is essential for the understanding of the solar interior (Christensen-Dalsgaard 2021) and the predictions of future solar activity (Nandy et al. 2021), but it could also reveal deviations from GR by measuring a $\dot{\mu}_\odot$ consistent with a non-constant gravitational constant, i.e., $\dot{G} \neq 0$ (Will 2014). Despite the technical challenge of accurately measuring the small signatures in interplanetary ranges caused by $\dot{\mu}_\odot$, these are within the theoretical limits of measurement accuracy achievable by Interplanetary Laser Ranging (ILR; Degnan 2002; Dirkx 2015; Dirkx et al. 2019).

Subsequent studies analyzing the mission concept followed the original proposal. Cascioli et al. (2019) confirmed the potential of the enclosed ranging triangle concept to reduce the present uncertainties in $\dot{G}$ and Parametrized Post-Newtonian (PPN) parameters (Hohmann 2021); Bills & Gorski (2022) demonstrated how the combination of measurements from the three ranging legs can help locate sources of gravitational attraction via trilateration; and Bills & Skillman (2022) highlighted the potential of Trilogy as a planetary gyroscope to measure the rotation of the Solar System better than current techniques. Finally, preliminary calculations by Fienga (2023a), simulating the resulting covariance of the INPOP planetary ephemerides (Fienga et al. 2021) when using Trilogy measurements, found an expected significant improvement in the formal errors of asteroid masses and concluded the mission to have great potential for a better understanding of the mass distribution of the Solar System. Despite the preliminary nature of all these results, the community has acknowledged the potential of the Trilogy mission and it is being considered in multiple reviews of future prospects of planetary and fundamental physics research (Asmar et al. 2021; Bassi et al. 2022; Fienga & Minazzoli 2024).

With the aim of putting past studies together and defining future efforts, the Interplanetary Laser Trilateration Network (ILTN) Workshop was held in February 2023[1]. The final minutes detailed that higher fidelity simulations of the mission were required to further assess the expected quality of the science output. The aim of this study is to make a contribution in this regard by simulating not only the result of using highly accurate planet-to-planet ranges but a fuller pipeline of an operational scenario, starting from the obtention of range measurements between spacecraft affected by not-fully-modeled orbital perturbations.

Despite the original conception of the mission by Smith et al. (2018) was focused on measuring the variation of the solar gravitational parameter, we expect this science objective to be challenging to assess without a thorough improvement in our understanding of the mass distribution of the Solar System: the expected signature of $\dot{\mu}_\odot$ to interplanetary ranges is expected to be smaller than the one corresponding to the uncertainties of many masses (section 2.1.2), and it has been in fact shown how the estimation of asteroid gravitational parameters does degrade the fitting of $\dot{\mu}_\odot$ due to their high correlations (Pitjeva et al. 2021; Fienga et al. 2015). A similar story happens with PPN parameters, since uncertainties in Solar System masses have been found to significantly degrade the fitted solutions (De Marchi et al. 2016). As per the assessment of the Solar System rotation (Bills & Skillman 2022), we judge it to be a science objective less relevant than the understanding of mass distribution, given its virtual lack of effect into the fitting of $\dot{\mu}_\odot$ and GR parameters from ephemerides, and especially given the last advancements (Liu et al. 2023) that constrain the current error of planetary ephemerides reference frames to the sub-milliarcsecond level. With this in mind, we focus this study on the estimation of planetary ephemerides and asteroid masses from Trilogy observations with the aim of assessing if they would suffice to constrain mass uncertainties to the levels predicted by Fienga (2023a), who did not consider any spacecraft orbit determination errors.

The structure of this article is as follows: section 2 summarizes the state of the art of planetary ephemerides, our understanding of the mass distribution of the Solar System and ILR technology; section 3 describes the implemented simulation together with the settings and values used, based on the description given in the background section; and section 4 presents the results of the generated normal points and their usage in a batch estimation of planetary ephemerides and gravitational parameters of the main Solar System perturbers. Full results for the nominal scenario tested are presented in section 4.1, whereas alternative settings to assess the sensitivity to different design variables are summarized in section 4.2.

2. Background

This section summarizes the state of the art of the two main topics at play in this study: our knowledge of Solar System dynamics and our ability to conduct highly precise interplanetary range measurements via ILR. These are developed, respectively, in sections 2.1 and 2.2

2.1. Solar System dynamics

The most up-to-date knowledge of Solar System dynamics is described by planetary ephemerides, which are sets of tabulated data of the state vectors of the different Solar System bodies over time (Park et al. 2021; Fienga et al. 2021; Pitjeva et al. 2019). Modern models also include other parameters such asteroid masses and Kuiper Belt models, obtained as estimated parameters together with the planetary orbits. Such estimations are conducted by computing the planetary orbits that adjust best to a set of given observations (section 2.1.1). As of today, different models still present different values for such parameters and thus

[1] Slides and recordings available at https://grailteam.mit.edu/Trilateration

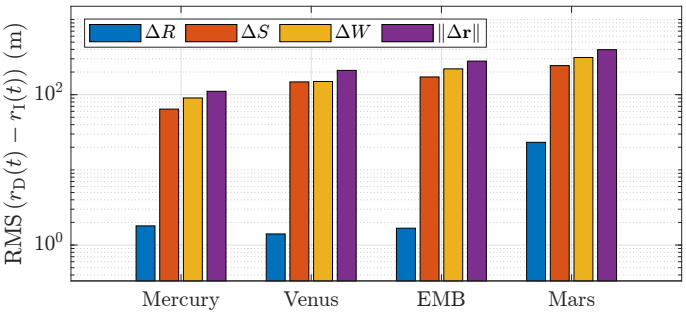

Fig. 1. Mean heliocentric position discrepancies in radial direction (R), along-track direction (S), cross-track direction (W) and norm of position vector difference for the planets of the inner Solar System when comparing DE440 and INPOP21a. Root mean square values computed between 2010 and 2040. EMB: Earth-Moon Barycenter.

desribe the Solar System dynamics in different manners. A good example for the impact of such model uncertainties can be found in the study by Farnocchia et al. (2021) when assessing the probability of Bennu impacting on Earth, who found that the usage of different ephemerides models resulted in uncertainties of order hundreds of kilometers in the Bennu-Earth miss distance. Uncertainties in solar parameters (i.,e., mass loss and oblateness), on the other hand, cause a 10-fold smaller error margin.

This section summarizes the state of the art of Solar System dynamics in two different sub-categories: uncertainties in planetary orbits themselves, developed in section 2.1.1, and uncertainties in the asteroid mass distribution, detailed in section 2.1.2.

2.1.1. Planetary ephemerides

The three main ephemerides models being independently developed and updated are the Developmental Ephemerides (DE) by JPL (Park et al. 2021), the Intégrateur Numérique Planetaire de l'Observatoire de Paris (INPOP) ephemerides by the Institute of Celestial Mechanics and Ephemerides Calculations (IMCCE) in France (Fienga et al. 2021) and the Ephemerides of Planets and Moon (EPM) developed by the Institute of Applied Astronomy of the Russian Academy of Sciences (Pitjeva et al. 2019). It is worth mentioning the recent addition of the PETREL ephemerides (Tian 2023), which have been developed using DE as a benchmark.

Ephemerides are computed by fitting numerically integrated orbits to a set of different ground-based and space-based observations of celestial bodies (Park et al. 2021). This is typically done with least squares estimation techniques (section 3.1). Around two thirds of the measurements used for DE and INPOP are obtained through radio ranges to interplanetary spacecraft, and around one third are optical angular observations (Fienga 2023b; Park et al. 2021). Very-Long Baseline Interferometry (VLBI) has also been used in recent missions to track interplanetary spacecraft with increased accuracy (Duev et al. 2012; Jones et al. 2014; Gurvits et al. 2023), and highly-accurate angular observations obtained by this technique are also included in the fits of DE and INPOP, although accounting for <1% of total observations used (Fienga 2023b; Park et al. 2021). With the advent of ILR in future missions like Trilogy, more precise range observations to interplanetary spacecraft are expected to be used in the fits to decrease the formal errors and capture finer temporal signatures.

Figure 1 shows the root mean square (RMS) of the discrepancy over time between DE440 and INPOP21a, computed from their publicly available spice kernels. The analyzed period has been chosen to be centered at present day, to get a fair representation of current discrepancies, with an integration period of 30 years. This is assessed to be enough to average out any particular error signatures of individual orbit revolutions while not being large enough to be corrupted by the uncertainty of events too far in the future. As observed, both models agree within hundreds of meters to the positions of the inner Solar System planets. On the other hand, discrepancies with respect to EPM have been found to be larger (Wenxiao et al. 2021), whereas PETREL is reported to match DE to the centimeter level for decades as a result of its usage as reference (Tian 2023).

The intercomparison between different ephemerides models can be used as an indicator of their true errors (Dirkx 2015; Imperi et al. 2018). Given that they have been independently developed, the increasing agreement between DE and INPOP (Fienga et al. 2021) can indicate that the two are converging to the true solution of planetary motion, while EPM may be missing some nuance in its modeling. We judge this option to be more likely than EPM being the most correct, simply because of the majority criterion. Hence, we take the discrepancies reported in Figure 1 as a valid indicator of the order of magnitude of true errors of state of the art planetary ephemerides. It is true, however, that despite DE and INPOP are based on independently-developed dynamical models, the two share most of the observations from interplanetary missions used in their fits. Our judgement is therefore subject to the assumption that such used measurements are not significantly affected by systematic errors pushing the dynamical solutions of DE and INPOP off in a common manner, nor by any common mismodeling caused by erroneous dynamical phenomena defined equivalently in both of them.

2.1.2. Mass distribution

Among the >1 million objects listed in JPL's Small Body database[2], individual mass estimates only exist for around four hundred. These are mostly the main perturbers (i.e., heaviest asteroids), but the bulk of smaller asteroids is estimated to account for the remaining 10% of total mass of the asteroid belt (Pitjeva & Pitjev 2015). Improving current asteroid mass estimates and enlarging the catalog to smaller asteroids is particularly relevant for the understanding of the Solar System formation (Hestroffer et al. 2019), for planetary defense (Wie et al. 2017) and for potential future asteroid mining mission plans (Ferus et al. 2022).

Methods of asteroid mass estimation can be grouped into five categories (Fienga et al. 2020a), spanning a trade-off between higher accuracy and greater availability. The most accurate methods consist of directly measuring orbital motion around the asteroid (Carry 2012), either from a spacecraft or from a binary partner body, which allow to solve for its gravitational parameter via Kepler's third law. Another approach is to combine optical and radar observations to infer the non-gravitational acceleration caused by the Yarkovsky effect, from which the mass of the asteroid can be computed (Chesley et al. 2003, 2014). Finally, the most fruitful methods are the fitting of masses from observations of asteroid-asteroid perturbations or asteroid-planet perturbations.

The measurement of asteroid-asteroid perturbations, also known as the astrometric method (Galád & Gray 2002), consists of obtaining angular observations of asteroids during peri-

[2] https://ssd.jpl.nasa.gov/tools/sbdb_lookup.html

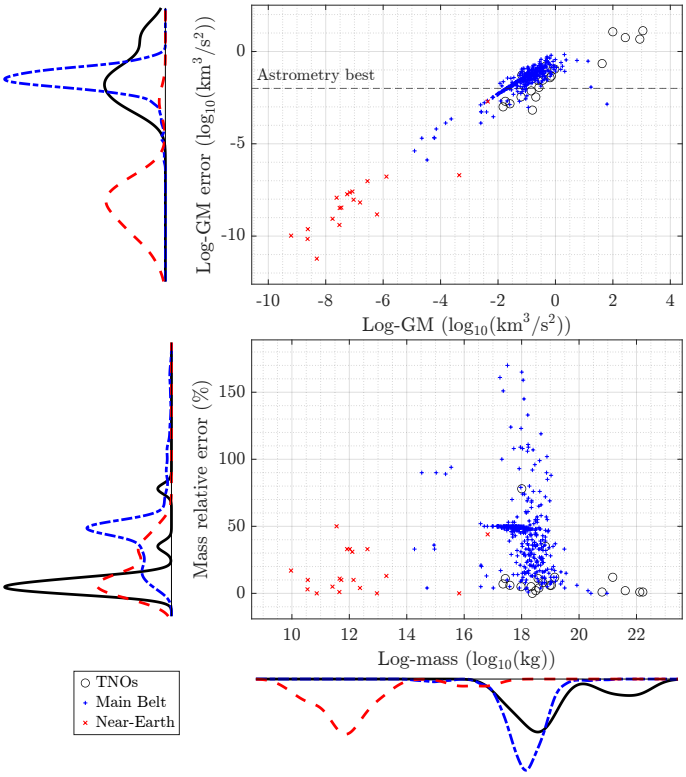

Fig. 2. Distribution of mass uncertainties for the objects with existing estimates. Data extracted from the SiMDA catalog (Kretlow 2020).

ods of close approaches to infer the mass of the heaviest from the observed trajectory deflection of the lighter[3]. This method relies on highly accurate astrometric observations of the asteroids during encounters, and ESA's Gaia mission (Gaia Collaboration 2016) has been a significant actor in this regard. Although the mission's data release DR2 was still found to involve significant challenges regarding the instrument's systematic errors (Deram et al. 2022; Murray 2023), the most recent data releases are already allowing mass estimations of improved accuracy (Li et al. 2023; Fuentes-Muñoz et al. 2024). A significant result is the recent mass estimation of (16) Psyche by Farnocchia et al. (2024), with a reported uncertainty of ±0.017 km^3/s^2. Mass estimates with uncertainty ranges of this same order of magnitude for most of the main perturbing asteroids are expected within the next years (Fuentes-Muñoz, 2024, priv. comm.). This is marked as the "astrometry best" boundary in Figure 2.

Finally, the estimation of asteroid masses from perturbations to the planetary motion is regularly conducted during the fits of planetary ephemerides (e.g., Folkner et al. 2014). The commonly accepted means of doing so is to introduce asteroid masses as parameters $\boldsymbol{p}$ to be estimated in a least squares problem (section 3.1), although this can result in some masses resulting negative if not properly constrained. To prevent this problem, Kuchynka & Folkner (2013) employed the Non-Negative least squares algorithm (Lawson & Hanson 1995), and Fienga et al. (2020a) introduced constraints of taxonomic class densities. The latter is representative of state-of-the-art asteroid mass estimation capabilities based on ephemerides fits, presenting 103 estimated masses with reported uncertainties lower than 33%. Despite this method is still unable to provide individual mass estimates for any other asteroids than the heaviest ~400, solid ring models (Liu et al. 2022) are used to absorb the effect of smaller asteroids and better model the influence of the complete Main Belt.

The different studies applying the different methods with different observations and different assumptions on the employed dynamical models have resulted in a list of many different estimated mass values for each of the main perturbing asteroids. Conveniently, Kretlow (2020) gathered all of them into a single catalog named Size, Mass and Density of Asteroids (SiMDA)[4][5], which also offers an average mass and an average formal uncertainty for each asteroid, resulting from combining all existing estimates with the Expected Value Method (Birch & Singh 2014). Despite the possible argument against combining all past estimates into a single uncertainty value due to the possible degradation of the result by mixing older and less precise estimations with newer and improved ones, the fact that this method is robust to outliers allows us to assume the reported average uncertainties in the SiMDA catalog to be a representative estimate of the true uncertainties of known asteroid masses.

The distribution of masses and uncertainties listed in the SiMDA catalog is displayed in Figure 2. It includes 19 Near-Earth asteroids, 377 Main Belt asteroids and 20 TNOs. It is clear to observe how most listed asteroids are around 10^{18} kg or 0.1 km^3/s^2. Smaller asteroids are notably less present, not because there are less of them in real life but because their masses have never been estimated. Regarding existing estimates, the distribution of relative errors in the bottom plot evinces how the bulk of main belt asteroids are estimated with uncertainties around 50%.

One can get an idea of the impact of these mass uncertainties to the individual asteroid signatures on the Trilogy ranging legs from the pre-fit signatures presented in Figure 3. Each curve is computed by subtracting the history of interplanetary lengths $l(t)$ after an numerical integration without (w/o) the asteroid from the history of $l(t)$ with (w/) it[6], starting from the same initial state and employing the same propagation settings as those described in section 3.3.1. It is immediate to observe how the legs that have Mars as one of the ends are significantly more perturbed than the Earth-Venus leg, just as expected as a result of the greater sensitivity of the Red Planet to the Asteroid Belt (Kuchynka & Folkner 2013). For these legs, is clear how mass uncertainties throughout most of the asteroid catalog map into range uncertainties in the order of a meter or larger. Some signatures—e.g., (15) Eunomia or (617) Patroclus—show a clear frequency component corresponding to the synodic period of the two leg ends (Earth-Mars: 2.14 years; Venus-Mars: 0.91 years).

It is worth comparing these figures with the pre-fit signatures to the Trilogy legs caused by the Solar mass loss, presented by Smith et al. (2018)—these also follow the synodic period of each planet pair, and present magnitudes of order one meter over a similar timespan. Some uncertainty ranges shown in Figure 3 are larger than these signatures themselves, and this can cause high correlations between the two magnitudes if estimated concurrently. This is consistent with Fienga et al. (2015) and Pit-

[3] The estimation of the two masses concurrently has also been studied (Baer & Chesley 2017), but the most recent studies still do not incorporate this method due to the associated accuracy challenges (Fuentes-Muñoz, 2024, priv. comm.).

[4] Accessible at https://astro.kretlow.de/simda/catalog/

[5] The following update is expected to come in late 2024 (Kretlow, 2024, priv. comm.)

[6] For every asteroid i, we observed these results to be essentially identical no matter if the followed approach is to subtract the propagation with all asteroids except for i from the propagation with all asteroids or to substract the propagation with no asteroids at all from the propagation with asteroid i only. This motivates the development of analytical approximations, although this is not within the scope of this paper.

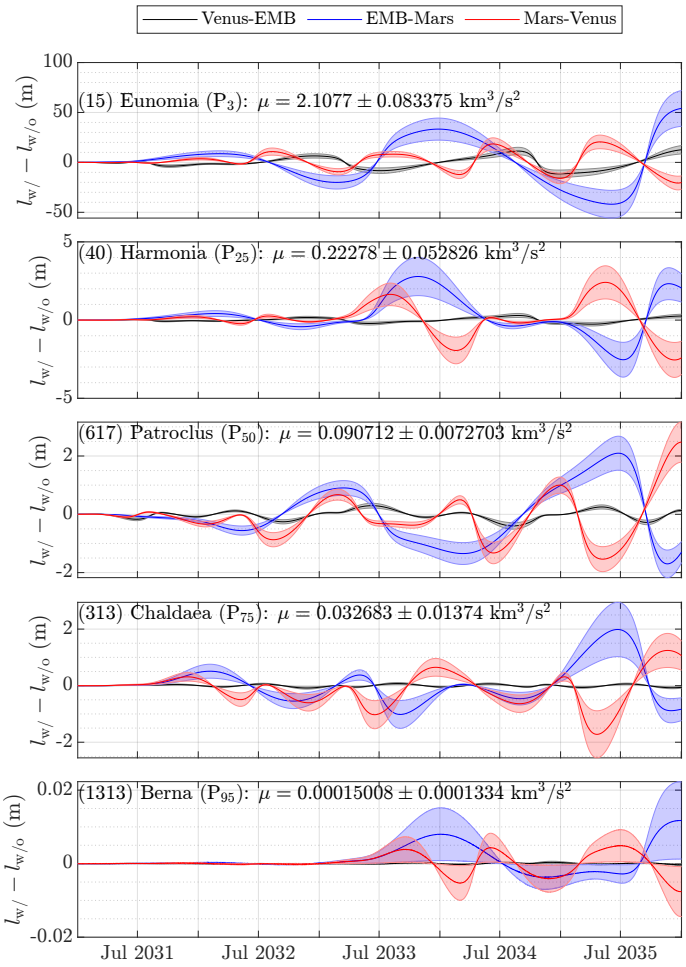

Fig. 3. Pre-fit temporal signatures to the Trilogy leg lengths caused by five representative asteroids, with shaded regions given by their corresponding ±1-sigma mass uncertainty. P_X stands for the X-th mass percentile, i.e., percentage of heavier asteroids in the catalog.

jeva et al. (2021), who reported difficulties when computing $\dot{\mu}_\odot$ in the same estimation where asteroid masses are included as estimable parameters. An assessment of how Trilogy measurements can constrain the fitted value of $\dot{\mu}_\odot$, therefore, still needs to be verified against the impact of correlations with asteroid mass uncertainties corrupting the solution. Instead, in this study, we focus on the constraint of asteroid masses while ignoring the much smaller signature of Solar mass loss. Demonstrating that mass uncertainties can be significantly lowered would pave the way for an estimation of $\dot{\mu}_\odot$ with expected lower correlations.

2.2. Interplanetary laser ranging

2.2.1. Overview

Nowadays, laser ranging is routinely conducted to measure distances to satellites via Satelite Laser Ranging (SLR; Combrinck 2010; Wilkinson et al. 2019) and to the Moon via Lunar Laser Ranging (LLR; Murphy 2013; Müller et al. 2014; Chabé et al. 2020). Both are based on the accurate measurement of the time of flight of two-way laser pulses which is passively reflected back to the emitting station thanks to a retrorreflector placed at the measured end. Although this is unfeasible at greater distances due to the power decay with the fourth power of the distance as a result of the retrorreflector usage (Birnbaum et al. 2010), the employment of transceivers at both ends was suggested as a feasible way to obtain accurate laser range measurements between different planets (Degnan 1996, 2002). Just as SLR and LLR, ILR can theoretically enable range measurements accurate to the mm or sub-mm level (Dirkx et al. 2019; Jain et al. 2024), and this possesses great potential of scientific return regarding planetary science (Dirkx et al. 2014b, 2015; Smith et al. 2018) and fundamental physics (Degnan 2007; Turyshev et al. 2010; Dirkx et al. 2016).

Successful or partially successful demonstrations of this technology have been conducted by the MESSENGER (Smith et al. 2006), Mars Global Surveyor (Abshire et al. 2006) and Hayabusa2 (Noda et al. 2017, 2023) missions. The Deep Space Optical Communications (DSOC) payload onboard NASA's Psyche spacecraft has recently proven interplanetary laser data transfer (Biswas et al. 2024a,b), and results on the quality of collateral range measurements are expected to be released soon. Although none of these tests has achieved to generate range measurements more precise than current state-of-the-art radio ranging methods (Border et al. 2020), it is worth mentioning that they have also not used any hardware fully dedicated to ILR and hence the technology has still not been pushed to the limits of its capabilities (Dirkx et al. 2019).

Apart from the *time-of-flight* approach, laser links can also be oriented to interferometric measurements. These allow highly precise range-rate measurements (Jain et al. 2024), and different approaches to extract ultra-precise range measurements exist (Lee et al. 2010). Interferometric inter-satellite ranging has been successfully applied in the GRACE Follow-On (Abich et al. 2019) and LISA Pathfinder (Armano et al. 2016) missions, both using closely spaced spacecraft in Earth's orbit. Interferometric ranging at interplanetary distances has never been conducted, and the most consolidated plan is currently the LISA mission (Danzmann 2000), now expected to be launched in 2035. Although its purpose of gravitational wave detection can be fulfilled with the time-delay interferometry method, which only requires an absolute ranging accuracy of order one meter (Thorpe 2010), recent calculations by Reinhardt et al. (2024) show how the adequate processing of output data can achieve pseudorange measurements accurate to sub-mm levels. In this work, however, the greater technological maturity makes us stick to the original suggestion to use time-tagged laser ranging for the Trilogy mission (Smith et al. 2018), in the line of present community trends in planetary mission proposals (Jain et al. 2024).

2.2.2. Measurement principles

There is consensus regarding the fact that the most suitable measurement architecture for ILR is two-way asynchronous (Degnan 2002; Birnbaum et al. 2010; Dirkx et al. 2016; Smith et al. 2018). This means that the two transceivers are continuously firing pulses to each other, and these are subsequently paired from the whole log of emitted and received transmissions at one end to generate individual two-way observations. The alternative would be to follow a synchronous—or *echo*—approach, where one of the two transceivers only responds to the pulses received by the other one, but the low signal-to-noise ratio (SNR) expected in ILR signals makes this inconvenient due to the expected number of response pulses mistakenly fired by noise (Degnan 2002). Another alternative would be to simply generate one-way observations by employing one end as emitter only and the other as receiver only, but this has the inconvenient that the emission and reception times are measured with different clocks and thus the requirements of clock stability in both ends become much

more stringent[7] (Dehant et al. 2017). With this in mind, the measurement principles detailed below correspond to asynchronous two-way ranging.

Consider the following one-way range measurements: $s^{(1)}_{BA}$ is the range corresponding to a laser pulse that has departed A at t_1 and has arrived at B at t_2; $s^{(1)}_{AB}$ is the range measurement corresponding to the pulse that has departed B at t_3 and has arrived at A at t_4; and δt_B is the difference $\delta t_B = t_3 - t_2$. The superscript (1) indicates one-way. Following Dirkx et al. (2016), the two-way range observable for $s^{(2)}_{BA_t}$ is constructed with the combination of the two one-way observations as

$$s^{(2)}_{BA_t} = s^{(1)}_{BA_t} + s^{(1)}_{AB_t} + c\delta t_B, \tag{1}$$

where

$$s^{(1)}_{BA_t} = \left\| \boldsymbol{r}_B\left(t_1 + \frac{s^{(1)}_{BA_t}}{c}\right) - \boldsymbol{r}_A(t_1) \right\| + \Delta s^{(1)}_{BA}; \tag{2a}$$

$$s^{(1)}_{AB_t} = \left\| \boldsymbol{r}_A\left(t_1 + \frac{s^{(1)}_{BA_t}}{c} + \delta t_B + \frac{s^{(1)}_{AB_t}}{c}\right) - \boldsymbol{r}_B\left(t_1 + \frac{s^{(1)}_{BA_t}}{c} + \delta t_B\right) \right\| + \Delta s^{(1)}_{AB}. \tag{2b}$$

$\mathbf{r}_X(t)$ indicates the position vector of end X at time t, c stands for the speed of light in vacuum, $\Delta s^{(1)}_{XY}$ is a correction term to the one-way ranges (e.g., relativistic or atmospheric effects) with respect to the assumption of Euclidean straight line light path at velocity c, and subscript t indicates that the measurement is referenced at the transmission time t_1. As detailed in equation (2), this means that all times are written in terms of t_1 only, which is straightforward from the measurement equations

$$s^{(1)}_{BA} = c\,(t_2 - t_1)\,; \tag{3a}$$

$$s^{(1)}_{AB} = c\,(t_4 - t_3)\,. \tag{3b}$$

The formulation for the two-way observable referenced at the reception time t_4, $s^{(2)}_{BA_r}$, has the equivalent formulation to equations (1) and (2) but writing all times as a function of t_4.

2.2.3. Measurement errors

The quality of ILR measurements will be limited by the intrinsic nature of laser pulses, hardware imperfections and model errors. Despite the challenge of accurately describing the exact probability distributions governing error sources and their time correlations (Jain et al. 2024), it is generally accepted to assume measurements to be affected by a normally distributed random noise and a systematic error (Dirkx 2015). Table 1 presents a summary of the main sources of both types.

The nature of the laser pulse limits the accuracy of the measurements due to its nonzero width. Current hardware allows pulses to be as short as 10 ps (Dirkx et al. 2014b; Dehant et al. 2017)—this introduces an uncertainty of 3 mm for each single-shot measurement, although it can be reduced by $\sqrt{N}$ by averaging over N single-photon measurements (Dirkx et al. 2019). Multi-photon measurements, on the other hand, introduce a systematic error due to the fact that the detector is more likely to be triggered by the front part of each photon pulse instead of its centroid—if 100 photons are detected, the resulting bias goes up to 2.5 times the pulse length (i.e., 7.5 mm for a pulse of 10 ps; Dirkx et al. 2014a). On top of this, imperfections in the Gaussianity of the pulse can be the source of an additional systematic error of few millimeters (Schreiber et al. 2018).

[7] Although not strictly interplanetary, one-way laser ranging was attempted by Bauer et al. (2017) to the Lunar Reconnaissance Orbiter (LRO), but the encountered challenges related to clock noise prevented it from being used at an operational level (Dirkx 2015). Largely based on these results, one-way laser ranging is considered a worse alternative than radio-based ranging (Dehant et al. 2017).

Table 1. Summary of random errors (top) and systematic errors (bottom) affecting laser ranging measurements

Error source	Magnitude	Reference
Pulse measurement	4-5 mm	Exertier et al. (2006)
	3-30 mm	Dehant et al. (2017)
	1.3-13 mm	Dirkx et al. (2019)
Detector precision	3-6 mm	Exertier et al. (2006)
	2 mm	Schreiber et al. (2018)
	3 mm	Dirkx et al. (2019)
Timer	2-3 mm	Exertier et al. (2006)
	<1 mm	Schreiber et al. (2018)
	≈ 0	Dirkx et al. (2019)
Clock	1 mm	Exertier et al. (2006)
	≈ 0	Schreiber et al. (2018)
	<1 mm	Dirkx et al. (2019)
Pulse measurement	2 mm	Schreiber et al. (2018)
Detector precision	0-12 mm	Schreiber et al. (2018)
Multi-photon pulses	0-8 mm	Dirkx et al. (2014a)
Hardware (other)	1-4 mm	Exertier et al. (2006)

The hardware components that can introduce measurement imperfections are the detector, timer and clock used in a transceiver station (Dirkx 2015). The detector introduces both a random error of a few mm due to its discrete resolution (Dirkx et al. 2019) and a systematic error due to the finite processing time, which can be calibrated but never to a perfect level due to its intrinsic instability (Schreiber et al. 2018). The finite resolution of event timers has historically also presented an additional source of random error to a few mm (Exertier et al. 2006), but newer technologies allow sub-ps precision and hence a negligible error even at interplanetary distances (Dirkx et al. 2019; Wilkinson et al. 2019). Finally, the clock can introduce a significant error if its instabilities accumulate in a significant manner during a range measurement. Notably, state-of-the art clocks are already stable enough to make this contribution negligible in SLR (Schreiber et al. 2018), and even considering interplanetary light time travels this is expected to yield to sub-mm errors (Dirkx et al. 2019). In asynchronous two-way ranging, the clock instability of the re-emmitting terminal accumulates during the lapse of time δt_B (section 2.2.2), which can introduce errors in the time-tagging of pulses. However, this time lapse is usually much lower than the light time travel and hence causes a negligible effect, as long as the corresponding clock fulfils reasonable stability requirements (Dehant et al. 2017).

Finally, environmental errors include the mismodeling of the random and systematic effects resulting from atmospheric refraction (Dirkx et al. 2014a), yet these do not play any role when the transceivers are placed in orbit, as suggested for Trilogy.

3. Methodology

The simulation settings chosen for the present study and the description of the implemented normal point generation approach are developed below. All simulations have been conducted with the TU Delft Astrodynamics Toolbox (Tudat)[8], which includes modules for orbit propagation, simulation of observations and precise orbit determination.

3.1. Batch least squares

The batch estimation algorithm is based on finding the parameters of a dynamical setup so that the difference between observed and predicted observations is minimized. Let vector $\boldsymbol{y}_0$ contain all such parameters, including the initial states $\boldsymbol{x}_0$ of each individual body $i = 1, \ldots, n_b$, and the constant environmental parameters $\boldsymbol{p}$ that affect the dynamical model (e.g., third body masses):

$$\boldsymbol{y}_0 = \begin{bmatrix} \boldsymbol{x}_{0_1} \\ \vdots \\ \boldsymbol{x}_{0_{n_b}} \\ \boldsymbol{p} \end{bmatrix} = \begin{bmatrix} \boldsymbol{x}_0 \\ \boldsymbol{p} \end{bmatrix}. \tag{4}$$

Now consider a vector $\boldsymbol{z}$ containing all available observations, together with its associated covariance $\mathbf{P}_z$, and an *a priori* knowledge of $\boldsymbol{y}_0$ given by a reference $\bar{\boldsymbol{y}}_0$ and its associated covariance $\mathbf{P}_0$. Then, the minimization problem can be formulated as

$$\hat{\boldsymbol{y}}_0 = \underset{\boldsymbol{y}_0}{\operatorname{argmin}} \left(\left\| \boldsymbol{z} - \boldsymbol{h}(\boldsymbol{y}_0) \right\|^2_{\mathbf{P}_z^{-1}} + \left\| \bar{\boldsymbol{y}}_0 - \boldsymbol{y}_0 \right\|^2_{\mathbf{P}_0^{-1}} \right), \tag{5}$$

where $\boldsymbol{h}$ is the function that maps $\boldsymbol{y}_0$ to the set of expected observations $\boldsymbol{z}$, and and the notation $\|.\|_{\mathbf{W}}$ stands for the weighted norm of a vector, i.e., $\|\boldsymbol{x}\|^2_{\mathbf{W}} = \boldsymbol{x}^\top \mathbf{W} \boldsymbol{x}$. The nonlinearity of the $\boldsymbol{h}$ function can be tackled by assuming an initial guess for $\hat{\boldsymbol{y}}_0$ (generally equal to $\bar{\boldsymbol{y}}_0$), and linearizing equation (5) around it. This yields the least squares solution

$$\Delta\hat{\boldsymbol{y}}_0 = \left(\mathbf{H}^\top \mathbf{W} \mathbf{H} + \mathbf{P}_0^{-1} \right)^{-1} \left(\mathbf{H}^\top \mathbf{W} \Delta\boldsymbol{z} + \mathbf{P}_0^{-1} \Delta\bar{\boldsymbol{y}}_0 \right), \tag{6}$$

where $\Delta\boldsymbol{z}$ is the vector of residuals $\Delta\boldsymbol{z} = \boldsymbol{z} - \boldsymbol{h}(\hat{\boldsymbol{y}}_0)$, $\Delta\bar{\boldsymbol{y}}_0$ is, equivalently, $\Delta\bar{\boldsymbol{y}}_0 = \bar{\boldsymbol{y}}_0 - \hat{\boldsymbol{y}}_0$, the weights matrix $\mathbf{W}$ is taken as the inverse of the covariance matrix of the observations, i.e., $\mathbf{W} = \mathbf{P}_z^{-1}$, and matrix $\mathbf{H}$, named the design matrix, is the Jacobian of the $\boldsymbol{h}$ function with respect to $\boldsymbol{y}_0$.

The covariance matrix of the observations is typically diagonal, which carries the assumption of different measurements being independent:

$$\mathbf{P}_z = \operatorname{diag}\left(\sigma_z, \ldots, \sigma_z\right), \tag{7}$$

where σ_z is the noise level of the observations. Building the design matrix, on the other hand, requires the computation of the partial derivatives of the observable equations (e.g., equation 1 when the observations are two-way ranges) with respect to the states $\boldsymbol{x}(t)$, as described by Moyer (2005); together with the computation of the state transition and sensitivity matrices, i.e.,

$$\boldsymbol{\Phi}(t, t_0) = \frac{\partial \boldsymbol{x}(t)}{\partial \boldsymbol{x}_0}; \qquad \mathbf{S}(t) = \frac{\partial \boldsymbol{x}(t)}{\partial \boldsymbol{p}}, \tag{8}$$

which are integrated by means of the variational equations, as described by Montenbruck & Gill (2001); Tapley et al. (2004).

[8] https://docs.tudat.space/en/latest/; Dirkx (2022)

Equation (6) is applied in an iterative manner to update the initial guess $\hat{\boldsymbol{y}}_0$ as

$$\hat{\boldsymbol{y}}_0 \leftarrow \hat{\boldsymbol{y}}_0 + \Delta\hat{\boldsymbol{y}}_0 \tag{9}$$

until a certain convergence criteria is met. At every iteration, the residuals $\Delta\boldsymbol{z}$, $\Delta\bar{\boldsymbol{y}}_0$, and the design matrix $\mathbf{H}$ are recomputed with the updated $\hat{\boldsymbol{y}}_0$. This procedure is also named "differential correction" (Milani & Gronchi 2010).

Equation (6) is commonly known as the set of "normal equations". An important remark is that its left hand side after convergence is the covariance matrix of the fitted solution, i.e.,

$$\hat{\mathbf{P}}_0 = \left(\mathbf{H}^\top \mathbf{W} \mathbf{H} + \mathbf{P}_0^{-1} \right)^{-1}. \tag{10}$$

The square root of the diagonal terms of $\hat{\mathbf{P}}_0$ is the set of formal errors, which define the individual uncertainties of the fitted parameters as long as the underlying assumptions of the batch least squares estimation (i.e., Gaussianity of observation errors with representative $\mathbf{P}_z$, absence of significant model errors) hold. Finally, this covariance matrix can be linearly propagated by means of the state transition and sensitivity matrices as

$$\hat{\mathbf{P}}(t) = \boldsymbol{\Psi}(t) \hat{\mathbf{P}}_0 \boldsymbol{\Psi}^\top(t), \tag{11}$$

where

$$\boldsymbol{\Psi}(t) = \begin{pmatrix} \boldsymbol{\Phi}(t, t_0) & \mathbf{S}(t) \\ \mathbf{0} & \boldsymbol{I} \end{pmatrix}.$$

3.2. Description of the implemented approach

Orbit determination of interplanetary orbiters is commonly conducted through a multi-arc batch estimation approach (e.g., Konopliv et al. 2011; Notaro et al. 2019; Andolfo et al. 2024), where the spacecraft trajectory is divided into different arcs of a few days and an independent orbit solution is computed at each of them. This decouples the estimation of the spacecraft and the planets' orbits, since the former are mainly based on range-rate (Doppler) observations and the latter are computed in a subsequent, single-arc estimation using range data without adjusting the spacecraft orbit (Dirkx et al. 2019). The inconvenience of this approach is that the errors in spacecraft position resulting from the orbit determination affect the the range measurements to be used in the planetary estimation in the form of an extra source of model error. This does not represent any significant corruption of the measurements as long as the inherent uncertainty of the ranging system introduces an error of a similar or greater order of magnitude, but with more accurate ranging systems such as ILR this might no longer be the case.

The advent of these newer ranging technologies has motivated the development of more sophisticated approaches, coupling the estimation of the planetary and spacecraft parameters. The batch estimation algorithm can still be applied in a concurrent estimation, although the fact that the spacecraft orbit is still divided into independent arcs while the planet's orbit is not makes the variational equations to compute equation (8) more complicated (see, e.g., Fayolle et al. 2022). This was successfully applied by Genova et al. (2018) when estimating the orbit of MESSENGER together with that of Mercury, who found that the coupling helped reducing the systematic error related to the spacecraft orbit determination. A further refined coupled approach was presented by Alessi et al. (2012), who suggested to introduce a penalty term to minimize the discontinuity between different spacecraft arcs. This has the advantage of not losing

all the information that can be extracted from distant states of the spacecraft (Lari & Milani 2019) while still allowing for the multi-arc setup to mitigate the effect of unknown and/or chaotic spacecraft dynamics.

Future missions employing ILR have been suggested to require a coupled estimation approach (Dirkx et al. 2019), due to the fact that range observations are more sensitive than range-rate to the slow dynamics such as planetary motion and the expected ranging accuracy can be orders of magnitude below the spacecraft position error resulting from Doppler tracking, whcich can easily be in the order of one meter (e.g., Cappuccio et al. 2020). On the other hand, it is also reasonable to think that precisely the usage of highly accurate ranging can potentially improve the orbit determination of the interplanetary spacecraft, just as it has been suggested for satellite constellations both in Earth's orbit (Davis & Gunter 2022) and interplanetary distances (Hill & Born 2007). This might be especially true for the Trilogy mission, since the presence of the closed triangle will potentially constrain the orbit determination of the spacecraft in two different directions. With the aim of assessing the validity of these latter claims, we chose to follow a decoupled estimation approach in which the spacecraft orbit determination allows for the subsequent generation of planet-to-planet ranges, i.e., normal points for planetary estimation.

The implemented algorithm follows the classical method for normal point generation from spacecraft orbit determination (e.g., Park et al. 2017; Konopliv et al. 2020; di Ruscio et al. 2020), with the novelty of using three ranging legs simultaneously. This can be summarized as follows: each orbit determination (OD) arc is solved with a batch least squares filter including both Doppler and range measurements in the observation set—following the judgment by Dirkx et al. (2019) that missions employing ILR will still need Doppler tracking. During this estimation, apart from the spacecraft initial state, a constant range bias b for each ranging link is included in the set of estimatable parameters. The observation equation is adapted by simply adding $+b$ to the right hand side of equation (1), which makes its Jacobian with respect to b equal to 1. The vector of parameters $\boldsymbol{y}_i$ estimated at each OD arc i is therefore 15×1, including the initial states of the two spacecraft and the three biases:

$$\boldsymbol{y}_i = \begin{bmatrix} \boldsymbol{x}_{0,i_{S/CV}}^\top & \boldsymbol{x}_{0,i_{S/CM}}^\top & b_{EM,i} & b_{VE,i} & b_{VM,i} \end{bmatrix}^\top . \tag{12}$$

The three estimated biases absorb the range difference between the real interplanetary distances and the one given by the *a priori* planetary model. Planet-to-planet range measurements at any arbitrary reference epoch t during an arc i can be generated by applying the measurement equation (1) while retrieving the planet's positions from the *a priori* ephemerides $\overline{\boldsymbol{x}}$, i.e.,

$$s_{EM}^{(2)}(t) = s_{EM}^{(1)}\left(\overline{\boldsymbol{x}}_{EMB}, \overline{\boldsymbol{x}}_M; t\right) + s_{ME}^{(1)}\left(\overline{\boldsymbol{x}}_{EMB}, \overline{\boldsymbol{x}}_M; t\right) + c\delta t_M \tag{13a}$$

$$s_{VE}^{(2)}(t) = s_{VE}^{(1)}\left(\overline{\boldsymbol{x}}_{EMB}, \overline{\boldsymbol{x}}_V; t\right) + s_{EV}^{(1)}\left(\overline{\boldsymbol{x}}_{EMB}, \overline{\boldsymbol{x}}_V; t\right) + c\delta t_E \tag{13b}$$

$$s_{VM}^{(2)}(t) = s_{VM}^{(1)}\left(\overline{\boldsymbol{x}}_M, \overline{\boldsymbol{x}}_V; t\right) + s_{MV}^{(1)}\left(\overline{\boldsymbol{x}}_M, \overline{\boldsymbol{x}}_V; t\right) + c\delta t_M, \tag{13c}$$

but after completing the OD process for all arcs, the resulting ranges are then corrected by adding the estimated biases in OD arc i:

$$s_{EM}^{(2)}(t) \leftarrow s_{EM}^{(2)}(t) + b_{EM,i} \tag{14a}$$

$$s_{VE}^{(2)}(t) \leftarrow s_{VE}^{(2)}(t) + b_{VE,i} \tag{14b}$$

$$s_{VM}^{(2)}(t) \leftarrow s_{VM}^{(2)}(t) + b_{VM,i} \tag{14c}$$

Following di Ruscio et al. (2020), the reference time t at which these planet-to-planet ranges are generated is set to be the mid epoch of the OD arc at which the corresponding biases are estimated. These corrected planet-to-planet ranges are then used in a batch planetary estimation, from which new ephemerides are computed. These new ephemerides and their corresponding post-fit covariance now become the new *a priori* model in a subsequent iteration, and the whole process is repeated until convergence is met.

The accuracy of the normal points produced by this approach will improve the more the random error of the range observations is averaged out through the OD arcs, and the same can be expected for spacecraft position errors as long as they are contained within reasonable limits and/or averaged over a sufficient number of orbits. Systematic errors of the ranging system, on the other hand, are a fundamental limit that cannot be mitigated. This is because the estimated range biases at each OD arc will absorb the true discrepancy between the *a priori* planetary model and reality together with the range measurement bias into a single scalar, so the two cannot be disentangled as long as the systematic error behaves truly as a constant, unknown observation bias. Estimations for the time variability of the systematic errors of the ILR system can help tackle this limit, yet this is highly dependent on the exact specifications of the particular system at use and hence is out of the scope of this study.

3.3. Simulation settings

3.3.1. Planetary dynamics

We simulate the dynamics of the Solar System by numerically integrating the orbits of the three Trilogy vertices when subject to the (Newtonian) gravity of the Sun and the third body perturbations of all other planets plus the 415 objects listed in the SiMDA catalog (section 2.1.2). The choice of using Newtonian gravity instead of taking into account the relativistic effects described by the Einstein–Infeld–Hoffmann equations as modern ephemerides do (Park et al. 2021; Fienga et al. 2021) is motivated consistently with Gomes et al. (2023): given the high-order effects of GR, together with our assumption of GR to be valid—at least enough not to introduce any significant effect on the measurements at the accuracy levels under study (section 2.2.3)—the difference between true and estimation models neglecting GR is judged to be still representative of the difference between reality and estimation models accounting for it. For the Earth-Moon system, we propagate the position of the Earth-Moon Barycenter (EMB) as if it were a single body with the masses of the Earth and the Moon combined. We retrieve the states of the planets and Sun from the INPOP19a kernels (Fienga et al. 2019b) and the states of the asteroids from JPL's Horizons database (Giorgini 2015).

Integration analysis led us to using the Encke formulation of the equations of motion (e.g., Wakker 2015) with a fixed step size Runge–Kutta–Fehlber (RKF) integrator of order 14. The Encke formulation is found to clearly outperform other propagators (e.g., Cowell, Gauss Modified Equinoctial, Unified State Model) by containing the accumulated integration error over the whole mission duration to a rounding error regime of magnitude below 10^{-4} meters when using standard double precision. The RKF14 integrator is used by fixing the step size in the RKF14(12) formulation, which we consider to be reasonable given the low eccentricity of the planetary orbits. With the Encke propagator for the problem under study, we find RKF14 to constrain the integrated solution to the rounding error regime with any step size below 2×10^5 seconds.

The initial states of the EMB, Venus and Mars will be parameters to estimate from Trilogy measurements. In order to assess how well such estimation will reduce the current uncertainties in the ephemerides of the three vertices, we need to use a covariance matrix for the intial states that is consistent with both the estimated true errors of planetary ephemerides and the dynamical model at use. Following Zenk et al. (2023), we obtain such covariance with the following procedure:

1. Using cartesian position observations of the planets retrieved from the ephemerides, we compute a best-fit intial state $\boldsymbol{x}_0$ by using the batch estimation algorithm (section 3.1) with the dynamical model described above and an identity weight matrix, i.e., $\mathbf{W} = \mathbf{I}$.
2. We re-compute the covariance (equation 10) but with modified weights $\mathbf{W}$ so that its propagation (equation 11) yields formal RSW errors through time that match the levels of estimated true errors of the planet's positions displayed in Figure 1. After iteratively choosing these weights, we take the final covariance $\hat{\mathbf{P}}_0$ to best represent planetary true uncertainties consistently with our dynamical model.

This covariance is used as the initial *a priori* during the planetary estimation step (section 3.2). Together with the asteroid mass uncertainties reported in section 2, it also allows us to define the two different *true* and *nominal* dynamical models to be used in the simulations, with the idea that their discrepancy mimics the true expected discrepancy between state of the art models and reality:

- The **nominal** model integrates the planetary orbits as described above, retrieving the planets' intial states from the ephemerides and assigning to every asteroid mass the mean value reported in the SiMDA catalog.
- In the **true** model, the initial states of the planets are perturbed following the multivariate distribution given by the estimated covariance $\hat{\mathbf{P}}_0$, and all asteroid masses are perturbed according to their corresponding ±1-sigma uncertainties reported in the SiMDA catalog (Figure 2)

3.3.2. Spacecraft dynamics

The dynamic effects that the Trilogy spacecraft will undergo will depend on their orbital configuration, and the most suitable choice to place the individual Trilogy transceivers is currently unknown and subject to discussion. The original mission assessment (Smith et al. 2018) described high planetary orbits to be preferable, given the lower influence of high-order and time-variable terms of the gravity field, the absence of atmospheric drag and the lower eclipse/occultation time. On the other hand, the higher the orbit, the greater the effect of the perturbation by Solar Radiation Pressure (SRP), which can be challenging to model, and the worse the orbit determination from range-rate measurements might perform due to its lower velocity.

To get a clearer understanding of the dynamical effects at play, the magnitudes of different sources of gravitational accelerations affecting spacecraft around Mars and Venus are presented in Figure 4. Solar Radiation Pressure (SRP), computed with an area-to-mass ratio of 0.0067 m^2/kg, is also plotted as a reference for being the most significant non-conservative perturbation. The left plots show the mean acceleration over a 7 day arc as a function of altitude, whereas the right figures map such accelerations to the maximum position difference caused by each acceleration over the same period. For SRP and third bodies, these are pre-fit displacements computed by comparing the propagated trajectory of the spacecraft with all perturbations vs. the result of turning each perturbation off. For gravity field terms, on the other hand, the pre-fit displacement caused by degree i is computed by turning off all terms of degree $\geq i$.

Other perturbing forces not seen in the figure include planetary radiation, spacecraft antenna thrust and GR correction terms. Each of them can introduce accelerations of the order 10^{-10}-10^{-9} m/s^2 (Hugentobler & Montenbruck 2017), and contributions of smaller magnitude are typically deemed negligible in Earth orbit operations (e.g., Bhattarai et al. 2022). In real life, modeling non-conservative forces at these levels is extremely challenging due to the number of sensitive factors at play that need to be precisely understood. These include, for example, the accurate description of the spacecraft infrared radiation (Shoemaker et al. 2012), the modeling of self-shadowing effects caused by its attitude (Mazarico et al. 2009), the accurate prediction of solar ray reflection paths (Li et al. 2018) or the precise determination of the location of the spacecraft antenna phase center with respect to its center of mass (Cascioli & Genova 2021). Real orbit determination operations commonly deal with such uncertainties by adding empirical accelerations as estimable orbit determination parameters that can absorb the remaining mismodeling, both for Earth satellites (e.g., Bock et al. 2014) and interplanetary spacecraft (e.g., Yang et al. 2022). Additionally, some missions are equipped with on-board accelerometers that can be used to provide high-sensitivity measurements of non-gravitational accelerations (Christophe et al. 2015; Santoli et al. 2020).

Figure 4 evinces how most third-body perturbations will be completely insignificant in the OD of the Trilogy spacecraft: all planets cause accelerations below 10^{-10} m/s^2, i.e., mostly smaller than the limits of dynamical modeling, and which translates to displacements of few centimeters at most after a seven-day arc. More importantly, even the heaviest asteroids cause even weaker perturbing accelerations and sub-millimetric displacements. It is therefore safe to conclude that while the signals of asteroid masses will be manifested into interplanetary ranges with a measurable amplitude (Figure 3), no retrievable information will be contained in the individual estimated spacecraft trajectories as long as they are computed with an unconstrained multi-arc approach (section 3.2). The only exception to be considered might be smaller bodies during episodes of close approaches to the planets, although these are out of the scope of this study.

Simulating a precise dynamical model of the Trilogy spacecraft is not only out of the aim of this work, but impossible without defined spacecraft designs and mission architecture. Instead, we use *true* and *estimation* dynamical models so that their discrepancy mimics the expected dynamical discrepancy between the fitted solutions of a Precise Orbit Determination (POD) process and reality:

- The **true** dynamical model is generated by integrating the spacecraft orbits for the whole mission duration, including cannonball radiation pressure, spherical harmonic terms and the third-body perturbations of the Sun and all planets (the list of exact simulation settings is presented in section 3.3.3).
- The **estimation** dynamical model is identical as the true one, with the exception of an added empirical acceleration that aims to account for any remaining mismodeled acceleration after POD. The empirical acceleration takes the form defined by Montenbruck & Gill (2001):

$$\boldsymbol{a} = \mathbf{R}^{I/RSW} \left(\boldsymbol{a}_{\text{const.}} + \boldsymbol{a}_{\sin} \sin\theta + \boldsymbol{a}_{\cos} \cos\theta \right), \tag{15}$$

where the $\boldsymbol{a}$ vectors are three different acceleration contributions, θ is the true anomaly of the spacecraft with respect

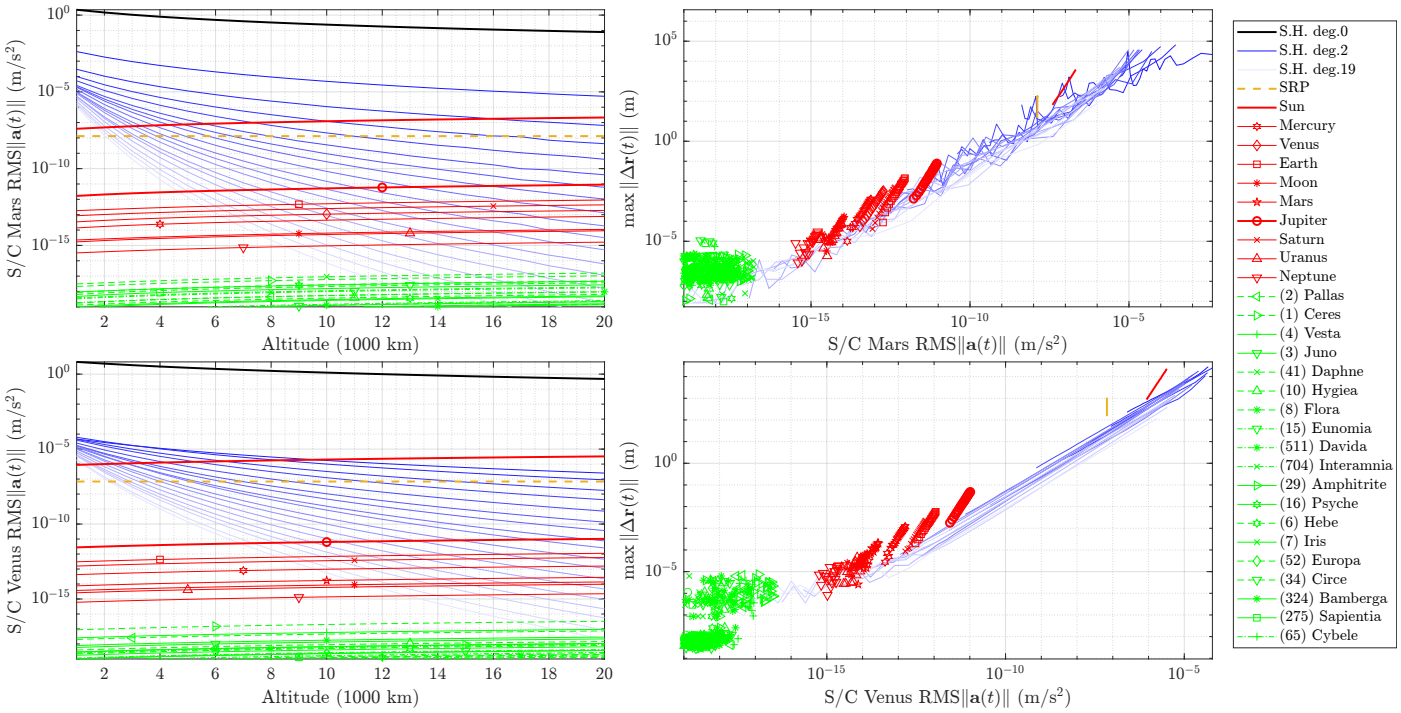

Fig. 4. Magnitude of gravitational accelerations and SRP affecting spacecraft around Mars and Venus as a function of altitude (left), and corresponding maximum trajectory deviation over a 7-day arc (right). Each curve for Spherical Harmonic (S.H.) of degree i is computed from the norm of the vector sum of all contributions from order 0 to i. individual S.H. curves correspond to all degrees 0 to 19.

to the central body and $\mathbf{R}^{I/RSW}$ is the rotation matrix from the spacecraft's RSW frame to inertial frame. The values assigned to this empirical acceleration are re-initiated at every OD arc, and depend on which scenario of dynamical mismodeling is considered:

- In the **optimistic** case, we sample the nine scalar components of the empirical acceleration from a standard normal distribution scaled by 10^{-11} m/s^2. This follows from di Stefano et al. (2023), where a highly accurate model of nonconservative forces on the BepiColombo spacecraft achieves flat ranging residuals after POD with uncertainties of this order in the estimated empirical accelerations.
- In the **conservative** case, the empirical acceleration components are sampled equivalently but with a ×50 factor, i.e., with a variance of 5×10^{-10} m/s^2. This follows from the acceleration residuals found by Hładczuk et al. (2024) when assessing the accelerometer measurements on GRACE-FO. Additionally, we add a mismodeling of the SRP coefficient by scaling it by a factor randomly sampled from 1 ± 0.02, following the standard deviation in the true error of estimated SRP coefficients found by Rosenblatt et al. (2021) when simulating POD of a Venus orbiter with similar area-to-mass ratio.

The results by di Stefano et al. (2023), which were obtained during interplanetary cruise, might be too optimistic for Trilogy if the planetary albedo and eclipse time introduces a significant extra source of uncertainty. On the other hand, BepiColombo has large solar panels, and if the Trilogy spacecraft turned out to be more compact and hence less sensitive to these small forces, just as Cassini was (Bertotti et al. 2003), our optimistic case might be perfectly reasonable (di Ruscio et al. 2020). On the other hand, the availability of an accelerometer onboard of GRACE-FO can make the modeling by Hładczuk et al. (2024) too optimistic with respect to spacecraft that do not have one, but this mission is in a Low Earth Orbit (LEO) and hence more affected by atmospheric drag and eclipses than in a higher altitude. In the end, the optimistic and conservative cases presented here are simply chosen as two representative points in the whole space of dynamical mismodeling possibilities, with the aim of offering some insight on this aspect for the next stages of the study of the Trilogy concept.

Finally, for the simulation settings under study, integration analysis led us to choosing a fixed step size RKF integrator of 10th order with the Gauss Modified Equinoctial Elements (MEE) formulation of the equations of motion (Walker et al. 1985; Walker 1986). This is found to outperform other propagators by containing the rounding error regime of the spacecraft position after a seven-day propagation below 10^{-5} meters. The integrator is set by fixing the step size of the RKF10(8) formulation, and it allows to reach rounding error levels with any step size below ~900 seconds.

3.3.3. Choice of simulation settings values

The numerical values assigned to the different design variables for the main simulation case presented in this study are listed in Table 2. These constitute a base case, which we then modify in individual subcases to assess the sensitivity of the results to the design parameters (section 4.2).

The spacecraft orbits are set to an altitude of 10000 km above the surface of each planet, which we consider to be consistent with the requirements outlined by Smith et al. (2018) of not being sensitive to too-high order terms of the gravity field, while still not making non-conservative forces dominant (Figure 4). This results in orbital periods of 5h 47', 6h 14'and 13h 10', respectively, for the spacecraft around Venus, the Earth and Mars. Inclinations are set to 80°, following the recommendation by Smith et al. (2018) of avoiding purely polar orbits while ac-

Table 2. Nominal simulation settings

Spacecraft propagation	
Orbital elements:	
Altitude h	10000 km
Inclination (wrt. ecliptic) i	80°
Eccentricity e	10^{-4}
Dynamical model settings	
Maximum gravity field degree/order	25
Third bodies (point masses)	Sun + all planets
Radiation pressure factor C_rA/m	0.008 m^2/kg
Dynamical mismodeling case	Optimistic
Measurement strategy	
Trilogy (two-way range):	
Cadence	60 sec
Random error (1-σ)	3 mm
Systematic error (constant)	-3.6 mm
Sun avoidance angle	5°
Retransmission time $\delta t_V = \delta t_E = \delta t_M$	0 sec
Doppler (one-way averaged):	
Cadence	60 sec
Random error (1-σ)	0.012 mm/s
Integration time	60 sec
Sun avoidance angle	5°
Estimation strategy	
OD arc length	12 h
OD arcs per day	1
A priori S/C $\overline{\mathbf{P}_0}$	1 km 0.1 mm/s
Asteroids estimated	350
Mission duration	5 years
Start date	Jan. 1st 2031

knowledging that highly inclined orbits can lead to more fruitful science related to the host planet, and the fact that near-equatorial orbits are subject to more frequent occultations for the ILR links. The eccentricity is set to a near-zero value, acknowledging that there is no clear interest for placing the transceivers at an elliptical orbit, while it is in practice impossible to reach an eccentricity of absolute zero.

Regarding the spacecraft dynamical model, the choice of degree and order 25 is made with the aim of introducing all gravity terms relevant for individual OD arcs together with some higher-frequency terms that can make the exact measurements of inter-spacecraft two-way ranges more realistic in the frequency domain, while not requiring too many computational resources for the simulated OD process. SRP is defined with a cannonball model, and the value used for the product of the radiation pressure coefficient C_r and the area-to-mass ratio A/m can arise, for instance, from $C_r = 1.2$ (e.g., Yan et al. 2017), $m = 1500$ kg and $A = 10$ m^2, which is consistent with typical interplanetary spacecraft with solar panels (Rosenblatt et al. 2021).

The observations from Trilogy and Doppler are set to be conducted every 60 seconds. ILR systems can be fired at a higher frequency, and in fact for the Trilogy concept Bills & Gorski (2022) suggested to use one second. Retrieving observations at lower frequencies can however reduce the random error contribution by averaging different measurements, and in this study we use one minute due to the lack of higher frequency dynamics to be solved during our simulated OD process.

For ILR measurements we introduce a Gaussian noise of ±3 mm, which is consistent with the optimistic case of a single 10 ps pulse length with no additional hardware errors or with the averaging of several pulses with an extra random error introduced by the detector (section 2.2.3). Additionally, we introduce a bias of -3.6 mm, which is expected from multi-photon signals of 5 photons with a pulse length of 10 ps (Dirkx et al. 2014a). For Doppler observations, on the other hand, we assume a random error of 1.2×10^{-5} m/s at 60 seconds of integration time (Cappuccio et al. 2020) and no systematic errors.Finally, the retransmission time δt for the two-way range measurements is set to zero—in real life, the pairing of one-way ranges to form a two-way measurement (section 2.2.2) will result in arbitrary (small) nonzero retransmission times, but this has no effect from the standpoint of the information encoded in the measurement.

Finally, we consider both systems to work only when the solar separation angle is greater than 5°, following the assessment for ILR by Dirkx et al. (2014b). While radio-based links might function at smaller angles (e.g., Cascioli et al. 2019), we are not interested in assessing our OD scenario during these periods if Trilogy measurements are not available.

With the aim of obtaining one normal point per day as in the preliminary study by Fienga (2023a), we separate the starting epochs of consecutive OD arcs by 24 hours. The duration of each arc is a trade off between the effect of averaging out the resulting OD error, which is beneficial for the estimation of the range biases, with the increase in this OD error caused by the dynamical mismodeling being accumulated over time. Typical OD arcs for Mars spacecraft span between two and seven days (Yan et al. 2017), although highly precise applications require shorter arcs to mitigate the effect of unmodelled dynamics: e.g., di Stefano et al. (2023) found that the observation residuals degraded with arcs over 24 hours and fixed them to 6h. As a middle-ground nominal case, but acknowledging that precise dynamical modeling will be an important aspect of the Trilogy mission, we fix the length of the OD arcs to 12 hours. This also accounts for the fact that it is in practice impossible to have Doppler tracking of interplanetary spacecraft available for 24 hours every day, due to the limitations of the ground station infrastructure.

The *a priori* covariance for the spacecraft initial states is set to 1 km in RSW positions, assuming only preliminary orbit determination has been carried out before. If POD has already been conducted without the Trilogy measurements for the sake of science related to the host planets, this initial covariance may well be smaller, yet we assume that ILR measurements will be used for the POD of this mission from the very beginning.

Besides the exact settings of spacecraft OD, the planetary estimation process is also part of the algorithm outlined in section 3.2. In this step, we estimate the initial states of Venus, the EMB and Mars together with the masses of 350 asteroids, updating the *a priori* model from the nominal one described in section 3.3.1 at every new iteration. The number of selected asteroids is comparable to the number of fitted masses in modern planetary ephemerides (Folkner et al. 2014; Pitjeva et al. 2019), and they are selected to be the ones expected to cause strongest signal to the Trilogy range measurements: consistently with Somenzi et al. (2010), we check the individual signal amplitudes of each asteroid at its nominal mass (solid lines in Figure 3) and we compute its signal strength as the average of the maximum amplitudes between the three legs. Then, we take the first 350 asteroids from the list of signal strengths in descending order.

Finally, the mission duration is set to 5 years, consistently with the maximum duration considered in the preliminary study by Fienga (2023a). The starting date is set to January 1st 2031, following our judgment of a Trilogy-like mission to be very unlikely to fly this decade.

4. Results

The results on the quality of both spacecraft OD and the produced planet-to-planet ranges are presented in this section: section 4.1 lists them for the nominal settings described in section 3.3, whereas section 4.2 presents the impact of tweaking some of the chosen settings.

As described in section 3.2, the implemented approach consists of fitting range biases during simultaneous spacecraft OD and using them to correct the planet-to-planet ranges resulting from the *a priori* planetary ephemerides, then using these ranges as normal points for a batch estimation (section 3.1) to obtain further improved ephemerides, and iterating the whole process. For all tested cases, we find that the resulting normal point errors (i.e., the true errors in planet-to-planet ranges) remain essentially identical between iterations 2 and 3, hence we don't run further estimations as convergence is assessed to be reached. All figures presented below correspond to this final iteration of the process, which represents the final solution of the simulated orbit determination.

4.1. Nominal case

4.1.1. Generation of normal points

As detailed in section 3.2, normal points to be used in the planetary estimation are obtained form a simultaneous spacecraft OD of the Venus and Mars spacecraft in which range biases are fitted for each of the Trilogy legs. Given that the quality of the spacecraft OD is expected to constrain the quality of the planet-to-planet ranges, the two key questions to address are 1) to what extent the presence of the Trilogy ranging links can improve the OD of the interplanetary spacecraft and 2) how much this OD error degrades the quality of the generated planet-to-planet ranges. To give some insight into these matters, the resulting spacecraft true OD errors and the resulting normal point errors are presented, respectively, in Figure 5 and Figure 7.

The errors displayed in Figure 5 are computed as the RMS along every individual arc of the norm of the vector difference between the estimated and true trajectories. Figure 5 also presents the RMS of the projection of the vector difference into the two directions of ILR links. Each shaded area indicates a period where the corresponding link is unavailable due to the constraint on the solar separation angle not being fulfilled. Finally, the resulting error after performing the equivalent OD process at the same iteration (i.e., with the most updated planetary model) but with Doppler observations only is also displayed for the sake of comparison.

It is immediate to observe how the presence of the two simultaneous ILR links achieves to significantly reduce the resulting true error to the centimeter level, in contrast with the several-meter level achieved with Doppler only. The availability of a single ranging link, on the other hand, constrains the error to this level in its own direction only, without avoiding the true error from reaching several meters due to the lack of precise ranging constraint in a perpendicular direction. Finally, a distinct case is also observed in may 2031, June 2033 and September 2035, where the Earth-Mars link is inhibited for short (2-week) periods. These happen to be the configurations where the Earth is between the Sun and Mars, so that the two-way ranging link is blocked but the one-way Doppler link to Mars does function. The resulting OD error increases due to the absence of accurate ranging from Earth, but in a much more modest way than in the other solar conjunction events due to the fact that the available constraints of position (from Venus through ILR) and velocity (from Earth through Doppler) do still restrict two different spatial directions.

Figure 5 also evinces how the average OD error of the Martian spacecraft is larger than the Venusian one, following a long periodic signature that brings it up to 10 cm even with all Trilogy links working. Additionally, the errors of both spacecraft present certain peaks of varying amplitude at certain—and sometimes common—instants. To get furher insight on the physical causes of these, Figure 6 and Figure 8 present the time evolution of two different relevant magnitudes: the angle between the spacecraft orbital planes and the line of sight to the other two planets, and the collinearity between the three vertices.

The former are found to have an impact on the spacecraft OD error—this is evinced at the instants at which the angles φ between the ILR links and the spacecraft orbital planes are maximum, which are marked with dashed vertical lines of the corresponding color, both in Figure 6 and Figure 5. In the case of the Venus spacecraft, it is evident to note how these "near-perpendicularity" peaks with respect to the link with Earth neatly coincide with the instants at which the projection of the spacecraft OD error to the line of sight of Earth is minimum. This is consistent with the fact that if the spacecraft is located at a perfectly perpendicular orbital plane, the oscillatory component of the range measurement that follows the spacecraft orbital period is removed, resulting in one less degree of freedom to introduce errors. The OD errors in the direction of the link to Mars do not show as many dips, given the fewer near-perpendicularity peaks (Figure 6) and the fact that most of them happen to coincide with solar obstruction of the Venus-Mars link (Figure 5), as a result of the particular chosen initial conditions. A good example of more lucky conditions happens in September 2035: the Venus-Mars link is nearly perpendicular to the orbital planes of both the Venus and Mars spacecraft (Figure 6), and this is translated into a clear dip in the spacecraft OD error in both directions (Figure 5). It must be noted that the total 3D position error never goes below 1-10 cm, which is hardly possible to reduce due to the challenges in dynamical modeling (section 3.3.2), but it is in these optimal geometry windows that the projection of the OD error to the directions of the ILR links can achieve mm or even sub-mm levels.

On the other hand, the collinearity peaks seen in Figure 8 are also displayed in Figure 5 with dotted vertical lines, given its expected impact in the resulting OD error—if the three planets were ever perfectly aligned, the dynamical constraints given by the observations would no longer be established in different spatial directions. This collinearity is computed as the inverse of the area enclosed by the Trilogy triangle—for perfectly aligned points, their enclosed area becomes zero and hence their collinearity blows up—both in its dimensional form A and nondimensional form $\overline{A}$, defined as

$$\overline{A} = \frac{A}{\left(\prod_i^3 l_i\right)^{2/3}}, \tag{16}$$

where l_i is the length of each of the three Trilogy legs. The fact that the two magnitudes yield to the same peaks (Figure 8) suggests that both are valid metrics to assess collinearity.

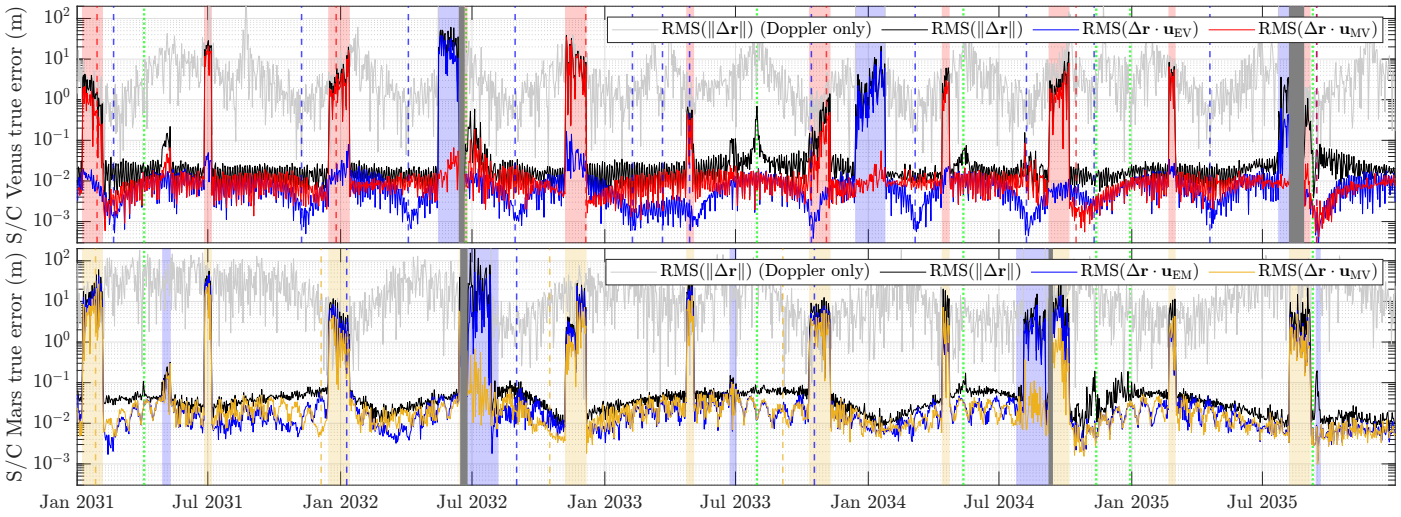

Fig. 5. Mean true spacecraft position errors at each OD arc (black) and corresponding projections to the ILR link directions (coloured), compared to the case where only Doppler tracking is used (gray). EV: Earth-Venus; EM: Earth-Mars; MV: Mars-Venus. For the coloured vertical lines, refer to Figure 6 and Figure 8.

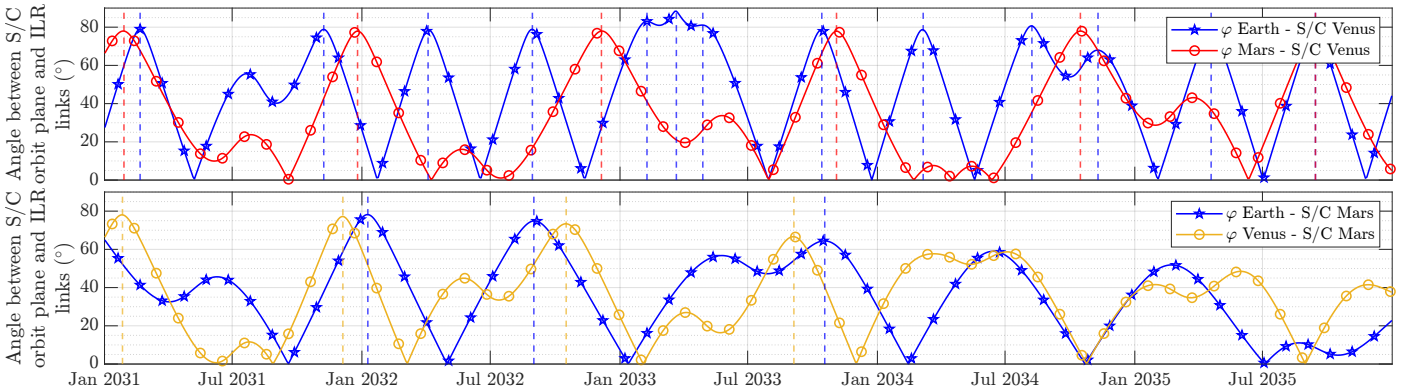

Fig. 6. Angle between the orbital planes of the Venus spacecraft (top) and Mars spacecraft (bottom) and the direction of their two ILR links. Dashed vertical lines correspond to local maximums with $\varphi > 60°$.

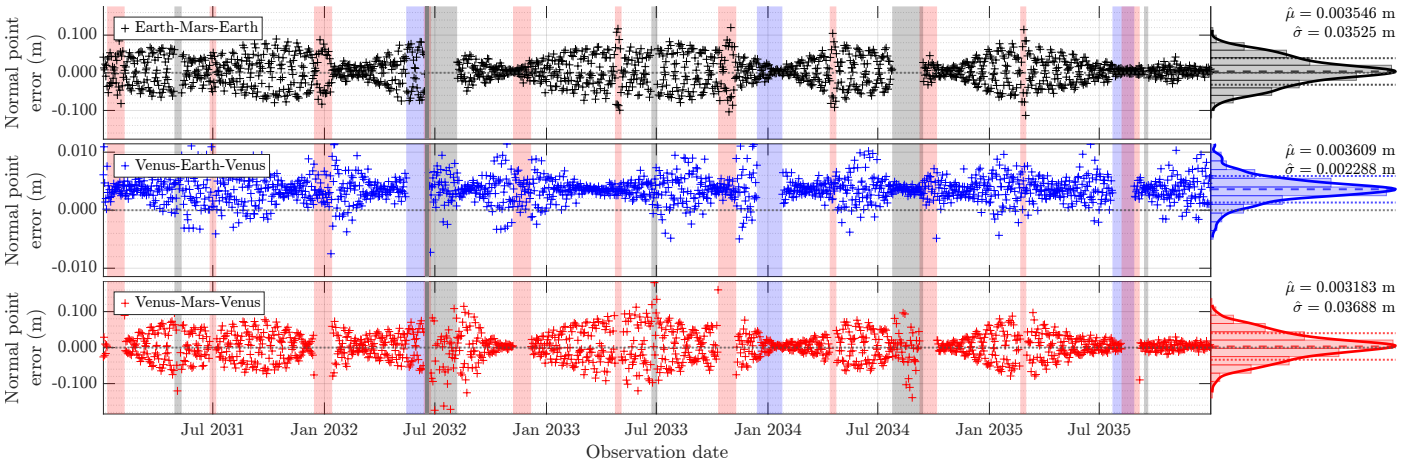

Fig. 7. True errors in planet-to-planet two-way ranges (normal points) after being corrected with the fitted biases

It is clear to observe how collinearity peaks coincide with true error peaks in the OD position error of the Martian spacecraft, namely, on April 2031, May 2034 and November 2034. In contrast, the collinearity peaks only seem to have an impact to the OD error of the Venusian spacecraft when they coincide with small angles between spacecraft orbital plane and ILR links (i.e., late July 2033 and May 2034). This suggests that, at these low φ angles, ILR measurements are less capable of constraining the spacecraft OD errors as much as they do with greater perpendicularity with the spacecraft orbital planes.

As described in section 3.2, the range biases fitted during spacecraft OD are then used to correct the planetary *a priori* model by adding such biases to the simulated planet-to-planet two-way ranges. Figure 7 shows the resulting true errors in these

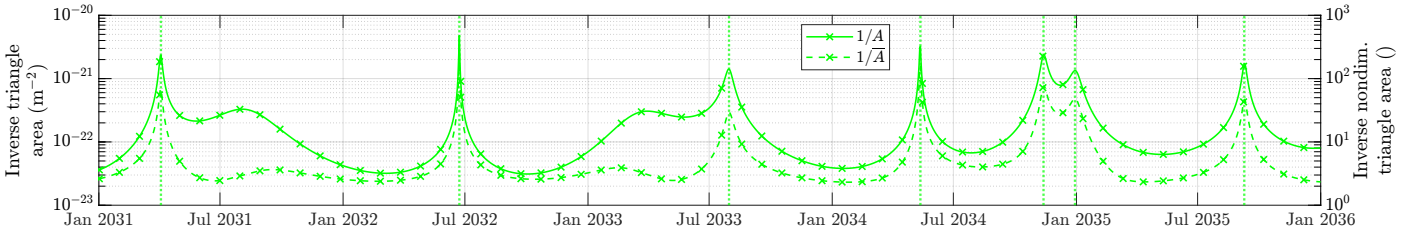

Fig. 8. Collinearity between the three Trilogy planets, computed as the inverse of the enclosed area A and the inverse of the non-dimensional enclosed area $\overline{A}$.

two way ranges after having followed this procedure for the last time (i.e., these are the errors of the normal points to be used in the last iteration of planetary estimation).

The two metrics that best describe the quality of the produced normal points are the mean and standard deviation of their true errors. As observed in the histograms of Figure 7, the three links converge to a mean error that coincides remarkably well to the 3.6 mm of true systematic error added to the measurements (section 3.3.3). The link that does so with less precision (0.4 mm or 11%) is the Venus-Mars link, which is consistent with the fact that it is the only link of the three affected by the OD errors of both the Venus and Mars spacecraft.

Random errors, on the other hand, appear to follow a more complex behaviour. The aggregate statistical distributions show how the Earth-Venus link is able to provide normal points with a variance of about 2 mm, which is smaller than the 3 mm of random error affecting the ILR measurements. Moreover, it is clear how during the periods when the orbit of the Venus spacecraft is determined with millimetric position errors in the Earth-Venus line of sight (e.g., February-May 2033; Figure 5), the variance of the produced normal points is significantly narrowed, possibly reaching single- or few-mm levels. Looking at Figure 5 and Figure 6, these periods appear to coincide with the times where the angle between the orbit plane and the Earth-Venus link is maximum, thus the OD error of the Venus spacecraft is minimum in the direction of the Earth-Venus link.

The dispersion of normal point errors for the two legs with Mars as one end, on the other hand, appears to be an entire order of magnitude greater than for the Earth-Venus leg, showing more than 3 cm of standard deviation. The error signal appears clearly modulated in time, with an amplitude that is directly proportional to the resulting position OD error for the Mars spacecraft (Figure 5). The interpretation that follows is that the orbit of the spacecraft around the Red Planet is determined with an error level that is still dominant over the generated normal points, whereas the slight increase in the accuracy of the orbit determination of the Venusian spacecraft is enough to let the normal points reach levels of, at least, the original inter-spacecraft measurement accuracy. The reasons behind this different behavior are further analyzed in section 4.2.

As described in section 3.2, these planet-to-planet ranges are now to be used in a batch estimation of ephemerides and asteroid masses, whose results are shown in the next section (4.1.2). Before that, however, it is important to define how these observations will be weighted in the application of the batch filter (section 3.1), to ensure proper convergence of the estimator. The common approach (e.g., di Ruscio et al. 2020) consists of assigning the values of formal errors of the biases fitted during the spacecraft OD step, $\sigma_{b,i}$, as observation covariances for the corresponding normal points, so that

$$W_{ii} = \sigma_{b,i}^{-2}. \tag{17}$$

This is subject to the assumption that such formal errors are an accurate representation of the true errors of the resulting normal points, which is reasonable as long as 1) the normal point errors are mainly driven by errors in the estimated biases, and 2) these bias errors are in turn properly described by the post-fit covariance after OD.

For the purpose of evaluating such assumptions, the overlapped distributions of range bias formal errors after OD and true errors of the normal points generated with such biases, both corresponding to the last iteration of the procedure, are presented in Figure 9. One can clearly observe how the true error distributions are shaped considerably different than the formal error ones in the cases of links including Mars, which are the ones with highest and most modulated errors (Figure 7). In this cases, the true-to-formal error factor has the order of several tens. The Earth-Venus link, despite presenting a true error distribution much closer in shape to that of formal errors, is still a factor ~10 ahead of the formal errors.

The conclusion that follows is that using the formal errors of the fitted biases directly (equation 17) is too optimistic. This is essentially equivalent to assigning a too small observation covariance $\mathbf{P}_z$ to the cost function (equation 6), which can be problematic by potentially penalizing the true solution too much[9] and thus forcing the estimator to converge somewhere else. With this in mind, we construct the diagonal[10] weight matrix $\mathbf{W}$ to be used in the estimator by assigning to each observation covariance the square of the product of the formal error of the corresponding fitted bias times a conservative true-to-formal error ratio of 50. This is found to be valid for both iterations 2 and 3, while for iteration 1 we use a true-to-formal error ratio of 3×10^3. Figure 9 only shows the results of iteration 3 for the sake of compactness.

In a real-world scenario, by definition, the true errors would be unknown. However, running this analysis (with all simulation settings matching the real mission) would enable using a valid figure for the true-to-formal error ratios, so that the observations used in the planetary estimation step can be weighted properly. The correct convergence of the estimator observed in the results (section 4.1.2) supports the validity of this method, suggesting that the found true-to-formal error ratios can be deemed valid as long as the mission configuration matches the used simulation settings (Table 2).

[9] "Penalizing X solution" is short for "increasing the value of the cost function associated to X solution". The cost function of the batch estimator (e.g. Montenbruck & Gill 2001) is defined by the interior of the argmin operator in eq. (5).

[10] Strictly, we should make use of the whole 3×3 post-fit covariance matrix of the fitted biases, but we stick to the diagonal terms only due to the impossibility to assign non-diagonal weight matrices in Tudat.

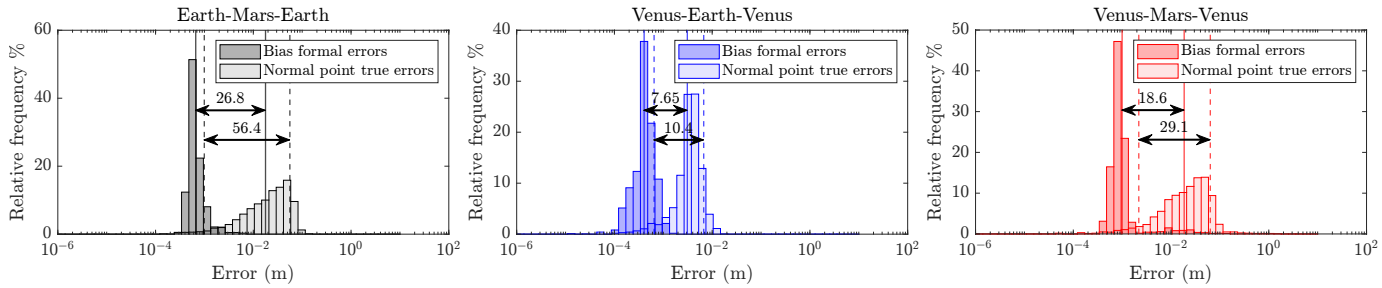

Fig. 9. Distributions of (absolute) true normal point errors (Figure 7) and formal errors of the fitted biases. The horizontal arrows indicate the true-to-formal error ratios computed at the (geometric) mean (solid) and mean + one-sigma (dashed) of the distributions.

4.1.2. Estimation of planetary ephemerides and asteroid masses

As described in section 3.2, the normal points generated after every iteration of spacecraft orbit determination are used in an estimation of the initial states of the three Trilogy host bodies together with 350 asteroid masses. The quality of this estimation is then measured with the true errors in estimated planetary states and asteroid masses, to check the extent to which true and formal errors of the *a priori* model can be reduced.

The results of the initial state estimation at each of the three consecutive iterations are presented in Figure 10, Figure 11 and Figure 12. Each figure shows the pre- and post-fit states and covariances together with the true state given by the true model (section 3.3.1), which is the one to be estimated. Each covariance $\mathbf{P}$ is plotted as an uncertainty ellipsoid, which has the form

$$\boldsymbol{x}^\top \mathbf{P}^{-1} \boldsymbol{x} = l^2. \tag{18}$$

Given that $\boldsymbol{x} \in \mathbb{R}^6$ is the state vector of the three position and velocity components of a body, the confidence bound of the ellipsoid is given by $l^2 \sim \chi^2(\nu = 6)$, hence the ellipsoids plotted with $l = 3$ decribe a confidence region of 82.64%[11]. It is important to note that these are not 2D level curves resulting of partially evaluating the ellipsoid at a given state, but projections of the whole six-dimensional ellipsoid into different two-dimensional subspaces.

It is clear to see how the final solution converges to the true initial states within a centimeter in radial position, whereas cross-track positions are unable to converge to less than some tens of meters. To get better insight of the exact convergence evolution, the values of true errors in the different RSW components are listed per iteration in Table 3. From it, it is clear to see how the second iteration still introduces some improvement in radial positions and some velocity components, whereas the change after the third iteration is marginal.

The results of asteroid mass estimations after the last iteration are summarized in Figure 13 and Figure 14. Both figures show comparisons between pre- and post-fit mass errros, yet it is important to note that, rather than using pre- and post-fit errors corresponding to a single estimation, the pre-fit mass values used correspond to those of the initial *a priori* model (i.e., the one based on the SiMDA catalog; section 2.1.2), while the post-fit results correspond to those of the third (i.e., last) iteration. Despite the *a priori* masses and covariance matrix are updated with the results of every iteration for the following one, this gives a better insight by encompassing the estimation results of the whole procedure in a single figure. We acknowledge that

[11] From the cumulative distribution function of the χ^2 distribution: $F_{\chi^2_6}(3^2) = 0.8264$.

Table 3. True errors in initial states of Venus, EMB and Mars (top) and asteroid mass improvement metrics (bottom) after the planetary estimation step at each iteration. Post-to-pre true (t.) and formal (f.) error values correspond to the median of the corresponding distributions.

		Iteration number			
		1	2	3	
Venus	R	−0.0398	0.0022	0.0023	m
	S	1.549	1.590	1.590	m
	W	−57.339	−57.628	−57.629	m
	v_R	−0.507	−0.502	−0.502	$\times 10^{-6}$ m/s
	v_S	0.0181	−0.0031	−0.0032	$\times 10^{-6}$ m/s
	v_W	20.878	20.670	20.671	$\times 10^{-6}$ m/s
EMB	R	0.1367	0.0106	0.00987	m
	S	−4.409	−4.493	−4.493	m
	W	116.761	116.257	116.264	m
	v_R	0.858	0.922	0.922	$\times 10^{-6}$ m/s
	v_S	−0.0195	0.00060	0.00072	$\times 10^{-6}$ m/s
	v_W	−2.722	−2.513	−2.514	$\times 10^{-6}$ m/s
Mars	R	0.0400	−0.0118	−0.0113	m
	S	−3.050	−3.080	−3.080	m
	W	60.544	59.329	59.325	m
	v_R	0.292	0.277	0.276	$\times 10^{-6}$ m/s
	v_S	0.0281	0.00091	0.00102	$\times 10^{-6}$ m/s
	v_W	−16.561	−16.778	−16.779	$\times 10^{-6}$ m/s
% improved		52.0	63.4	64.9	%
Post/pre t. err.		0.997	0.893	0.869	
Post/pre f. err.		0.993	0.914	0.936	
post/pre <0.5		12.00	27.71	27.14	%

individual asteroid mass improvements might be strongly subject to the particular settings used in this simulation case (e.g., randomly-generated value of true mass; section 3.3.1), hence the following analysis is mainly focused on the statistical, macroscale performance of the estimation rather than any specific asteroids.

Figure 14 shows the distribution of errors after the last iteration divided by the corresponding true errors of the *a priori* model. A true error ratio smaller than 1 means the estimated mass is closer to the true one than before estimation. As seen in the left histogram, this happens for 65% of asteroids, which represents a modest overall improvement. The median of the distribution is taken as a representative metric for the GM error improvement, given that it is not directly determined by the actual magnitude of errors and masses and hence is not biased towards

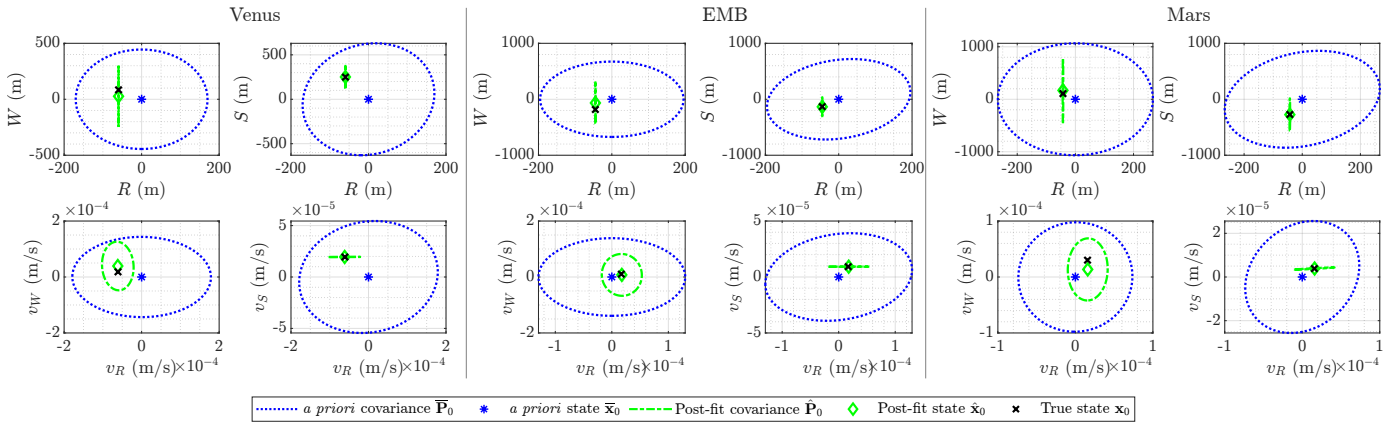

Fig. 10. Results of initial states after the planetary estimation step at iteration 1. The *a priori* covariance (blue) is the one described in section 3.3.1. All ellipses are 2D projections of the 6D ellisoid given by the covariance matrices with $l^2 = 9$ (i.e., $p = 0.826$)

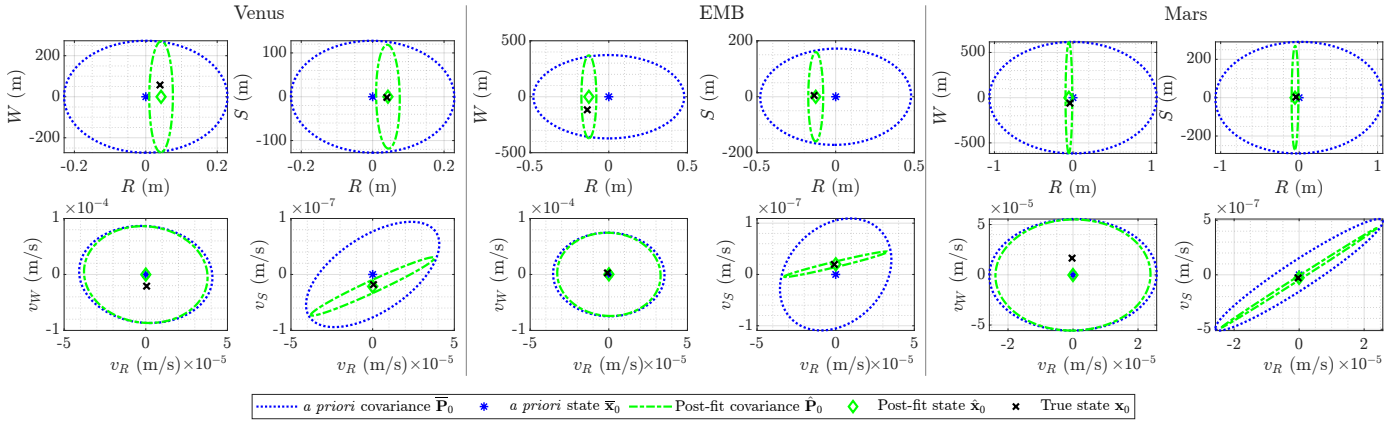

Fig. 11. Results of initial states after the planetary estimation step of iteration 2. The *a priori* covariance (blue) is the post-fit covariance from iteration 1 (Figure 10). All ellipses are 2D projections of the 6D ellisoid given by the covariance matrices with $l^2 = 9$ (i.e., $p = 0.826$)

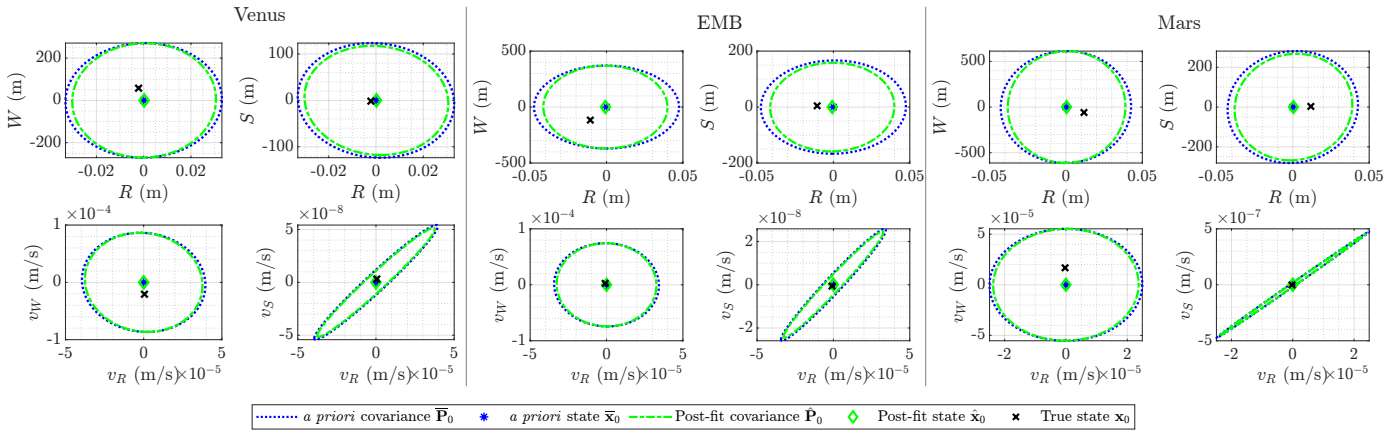

Fig. 12. Results of initial states after the planetary estimation step of iteration 3. The *a priori* covariance (blue) is the post-fit covariance from iteration 1 (Figure 11). All ellipses are 2D projections of the 6D ellisoid given by the covariance matrices with $l^2 = 9$ (i.e., $p = 0.826$)

being more representative of large asteroids. In Table 3, this is listed for all three iterations as "Post/pre error", and it is clear to see how the first iteration provides a marginal improvement and it is only after the planetary initial states have been better solved that the post-fit overall accuracy is more significantly increased. The limited reach of the mass estimation improvements is also evinced by the last row of Table 3, showing how around 27% of asteroids get their true errors reduced by a post-to-pre error ratio smaller than 50%. As it can be seen in the left histogram of Figure 14, asteroids with more significant (e.g., < 90%) improvements are scarce.

Despite the limited global improvement expressed by this metric, Figure 13 evinces how it is significant for asteroids with particularly high true errors in the *a priori* model. A good indicator for this is the color shading, which displays the relative improvement of each individual asteroid: a stronger green therefore means that the GM error reduction is of a similar order of magnitude as the true mass itself. Among the first 50 asteroids with largest pre-fit true errors, stronger green is completely dominant,

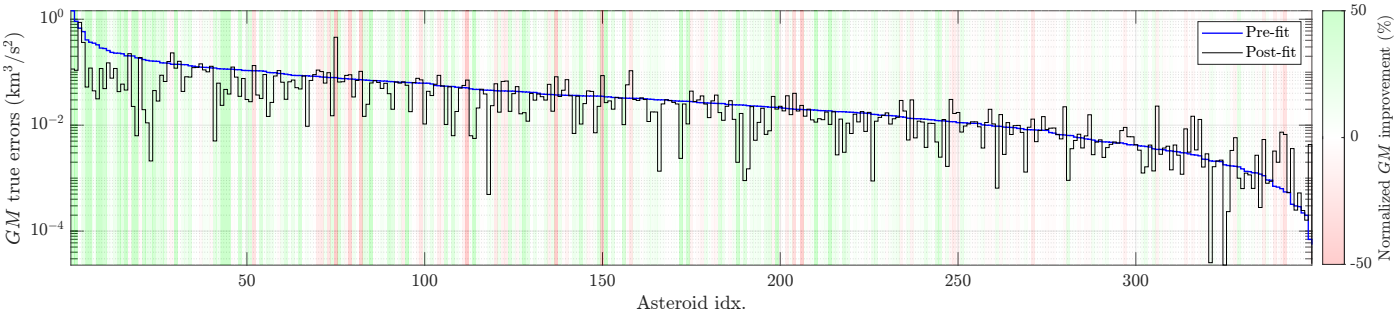

Fig. 13. Pre-fit (blue) and post-fit (black) absolute errors in individual asteroid GMs, in descending order of pre-fit true errors. Color shades indicate improvement (green) and worsening (red) of the estimated GMs, with color intensity proportional to the GM improvement (i.e., absolute value of pre-fit error minus absolute value of post-fit error) divided by the true GM. Color saturation happens at ±50%.

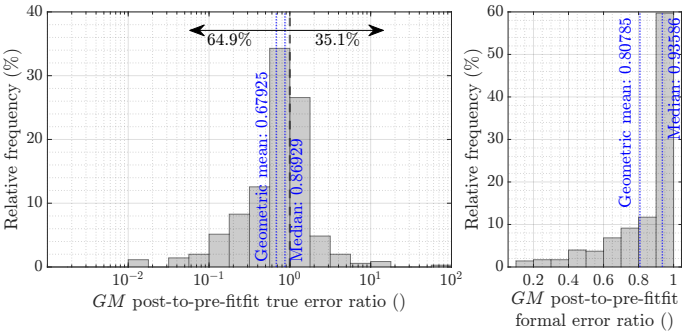

Fig. 14. Ratios of true (left) and formal (right) asteroid mass errors between the final iteration and the initial *a priori* model (section 3.3.1).

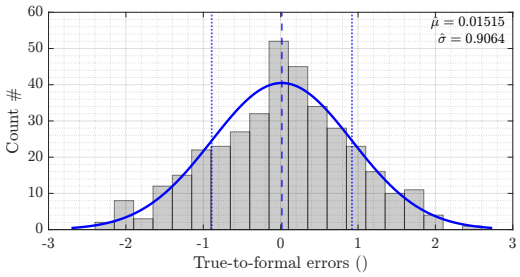

Fig. 15. Distribution of post-fit true-to-formal error ratios.

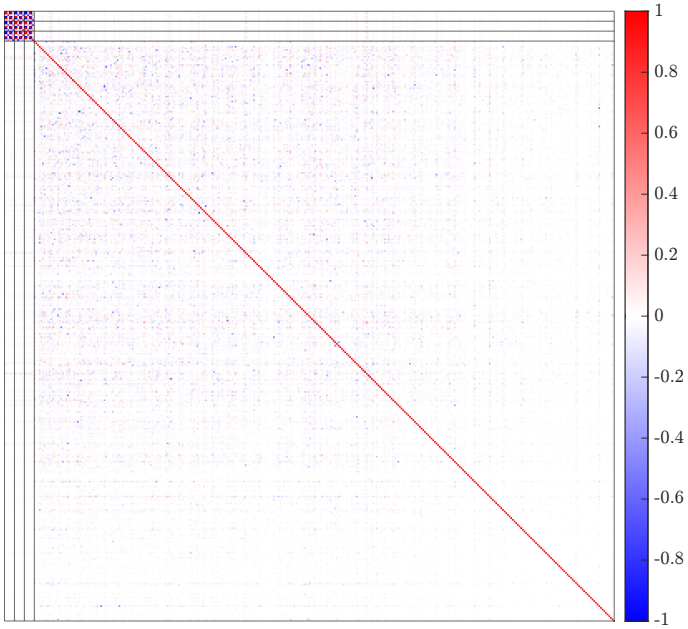

Fig. 16. Correlation matrix after iteration 3 of the 368 estimated parameters, including the initial states of Venus, the EMB and Mars together with the 350 asteroid masses.

and stronger red—indicating a significant worsening of the mass estimate relative to the true asteroid mass—is significantly less present in the whole figure. The dominant whiter shading corresponding to the ∼100 asteroids with smallest *a priori* errors, on the other hand, indicates that any significant improvements or worsenings in absolute mass are less relevant relative to the individual masses. These include asteroids with large masses and lighter asteroids with small true *a priori* errors.

Formal errors, as seen in the right histogram of Figure 14, mostly remain similar to the used *a priori* uncertainties, which are taken from the SiMDA catalog (section 2.1.2). This evinces how the information available in the observations, when weighted as detailed in section 4.1.1, is not enough to constrain the estimated mass uncertainty ranges in a significant manner. This is in clear contrast with the significant formal error reduction in asteroid masses found by Fienga (2023a) when studying the Trilogy concept in a preliminary manner, which is due to the fact that this study assumed true submillimetric (10^{-6}-10^{-4} m) precision and no systematic errors in the normal points to be used. With the bias formal errors and true-to-formal error ratios found in the present study, however, these assumptions are not found to be met.

Figure 15 shows the distribution of true-to-formal errors in the third (i.e., last) iteration of planetary estimation. This figure is expected to have the appearance of a standard normal distribution under correct performance of the batch estimator (Montenbruck & Gill 2001). Its consistent shape supports the validity of the planetary estimation results and, by extension, of the underlying assumptions such as the weighing of the observations based on the estimated true-to-formal error ratios (section 4.1.1).

Finally, the correlations between all estimated parameters are displayed in Figure 16 and Figure 17. Low correlations between asteroids are a result of the initial *a priori* constraint, which is diagonal. This can be seen to be more dominant the higher the asteroid index (i.e., lower in the covariance matrix) as evinced by the increasingly white color gradient from the top-left to the bottom-right. Since the asteroids have been ordered following their signal strength to the Trilogy legs (section 3.3.3), this appears to confirm that asteroids causing smaller signals are less likely to encode enough information to the measurements to introduce any improvement to the *a priori* constraint. The correlations between initial states of different planets, on the other hand,

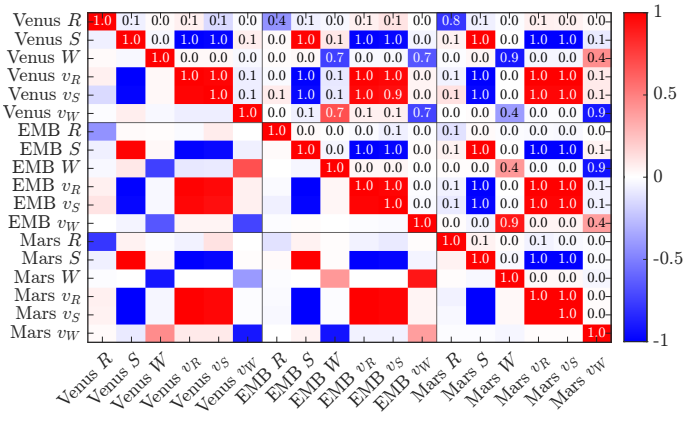

Fig. 17. Correlations of the estimated initial states displayed at the top left of Figure 16, transformed to the RSW frame

are more pronounced, consistently with being significantly narrowed from the *a priori* based on observations always involving two of the estimated bodies simultaneously. For every body, it is clear to observe how the correlations between R, S and W positions are low, consistently with the ellipses with axes parallel to these directions represented in the top plots of Figure 12. The high correlation between v_R and v_S, on the other hand, is clear from the inclined ellipses of the bottom-right quadrants. Finally, the null correlations between the W positions and all other variables of the planetary initial states are consistent with the fact that in this last iteration it has not modified its *a priori* covariance, as evinced by the overlapping pre- and post-fit covariances in W direction in Figure 12.

The correlations between the initial states of different bodies (i.e., off-diagonal blocks in the correlations matrix), which are not visualized in Figures 10-12, present the same correlation scheme between individual components. This suggests that the ellipsoid projections in the 2D subspaces equivalent to those plotted in the figures but with a different body at each axis would present a comparable appearance. These correlations might introduce the effect of some estimated initial state components of a body being wrongly absorbed by another one, but given that the true errors visualized in Figure 12 are caused by the estimated parameters remaining in their *a priori* value instead of mistakenly going to a wrong one, we do not judge this effect to play a significant role. Strategies to mitigate these correlations might include adding angular (i.e., VLBI) observations in the estimation, yet these are still not expected to fully remove correlations between the Earth and the other planets as long as these observations are Earth-based and the state of the EMB is still estimated.

4.2. Sensitivity to design parameters

All results presented above have been obtained with the nominal case configuration presented in section 3.3.3. In order to examine the sensitivity of the results to some of the design parameters, we also present summarized results after following the same procedure (section 3.2) with the modified cases below. Each of these is identical to the nominal, except for its own modified design parameter.

1. The **pessimistic** dynamical mismodeling scenario is used instead of the optimistic one.
2. All spacecraft orbits are fixed to **12 hour periods**. This means orbital altitudes of 18804 km, 20240 km and 9300 km, respectively, for the Venus, Earth and Mars spacecraft.
3. The random error of the Trilogy range measurements is increased from 3 mm to **3 cm**.
4. The *a priori* orbit determination uncertainty of the spacecraft is reduced from 1 km in RSW position and 0.1 mm/s in RSW velocity to **1 cm in RSW** position and 1 nm/s in RSW velocity.
5. The Mars spacecraft is placed at a lower altitude of **1350 km**, which has an orbital period of 2h 49'.

The summarized results for the final iteration of each subcase are presented in Table 4. The values listed under "normal point errors" correspond to the fitted standard deviations of true errors in the generated normal points, which for the nominal case are shown in Figure 7, and the results under "post-fit true errors" and "asteroid mass estimation" are the equivalent of Table 3. The results of the last iteration of the nominal case are reproduced in the first column to facilitate comparison.

4.2.1. Spacecraft dynamical mismodeling

The results of reproducing the same simulation but assuming the pessimistic spacecraft dynamical mismodeling scenario instead of the optimistic one (section 3.3.2), listed under case 1 in Table 4, evince how the generated normal points perform significantly worse, reaching order 10 cm. The Venus-Earth link, despite performing better than the other two, shows a ×27 worsening factor, and none of the three ranging links are found to yield normal points at the accuracy levels of the inter-spacecraft measurement system. Spacecraft OD errors, although not reproduced here for the sake of compactness, are between 10 cm and 1 m for most of the OD arcs even when all Trilogy links and Doppler observations are available.

The dramatically worse performance of asteroid mass estimations likely indicates the invalidity of the assumptions on true-to-formal errors when weighting the observations rather than an intrinsic limitation on the estimation capabilities with this range of normal point errors. We make this judgment based on the fact that the normal point errors through time, although not reproduced here as in Figure 7, appear to be nearly randomly distributed with few temporal modulation, but with a significantly larger spread, as seen in the $\hat{\sigma}$ values reported in Table 4. Hence, given that ILR observations have the same amount of noise and are thus weighted the same way, yielding to the same OD formal errors as in the nominal case, the true-to-formal error ratios are significantly larger than those shown in Figure 9. As described in section 4.1.1, poor observation weighting can cause the batch estimator to converge to false solutions, which is what we judge to happen in this case for the asteroid mass estimation.

The estimation of planetary initial states, on the other hand, performs comparably to the nominal case. This suggests that, unlike with the mass determination of most asteroids, the information encoded in the set of enclosed range measurements is enough to properly constrain the planetary motion—especially in the radial direction, and to some degree in the along-track direction. The only noticeable difference is the final true error of the planets' radial component of the initial state, which remains at the centimeter instead of millimeter level for Venus and the EMB (Table 4). This suggests that the larger normal point error might make it harder for the planetary estimation to reach such millimeter-level true errors, although the fact that the value corresponding to the radial initial state of Mars in does achieve a 5 mm true error indicates that this is not a hard limit and might be due to the statistical behavior of this particular tested case.

Table 4. Results on normal point precision, planetary initial state true errors and asteroid mass estimation improvements after the last iteration for the five variations of the nominal case configuration

		Nom.	**1** ↑ mismod.	**2** T = 12 h	**3** σ = 3 cm	**4** $\mathbf{P}_0 \sim 1$ cm	**5** $\downarrow h_{\mathrm{S/C\ Mars}}$	
Normal point errors ($\hat{\sigma}$)								
E-M-E		35.3	116.4	1.91	29.9	33.7	3.61	mm
V-E-V		2.3	62.1	1.79	4.2	2.3	5.38	mm
V-M-V		36.9	132.5	2.90	32.1	36.6	8.29	mm
Post-fit true errors								
Venus	R	0.0023	−0.0234	0.0094	−0.0021	0.0035	0.0068	m
	S	1.590	1.435	−7.431	2.535	1.601	61.757	m
	W	−57.629	−57.651	214.276	−51.862	−57.721	98.65	m
	v_R	−0.502	−0.444	2.374	−0.807	−0.506	−19.72	$\times 10^{-6}$ m/s
	v_S	−0.0032	0.0027	0.00057	−0.00079	−0.0034	−0.0291	$\times 10^{-6}$ m/s
	v_W	20.671	20.628	1.351	20.996	20.702	−51.491	$\times 10^{-6}$ m/s
EMB	R	0.00987	0.0216	0.00004	0.0110	0.0095	0.0013	m
	S	−4.493	−4.662	−3.461	−3.079	−4.479	98.206	m
	W	116.264	116.161	−210.221	111.450	116.439	−240.068	m
	v_R	0.922	0.950	0.708	0.630	0.920	20.219	$\times 10^{-6}$ m/s
	v_S	0.00072	0.0075	0.0027	0.0011	0.00022	−0.0167	$\times 10^{-6}$ m/s
	v_W	−2.514	−2.465	−40.978	−3.811	−2.516	14.241	$\times 10^{-6}$ m/s
Mars	R	−0.0113	−0.0049	−0.0102	−0.0052	−0.010	−0.0066	m
	S	−3.080	−3.407	−4.590	−0.602	−3.054	154.851	m
	W	59.325	60.124	−450.774	46.600	59.638	52.535	m
	v_R	0.276	0.319	0.410	0.060	0.274	−13.701	$\times 10^{-6}$ m/s
	v_S	0.00102	0.0128	0.0094	−0.0029	0.00008	−0.266	$\times 10^{-6}$ m/s
	v_W	−16.779	−16.773	17.723	−16.459	−16.815	37.589	$\times 10^{-6}$ m/s
Asteroid mass estimation								
% improved		64.9	35.1	63.1	62	64	62.6	%
Pre/post true error		0.869	1.33	0.928	0.933	0.9315	0.948	
Pre/post formal error		0.936	0.936	0.935	0.974	0.946	0.943	
% Pre/post true <50%		27.14	15.43	22.86	20.29	26.00	23.43	%

4.2.2. Spacecraft orbital altitude/period

In the nominal case, where all spacecraft are placed at 10000 km altitudes, their orbital periods are 6h 14' 5h 47' and 13h 11', respectively, for Venus, Earth and Mars spacecraft. These have been checked to remain essentially constant throughout the whole mission duration, even with all orbital perturbations at play. A reasonable explanation for the reason behind the Martian normal points being significantly worse than for Earth-Venus (Figure 7) is that the OD arcs of 12 h are long enough to let the OD position error average out along two almost complete orbits for Venus, whereas they are less than an entire orbital revolution long for the Martian spacecraft and therefore this averaging is not achievable to the same extent. To test the validity of this hypothesis, simulation case 2 assesses a similar scenario but with all spacecraft forced to follow 12-hour period orbits. It is clear from its results in Table 4 how this produces the highest-quality normal points, with the three legs reaching millimeter levels below the actual random error of the ranging system. The figures equivalent to Figure 5 and Figure 7 are not reproduced here for the sake of compactness, but we point out how the resulting distribution of normal point errors through time does not show strong temporal modulation and it is more similar to pure random noise.

The interpretation that follows is that taking OD arc durations that do allow for at least one full spacecraft orbit revolution does have the effect of improving the generated normal points by enabling the averaging of OD position errors, yet the generalization must be done with care since it might be strongly dependent on the exact assumptions considered for this simulation case. Particularly, we assess the remaining dynamical mismodeling by adding an empirical acceleration that has two out of three components oscillating cyclically with the true anomaly (equation 15), hence with the orbital period. To further assess this fact, we simulate a last subcase, number 5, which is identical to the nominal except for the Martian spacecraft being placed at a much lower orbit of 1350 km, which is equivalent to a period of 2h 49'.

The results listed in Table 4 evince how the true normal point errors arising from this case do degrade with respect to the case where all spacecraft followed 12-hour periods, which is in accordance with the claims on the dependence of the empirical acceleration cycle stated above. However, the normal points of the three ranging legs still achieve sub-centimeter levels, improving the results from the nominal case for the Earth-Mars and Venus-Mars spacecraft and hence suggesting that letting the OD position error average out through at least one complete revolution is beneficial. It is nevertheless important to note that such

a low orbit around Mars would make our considered optimistic dynamical mismodeling case very unrealistic, and further variations of the design variables should be analyzed, together with different mismodeling assumptions, to confirm what orbital configuration around the Red Planet is optimal for the production of high-quality normal points.

4.2.3. Measurement errors

The tested subcase number 3 used a random noise for the ranging system with a standard deviation of 3 cm instead of 3 mm, which is achievable with state of the art radiometric ranging (e.g., Cascioli et al. 2019; di Stefano et al. 2023). The results listed in Table 4 show how the worsening of the resulting normal points is not dramatic, with the best case (Earth-Venus link) increasing from 2.3 to 4.2 mm with respect to the nominal case. The observed performance in the estimation of planetary initial states is essentially equivalent, while the improvement of asteroid mass estimations is more noticeably degraded, reaching a post-to-pre-fit true error ratio of 0.93 instead of the nominal 0.87. This evinces how sensitive the estimation of asteroid masses is to the error levels of the used normal points, yet we acknowledge that this might be subject to the exact specifications of our estimation setup (e.g., number of asteroids estimated, exact values of *a priori* constraints) and thus might not be a conclusion extensible to the setups of modern state of the art ephemerides.

An important argument against the usage of radio-based ranging is pointed out by Smith et al. (2018), who mention the need for large spacecraft antennae, in contrast to ILR. In a planetary orbit where blackbody radiation and eclipses come into play, this can introduce significant dynamical modeling challenges, and hence make the optimistic scenario used for this simulation subcase too irrealistic. Notably, when the pessimistic scenario is at use, as seen in section 4.2.1, the spacecraft OD error becomes a much more dominant source of error to the normal points than the actual ranging error.

The other error component that deserves attention is the contribution of systematic errors. In this study, we assumed them to be constant throughout the whole mission and this is seen as a clear mean shift in the normal point true errors (Figure 7). If systematic errors were instead randomly re-initialized at each OD arc, this would appear as an increased random noise in the final normal point error distribution, which would in turn present an equivalent performance similar to the results shown in this particular subcase. In reality, the behavior of systematic errors is likely to behave somewhere in between, and more advance modeling techniques can be employed to mitigate them further.

As a test exercise, we ran the same planetary estimation from the third iteration of the nominal case but removing the systematic error contribution to the normal points (i.e., shifting them by 3.6 mm). The results behave virtually identically, also achieving to improve 64.9% of asteroid mass estimations. The conclusion that follows is that systematic errors present in state of the art ILR are not expected to be a dominant error source in the estimation of planetary variables from range measurements.

4.2.4. Spacecraft prior orbit determination uncertainty

The tested subcase number 4 is equivalent to the nominal one but with a spacecraft prior uncertainty if 1 cm in RSW position instead of 1 km. This follows the assumption of an already-conducted precise OD being available as *a priori*, with an accuracy level similar to that expected for instance, from a GNSS system around Mars (Kozar et al. 2016). As observed in the resulting normal point errors and post-fit true errors (Table 4), this behaves essentially identically to the nominal case, meaning that such *a priori* covariance is not enough to effectively constrain the resulting spacecraft OD error to smaller levels. This is because the covariance component arising from the observations is still smaller than an an *a priori* of order 1 cm in position, which is due to the high weighting of the range observations in accordance with their millimeter-level errors. This is a clear case of post-fit covariance resulting from observations being too optimistic due to not taking dynamical mismodeling into account.

Some trial and error has evinced how, in order to constrain the spacecraft to its true trajectory—hence making the *a priori* contribution more dominant than the observations—the levels of position uncertainty to introduce are completely unrealistic, going down to micrometric levels. The conclusion that follows is that we do not expect to achieve better performance of the normal point generation procedure by running the estimation algorithm after a previous precise orbit determination has already narrowed the true errors in spacecraft position to the limits achievable by the state of the art.

5. Conclusions and recommendations

This study had the aim of simulating a realistic operational scenario for the Trilogy mission concept as suggested by Smith et al. (2018) to assess the expected improvement in the ephemerides estimation of Venus, the Earth and Mars and whether or not the current uncertainties of asteroid masses can potentially be reduced as much as predicted by the covariance analysis performed by Fienga (2023a). We have conducted this assessment by simulating the classical method for normal point generation from unconstrained multi-arc spacecraft orbit determination, which we perform to the two interplanetary spacecraft simultaneously while including the range measurements from the three Trilogy legs.

Our results suggest that the presence of the range constraint in two different spatial directions can significantly improve the orbit determination of the interplanetary orbiters, constraining their true 3D position errors to cm levels as compared to the errors 10-100 times larger when using only Doppler observations or Doppler combined with range from the same direction. This level of interplanetary spacecraft true errors has the potential of enabling the generation of planet-to-planet two way ranges accurate to a few millimeters.

This result is highly dependent, however, on the exact configuration of spacecraft orbits and any remaining errors in their force models. We find these millimeter-level normal points to be achievable in cases where residual accelerations are of the order of 10^{-11} m/s^2, which is optimistic but within the limits of the state of the art as long as the dynamical model is not corrupted by significant eclipses and planetary radiation (e.g., di Stefano et al. 2023). Moreover, we assumed this remaining mismodeled acceleration to be composed of a sum of constant and periodic terms following the spacecraft orbital period, and it remains to be seen how the results are affected with higher frequencies of residual forces. A mismodeling of order 2% of the Solar Radiation Pressure coefficient, on the other hand, appears to be enough to worsen the generated normal points up to the several centimeter level, making the usage of laser ranging less relevant as opposed to traditional radio-based ranging, which is already able to achieve this range of error levels. This evinces how the spacecraft dynamical modeling is expected to be a strong limitation in the generation of planet-to-planet ranges, and we encourage

further analyses to assess middle ground scenarios and more sophisticated forms of dynamical mismodeling (e.g., adding higher frequency unmodeled accelerations) to determine the exact requirements the Trilogy mission shall fulfill.

Regarding orbital configuration, we find that allowing the length of the spacecraft OD arcs include at least a full orbit revolution seems to help mitigate the impact of the positioning error to the generated normal points. As per the spacecraft orbit configuration, we notice that the quality of the spacecraft OD in the direction of a given range link seems to maximize the more perpendicular such range link is to the orbital plane of the spacecraft. When this geometry is fulfilled, the generated normal points appear to be able to reach single-mm precision levels as long as there are no dynamical mismodelings that significantly worsen the estimation. This opens the possibility of optimization problems that aim to maximize this effect as much as possible for the three legs during the whole mission duration, taking into account the dynamical evolution of the orbital planes when subject to orbit perturbations.

Another important line to assess in future studies is related to the orbit determination of the Earth spacecraft, which we have considered to be fully known around the Earth-Moon system given the availability of GNSS. Our finding of the interplanetary spacecraft achieving centimeter-level orbit determination errors needs to be assessed when introducing the uncertainties around the Earth vertex as well. These should include the inclusion of GNSS and/or Satellite Laser Ranging signals to the Earth spacecraft during the simultaneous orbit determination we simulated, together with the uncertainties in the positioning of the Earth around the Earth-Moon barycenter. This analysis could include the assessment on the suggestion by Smith et al. (2018) to let the Earth vertex of Trilogy be an orbiter around the Moon instead, with potential scientific output for the Earth-Moon system when complemented with Lunar Laser Ranging.

When using the generated normal points to constrain Solar System dynamics, we find that the positions of Venus, the EMB and Mars can be narrowed down to millimetric levels in their radial directions and 1-10 meter levels in along track directions, whereas cross-track is found to be less constrained and true errors of order 100 meters can easily remain. At 1AU, these 100 m are at the measurement limits for highly accurate angular observations using VLBI (e.g., Jones et al. 2014), with the most optimistic future prospects expecting to improve by one order of magnitude (Gurvits et al. 2023). To assess how Trilogy at its full potential compares, we suggest to study the performance of the mission with one of the vertices placed at a higher inclination orbit, as suggested by Bills & Gorski (2022). It is also important to note that the final error levels of the planetary initial states appear to be achievable even in the tested cases with higher ranging error or spacecraft force model errors, which evinces how these achievable error levels come from the large-scale mission parameters (namely, duration and measurement configuration) rather than from the usage of highly precise laser ranging.

As per the constraints on the asteroid masses, the quality of the generated measurements is found to allow modest improvements only with respect to the present uncertainties, achieving post-to-pre errors of around 0.8-0.9 and only some tens of asteroids getting their true errors reduced by more than 50%. Despite most of the ~400 cataloged asteroids are found to affect the interplanetary ranges with amplitudes greater than the error levels of the used normal points (Figure 3), the batch estimation fails to accurately converge to the true solution for a significant portion of them. This evinces how the measurements used, with their found levels of error and according weighting, do not encode enough information to significantly reduce their *a priori* constraints, which is in contrast with the covariance analysis performed by Fienga (2023a). The reason of this discrepancy is that this study assumed sub-millimetric normal point accuracy, which we find to be virtually impossible to achieve on a regular basis with the mission configuration tested in our work.

Future studies shall address the optimization of the orbital configuration to maximize the quality of the generated normal points and confirm whether or not sub-millimetric levels are achievable for the entire mission time span. Further refined approaches may include constrained multi-arc spacecraft orbit determination (Alessi et al. 2012), which has the potential of taking advantage of the information of planetary dynamics encoded in the long-term evolution of the spacecraft orbits. Coupling the estimation of the spacecraft and planetary dynamics, as suggested by Dirkx et al. (2019), can also improve the results of planetary estimation by making its errors less dependent on the spacecraft orbit determination error—which, as shown above, is a strong limiting factor for the quality of the produced normal points. Although coupled analyses have been confirmed to reduce such dependency (Genova et al. 2018), it remains to be tested whether or not this still marks a significant difference with respect to following the classical approach when using not one but two simultaneous high-precision ranging links.

Acknowledgements. Part of this work was supported by the Europe-Colorado Program of the University of Colorado Boulder and the FAST Student funding by Delft University of Technology.

References

Abich, K., Abramovici, A., Amparan, B., et al. 2019, Phys. Rev. Lett., 123, 031101
Abshire, J. B., Sun, X., Neumann, G., et al. 2006, in Conference on Lasers and Electro-Optics/Quantum Electronics and Laser Science Conference and Photonic Applications Systems Technologies (Optica Publishing Group), CThT6
Alessi, E. M., Cicalò, S., Milani, A., & Tommei, G. 2012, Monthly Notices of the Royal Astronomical Society, 423, 2270
Andolfo, S., Genova, A., & Del Vecchio, E. 2024, Journal of Guidance, Control, and Dynamics, 47, 518
Armano, M., Audley, H., Auger, G., et al. 2016, Phys. Rev. Lett., 116, 231101
Asmar, S., Preston, R., Vergados, P., et al. 2021, Bulletin of the American Astronomical Society, 53
Baer, J. & Chesley, S. R. 2017, The Astronomical Journal, 154, 76
Bassi, A., Cacciapuoti, L., Capozziello, S., et al. 2022, A way forward for fundamental physics in space
Bauer, S., Hussmann, H., Oberst, J., et al. 2017, Icarus, 283, 38
Bernus, L., Minazzoli, O., Fienga, A., et al. 2020, Physical Review D, 102
Bertotti, B., Iess, L., & Tortora, P. 2003, Nature, 425, 374
Bhattarai, S., Ziebart, M., Springer, T., Gonzalez, F., & Tobias, G. 2022, Advances in Space Research, 69, 4141
Bills, B. G. & Gorski, K. M. 2022, Planetary and Space Science, 215, 105423
Bills, B. G. & Skillman, D. 2022, Planetary and Space Science, 214, 105415
Birch, M. & Singh, B. 2014, Nuclear Data Sheets, 120, 106
Birnbaum, K. M., Chen, Y., & Hemmati, H. 2010, 7587, 86
Biswas, A., Srinivasan, M., Andrews, K., et al. 2024a, in Free-Space Laser Communications XXXVI, ed. H. Hemmati & B. S. Robinson, Vol. 12877, International Society for Optics and Photonics (SPIE), 1287706
Biswas, A., Srinivasan, M., Wollman, E., et al. 2024b, in Advanced Photon Counting Techniques XVIII, ed. M. A. Itzler, J. C. Bienfang, & K. A. McIntosh, Vol. 13025, International Society for Optics and Photonics (SPIE), 1302508
Bock, H., Jäggi, A., Beutler, G., & Meyer, U. 2014, Journal of Geodesy, 88, 1047
Border, J. S., Paik, M., Lee, C., Shin, D. K., & Volk, C. P. 2020, IPN Progress Report, 42
Cappuccio, P., Hickey, A., Durante, D., et al. 2020, Planetary and Space Science, 187, 104902
Carry, B. 2012, Planetary and Space Science, 73, 98
Cascioli, G. & Genova, A. 2021, Journal of Spacecraft and Rockets, 58, 581
Cascioli, G., Marchi, F. D., Genova, A., et al. 2019, in 2019 IEEE 5th International Workshop on Metrology for AeroSpace (MetroAeroSpace), 579–583

Chabé, J., Courde, C., Torre, J.-M., et al. 2020, Earth and Space Science, 7, e2019EA000785, e2019EA000785 10.1029/2019EA000785
Chesley, S. R., Farnocchia, D., Nolan, M. C., et al. 2014, Icarus, 235, 5
Chesley, S. R., Ostro, S. J., Vokrouhlický, D., et al. 2003, Science, 302, 1739
Christensen-Dalsgaard, J. 2021, Living Reviews in Solar Physics, 18, 2
Christophe, B., Boulanger, D., Foulon, B., et al. 2015, Acta Astronautica, 117, 1
Combrinck, L. 2010, Sciences of Geodesy - I: Advances and Future Directions, 301
Danzmann, K. 2000, Advances in Space Research, 25, 1129, fundamental Physics in Space
Davis, B. & Gunter, B. C. 2022, Journal of Guidance, Control, and Dynamics, 45, 2403
De Marchi, F., Tommei, G., Milani, A., & Schettino, G. 2016, Phys. Rev. D, 93, 123014
Degnan, J. J. 1996, in Proc. 10th International Workshop on Laser Ranging. Shanghai, China, 11–15
Degnan, J. J. 2002, Journal of Geodynamics, 34, 551
Degnan, J. J. 2007, International Journal of Modern Physics D, 16, 2137
Dehant, V., Park, R., Dirkx, D., et al. 2017, Space Science Reviews, 212, 1433
Deram, P., Fienga, A., Verma, A. K., Gastineau, M., & Laskar, J. 2022, Celestial Mechanics and Dynamical Astronomy, 134, 1
di Ruscio, A., Fienga, A., Durante, D., et al. 2020, Astronomy & Astrophysics, 640, A7
di Stefano, I., Cappuccio, P., & Iess, L. 2023, Journal of Spacecraft and Rockets, 60, 1625
Dirkx, D. 2015, PhD thesis, Delft University of Technology
Dirkx, D. 2022, Tudat mathematical model definition, Tech. rep., Delft University of Technology
Dirkx, D., Noomen, R., Prochazka, I., Bauer, S., & Vermeersen, L. L. 2014a, Advances in Space Research, 54, 2349
Dirkx, D., Noomen, R., Visser, P. N., Bauer, S., & Vermeersen, L. L. 2015, Planetary and Space Science, 117, 159
Dirkx, D., Noomen, R., Visser, P. N. A. M., Gurvits, L. I., & Vermeersen, L. L. A. 2016, A&A, 587, A156
Dirkx, D., Prochazka, I., Bauer, S., et al. 2019, Journal of Geodesy, 93, 2405
Dirkx, D., Vermeersen, L. L., Noomen, R., & Visser, P. N. 2014b, Planetary and Space Science, 99, 84
Duev, D. A., Calvés, G. M., Pogrebenko, S. V., et al. 2012, Astronomy & Astrophysics, 541, A43
Exertier, P., Bonnefond, P., Deleflie, F., et al. 2006, Comptes Rendus Geoscience, 338, 958
Farnocchia, D., Chesley, S. R., Takahashi, Y., et al. 2021, Icarus, 369, 114594
Farnocchia, D., Fuentes-Muñoz, O., Park, R. S., Baer, J., & Chesley, S. R. 2024, The Astronomical Journal, 168, 21
Fayolle, M., Dirkx, D., Lainey, V., Gurvits, L., & Visser, P. 2022, Planetary and Space Science, 219, 105531
Ferus, M., Žabka, J., Schmidt, N., & Heays, A. 2022, Asteroid Prospecting and Space Mining, ed. N. Schmidt (Cham: Springer International Publishing), 217–232
Fienga, A. 2023a
Fienga, A. 2023b, in Interplanetary Trilateration Network Workshop
Fienga, A., Avdellidou, C., & Hanuš, J. 2020a, Monthly Notices of the Royal Astronomical Society, 492, 589
Fienga, A., Bigot, L., Mary, D., et al. 2019a, Proceedings of the International Astronomical Union, 15, 31
Fienga, A., Deram, P., Ruscio, A. D., et al. 2021, INPOP21a planetary ephemerides, Scientific and technical notes S110, Institut de Mécanique Céleste et de Calculs des Éphémérides (IMCCE)
Fienga, A., Deram, P., Viswanathan, V., et al. 2019b, INPOP19a planetary ephemerides, Scientific and technical notes S109, Institut de mécanique céleste et de calculs des éphémérides
Fienga, A., Laskar, J., Exertier, P., Manche, H., & Gastineau, M. 2015, Celestial Mechanics and Dynamical Astronomy, 123, 325
Fienga, A. & Minazzoli, O. 2024, Living Reviews in Relativity 2024 27:1, 27, 1
Fienga, A., Ruscio, A. D., Bernus, L., et al. 2020b, Astronomy & Astrophysics, 640, A6
Folkner, W. M., Williams, J. G., Boggs, D. H., Park, R. S., & Kuchynka, P. 2014, Interplanetary Network Progress Report, 196, 42
Fuentes-Muñoz, O., Farnocchia, D., Naidu, S. P., & Park, R. S. 2024, The Astronomical Journal, 167, 290
Gaia Collaboration. 2016, Astronomy & Astrophysics, 595, A1
Galád, A. & Gray, B. 2002, Astronomy & Astrophysics, 391, 1115
Genova, A., Mazarico, E., Goossens, S., et al. 2018, Nature communications, 9, 289
Giorgini, J. D. 2015, in IAU General Assembly, Vol. 29, 2256293
Gomes, D. C. H., Murray, Z., Gomes, R. C. H., Holman, M. J., & Bernstein, G. M. 2023, The Planetary Science Journal, 4, 66
Gurvits, L. I., Cimò, G., Dirkx, D., et al. 2023, Space Science Reviews 2023 219:8, 219, 1
Hestroffer, D., Sánchez, P., Staron, L., et al. 2019, The Astronomy and Astrophysics Review, 27, 6
Hill, K. & Born, G. H. 2007, Journal of Guidance, Control, and Dynamics, 30, 679
Hohmann, M. 2021, Parametrized Post-Newtonian Formalism, ed. E. N. Saridakis, R. Lazkoz, V. Salzano, P. V. Moniz, S. Capozziello, J. Beltrán Jiménez, M. De Laurentis, & G. J. Olmo (Cham: Springer International Publishing), 357–373
Hugentobler, U. & Montenbruck, O. 2017, Satellite Orbits and Attitude, ed. P. J. Teunissen & O. Montenbruck (Cham: Springer International Publishing), 59–90
Hładczuk, N., van den IJssel, J., Kodikara, T., Siemes, C., & Visser, P. 2024, Advances in Space Research, 73, 2355
Imperi, L., Iess, L., & Mariani, M. J. 2018, Icarus, 301, 9
Jain, R., Speretta, S., Dirkx, D., & Gill, E. 2024, Advances in Space Research, 74, 3877
Jones, D. L., Folkner, W. M., Jacobson, R. A., et al. 2014, The Astronomical Journal, 149, 28
Konopliv, A., Park, R., & Ermakov, A. 2020, Icarus, 335, 113386
Konopliv, A. S., Asmar, S. W., Folkner, W. M., et al. 2011, Icarus, 211, 401
Kozar, J., Durco, S., & Adamcik, F. 2016, Aviation, 20, 183
Kretlow, M. 2020, in EPSC2020-690, Vol. 14, Europlanet Science Congress 2020 (Copernicus GmbH), virtual meeting, 21 September–9 October 2020
Kuchynka, P. & Folkner, W. M. 2013, Icarus, 222, 243
Lari, G. & Milani, A. 2019, Planetary and Space Science, 176, 104679
Lawson, C. L. & Hanson, R. J. 1995, Solving least squares problems (SIAM)
Lee, J., Kim, Y.-J., Lee, K., Lee, S., & Kim, S.-W. 2010, Nature photonics, 4, 716
Li, F., Yuan, Y., Fu, Y., & Chen, J. 2023, The Astronomical Journal, 166, 93
Li, Z., Ziebart, M., Bhattarai, S., Harrison, D., & Grey, S. 2018, Advances in Space Research, 61, 2352
Liu, N., Zhu, Z., Antoniadis, J., Liu, J. C., & Zhang, H. 2023, Astronomy & Astrophysics, 674, A187
Liu, S., Fienga, A., & Yan, J. 2022, Icarus, 376, 114845
Mariani, V., Minazzoli, O., Gastineau, M., & Laskar, J. 2023, Physical Review D, 108
Mazarico, E., Zuber, M. T., Lemoine, F. G., & Smith, D. E. 2009, Journal of Spacecraft and Rockets, 46, 662
Milani, A. & Gronchi, G. 2010, Theory of orbit determination (Cambridge University Press)
Montenbruck, O. & Gill, E. 2001, Satellite orbits: models, methods, and applications, 2nd edn., Physics and Astronomy (Springer)
Moyer, T. D. 2005, Formulation for observed and computed values of Deep Space Network data types for navigation (John Wiley & Sons)
Murphy, T. W. 2013, Reports on Progress in Physics, 76, 076901
Murray, Z. 2023, The Planetary Science Journal, 4, 239
Müller, J., Hofmann, F., Fang, X., & Biskupek, L. 2014, 447
Nandy, D., Martens, P. C. H., Obridko, V., Dash, S., & Georgieva, K. 2021, Progress in Earth and Planetary Science 2021 8:1, 8, 1
Noda, H., Kunimori, H., Mizuno, T., et al. 2017, Earth, Planets and Space, 69, 1
Noda, H., Senshu, H., Otsubo, T., et al. 2023, Advances in Space Research, 71, 4196
Notaro, V., Durante, D., & Iess, L. 2019, Planetary and Space Science, 175, 34
Park, R. S., Folkner, W. M., Konopliv, A. S., et al. 2017, The Astronomical Journal, 153, 121
Park, R. S., Folkner, W. M., Williams, J. G., & Boggs, D. H. 2021, The Astronomical Journal, 161, 105
Pinto, R. F., Brun, A. S., Jouve, L., & Grappin, R. 2011, The Astrophysical Journal, 737, 72
Pitjeva, E. V. 2015, Journal of Physical and Chemical Reference Data, 44, 031210
Pitjeva, E. V., Pavlov, D., Aksim, D., & Kan, M. 2019, Proceedings of the International Astronomical Union, 15, 220–225
Pitjeva, E. V. & Pitjev, N. P. 2012, Solar System Research, 46, 78
Pitjeva, E. V. & Pitjev, N. P. 2015, Proceedings of the International Astronomical Union, 10, 212–217
Pitjeva, E. V. & Pitjev, N. P. 2018, Astronomy Letters, 44, 604
Pitjeva, E. V., Pitjev, N. P., Pavlov, D. A., & Turygin, C. C. 2021, Astronomy & Astrophysics, 647, A141
Reinhardt, J. N., Staab, M., Yamamoto, K., et al. 2024, Phys. Rev. D, 109, 022004
Rosenblatt, P., Dumoulin, C., Marty, J.-C., & Genova, A. 2021, Remote Sensing, 13
Santoli, F., Fiorenza, E., Lefevre, C., et al. 2020, Space Science Reviews, 216, 145
Schreiber, K. U., Kodet, J., Rodrigo, R., et al. 2018, Space Sci Rev, 214, 22
Shoemaker, M., Van Der Ha, J. C., & Morley, T. 2012, Journal of Spacecraft and Rockets, 49, 212

Smith, D. E., Zuber, M. T., Mazarico, E., et al. 2018, Planetary and Space Science, 153, 127
Smith, D. E., Zuber, M. T., Sun, X., et al. 2006, Science, 311, 53
Somenzi, L., Fienga, A., Laskar, J., & Kuchynka, P. 2010, Planetary and Space Science, 58, 858
Tapley, B. D., Schutz, B. E., & Born, G. H. 2004, Statistical orbit determination (Elsevier Academic Press)
Thorpe, J. I. 2010, Classical and Quantum Gravity, 27, 084008
Tian, W. 2023, Celestial Mechanics and Dynamical Astronomy 2023 135:4, 135, 1
Turyshev, S. G., Farr, W., Folkner, W. M., et al. 2010, Experimental Astronomy, 28, 209
Wakker, K. F. 2015, Fundamentals of astrodynamics (TU Delft Repository, Delft)
Walker, M. J. 1986, Celestial Mechanics, 38, 391
Walker, M. J., Ireland, B., & Owens, J. 1985, Celestial Mechanics, 36, 409
Wenxiao, L., Jinsong, P., & Wenzhao, Z. 2021, Journal of University of Chinese Academy of Sciences, 38, 114
Wie, B., Zimmerman, B., Lyzhoft, J., & Vardaxis, G. 2017, Astrodynamics, 1, 3
Wilkinson, M., Schreiber, U., Procházka, I., et al. 2019, Journal of Geodesy, 93, 2227
Will, C. M. 2014, Living Reviews in Relativity 2014 17:1, 17, 1
Yan, J., Yang, X., Ye, M., et al. 2017, Astrophysics and Space Science, 362, 123
Yang, P., Huang, Y., Li, P., et al. 2022, Advances in Space Research, 69, 1060
Zenk, K., Dirkx, D., & Fayolle, M. 2023, Master's thesis, Delft University of Technology, Delft, Netherlands, available at TU Delft repository

Part V

Conclusions

8

Conclusions

8.1. Overview

The Trilogy mission concept has been assessed to possess significant scientific potential by a number of different studies addressing different research sub-fields (section 2.1). Among these, the improvement of current constraints in estimated masses of asteroids is one with a potential high impact, not only due to the possibility to improve our understanding of Solar System bodies but due to its current effect in hindering estimations of other unknowns such as solar mass variation (section 5.5.1) or relativistic parameters (section 5.5.3).

Asynchronous two-way interplanetary laser ranging (ILR) has been confirmed to have the potential to enable range measurements accurate to sub-centimeter levels (section 3.2.2), which is within the required quality to reduce several of present Solar System dynamical uncertainties. Despite the lack of past missions fully dedicated to ILR, the technology is mature and different experimental tests have proven its feasibility (section 3.3.2).

Although future missions employing ILR have been suggested to require the coupling of the computation of both natural and artificial bodies in a single estimation to take the most scientific output out of the generated data (section 4.2.2), in this work we followed the classical approach of generating planet-to-planet ranges based on an independent, multi-arc estimation of the interplanetary spacecraft (Algorithm 6). The novelty is the usage of three ranging legs simultaneously, which links the orbit determination of the different spacecraft (section 7.2). The results have suggested how this suffices to generate highly accurate planet-to-planet ranges (in the most optimistic cases, down to the level of millimetric true errors; section 7.2.3), which can subsequently be used in a batch estimation of ephemerides and asteroid masses. The conclusions following from this are detailed in more detail below (section 8.2) and in section 5 in Part IV.

8.2. Response to the research questions

1. **What is the expected sensitivity of Trilogy to the present uncertainty in asteroid masses?**

   As observed thanks to the computed pre-fit signatures of the asteroids with cataloged masses to the interplanetary distances of the three Trilogy vertices (figures 6.2 and 6.3 and table 6.2), most of the asteroids for which mass estimations exist are expected to cause perturbations of an amplitude above the limits in measurement quality theoretically achievable by ILR over a mission of five years. Such measurement quality is also below the amplitude of the uncertainty ranges of such signals caused by the mass uncertainties of many asteroids (Figure 3 in Part IV), which suggests that such measurements have the potential of constraining them further.

   Additionally, light asteroids for which mass estimates do not exist (i.e., the bulk of bodies with masses between 10^{-3} and 10^{-2} km^3/s^2) are expected to perturb the Venus-Mars and Earth-Mars range legs with amplitudes above 1 cm (Figure 6.5), which is also within the capabilities of the ILR technology and within the limit of achievable quality of generated planet-to-planet ranges under the tested simulation scenario (Part IV). In summary, it is safe to conclude that the Trilogy mission, as suggested by Smith et al. (2018), is significantly sensitive to the effects of a quantity of asteroids that outnumbers the extension of existing asteroid mass catalogs. Direct alternative methods for asteroid mass estimations, which mainly consist of astrometric observations (section 5.2), are not expected to be as sensitive to such a high number of asteroids in the next few years (section 2.1.2 in Part IV)

2. **How well can the existence of enclosed, highly accurate inter-satellite range measurements at interplanetary distances improve the spacecraft orbit determination and the quality of the generated planet-to-planet ranges?**

The main finding reported from the results of the main simulation scenario carried out in this work is that the presence of the highly accurate range constraint from different spatial directions has the potential of containing the true 3D errors of interplanetary spacecraft to the few centimeter level, which represents an improvement of between one and two orders of magnitude with respect to the traditional approach of using range-rate measurements alone or range-rate combined with range from a single spatial direction (subsection 7.2.3). This allows the generation of planet-to-planet ranges accurate to few mm, although under the tested simulation settings this is found subject to two conditions: first, planet-to-planet ranges are found to achieve these quality levels if the spacecraft orbit determination arcs in which they are obtained last (close to) one orbital revolution, which allows the impact of the accumulated orbit determination error to average out to some extent (section 4.2.2 in Part IV). Second, these error levels have been found to arise with a spacecraft dynamical mismodeling of order 10^{-11} m/s^2 and acting in constant components and oscillatory components with the period of the spacecraft orbit around their host planet. Higher levels of dynamical mismodeling (i.e., including residual accelerations 50-100 times higher), on the other hand, are found to degrade the spacecraft orbit determination further, but still perform significantly better than in the cases where range constraints from two directions are not available, containing true errors below 1 m (Figure 7.13). The resulting planet-to-planet ranges in this case are produced with an accuracy of some centimeters, also showing signs to improve with a full averaging over one orbit determination arc (Figure 7.14) Finally, it is relevant to mention that in the favorable cases where spacecraft orbit determination is constrained to the cm level thanks to the two range constraints and no significant mismodeling, planet-to-planet ranges are found to be best reconstructed when the corresponding inter-spacecraft link is nearly perpendicular to the orbital plane of the spacecraft at its ends (Figures 5-6 in Part IV). This opens the door for optimization problems that can seek to exploit this behavior as much as possible, which we leave for future work (section 8.3).

3. **Is this measurement quality enough to get current uncertainty levels in planetary ephemerides and asteroid masses significantly reduced by using a straightforward batch estimation?**

   When applying the planet-to-planet ranges resulting from the implemented simulation scenario, the planetary ephemerides have been found to significantly reduce current uncertainties in the radial directions of the Trilogy planet positions, reaching millimeter-level errors, whereas cross-track errors mainly remain in the order of 100 meters and along track errors are found to result in a middle ground between the two (Figure 12 in Part IV). On the other hand, most of the estimated asteroid masses do not become significantly reduced from current uncertainty levels (Tables 3-4 in Part IV), which indicates that the Trilogy mission, at least in its variant of five years duration obtaining one daily precise planet-to-planet range under the estimation settings employed in this study, is not expected to generate enough or precise enough measurements to significantly reduce the formal errors in existing asteroid mass estimations. Most asteroid mass formal errors thus remain roughly at their *a priori* values (Figure 14 in Part IV), which we have taken from representative estimates of current asteroid mass uncertainties (section 5.2, equation 6.1). Consequently, the corresponding post-fit true errors do not show a significant improvement with respect to those resulting from their *a priori* values. With the same normal point accuracy, formal errors—and thus expected true errors—can be further reduced by using more frequent measurements (Figure 6.10). In our approach, each orbit determination arc produces one normal point, but more complex approaches such as more frequent, partially overlapping orbit determination arcs might lead to more frequent normal points to use in the estimation. We suggest to explore these possibilities in future research (section 8.3).

   It is important to note, however, that this limited performance is subject to two particular choices regarding the employed simulation settings: first, the simulated estimation of asteroid masses has not included some of the most advanced features that present research employs to facilitate satisfactory estimations, such as the addition of mass constraints given by taxonomic classes (Fienga, Avdellidou, & Hanuvs, 2019) or the combination of range data from different missions (e.g. Folkner et al., 2014) plus astrometric observations combined with the range data. Additionally, all asteroid mass *a priori* ucnertainties have been assumed to be uncorrelated due to lack of data. A more faithful simulation of a full asteroid mass estimation based on Trilogy measurements when including these features is still required to assess the full science potential of Trilogy in this regard. Second, the estimation simulation has been performed by assigning observation weights based on the formal errors of the fitted biases in the different orbit determination arcs, multiplied by a conservative true-to-formal error ratio of 50 (section 4.1.1 in Part IV). This has been maintained in all tested simulation sub-cases, although the true-to-formal errors seen for the Venus-Earth link in Figure 8 of Part IV evince how this can go down to $\sim$10 in optimistic scenarios. Such magnitudes can be achievable for all three Trilogy links given the proper orbital configurations of the spacecraft (Figure 7.18), and using this factor 10 instead of the used 50 would reduce the post-fit formal errors with respect to the levels resulting in the tested cases. Smaller formal errors means a corresponding reduction of expected true errors of the batch filter results (see expected true-to-formal error distribution, Figure 15 in Part IV), although

it is not expected that a simple factor ~ 5 introduces any dramatic improvements with respect to the estimation performance reported under the employed settings.

8.3. Recommendations for future research

Considering the points mentioned above, the following recommendations can be made for future studies:

- Re-run the implemented simulation with more variations of the spacecraft orbital configuration: for instance, test cases in which all orbiters are fixed to have periods of 11 to 6 hours around their host planets, while still using orbit determination arcs of 12 hours. These results, compared to the tested case where al orbiters are fixed to 12 hours, will give a more solid insight on the actual impact of setting such orbit determination arcs to span over an integer number of spacecraft orbits.
- Address the optimization problem of keeping spacecraft orbital planes as perpendicular as possible to the ILR Trilogy links. This can take advantage of the perturbations caused by the high-order terms of the planets' gravity fields to seek the optimal evolution of spacecraft orbit plane orientations during the whole mission.
- Remove the assumption of the Earth spacecraft being fully solved, introducing the estimation of its state together with those of the two interplanetary orbiters at every orbit determination arc. Assess how this supports or compares to orbit determination of Earth satellites using GNSS, and check whether this degrades the results presented in this study regarding the orbit determination quality of the other two orbiters. This will also require to remove the assumption of the Earth spacecraft orbiting the EMB directly (Figure 7.5), and place it around the Earth or Moon. The dynamics of the two bodies around the EMB will need to be considered in the estimation, instead of assuming a single body directly at the EMB as we did in this study (section 7.2.1).
- Introduce more realistic dynamical mismodeling scenarios, such as unmodeled accelerations with higher frequencies or accurate representation of dynamical effects introduced at eclipse zones.
- Explore the possibilities to increase the frequency of normal point generation without hindering their resulting quality: for instance, perform the same independent, arc-wise orbit determination but with overlapping arcs starting every one hour instead of every 24 hours.
- Re-do the simulations changing the Venus vertex for a spacecraft around a highly inclined asteroid, e.g., (2) Pallas. This would not only increase the sensitivity of the third Trilogy leg to asteroid perturbations, potentially improving the resulting asteroid mass estimations, but it might constrain the cross-track direction of planetary motion in a more significant way than if the range measurements are taken closer to a single plane, hence improving the results in expected planetary cross-track W position constraints presented in this work.
- Implement the simulation of a coupled estimation of spacecraft states and planetary parameters and compare the results with the ones presented in this work. This has the potential of removing the fundamental limit of ILR systematic errors as an accuracy floor for the generated planet-to-planet ranges (section 7.2.3), but since this effect has not been found to significantly degrade the estimation results (section 4.2.3 in Part IV), it is unclear if this will introduce any significant advantage.
- Assess the constrained multi-arc approach (Alessi et al., 2012) to evaluate if it can help reconstruct long-period dynamics to the Trilogy spacecraft, such as third-body perturbations, besides relying on the perturbations to planetary orbits only. These perturbations are found to cause negligible effects for typical orbit determination arcs (Figure 4 in Part IV), but it remains to be tested what the expected impact is after several months or years of orbits.

Part VI

Appendices

A

Integrator analyses

The implemented simulations are based on numerically integrating the equations of motion (section 4.1.1) to propagate the states of the bodies of interest, either the Trilogy host planets when subject to the third-body influence of all considered asteroids or the spacecraft around these host planets. In order to produce trustworthy results, it is imperative to use a numerical integration configuration that does not corrupt the results by introducing too large integration errors.

The Global Truncation Error (GTE) of a fixed-step size numerical integrator of order p is known to grow with the step size Δt as $\mathcal{O}(\Delta t^p)$ (Dirkx & Cowan, 2019). This means that the results of two different integrations, one using Δt and the other using $\Delta t/2$, will have a relative GTE of

$$\frac{\text{GTE}(\Delta t)}{\text{GTE}(\Delta t')} \sim 2^p. \tag{A.1}$$

Tudat has several different integrations available, which can be set through the class `CoefficientSets`. Among these, four have been chosen as a representative sample between low and high order.

- RK4: Runge-Kutta of order $p = 4$;
- RKDP87: Runge-Kutta-Dormand-Prince of order $p = 7$ with an embedded 8th order;
- RKF108: Runge-Kutta-Feagin of order $p = 8$ with an embedded 10th order;
- RKF1412: Runge-Kutta-Feagin of order $p = 12$ with an embedded 14th order.

It must be noted that the three last methods have embedded integrators of higher order. This is because they are variable step-size methods, and the embedded integrator is internally used to estimate the error levels for step size control. Here, however, in order to assess the integration error by making use of equation (A.1), these have been forced to follow a fixed step size by setting equal minimum and maximum step sizes.

The key idea behind this analysis is that the GTE in the propagated position history $\mathbf{r}(t)$ after integration with step size Δt will be much larger than that in the position history $\mathbf{r}'(t)$ after integration with step size $\Delta t/2$ (equation A.1). Hence, in the difference between $\mathbf{r}(t)$ and $\mathbf{r}'(t)$, the error contribution of the former will be dominant and thus this difference is a good metric for the integration error in the propagated state after numerical integration with step size Δt. Applying this principle, it is possible to compute the expected integration error for any given step size Δt and plot their relationship, which should follow a line of slope p in a logarithmic plot (equation A.1). This behavior does not, however, extend all the way down to infinitesimally low errors, but saturates at a certain error level due to the limited numerical precision of floating point numbers. The following analysis facilitates the assessment of both the expected error levels achieved by different step sizes and the step size and error level at which this rounding error regime begins.

The integration error is also dependent on the exact formulation of the equations of motion used (section 4.1.1). We chose to test all formulations available in Tudat (`TranslationalPropagatorType`) except for the Gauss Planetary Equations with Keplerian elements, given the singularities they exhibit (Wakker, 2015). In the implemented code, both the propagator and the integrator are defined inside the `planets_and_asteroids_propagation_settings()` function, when creating the propagator settings.

A.1. Planetary integrator

Cowell propagator

The integration error curves for the analyzed integrators using the Cowell formulation of the equations of motion (section 4.1.1) are presented in Figure A.1. It can be observed how higher integration orders reach the rounding error regime with

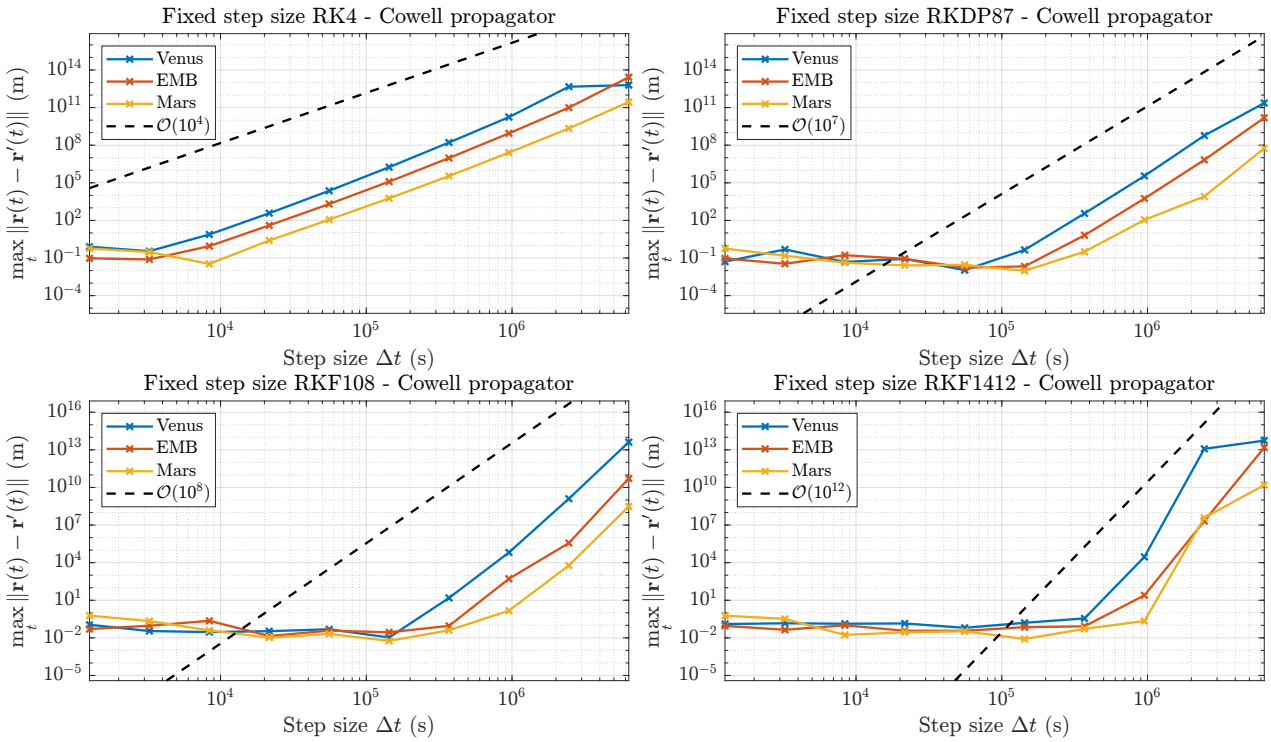

Figure A.1: Convergence curves of planetary integration error with the Cowell propagator and different fixed-step Runge-Kutta integrators

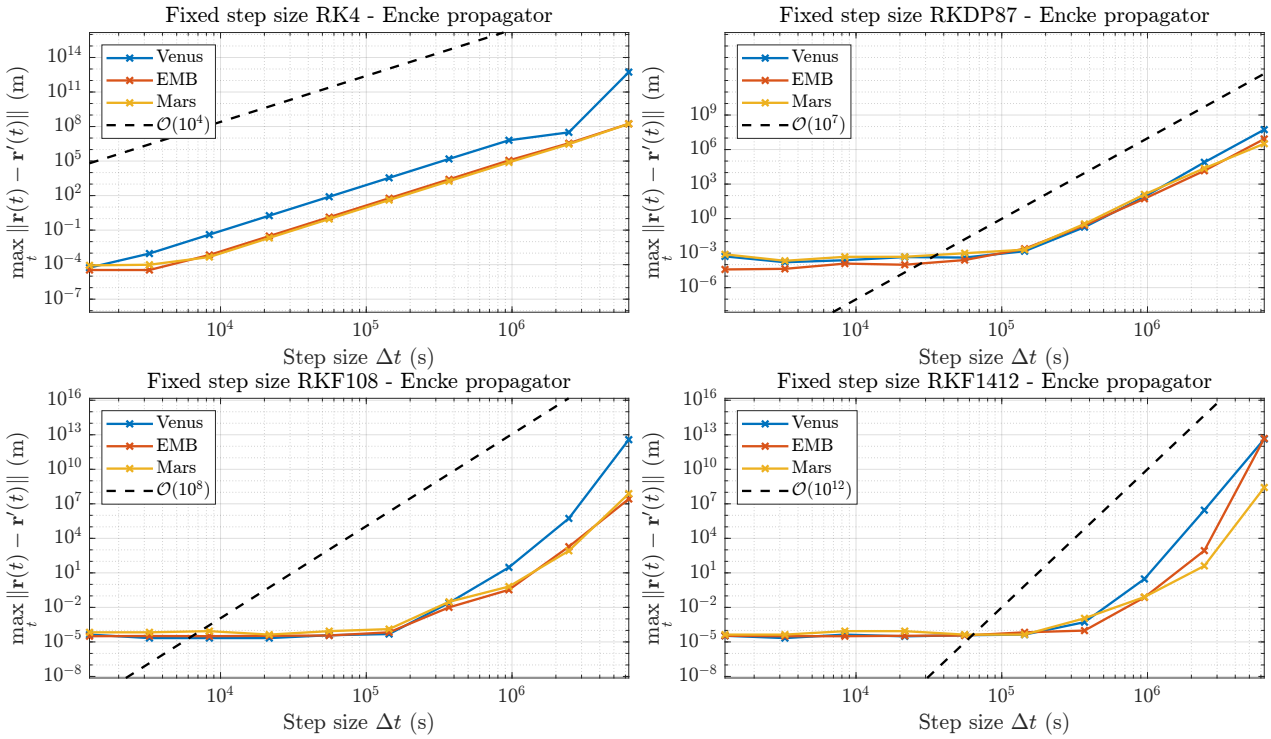

Figure A.2: Convergence curves of planetary integration error with the Encke formulation of the equations of motion and Runge-Kutta integrators

higher step sizes, as expected due to their steeper error reduction curve. This rounding error regime, however, remains between the centimeter and meter level. This is not precise enough to confidently capture signals in the order of centimeters (section 6.2) with confidence that they are not corrupted by integration error.

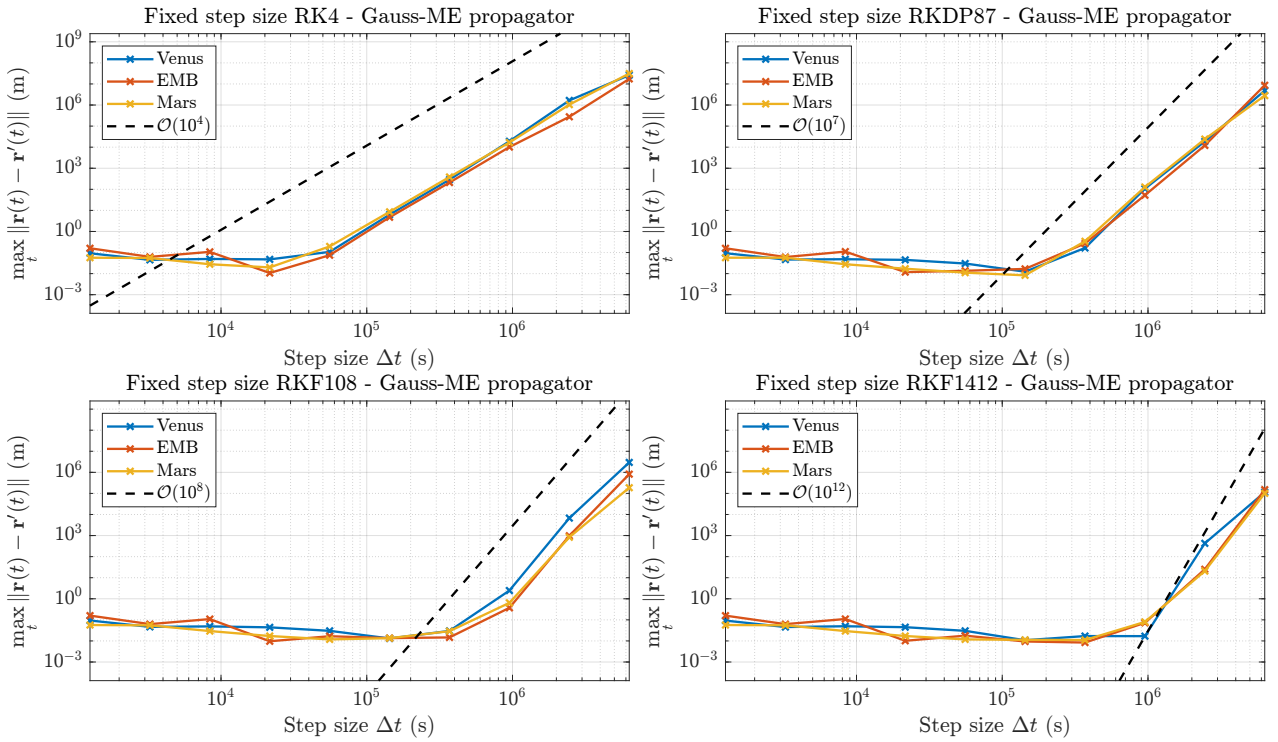

Figure A.3: Convergence curves of planetary integration error with the Gauss-ME formulation of the equations of motion and Runge-Kutta integrators

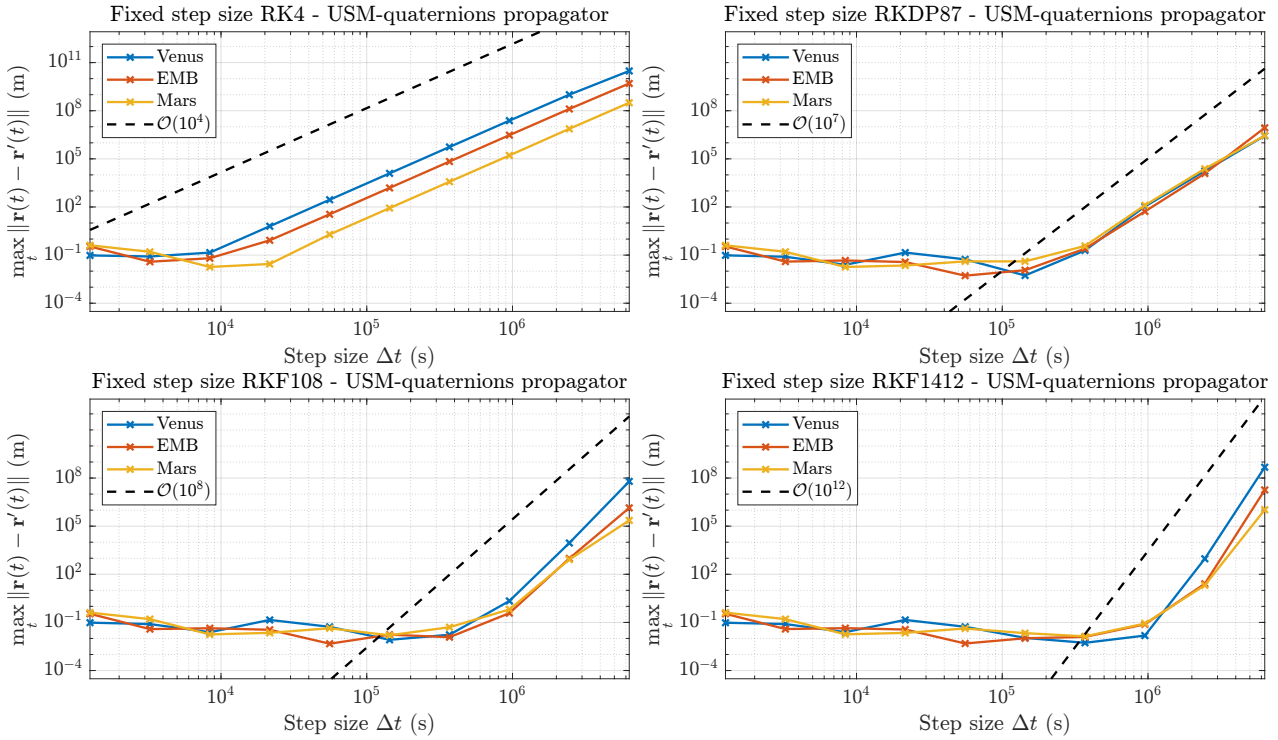

Figure A.4: Convergence curves of planetary integration error with the USM-quaternions formulation of the equations of motion and Runge-Kutta integrators.

Encke propagator

The integration error curves for the analyzed integrators using the Encke formulation of the equations of motion (section 4.1.1) are presented in Figure A.2. It can be observed how the rounding is of order 10^{-4} meters, significantly lower than

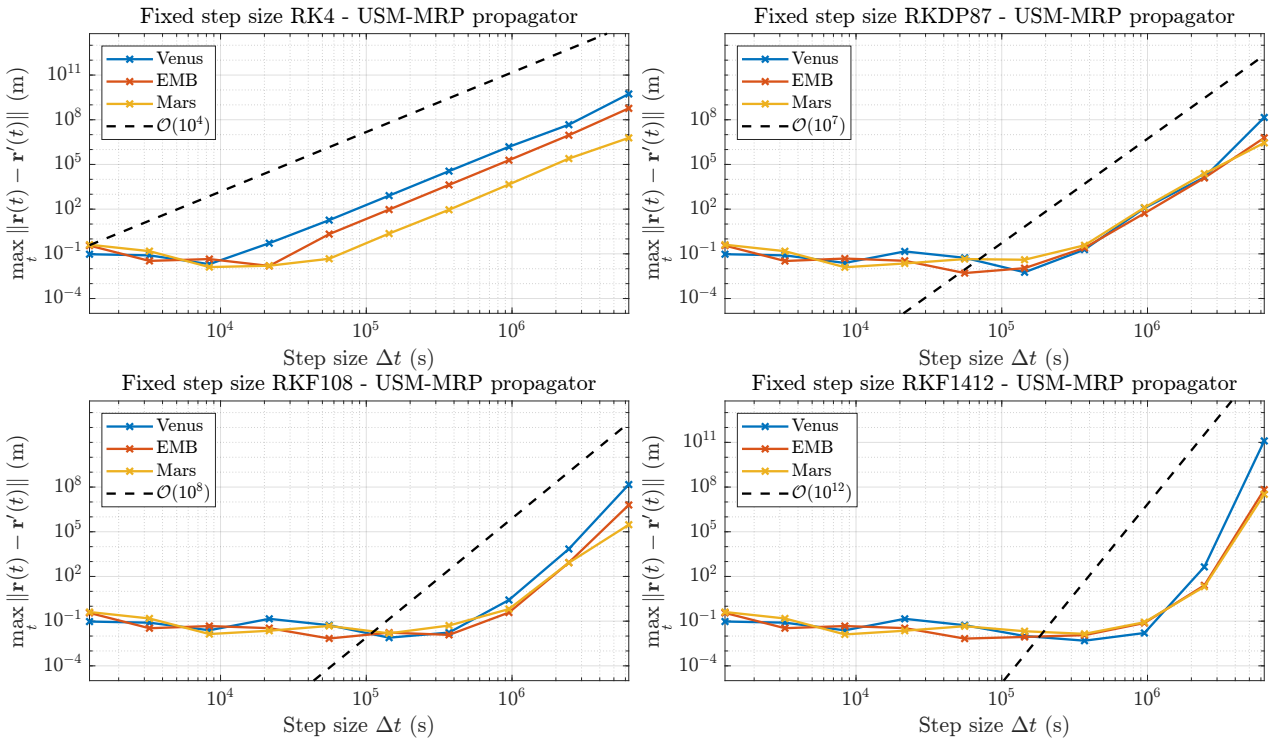

Figure A.5: Convergence curves of planetary integration error with the USM-MRP formulation of the equations of motion and Runge-Kutta integrators.

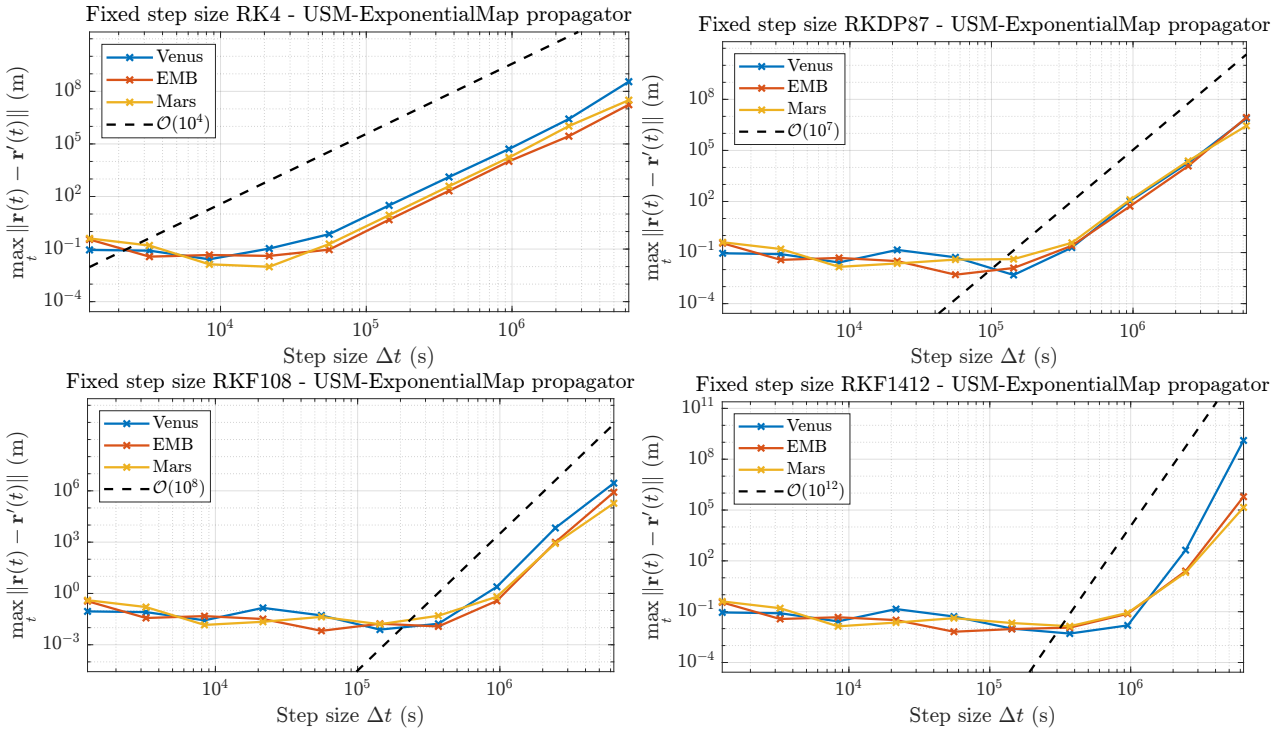

Figure A.6: Convergence curves of planetary integration error with the USM-Esponential Map formulation of the equations of motion and Runge-Kutta integrators.

the one resulting from Cowell. This is likely due to the fact that in this formulation the integrated vector has a much smaller magnitude than the actual state vector itself (Wakker, 2015), which brings the limiting numerical precision of floating point numbers away from the millimetric levels.

Gauss' planetary equations propagator with Modified Equinoctal Elements

Figure A.3 presents the integration error curves resulting from the usage of the Gauss formulation of the equations of motion with Modified Equinoctial Elements. The rounding error regime yields errors of order 1-10 cm, which outperforms Cowell, but is still significantly worse than Encke. A positive remark to be made is that, for a given integrator type, this propagator achieves to reach rounding error levels with generally higher step sizes than Cowell and especially Encke. For the problem under study, however, low errors are a stronger objective than speed, since no optimizations are being addressed and the estimations to be simulated are expected to be sensitive to signals in the order of centimeters (section 6.2).

Unified State Model propagator

Finally, the convergence curves resulting from the usage of the USM in its three different variations (section 4.1.1) are presented, respectively, in Figures A.4, A.5 and A.6. As observed, all of them achieve rounding error levels of order 1-10 cm, which is comparable to the errors achieved by the Cowell and Gauss formulations of the equations of motion.

Final choice on optimal integrator and propagator

Generally speaking, the integration error requirement must be between 1 and 2 orders of magnitude stricter than the general accuracy requirement for the problem under study. For the Trilogy case, where signals to be measured are expected to be as low as few centimeters or even some millimeters (section 6.2), numerical integration should aim for an accuracy requirement of 10^{-4} meters, which is only fulfilled by the Encke formulation of the equations of motion (Figure A.2). It is evident from the figure that any step size $\Delta t < 10^5$ seconds can yield such level of integration errors if the RKF108 or the RKF1412 integrators are used. In order to make a safe choice (i.e., allowing for slight changes in the dynamics without needing to re-run the whole integration analysis again), we chose to use an Encke propagator with a fixed-step size RKF1412 integrator.

The analysis based on fixed step sizes is generally used to define a benchmark integration configuration, for which error is known to be very low, and then test other configurations allowing for variable step sizes with different tolerances in order to find more efficient setups that fulfill the requirements. In our case, however, the best configuration found (i.e., rounding error regime with Encke propagator) is already at the limit of the requirements, so it is directly used as the most suitable propagation configuration. Fixing the step size is not expected to be significantly less efficient than allowing variable step sizes, given the low eccentricity of the planetary orbits, which are expected keep a variable step size close to constant.

A.2. Spacecraft integrator

The spacecraft trajectories around the Trilogy host bodies will also be propagated by means of numerical integration. A proper integrator analysis should be run as well, in order to verify that the results of the orbit determination simulations are not corrupted by significant integration error. The analysis has been run for a propagation arc of seven days, which is the maximum duration typically considered for Mars orbiters (Yan et al., 2017). As in section A.1, the same integrators and propagators are tested and the resulting convergence curves are presented below.

Cowell propagator

As observed in Figure A.7, the Cowell propagator is able to reach a rounding error level between 0.1 and 10 mm, depending on each particular spacecraft. It is also worth noting that too large step sizes cause the integration to diverge, reaching > 1 AU errors, likely due to the fact that the resulting integration error causes the spacecraft to be wrongly modeled to enter escape trajectories with respect to their host bodies.

Encke propagator

As observed in Figure A.8, the rounding error level reached when the Encke propagator is at use instead spans between 10^{-7} meters and 10^{-4} meters, depending on the exact spacecraft and integrator to be used. This significantly outperforms the Cowell formulation, which is likely due to comparable reasons as the ones causing this same behavior for the planetary propagation (section A.1): given that the main component of the propagated trajectories is their Keplerian contribution (Figure 4 in Part IV), propagating the difference with respect to such Keplerian orbit allows for more numerical nuance to be taken into account without being truncated by the finite precision of floating point numbers. It is also worth highlighting that, for large enough step sizes, the resulting errors diverge in a comparable way to the observed when the Cowell propagator is at use (Figure A.7).

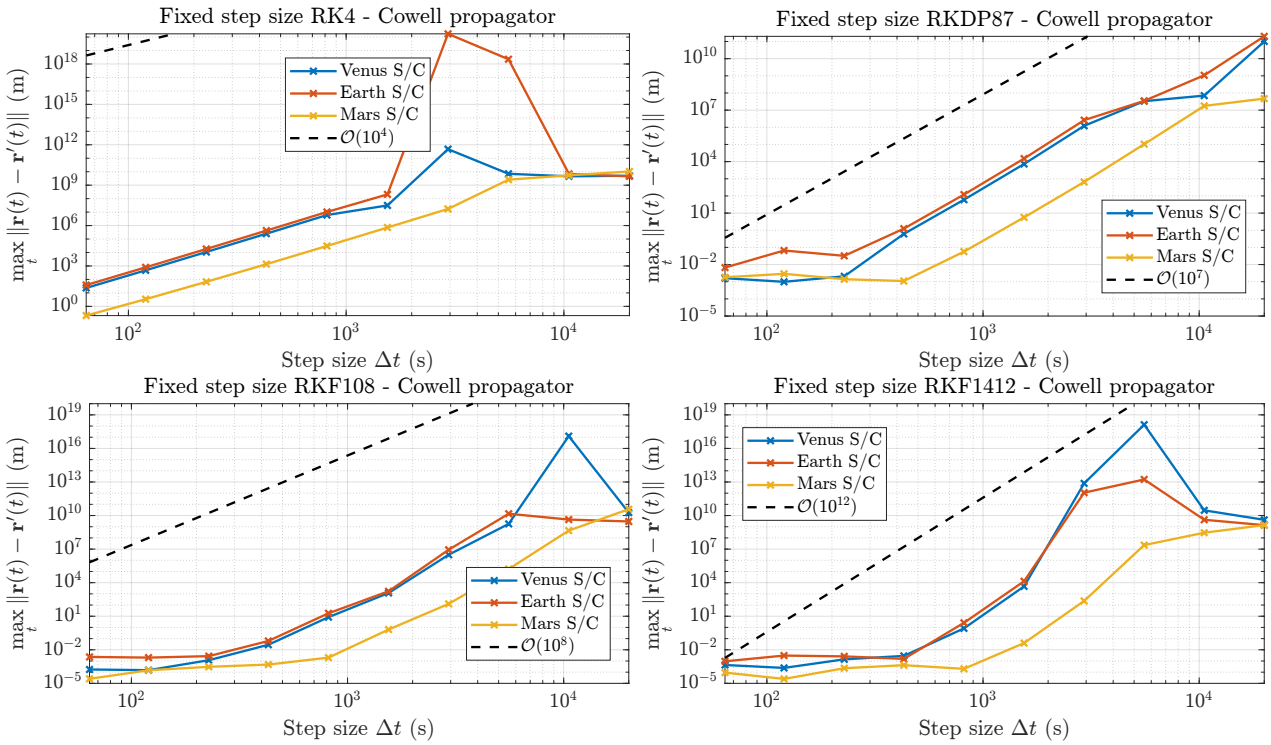

Figure A.7: Convergence curves of spacecraft integration error with the Cowell propagator and different fixed-step Runge-Kutta integrators

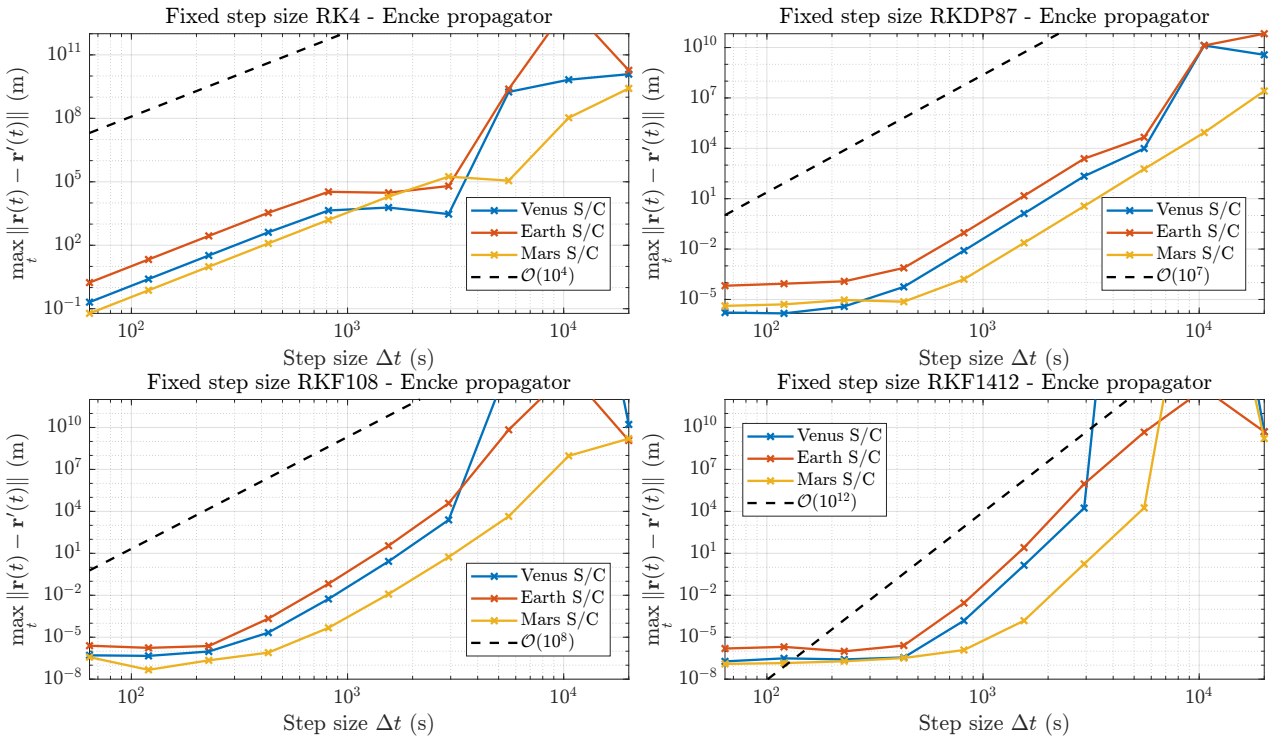

Figure A.8: Convergence curves of spacecraft integration error with the Encke formulation of the equations of motion and Runge-Kutta integrators

Gauss' planetary equations propagator

It can be noted from Figure A.9 that the Gauss propagator with Modified Equinoctial Elements achieves rounding error levels in the order of 10^{-5} meters for all spacecraft analyzed. This is a comparable performance to the one resulting from using the Encke propagator, with the plus that such rounding error regime is reached with higher step sizes (e.g.,

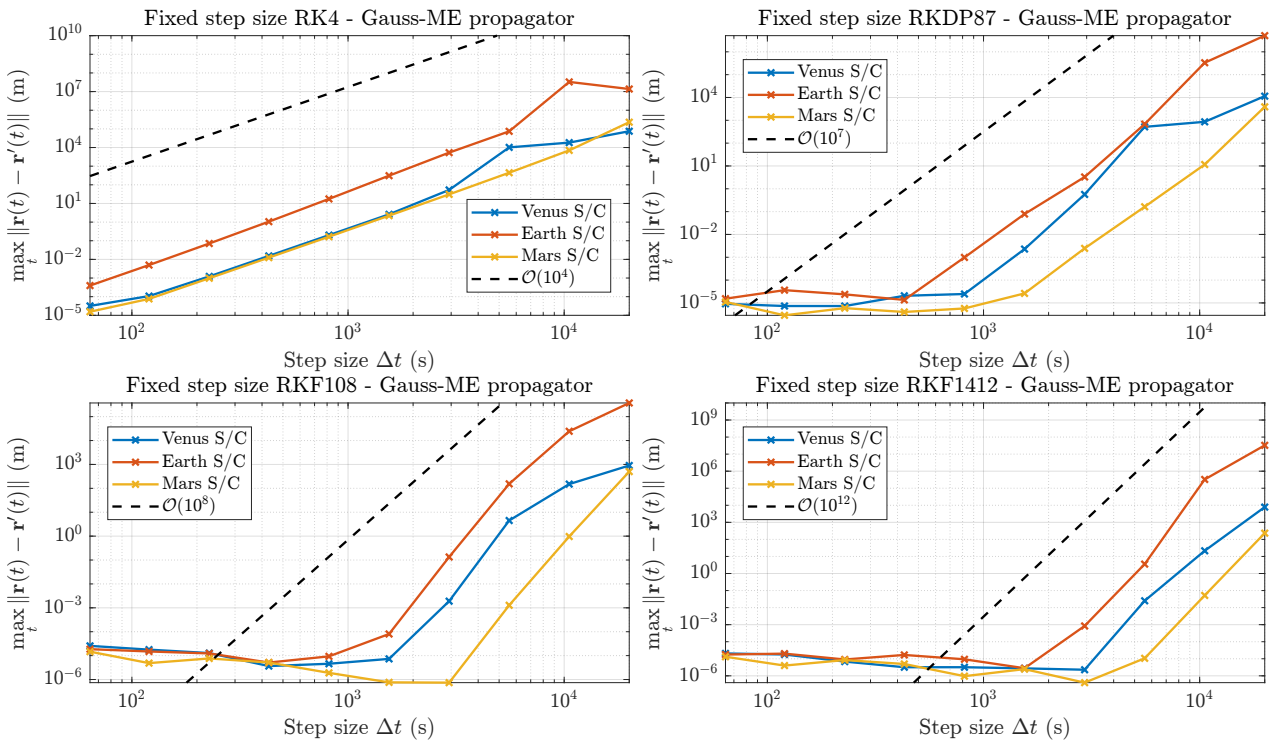

Figure A.9: Convergence curves of spacecraft integration error with the Gauss-ME formulation of the equations of motion and Runge-Kutta integrators

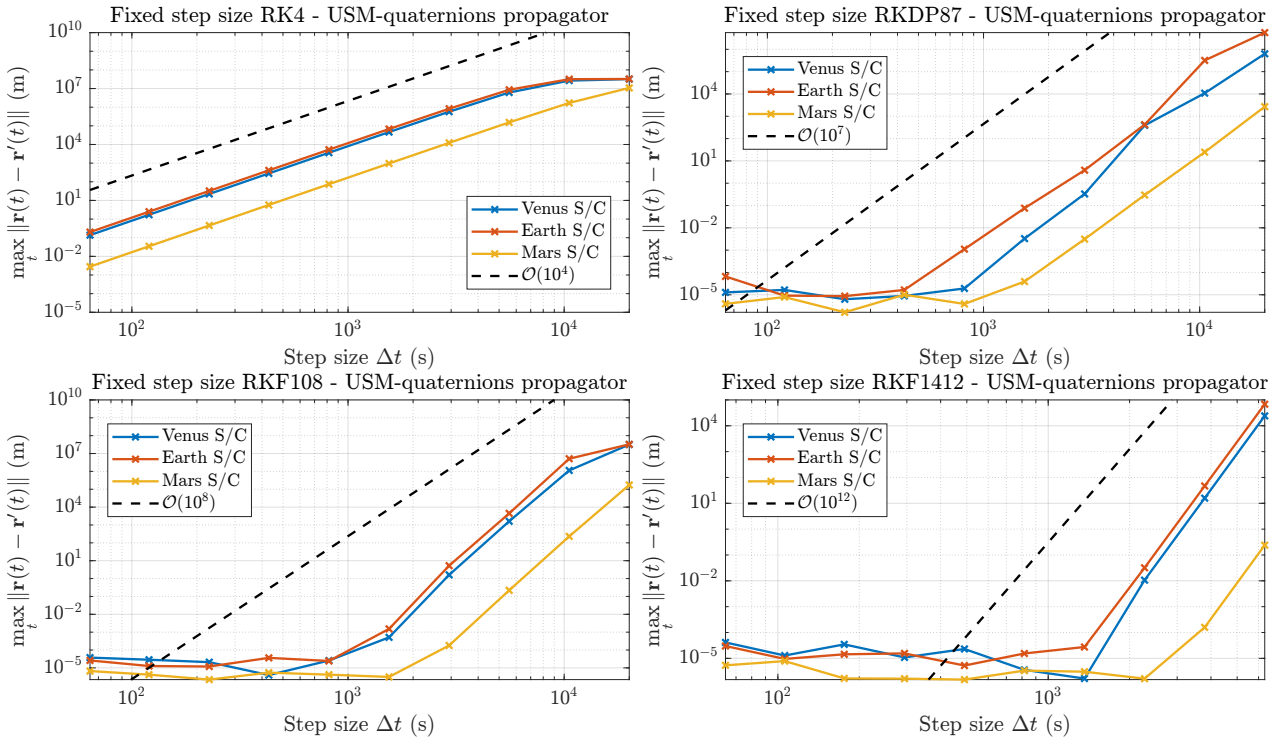

Figure A.10: Convergence curves of spacecraft integration error with the USM-quaternions formulation of the equations of motion and Runge-Kutta integrators.

when using RKF1412, the Gauss-ME propagator achieves the rounding error with ≈ 2000 seconds, whereas the Encke propagator does so with ≈ 500 seconds. Moreover, large step sizes are not observed to lead to such high divergences as with Cowell and Encke.

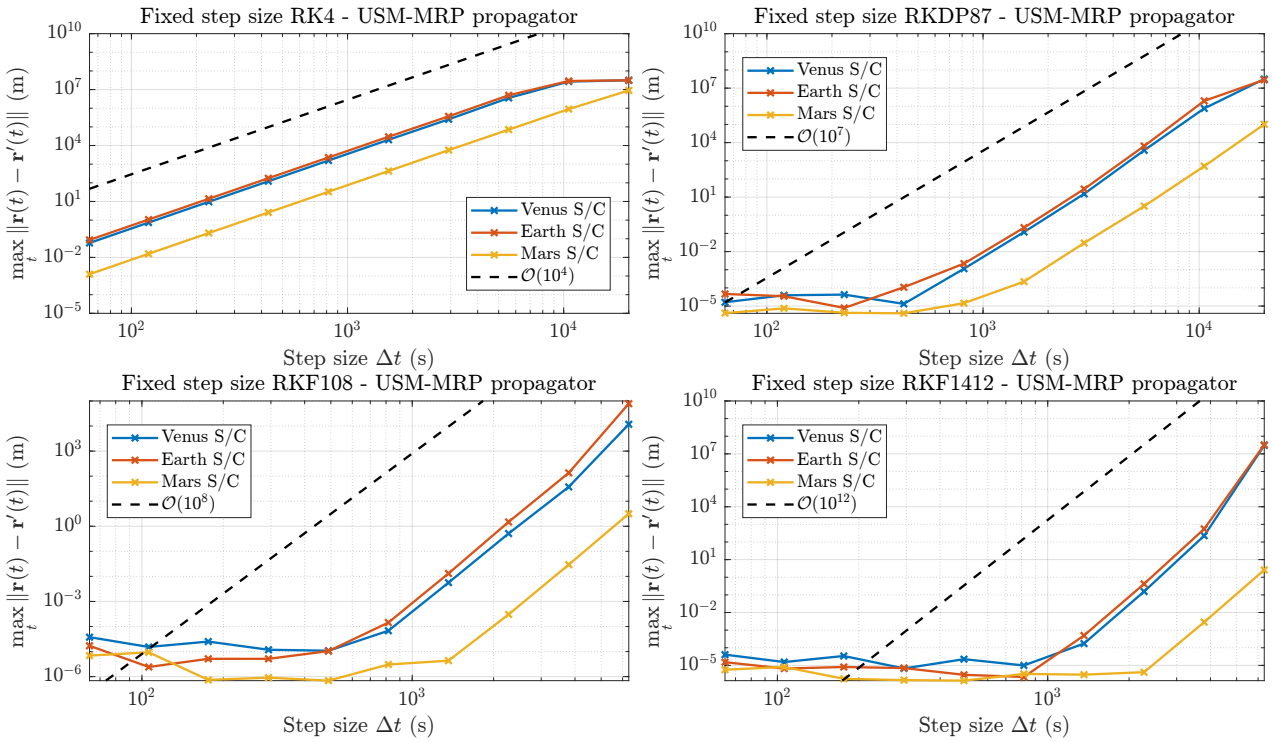

Figure A.11: Convergence curves of spacecraft integration error with the USM-MRP formulation of the equations of motion and Runge-Kutta integrators.

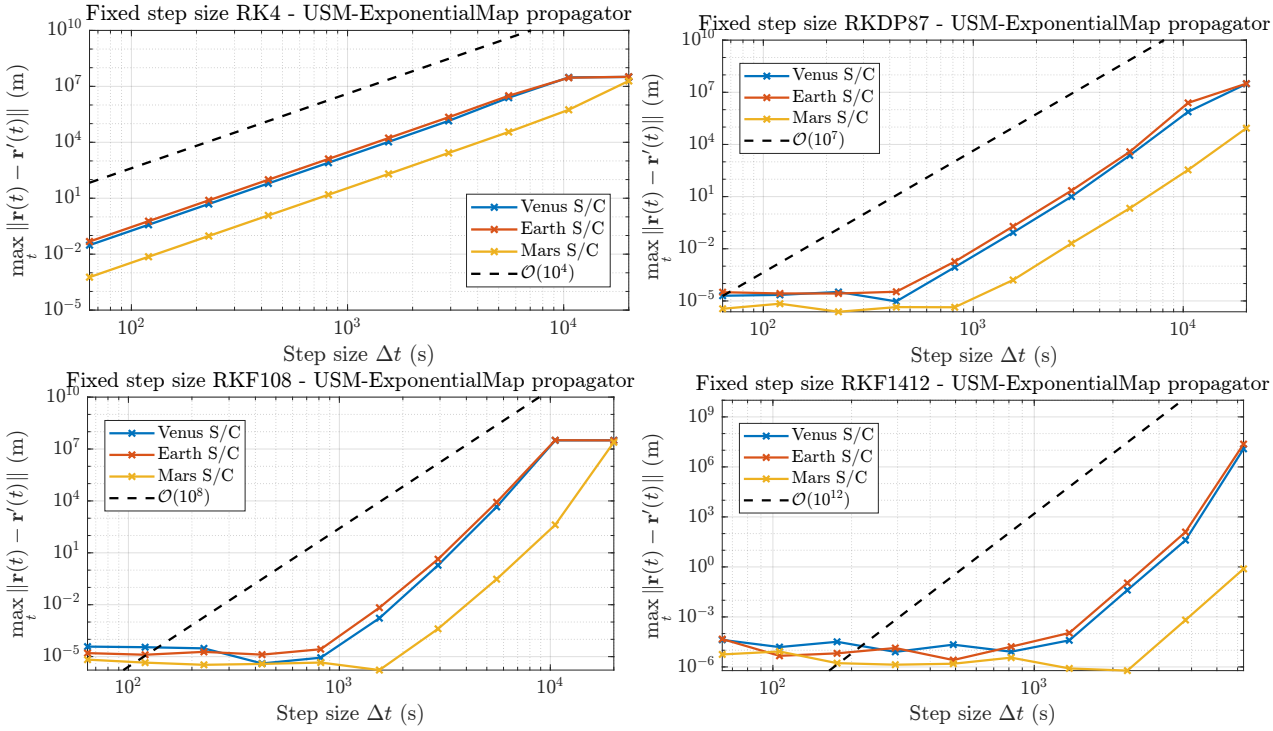

Figure A.12: Convergence curves of spacecraft integration error with the USM-Esponential Map formulation of the equations of motion and Runge-Kutta integrators.

Unified state model propagator

The convergence curves resulting from the usage of the three variations of the USM are presented in Figures A.10, A.11 and A.12. They present comparable performances, reaching rounding error levels between 10^{-6} and 10^{-4} meters with

step sizes of ≈ 1000 seconds, if RKF108 or RKF1412 are used. Similarly to the Gauss propagator (Figure A.9), high step sizes do not yield dramatic divergence as Cowell (Figure A.7) and Encke (Figure A.8) do.

Final choice on optimal integrator and propagator

Given the fact that the range measurements generated by Trilogy will be generated from spacecraft to spacecraft, the accuracy requirements applicable to the integration of the host planets' orbits are equally applicable to the integration of the spacecraft around them. This means that, in order to be confident about the simulation of the centimeter level signatures captured by Trilogy (section 6.2), this integration error shall be in the < 1 mm level.

The Encke propagator is able to reach rounding errors below 10^{-5} meters (Figure A.8). The Gauss-ME propagator, however, is able to reach 10^{-5} meter error levels with higher step sizes (e.g., for RKF108, ≈ 800 seconds, in contrast to the ≈ 200 seconds required for Encke). This also slightly outperforms the USM, both in terms of accuracy and step size allowed. Given the fact that the orbit determination of the spacecraft will need to run several independent arcs, performance is a somewhat greater concern than in the case of planetary motion only (section A.1), hence the usage of RKF108 is more preferable than the usage of RKF1412 for similar step sizes. With all this in mind, and allowing for some margin in case of slight changes in the dynamics, we chose to propagate the spacecraft orbits with the Gauss Modified Equinoctial Elements propagator and a RKF108 fixed-step integrator with a step size of 600 seconds.

Similarly to the case of planetary orbits, the outcome of this analysis is the setting of a propagator configuration that is expected not to yield truncation errors but only rounding errors, contained to requirement-fulfilling levels. Although new tests could be run from this point to assess variable step size configurations that are also compliant, we do not judge it to be necessary due to both the near-circularity of the integrated orbits and the closeness of the found resulting errors to the initial requirement of sub-millimetric errors. Additionally, the lack of optimization processes that require a large number of runs of the same settings do not make performance a significant enough concern as to optimize the run time of the propagation further.

B

Covariances of planetary ephemerides

This chapter presents the figures corresponding to the results of the obtention of planetary covariances as detailed in algorithm 4. As described in section 6.1.1, this method is used to obtain a covariance matrix that is consistent with both the dynamical model at use and the expected true errors of planetary ephemerides. These true errors can be estimated by means of comparing different ephemerides models, and the two that are presenting a most clear convergence are DE and INPOP (section 5.1). The computation of such discrepancies from the publicly available spice kernels of the two models is presented in section B.1, whereas the results of the application of algorithm 4 are presented in section B.2.

B.1. Comparison between DE and INPOP ephemerides

As described in section 6.1.1, an acceptable metric for the approximate true errors of current planetary ephemerides is the intercomparison between different models (Dirkx, 2015). Figures B.1, B.2, B.3, and B.4 present, respectively, the difference between INPOP21a and DE440 for the four rocky planets (subscript D stands for DE and subscript I stands for INPOP). Mercury is included because at the early stages of this work it had not been discarded from potential iterations

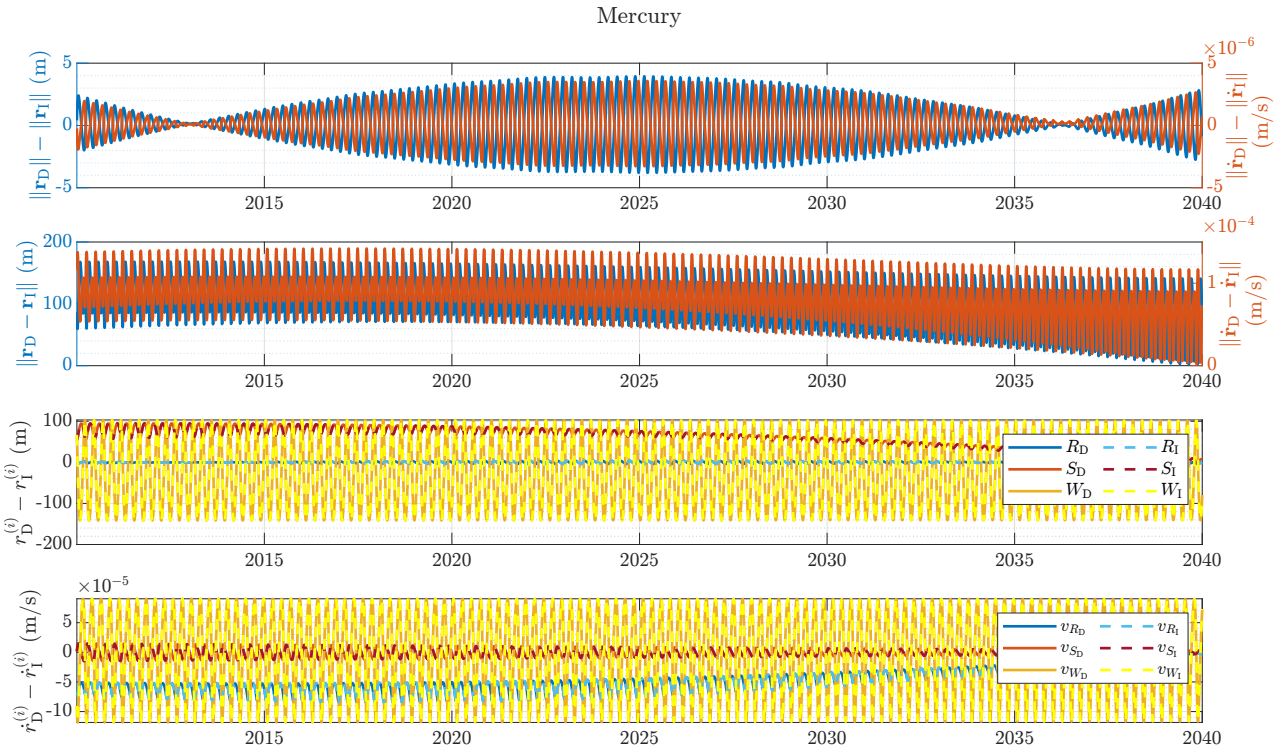

Figure B.1: Differences in Mercury's heliocentric state between DE440 and INPOP21a ephemerides for years 2010 to 2040.

of the Trilogy mission configuration to be tested besides the original Venus-Earth-Mars (Smith et al., 2018). These differences are presented in four figures, showing, respectively, the difference in position and velocity norms, the norms of position and velocity differences, and component-wise differences in both position and velocity in the RSW frame. The

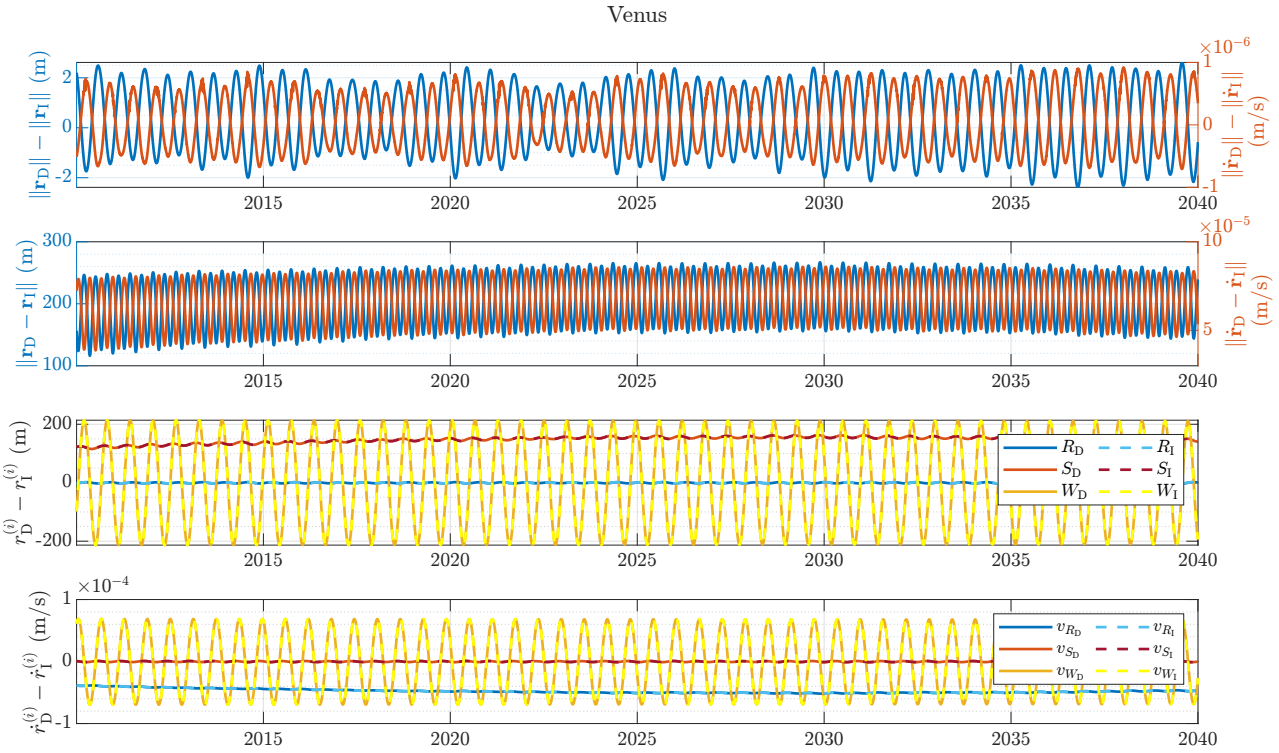

Figure B.2: Differences in Venus' heliocentric state between DE440 and INPOP21a ephemerides for years 2010 to 2040.

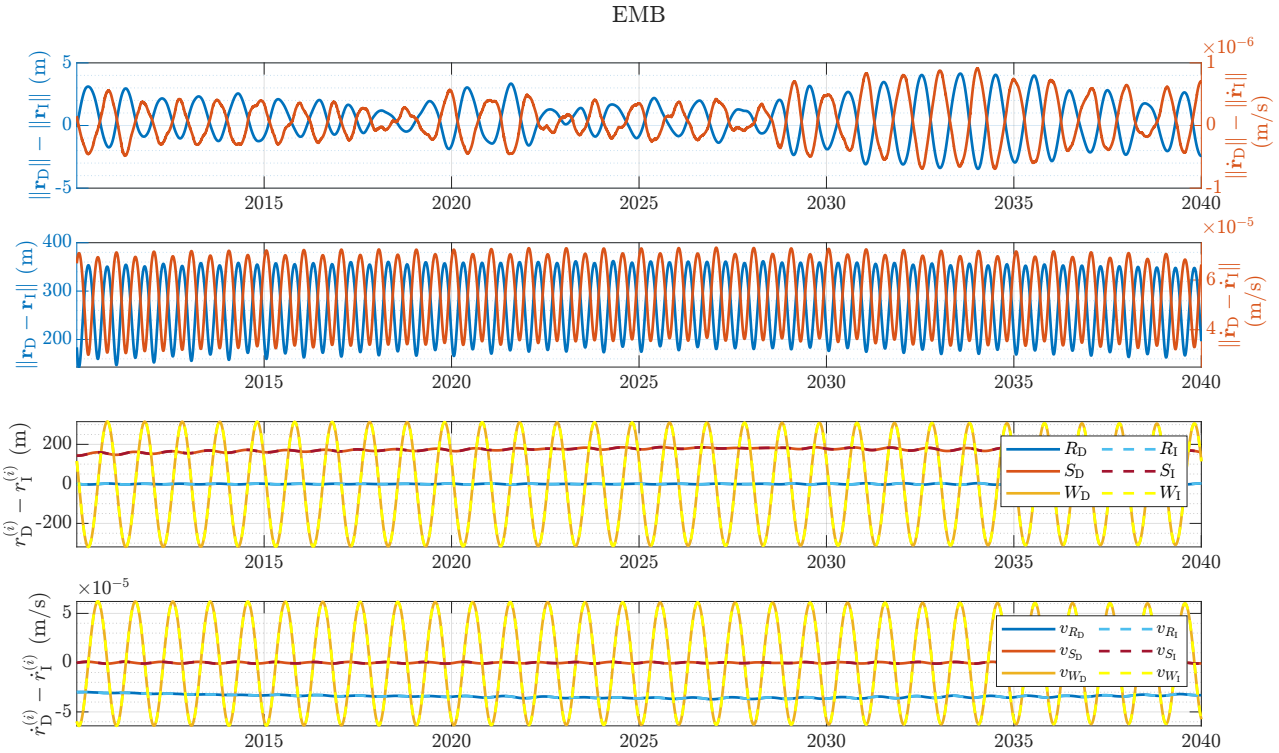

Figure B.3: Differences in the heliocentric state of the EMB between DE440 and INPOP21a ephemerides for years 2010 to 2040.

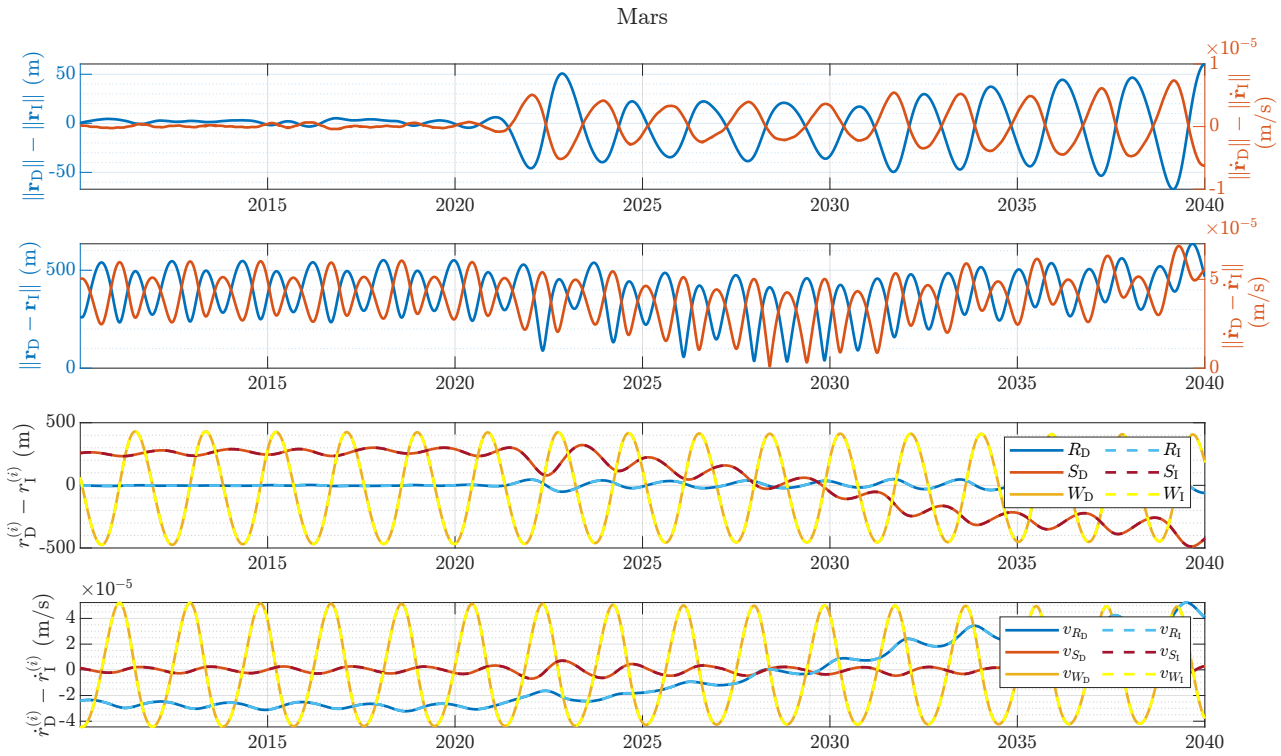

Figure B.4: Differences in Mars' heliocentric state between DE440 and INPOP21a ephemerides for years 2010 to 2040.

plots presenting component-wise differences display two overlapped curves for each component: the one resulting from transforming the two XYZ states to RSW by means of the rotation given by the DE state, and the one resulting from doing so with the rotation matrix given by the INPOP states. When computing component-wise differences between the two states, transforming each of them with their own $\boldsymbol{R}^{RSW/I}$ before subtraction yields to misleading null differences in radial direction, since the R direction of each particular body is, by definition, aligned with its position vector.

Figures B.1, B.2, B.3, and B.4 match the results presented by Fienga et al. (2021), who show similar comparison figures between INPOP21a and DE440 in their appendix. In particular, the differences in heliocentric distances (the topmost plots in each figure) are replicated and can be checked to fully match—despite the irregularities in the curves for Venus and the EMB, the appearnace of Mercury can be confirmed to match with its maximum in 2025 and two minimums around 2013 and 2036, and that of Mars can also be verified to match the significant discrepancy increase after 2020. This behavior is due to the fact that both DE and INPOP ephemerides have been computed by fitting range observations to Mars available up to 2021, when the two models were released (Fienga et al., 2021; Park et al., 2021).

These figures showing component-wise differences over time evince how the discrepancies between the two models oscillate, with a clear frequency component equal to the orbital period of each planet around the Sun. In order to get a single figure that describes the approximate average discrepancy levels, we compute the RMS of the component-wise temporal signals seen in figures B.1, B.2, B.3, B.4 over the entire represented period of time (i.e., 30 years, centered at present day). These are shown in Figure B.5, and are taken as the best estimate of true error levels of ephemerides models.

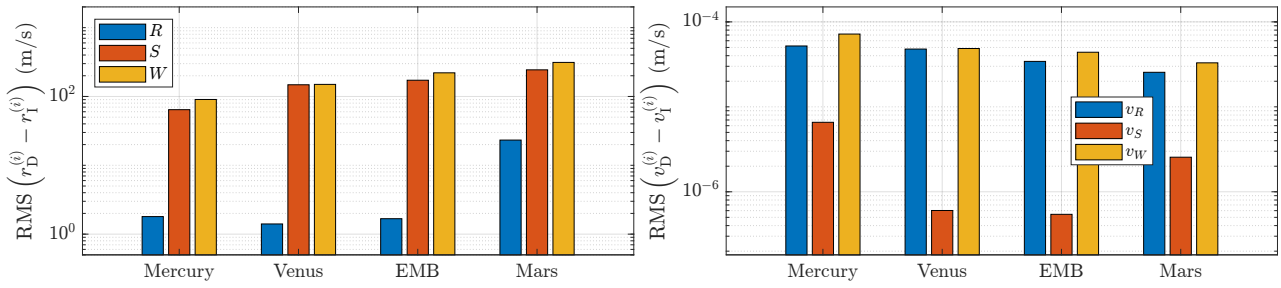

Figure B.5: RMS of component-wise position and velocity differences between DE440 and INPOP21a for the inner planets

B.2. Covariance obtention with dynamical model in use

As described in algorithm 4, the dynamical model at use must be fit to the planetary states given by ephemerides with the aim of finding an optimal initial state $\mathbf{x}_0$ that matches them as closely as possible. This $\mathbf{x}_0$ must be found for January 1st, 2031, as it is the starting date of the Trilogy mission simulations conducted in this work. Given the simulation settings that take INPOP19a as ephemerides model at use (section 6.1), observations consisting of the Cartesian positions of the planets are generated with a cadence of one day. These are presented in Figure B.6.

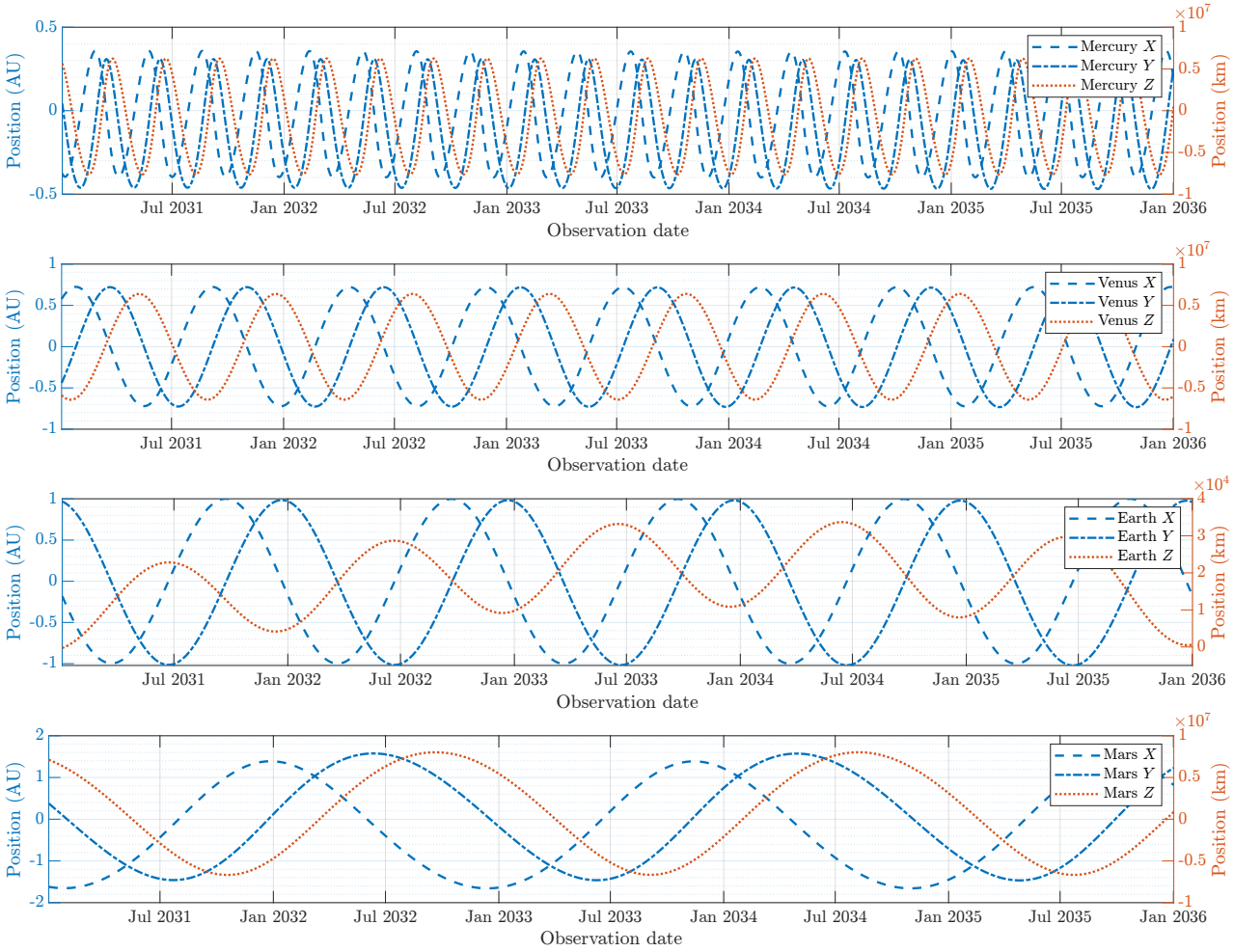

Figure B.6: Cartesian position observations obtained from planetary ephemerides

A batch estimation (algorithm 1) is then performed, taking these Cartesian positions as observations. The weights matrix is taken as the identity, i.e., $\boldsymbol{W} = \boldsymbol{I}$. The minimization of the observation residuals that leads to the final solution of $\mathbf{x}_0$ is presented in figures B.7, B.8, B.9 and B.10. Four iterations of the differential correction step have been found to yield to convergence (i.e., observation residuals not significantly changing afterward). Each figure shows the pre-fit residuals, i.e., observation differences when taking the initial state equal to that of the ephemerides and propagating it with the dynamical model at use (iteration 1) and post-fit residuals, i.e., observation differences when using the optimal initial state found instead (iteration 4). As discussed in section 6.3.1, the fact that the pre-fit residuals match the ephemerides down to the level of some hundred kilometers even after 5 years of propagation is a good indicator of the validity of the implemented dynamical model.

The second step of algorithm 4 is to tune the weights of the post-fit covariance matrix so that its propagation yields formal errors that match the expected levels of true errors of planetary ephemerides. These levels are taken from the RMS values reported in Figure B.5. It is important to note that the observations used only correspond to position (and not velocity) components, hence the final formal errors in position components are more directly affected by the weight tuning than those in velocities. For this reason, the weight-tuning analysis is focused on leading to RSW position component errors that match the desired levels of position errors (Figure B.5 left), while the resulting levels of velocity errors remain

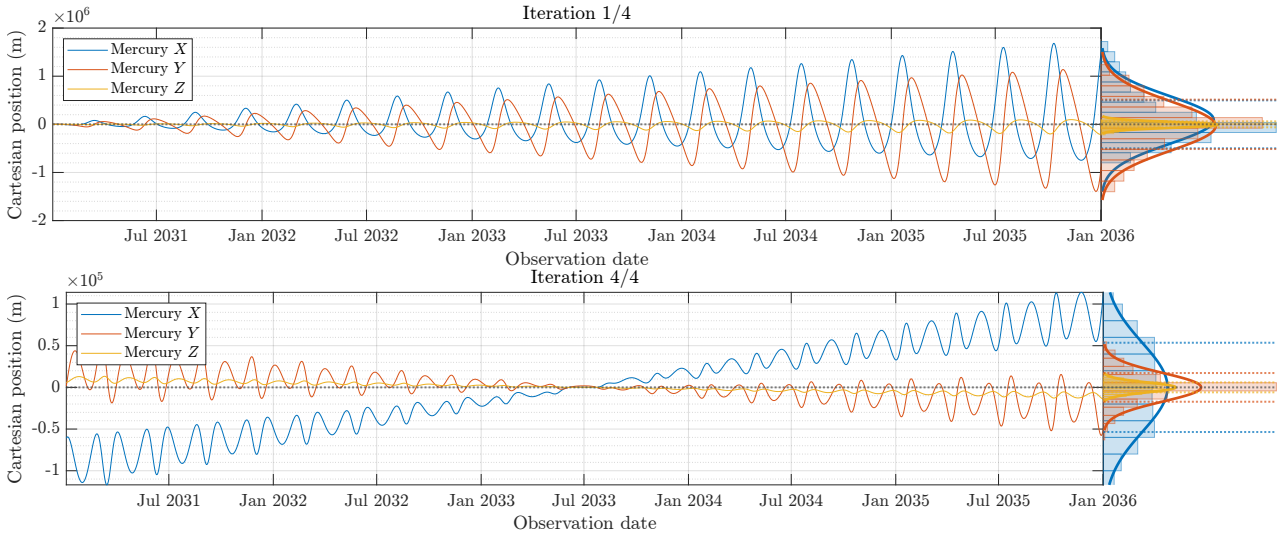

Figure B.7: Mercury observation residuals at the first and last iteration when fitting the dynamical model to the states observed from planetary ephemerides

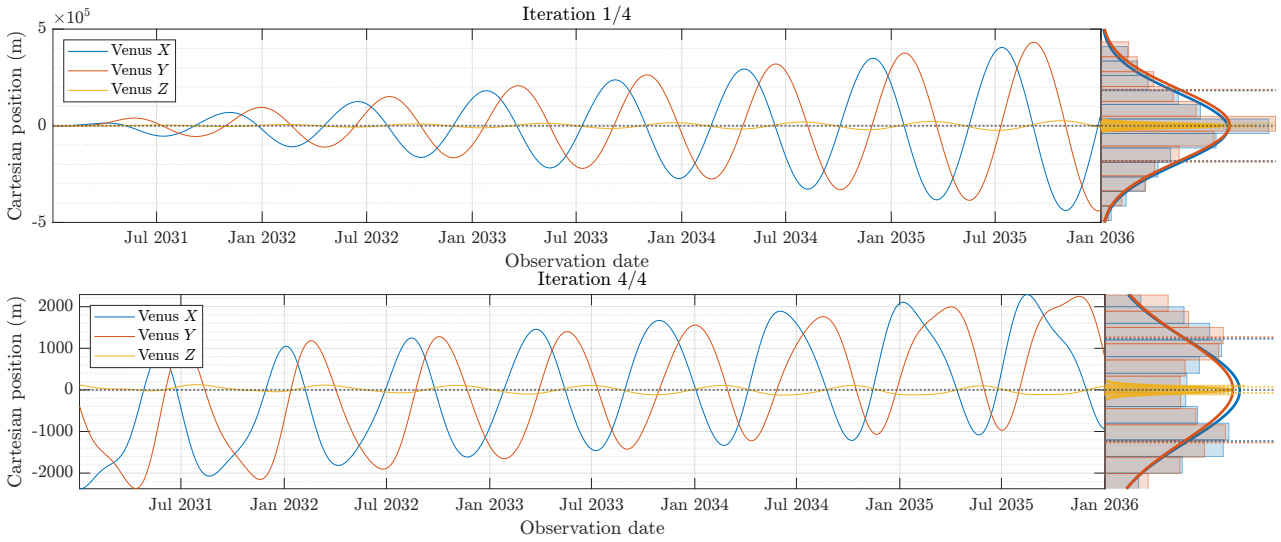

Figure B.8: Venus observation residuals at the first and last iteration when fitting the dynamical model to the states observed from planetary ephemerides

consequential to those.

As described in section 6.1, the position weights cannot be tuned in the RSW positions but only XYZ due to the impossibility to assign non-diagonal weight matrices in Tudat. For this reason, weights corresponding to observations of X and Y positions are tuned solitarily. The final weight combination found to yield optimal matching between the propagated true errors and the desired error levels (Figure B.5) is listed in Table B.1. In the implemented code, the method `covariance_analysis_method()` inside the `MainSimulationClass` has the option to call the `set_observation_weights()` function with the option `mode="custom"`, which makes use of Tudat's

	W_X	W_Y	W_Z
Mercury	4×10^{-7}	4×10^{-7}	1.2×10^{-7}
Venus	7×10^{-8}	7×10^{-8}	5×10^{-8}
EMB	5.5×10^{-8}	5.5×10^{-8}	2.1×10^{-8}
Mars	3×10^{-8}	3×10^{-8}	1×10^{-8}

Table B.1: Combination of weights found to yield to the propagation of initial state covariance matching the desired levels (Figure B.11)

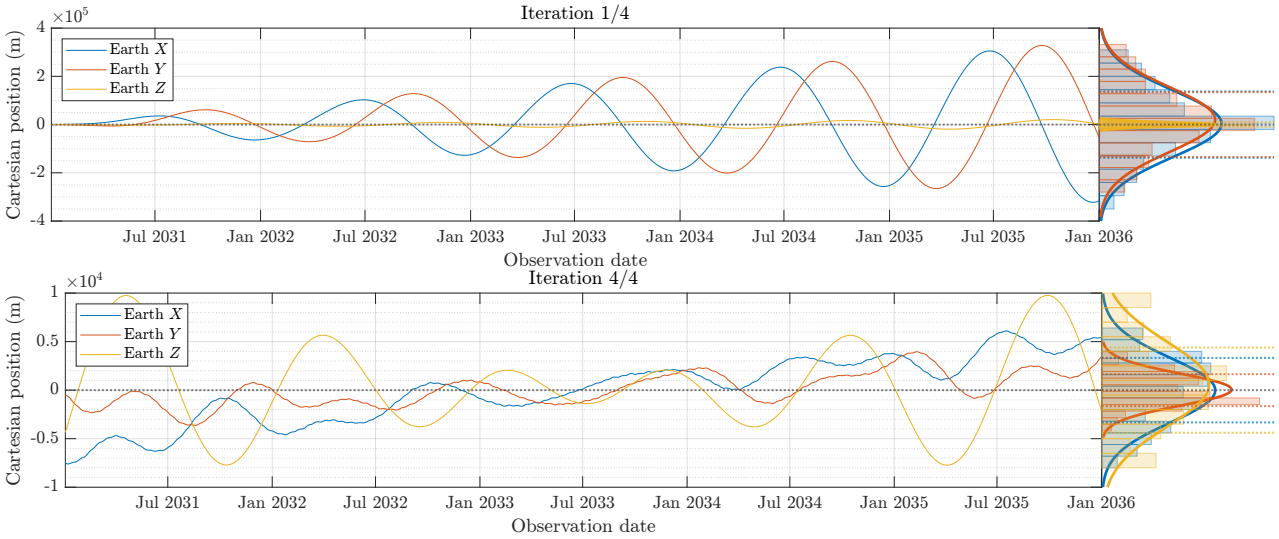

Figure B.9: EMB observation residuals at the first and last iteration when fitting the dynamical model to the states observed from planetary ephemerides

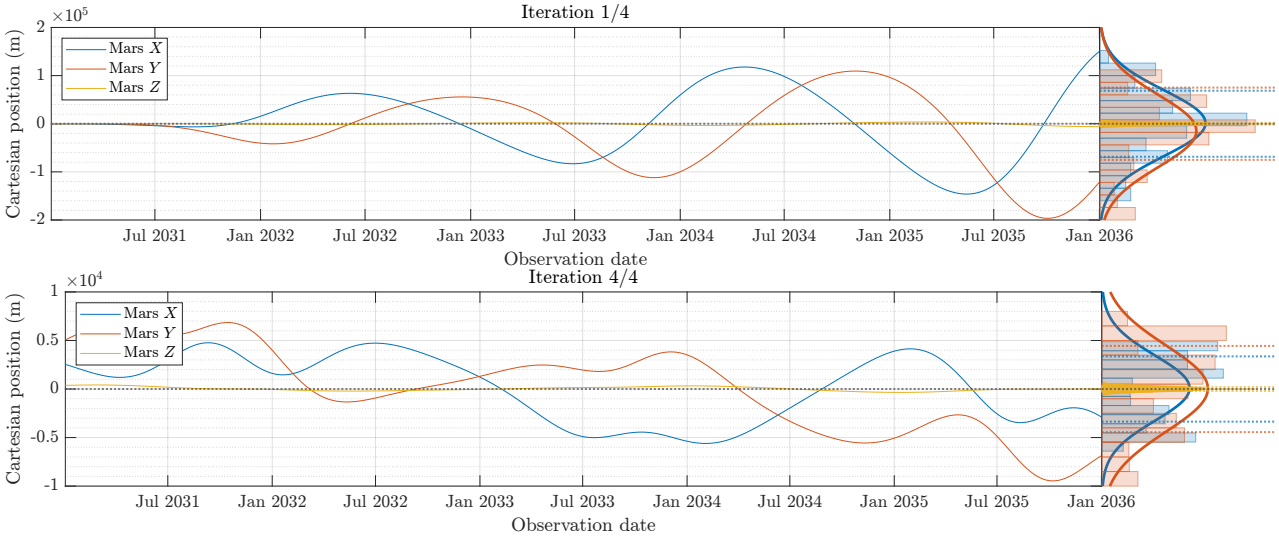

Figure B.10: Mars observation residuals at the first and last iteration when fitting the dynamical model to the states observed from planetary ephemerides

`set_constant_single_observable_and_link_end_vector_weight()` function to set individual weights for the X, Y and Z observation components.

The result of the covariance propagations resulting from the combination of weights from Table B.1 is presented in Figure B.11, where the dashed lines mark the error levels shown in Figure B.5. It can be observed how the propagation of the formal errors in S and W positions does match the desired levels reasonably well, whereas those in R positions happen to be much larger. This is a direct result of the fact that weights cannot be tuned individually in R, S and W components. Although this effect could have been mitigated by adding, for instance, radial observations on top of the Cartesian ones, we kept this somewhat conservative results on the radial uncertainties by judging it to have little expected impact on the results. As the results show (Part IV), radial uncertainties can still be reduced to sub-mm levels, which is still below the assumed levels of true errors (Figure B.5). This backs up the assumption that the usage of this conservative covariance matrix does not influence our final conclusions in a significant way.

Finally, the correlations matrix resulting from the found optimal covariance is presented in Figure B.12. As expected, despite having performed the batch estimation of all planetary initial states concurrently, correlations between initial states of different bodies are zero. Additionally, the only high correlations are found to be the ones between radial position and along-track velocity and vice-versa, which is consistent with the fact that, in nearly-circular orbits, orbital velocity depends mainly on radial distance. Mercury shows a higher correlation between radial velocity and radial position, which is due to

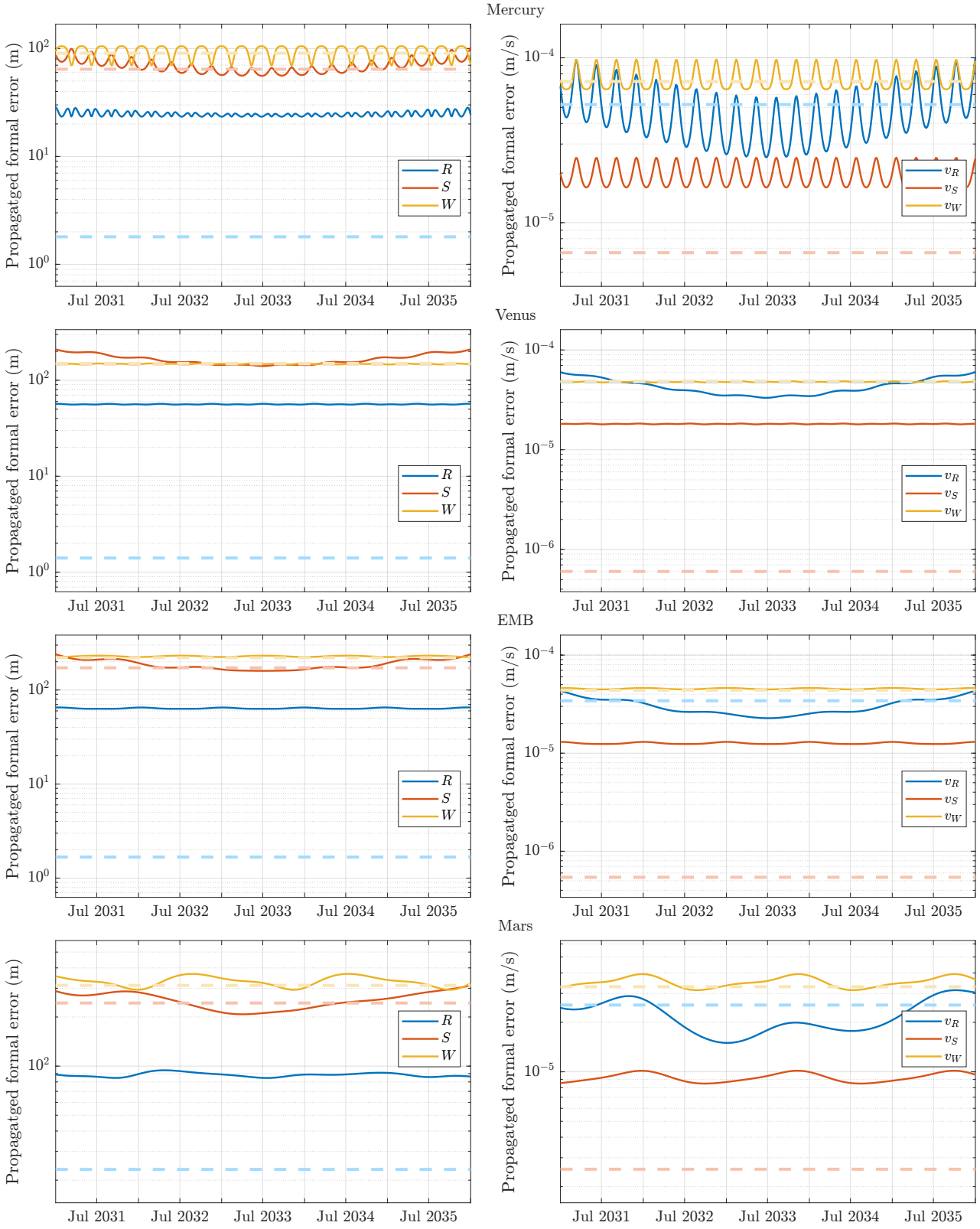

Figure B.11: Linear propagation of the final covariance matrix of planetary initial states after adjusting weights. Dashed lines mark the error levels shown in Figure B.5.

its higher eccentricity. Finally, cross-track position and velocity have almost null correlation with all other components for Venus, the EMB and Mars, which is due to their low inclinations, whereas the higher inclination of Mercury translates to

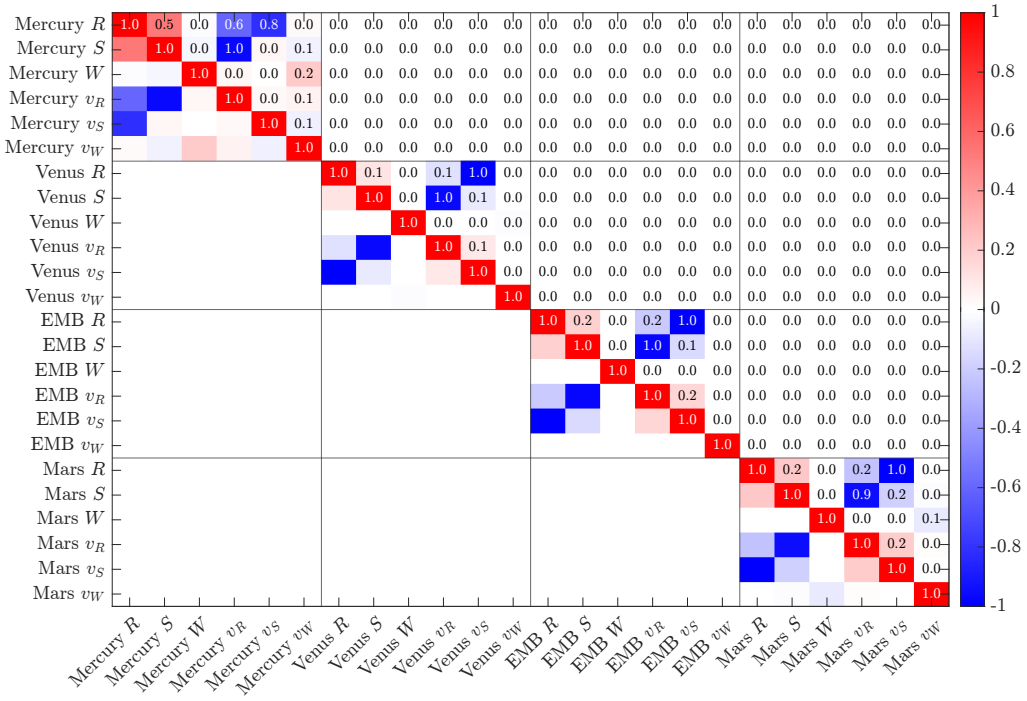

Figure B.12: Correlations matrix corresponding to the final covariance matrix after applying algorithm 4.

higher correlations between cross-track velocity and other components.

C

Analytical calculation of third-body perturbations to planets caused by asteroids

In the early stages of this work, when the final approach to be followed (Algorithm 6) had still not been decided, a secondary research objective related to the analytical modeling of the sensitivity of Trilogy measurements to asteroid masses was addressed. The main idea was to develop an analytical figure that could serve the role of the amplitude figures presented in section 6.2 with no need of numerical simulations. It was discussed that a good starting point was the Lagrange Planetary Equations, which describe the evolution of the orbital elements of an orbiting body affected by the perturbations of a conservative gravitational potential R (Vallado, 2013, Eq. 9-12):

$$\frac{da}{dt} = \frac{2}{na}\frac{\partial R}{\partial M_o}; \tag{C.1a}$$

$$\frac{de}{dt} = \frac{1-e^2}{na^2 e}\frac{\partial R}{\partial M_o} - \frac{\sqrt{1-e^2}}{na^2 e}\frac{\partial R}{\partial \omega}; \tag{C.1b}$$

$$\frac{di}{dt} = \frac{1}{na^2\sqrt{1-e^2}\sin(i)}\left\{\cos(i)\frac{\partial R}{\partial \omega} - \frac{\partial R}{\partial \Omega}\right\}; \tag{C.1c}$$

$$\frac{d\omega}{dt} = \frac{\sqrt{1-e^2}}{na^2 e}\frac{\partial R}{\partial e} - \frac{\cot(i)}{na^2\sqrt{1-e^2}}\frac{\partial R}{\partial i}; \tag{C.1d}$$

$$\frac{d\Omega}{dt} = \frac{1}{na^2\sqrt{1-e^2}\sin(i)}\frac{\partial R}{\partial i}; \tag{C.1e}$$

$$\frac{dM_o}{dt} = -\frac{1-e^2}{na^2 e}\frac{\partial R}{\partial e} - \frac{2}{na}\frac{\partial R}{\partial a}, \tag{C.1f}$$

where n is the mean motion and a, e, i, Ω, ω and M_0 is the classical orbital element set. In this context, these equations can be applied to assess the evolution of the orbits of the planets due to asteroid mass perturbations.

Given the third-body perturbation potential of an asteroid with $GM = \mu_p$ situated at a heliocentric position $\mathbf{r}_p$, its potential on a planet at a position $\mathbf{r}$ is

$$R = -\mu_p\left(\frac{1}{\|\mathbf{r}-\mathbf{r}_p\|} - \frac{\mathbf{r}\cdot\mathbf{r}_p}{\|\mathbf{r}_p\|^3}\right), \tag{C.2}$$

which can be re-written as

$$R = -\mu_p\left(\frac{1}{\sqrt{r^2 + r_p^2 - 2rr_p\cos(\theta)}} - \frac{r}{r_p^2}\cos(\theta)\right), \tag{C.3}$$

where $r = \|\mathbf{r}\|$, $r_p = \|\mathbf{r}_p\|$ and θ is the relative angle between the two inertial position vectors. With the help of Sympy,

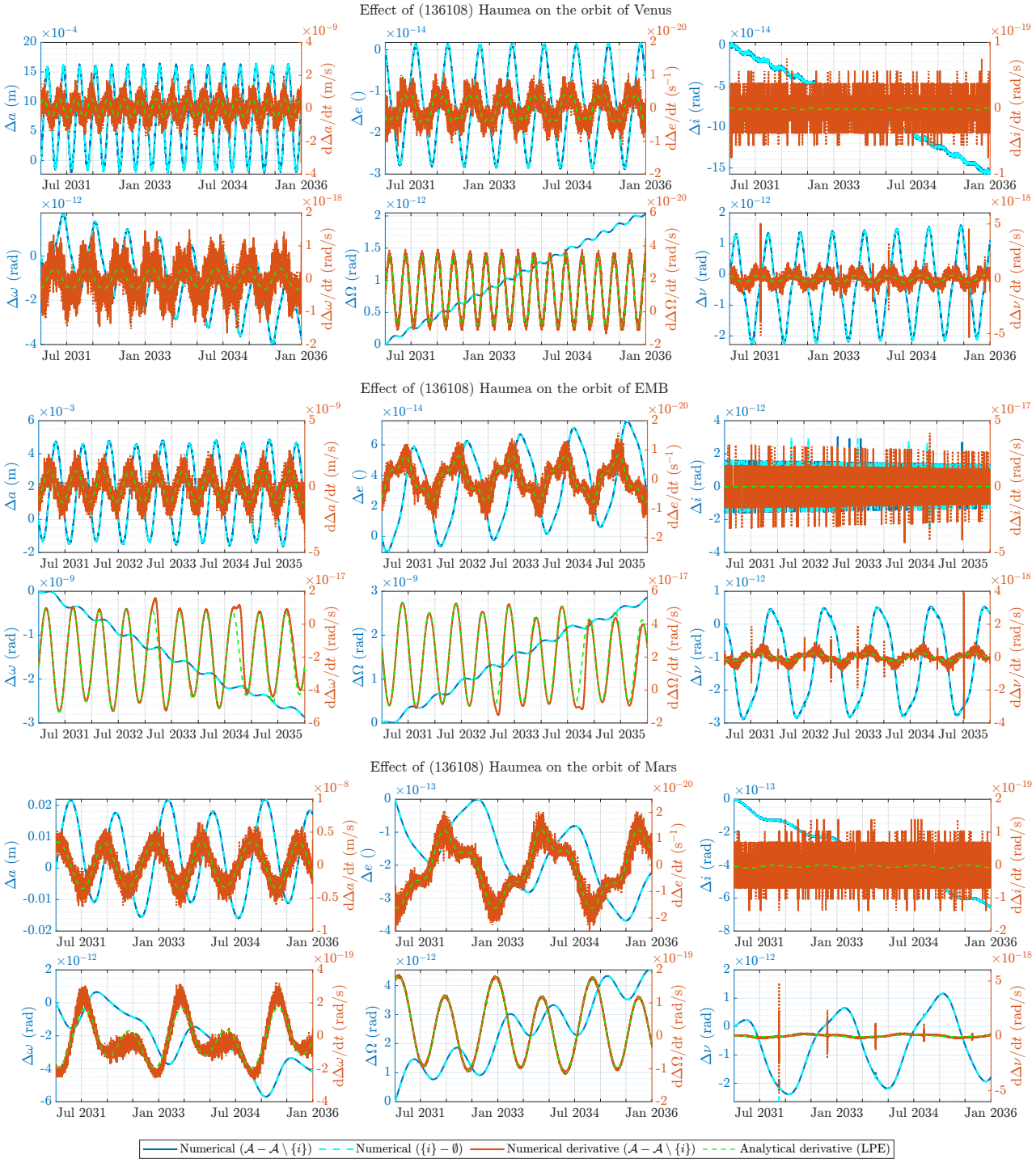

Figure C.1: Influence of Haumea on the orbital elements of Venus, the EMB and Mars. Their numerical derivatives (orange), computed from the results of each pre-fit signature (blue), are compared against the result of evaluating the set of LPE (green).

its relation to the orbital elements of the planet and asteroid orbits is found to be

$$\begin{aligned}\cos\theta = &\sin(i)\sin(i_p)\sin(\omega+\nu)\sin(\omega_p+\nu_p) - \\ &- \sin(\Omega-\Omega_p)\cos(i)\sin(\omega+\nu)\cos(\omega_p+\nu_2) + \\ &+ \sin(\Omega-\Omega_p)\cos(i_p)\cos(\omega+\nu)\sin(\omega_p+\nu_p) + \\ &+ \cos(\Omega-\Omega_p)\cos(i)\cos(i_p)\sin(\omega\nu)\sin(\omega_p+\nu_p) + \\ &+ \cos(\Omega-\Omega_p)\cos(\omega+\nu)\cos(\omega_p+\nu_p).\end{aligned} \tag{C.4}$$

Figure C.2: Influence of Ceres on the orbital elements of Venus, the EMB and Mars. Their numerical derivatives (orange), computed from the results of each pre-fit signature (blue), are compared against the result of evaluating the set of LPE (green).

This relationship can be used in equation (C.3), which can in turn be introduced to the Lagrange Planetary Equations (C.1) to compute the expected rates of change of the orbital elements of the planets as a result of the gravitational perturbation caused by each analyzed asteroid. The results of doing so with two representative perturbing objects are presented in Figure C.1 and Figure C.2: the former shows the impact of the TNO Haumea and the latter shows the influence of the asteroid Ceres.

In each figure, the blue curves represent the pre-fit impact on the orbital elements caused by the particular object. Similarly as in section 6.2, this pre-fit impact is computed two different ways (i.e., effect of all bodies minus all bodies except i; and effect of body i alone minus effect of no bodies at all), both of which are shown to coincide as the dark and light blue curves look overlapped to each other. The orange curves are the result of numerically differentiating these pre-fit effect curves, and the green curve is the straightforward application of the Lagrange Planetary Equations (C.1). It can be

noted how the orange and green curves coincide remarkably well for most of the orbital elements, with the exceptions of the argument of pericenter ω and true anomaly ν.

The reasons behind such disagreement have not been fully clarified at the end of this thesis. Published studies addressing similar problems typically use the framework of the Circular Restricted 3-Body Problem (Alessi & Sánchez, 2016; Neves et al., 2018), and their perturbing potential functions R are not fully equal to (C.3). Although these results show the potential of obtaining analytical approximations considering all orbital elements and without the need for circular restricted assumptions, it must be further confirmed whether the approach followed here is valid or some inconsistencies or mathematical nuances present in the literature have been overlooked.

D

Tudat limitations and improvements

During the development of this work, some issues related to Tudat have been encountered, some of which have been resolved and some of which have not. The aim of this chapter is to leave a record of them so that anyone finding similar issues in the future can have a description of the observed misperformance in the past, in case it is of any help to find the required solutions.

D.1. Occultation calculation bug

During the implementation of the spacecraft orbit estimation with Doppler observations, an odd behavior related to observation gaps due to planetary occultations was noticed. This is shown in Figure D.1 and Figure D.2, which were obtained with the spacecraft placed at low altitudes. The resulting observation gaps are therefore expected to last roughly half of the orbital period in the most unfavorable geometry (i.e., observation direction parallel to the spacecraft orbital plane) and to be non-existent in the most favorable geometry (i.e. observation direction perpendicular to the spacecraft orbital plane). However, the observed behavior shows more complex features, with some links displaying several short occultations in a single orbit cycle (see links to Venus in Figures D.1 and D.2). This is impossible given the quasi-spherical geometry of the planet and the orbit of the spacecraft around it.

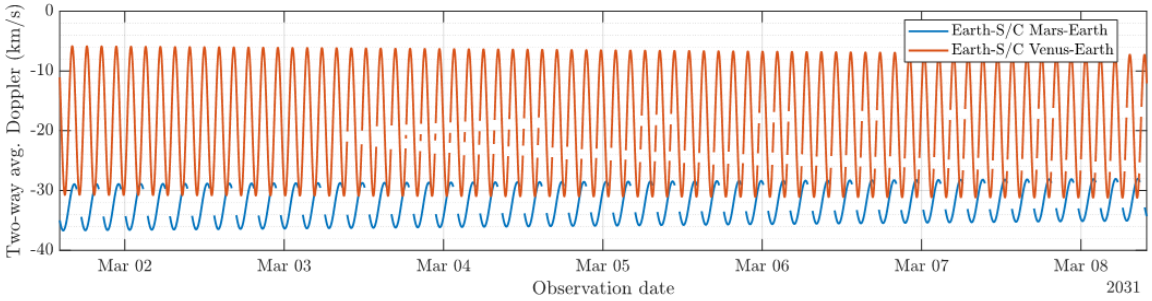

Figure D.1: Wrong observation occultations observed before patching

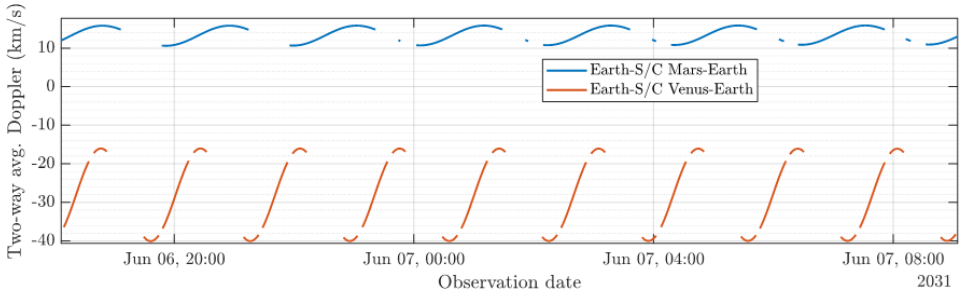

Figure D.2: Wrong observation occultations observed before patching

Revising the Tudat code led to finding a bug present in the `OccultationCalculator::isObservationViable()` function causing this issue. The cause of the problem was the computation of the epoch at which the planet location was used to check for link occultations, which was coded to always be the mid epoch between the sending and reception times. In the case of observations to spacecraft close to other planets, this epoch should be taken much closer to the epoch at which the spacecraft sends or receives the pulse instead.

After finding this issue, a patch was implemented and shared in the Tudat issue # 224. Although the technically correct way to code this would be through a convergence loop that computes the predicted time of interception of the observation signal to the location of the body that can cause occultations, the suggested patch makes use of a simpler linearly weighted mean to compute the proper epoch at which the position of the occulting body needs to be retrieved to check for the occultation condition. This is conceived to be a general approach, working for any arbitrary location of the occulting body with respect to the two ends of an observation.

This patch was observed to work just as expected for one-way observations, and this is how the observation settings remained in the main simulation. The correct behavior of Doppler observations can be observed in Figure 7.30. Two-way observations showed the appropriate gap lengths and distribution (i.e., no multiple, small gaps in a single spacecraft orbit), although occultations seemed delayed by a few minutes with respect to the periods they should appear. Further revision by the Tudat team lead to pull request 263, which introduced the fixed occultation computation together with a new function to compute the value of occultation. This is now part of the main branch of Tudat, after tests for both one-way and N-way observations passed.

D.2. Poor integration convergence

During the stage of integrator analyses, a couple configurations were found to unexpectedly worsen the convergence of the numerical solutions. These are developed below.

D.2.1. Effect of non-integer step sizes

The first strange effect was observed when generating the figures of integration error convergence after a planetary integration (section A.1), at different step sizes generated with a `np.logspace()` vector (Figure D.3). These yielded to strange behavior of the resulting integration error, which was fixed by simply adding a `np.round()` to the vector of step sizes to test. At the delivery date of this thesis, it has not been clarified whether the cause of this effect is some internal inconsistency (e.g., in decimal precision) between different Tudat functions or a more superficial effect introduced by the particular implementation of the planetary integrator analysis. This finding remains open under Tudat issue #209.

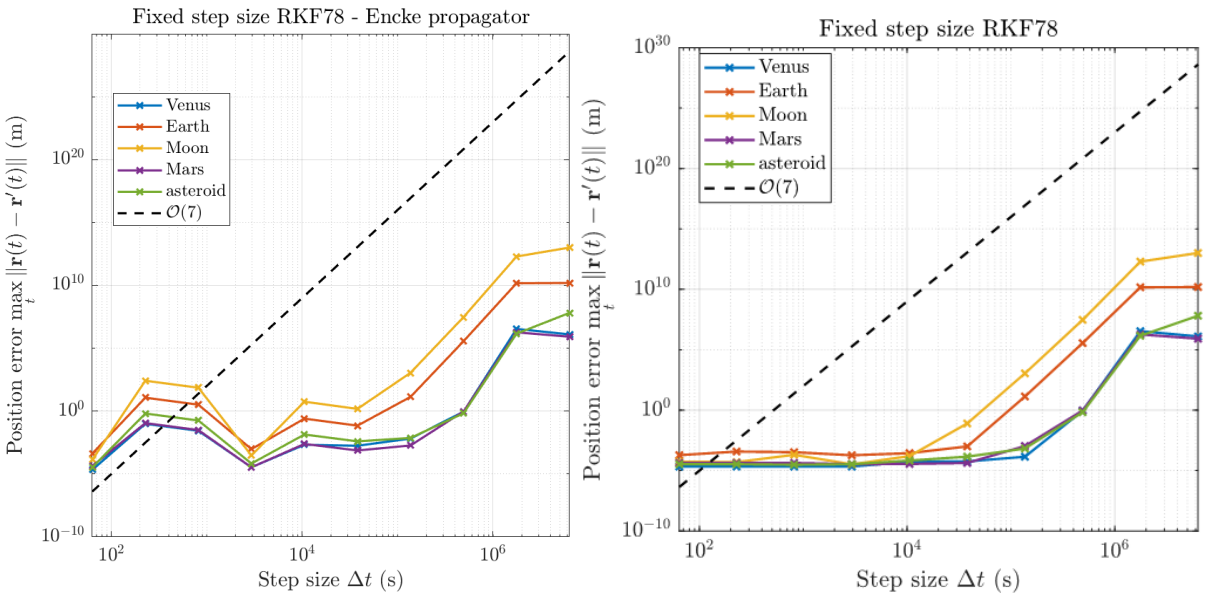

Figure D.3: Wrong integration convergence (left) vs right integration convergence (right). The only difference between the two figures is that the step sizes used in the right one are integer.

D.2.2. Effect of eclipsed Solar Radiation Pressure

The second situation in which integration convergence was not found to perform as expected was in the spacecraft integrator analysis (section A.2) in the case where SRP occultation due to planetary eclipses was introduced. This is presented in Figure D.4, where the only difference between the two figures is that the right one accounts for eclipses whereas the first one does not. This setting is modified by a single line in the `add_SC_to_system_of_bodies()` function.

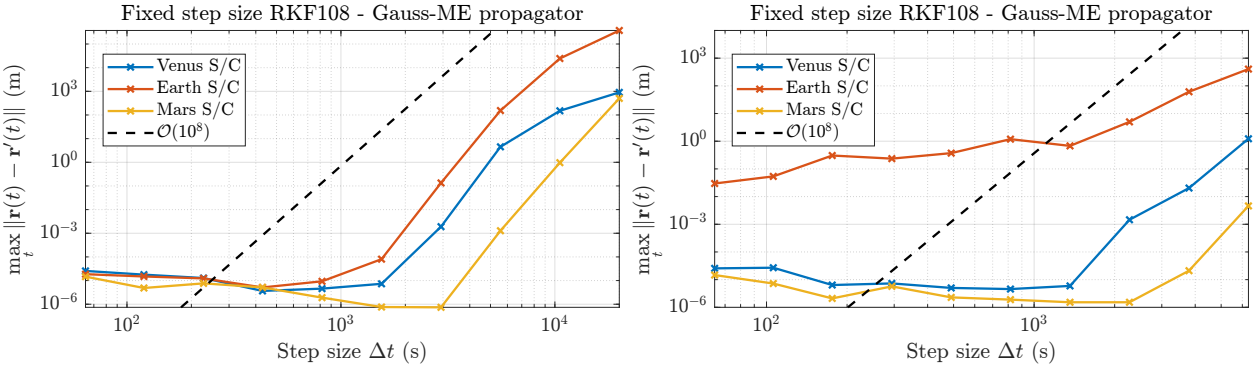

Figure D.4: Integration convergence when the SRP eclipse setting is turned off (left) vs. when it is turned on (right)

The reasons for this behavior have not been identified at the end of this thesis, and the workaround used has been to just ignore eclipses for SRP in the implemented simulations. Given the fact that the chosen orbits are relatively high (section 3.3.3 in Part IV), the effect of eclipses is not expected to impact the results of the simulations in any noticeable manner.

References

Abich, K., Abramovici, A., Amparan, B., Baatzsch, A., Okihiro, B. B., Barr, D. C., Bize, M. P., Bogan, C., Braxmaier, C., Burke, M. J., Clark, K. C., Dahl, C., Dahl, K., Danzmann, K., Davis, M. A., de Vine, G., Dickson, J. A., Dubovitsky, S., Eckardt, A., … Zimmermann, M. (2019). In-orbit performance of the grace follow-on laser ranging interferometer. *Phys. Rev. Lett.*, *123*, 031101. https://doi.org/10.1103/PhysRevLett.123.031101

Abshire, J. B., Sun, X., Neumann, G., McGarry, J., Zagwodzki, T., Jester, P., Riris, H., Zuber, M., & Smith, D. (2006). Laser pulses from earth detected at mars. *Conference on Lasers and Electro-Optics/Quantum Electronics and Laser Science Conference and Photonic Applications Systems Technologies*, CThT6. https://opg.optica.org/abstract.cfm?URI=CLEO-2006-CThT6

Alessi, E. M., Cicalò, S., Milani, A., & Tommei, G. (2012). Desaturation manoeuvres and precise orbit determination for the BepiColombo mission. *Monthly Notices of the Royal Astronomical Society*, *423*(3), 2270–2278. https://doi.org/10.1111/j.1365-2966.2012.21035.x

Alessi, E. M., & Sánchez, J. P. (2016). Semi-analytical approach for distant encounters in the spatial circular restricted three-body problem. *Journal of Guidance, Control, and Dynamics*, *39*(2), 351–359. https://doi.org/10.2514/1.G001237

Anderson, J. D., Schubert, G., Trimble, V., & Feldman, M. R. (2015). Measurements of newton's gravitational constant and the length of day. *Europhysics Letters*, *110*(1), 10002. https://doi.org/10.1209/0295-5075/110/10002

Antia, H., Chitre, S., & Gough, D. (2008). Temporal variations in the sun's rotational kinetic energy. *Astronomy & Astrophysics*, *477*(2), 657–663. https://doi.org/10.1051/0004-6361:20078209

Armano, M., Audley, H., Auger, G., Baird, J. T., Bassan, M., Binetruy, P., Born, M., Bortoluzzi, D., Brandt, N., Caleno, M., Carbone, L., Cavalleri, A., Cesarini, A., Ciani, G., Congedo, G., Cruise, A. M., Danzmann, K., de Deus Silva, M., De Rosa, R., … Zweifel, P. (2016). Sub-femto-g free fall for space-based gravitational wave observatories: Lisa pathfinder results. *Phys. Rev. Lett.*, *116*, 231101. https://doi.org/10.1103/PhysRevLett.116.231101

Arthur, R. T. W. (2019). Special relativity and the lapse of time. In *The reality of time flow: Local becoming in modern physics* (pp. 109–137). Springer International Publishing. https://doi.org/10.1007/978-3-030-15948-1_5

Bassi, A., Cacciapuoti, L., Capozziello, S., Dell'Agnello, S., Diamanti, E., Giulini, D., Iess, L., Jetzer, P., Joshi, S. K., Landragin, A., Poncin-Lafitte, C. L., Rasel, E., Roura, A., Salomon, C., & Ulbricht, H. (2022, December). A way forward for fundamental physics in space. https://doi.org/10.1038/s41526-022-00229-0

Batori, E., Almat, N., Affolderbach, C., & Mileti, G. (2021). Gnss-grade space atomic frequency standards: Current status and ongoing developments [Scientific and Fundamental Aspects of GNSS - Part 2]. *Advances in Space Research*, *68*(12), 4723–4733. https://doi.org/https://doi.org/10.1016/j.asr.2020.09.012

Batygin, K., Adams, F. C., Brown, M. E., & Becker, J. C. (2019). The planet nine hypothesis. *Physics Reports*, *805*, 1–53. https://doi.org/https://doi.org/10.1016/j.physrep.2019.01.009

Batygin, K., & Brown, M. E. (2016). Evidence for a distant giant planet in the solar system. *The Astronomical Journal*, *151*, 22. https://doi.org/10.3847/0004-6256/151/2/22

Batygin, K., Morbidelli, A., Brown, M. E., & Nesvorný, D. (2024). Generation of low-inclination, neptune-crossing trans-neptunian objects by planet nine. *The Astrophysical Journal Letters*, *966*(1), L8. https://doi.org/10.3847/2041-8213/ad3cd2

Bauer, S., Hussmann, H., Oberst, J., Dirkx, D., Mao, D., Neumann, G. A., Mazarico, E., Torrence, M. H., McGarry, J. F., Smith, D. E., & Zuber, M. T. (2017). Analysis of one-way laser ranging data to lro, time transfer and clock characterization. *Icarus*, *283*, 38–54. https://doi.org/10.1016/J.ICARUS.2016.09.026

Bellinger, E. P., & Christensen-Dalsgaard, J. (2019). Asteroseismic constraints on the cosmic-time variation of the gravitational constant from an ancient main-sequence star. *The Astrophysical Journal Letters*, *887*, L1. https://doi.org/10.3847/2041-8213/ab43e7

Belton, M. J., Chapman, C. R., Thomas, P. C., Davies, M. E., Greenberg, R., Klaasen, K., Byrnres, D., D'amario, L., Synnott, S., Johnson, J. V., Ewen, A. M., Merline, W. J., Davis, D. R., Petit, J. M., Storrs, A., Veverka, V., & Zellner, B. (1995). Bulk density of asteroid 243 ida from the orbit of its satellite dactyl. *Nature 1995 374:6525*, *374*, 785–788. https://doi.org/10.1038/374785a0

Belyakov, M., Bernardinelli, P. H., & Brown, M. E. (2022). Limits on the detection of planet nine in the dark energy survey. *The Astronomical Journal*, *163*, 216. https://doi.org/10.3847/1538-3881/ac5c56

Bernus, L., Minazzoli, O., Fienga, A., Gastineau, M., Laskar, J., Deram, P., & Ruscio, A. D. (2020). Constraint on the yukawa suppression of the newtonian potential from the planetary ephemeris inpop19a. *Physical Review D*, *102*. https://doi.org/10.1103/PhysRevD.102.021501

Bertotti, B., Iess, L., & Tortora, P. (2003). A test of general relativity using radio links with the cassini spacecraft. *Nature*, *425*(6956), 374–376. https://doi.org/10.1038/nature01997

Bills, B. G. (2023). Overview of planetary trilateration: Science, observations, measurements. *Interplanetary Trilateration Network Workshop*. http://grailteam.mit.edu/Trilateration/

Bills, B. G., & Gorski, K. M. (2022). Sensitivity and antenna pattern for an interplanetary laser trilateration network. *Planetary and Space Science*, *215*, 105423. https://doi.org/10.1016/J.PSS.2022.105423

Bills, B. G., & Skillman, D. (2022). Planetary orbit dynamics via trilateration: Prospectus for an interplanetary scale ring laser gyro with nominal area of 1 square au. *Planetary and Space Science*, *214*, 105415. https://doi.org/10.1016/J.PSS.2022.105415

Birch, M., & Singh, B. (2014). Method of best representation for averages in data evaluation. *Nuclear Data Sheets*, *120*, 106–108. https://doi.org/https://doi.org/10.1016/j.nds.2014.07.019

Birnbaum, K. M., Chen, Y., & Hemmati, H. (2010). Precision optical ranging by paired one-way time of flight. *7587*, 86–93. https://doi.org/10.1117/12.843315

Biskupek, L., Müller, J., Torre, J.-M., & Giulini, D. (2021). Benefit of new high-precision llr data for the determination of relativistic parameters. https://doi.org/10.3390/universe7020034

Biswas, A., Srinivasan, M., Andrews, K., Alerstam, E., Velasco, A., Wright, M., Kovalik, J., Douglas, B., Allmaras, J., Rhein, V. V., Wollman, E., Rogalin, R., Meenehan, S., Zhu, D., Conway, D., Alvarez-Salazar, O., Pong, C., Chang, H., Wilkerson, M., … Klipstein, W. (2024). Deep space optical communications technology demonstration. In H. Hemmati & B. S. Robinson (Eds.), *Free-space laser communications xxxvi* (p. 1287706, Vol. 12877). SPIE. https://doi.org/10.1117/12.3001750

Bonanno, A., & Fröhlich, H.-E. (2020). A new helioseismic constraint on a cosmic-time variation of g. *The Astrophysical Journal Letters*, *893*(2), L35. https://doi.org/10.3847/2041-8213/ab86b9

Boroson, D. M., Robinson, B. S., Murphy, D. V., Burianek, D. A., Khatri, F., Kovalik, J. M., Sodnik, Z., & Cornwell, D. M. (2014). Overview and results of the Lunar Laser Communication Demonstration. In H. Hemmati & D. M. Boroson (Eds.), *Free-space laser communication and atmospheric propagation xxvi* (89710S, Vol. 8971). SPIE. https://doi.org/10.1117/12.2045508

Bronnikov, K., Ivashchuk, V., & Khrushchev, V. (2022). Fundamental physical constants: Search results and variation descriptions. *Measurement Techniques*, *65*(3), 151–156. https://doi.org/10.1007/s11018-022-02062-z

Brown, M. E. (2017). Observational bias and the clustering of distant eccentric kuiper belt objects. *The Astronomical Journal*, *154*(2), 65. https://doi.org/10.3847/1538-3881/aa79f4

Brown, M. E., & Batygin, K. (2016). Observational constraints on the orbit and location of planet nine in the outer solar system. *The Astrophysical Journal Letters*, *824*(2), L23. https://doi.org/10.3847/2041-8205/824/2/L23

Brown, M. E., & Batygin, K. (2019). Orbital clustering in the distant solar system. *The Astronomical Journal*, *157*(2), 62. https://doi.org/10.3847/1538-3881/aaf051

Brown, M. E., & Batygin, K. (2021). The orbit of planet nine. *The Astronomical Journal*, *162*(5), 219. https://doi.org/10.3847/1538-3881/ac2056

Brown, M. E., Holman, M. J., & Batygin, K. (2024). A pan-starrs1 search for planet nine [arXiv preprint]. https://arxiv.org/abs/2401.17977

Cano, A., Pastor, A., Escobar, D., Míguez, J., & Sanjurjo-Rivo, M. (2023). Covariance determination for improving uncertainty realism in orbit determination and propagation [Space Environment Management and Space Sustainability]. *Advances in Space Research*, *72*(7), 2759–2777. https://doi.org/https://doi.org/10.1016/j.asr.2022.08.001

Cappuccio, P., Hickey, A., Durante, D., Di Benedetto, M., Iess, L., De Marchi, F., Plainaki, C., Milillo, A., & Mura, A. (2020). Ganymede's gravity, tides and rotational state from juice's 3gm experiment simulation. *Planetary and Space Science*, *187*, 104902. https://doi.org/https://doi.org/10.1016/j.pss.2020.104902

Carroll, S. M. (2004). *Spacetime and geometry. an introduction to general relativity* (1st ed.). Addison Wesley.

Carry, B. (2012). Density of asteroids. *Planetary and Space Science*, *73*, 98–118. https://doi.org/10.1016/J.PSS.2012.03.009

Cascioli, G., Marchi, F. D., Genova, A., Iess, L., Smith, D. E., & Zuber, M. T. (2019). The contribution of a large baseline intersatellite link to relativistic metrology. *2019 IEEE 5th International Workshop on Metrology for AeroSpace (MetroAeroSpace)*, 579–583. https://doi.org/10.1109/MetroAeroSpace.2019.8869641

Chesley, S. R., Farnocchia, D., Nolan, M. C., Vokrouhlický, D., Chodas, P. W., Milani, A., Spoto, F., Rozitis, B., Benner, L. A., Bottke, W. F., Busch, M. W., Emery, J. P., Howell, E. S., Lauretta, D. S., Margot, J. L., & Taylor, P. A. (2014). Orbit and bulk density of the osiris-rex target asteroid (101955) bennu. *Icarus*, *235*, 5–22. https://doi.org/10.1016/J.ICARUS.2014.02.020

Chesley, S. R., Ostro, S. J., Vokrouhlický, D., Čapek, D., Giorgini, J. D., Nolan, M. C., Margot, J.-L., Hine, A. A., Benner, L. A. M., & Chamberlin, A. B. (2003). Direct detection of the yarkovsky effect by radar ranging to asteroid 6489 golevka. *Science*, *302*(5651), 1739–1742. https://doi.org/10.1126/science.1091452

Christensen-Dalsgaard, J. (2021). Solar structure and evolution. *Living Reviews in Solar Physics*, *18*(1), 2. https://doi.org/10.1007/s41116-020-00028-3

Combrinck, L. (2010). Satellite laser ranging. *Sciences of Geodesy - I: Advances and Future Directions*, 301–338. https://doi.org/10.1007/978-3-642-11741-1_9

Compton, A. H. (1923). A quantum theory of the scattering of x-rays by light elements. *Phys. Rev.*, *21*, 483–502. https://doi.org/10.1103/PhysRev.21.483

Curtis, H. D. (2014). *Orbital mechanics for engineering students* (3rd ed.). Butterworth-Heinemann. https://www.sciencedirect.com/book/9780080977478/orbital-mechanics-for-engineering-students

Damiani, C., Rozelot, J. P., Lefebvre, S., Kilcik, A., & Kosovichev, A. G. (2011). A brief history of the solar oblateness. a review. *Journal of Atmospheric and Solar-Terrestrial Physics*, *73*, 241–250. https://doi.org/10.1016/J.JASTP.2010.02.021

Danzmann, K. (2000). Lisa mission overview [Fundamental Physics in Space]. *Advances in Space Research*, *25*(6), 1129–1136. https://doi.org/https://doi.org/10.1016/S0273-1177(99)00973-4

Danzmann, K., Rüdiger, A., Schilling, R., Winkler, W., Hough, J., Bender, P., & Edwards, C. (1993). *Lisa – proposal for a laser-interferometric gravitational wave detector in space* (Technical Report No. 177). Max-Planck-Institut fur Quantenoptik.

de Rham, C. (2014). Massive gravity. *Living reviews in relativity*, *17*(1), 1–189. https://doi.org/10.12942/lrr-2014-7

De Marchi, F., & Cascioli, G. (2020). Testing general relativity in the solar system: Present and future perspectives. *Classical and Quantum Gravity*, *37*(9), 095007. https://doi.org/10.1088/1361-6382/ab6ae0

De Marchi, F., Tommei, G., Milani, A., & Schettino, G. (2016). Constraining the nordtvedt parameter with the bepicolombo radioscience experiment. *Phys. Rev. D*, *93*, 123014. https://doi.org/10.1103/PhysRevD.93.123014

Degnan, J. J. (1993). Millimeter accuracy satellite laser ranging: A review. *Contributions of Space Geodesy to Geodynamics:Technology*, *25*, 133–162.

Degnan, J. J. (1996). Compact laser transponders for interplanetary ranging and time transfer. *Proc. 10th International Workshop on Laser Ranging. Shanghai, China*, 11–15.

Degnan, J. J. (2001). Unified approach to photon-counting microlaser rangers, transponders, and altimeters. *Surveys in Geophysics*, *22*, 431–447. https://doi.org/10.1023/A:1015659931843/METRICS

Degnan, J. J. (2002). Asynchronous laser transponders for precise interplanetary ranging and time transfer. *Journal of Geodynamics*, *34*, 551–594. https://doi.org/10.1016/S0264-3707(02)00044-3

Degnan, J. J., McGarry, J., Dabney, P., Zagwodzki, T., Tierney, M., & Weatherley, M. (1998). Design and test of a breadboard interplanetary laser transponder. *Proc. 11th International Workshop on Laser Ranging. Deggendorf, Germany*, 21–25.

Deram, P., Fienga, A., Verma, A. K., Gastineau, M., & Laskar, J. (2022). Gaia-dr2 asteroid observations and inpop planetary ephemerides. *Celestial Mechanics and Dynamical Astronomy*, *134*, 1–24. https://doi.org/10.1007/S10569-022-10084-6/TABLES/9

Descamps, P., Marchis, F., Pollock, J., Berthier, J., Vachier, F., Birlan, M., Kaasalainen, M., Harris, A., Wong, M., Romanishin, W., Cooper, E., Kettner, K., Wiggins, P., Kryszczynska, A., Polinska, M., Coliac, J.-F., Devyatkin, A., Verestchagina, I., & Gorshanov, D. (2008). New determination of the size and bulk density of the binary asteroid 22 kalliope from observations of mutual eclipses [Mars Polar Science IV]. *Icarus*, *196*(2), 578–600. https://doi.org/https://doi.org/10.1016/j.icarus.2008.03.014

di Ruscio, A., Fienga, A., Durante, D., Iess, L., Laskar, J., & Gastineau, M. (2020). Analysis of cassini radio tracking data for the construction of inpop19a: A new estimate of the kuiper belt mass. *Astronomy & Astrophysics*, *640*, A7. https://doi.org/10.1051/0004-6361/202037920

di Stefano, I., Cappuccio, P., & Iess, L. (2023). Precise modeling of non-gravitational accelerations of the spacecraft bepicolombo during cruise phase. *Journal of Spacecraft and Rockets*, *60*(5), 1625–1638. https://doi.org/10.2514/1.A35704

Ding, Y., Li, Z., Liu, C., Kang, Z., Sun, M., Sun, J., & Chen, L. (2023). Analysis of the impact of atmospheric models on the orbit prediction of space debris. *Sensors*, *23*(21). https://doi.org/10.3390/s23218993

Dirkx, D., Gurvits, L. I., Lainey, V., Lari, G., Milani, A., Cimò, G., Bocanegra-Bahamon, T. M., & Visser, P. N. (2017). On the contribution of pride-juice to jovian system ephemerides. *Planetary and Space Science*, *147*, 14–27. https://doi.org/10.1016/J.PSS.2017.09.004

Dirkx, D., Noomen, R., Prochazka, I., Bauer, S., & Vermeersen, L. L. (2014). Influence of atmospheric turbulence on planetary transceiver laser ranging. *Advances in Space Research*, *54*, 2349–2370. https://doi.org/10.1016/J.ASR.2014.08.022

Dirkx, D., Noomen, R., Visser, P. N. A. M., Gurvits, L. I., & Vermeersen, L. L. A. (2016). Space-time dynamics estimation from space mission tracking data. *Astronomy & Astrophysics*, *587*, A156. https://doi.org/10.1051/0004-6361/201527524

Dirkx, D., Noomen, R., Visser, P. N., Bauer, S., & Vermeersen, L. L. (2015). Comparative analysis of one- and two-way planetary laser ranging concepts. *Planetary and Space Science*, *117*, 159–176. https://doi.org/10.1016/J.PSS.2015.06.005

Dirkx, D., Vermeersen, L. L., Noomen, R., & Visser, P. N. (2014). Phobos laser ranging: Numerical geodesy experiments for martian system science. *Planetary and Space Science*, *99*, 84–102. https://doi.org/10.1016/J.PSS.2014.03.022

Dirkx, D. (2015). *Interplanetary laser ranging: Analysis for implementation in planetary science missions* [Doctoral dissertation, Delft University of Technology]. https://repository.tudelft.nl/islandora/object/uuid%3Abd728e02-f403-4cea-9e2b-65b04b47b3f7

Dirkx, D., & Cowan, K. (2019). Numerical integration – error sources [Lecture notes in Numerical in Astrodynamics course. Delft University of Technology].

Dirkx, D., & Cowan, K. (2023). Acceleration models (3) formulation – spherical harmonic gravity [Lecture notes in Numerical Astrodynamics course. Delft University of Technology].

Dirkx, D., & Mooij, E. (2019). Formulation of equations of motion [Lecture notes in Propagation and Optimization in Astrodynamics course. Delft University of Technology].

Dirkx, D., & Mooij, E. (2020). Acceleration modelling [Lecture notes in Propagation and Optimization in Astrodynamics course. Delft University of Technology].

Dirkx, D., Prochazka, I., Bauer, S., Visser, P., Noomen, R., Gurvits, L. I., & Vermeersen, B. (2019). Laser and radio tracking for planetary science missions-a comparison. *Journal of Geodesy*, *93*, 2405–2420. https://doi.org/10.1007/s00190-018-1171-x

Doornbos, E. (2012). *Thermospheric density and wind determination from satellite dynamics*. Springer Science & Business Media. https://doi.org/10.1007/978-3-642-25129-0

Duan, B., & Hugentobler, U. (2021). Enhanced solar radiation pressure model for gps satellites considering various physical effects. *GPS Solutions*, *25*(2), 42. https://doi.org/10.1007/s00190-018-1173-8

Duev, D. A., Calvés, G. M., Pogrebenko, S. V., Gurvits, L. I., Cimo, G., & Bahamon, T. B. (2012). Spacecraft vlbi and doppler tracking: Algorithms and implementation. *Astronomy & Astrophysics*, *541*, A43.

Eddington, A. S. (1923). *The mathematical theory of relativity*. The University Press.

Edgeworth, K. E. (1949). The Origin and Evolution of the Solar System. *Monthly Notices of the Royal Astronomical Society*, *109*(5), 600–609. https://doi.org/10.1093/mnras/109.5.600

Einstein, A. (1915). Die feldgleichungen der gravitation. *Sitzungsberichte der Königlich Preußischen Akademie der Wissenschaften*, 844–847.

Einstein, A., Infeld, L., & Hoffmann, B. (1938). The gravitational equations and the problem of motion. *Annals of mathematics*, 65–100.

Emmert, J. T., Drob, D. P., Picone, J. M., Siskind, D. E., Jones Jr., M., Mlynczak, M. G., Bernath, P. F., Chu, X., Doornbos, E., Funke, B., Goncharenko, L. P., Hervig, M. E., Schwartz, M. J., Sheese, P. E., Vargas, F., Williams, B. P., & Yuan, T. (2021). Nrlmsis 2.0: A whole-atmosphere empirical model of temperature and neutral species densities [e2020EA001321 2020EA001321]. *Earth and Space Science*, *8*(3), e2020EA001321. https://doi.org/https://doi.org/10.1029/2020EA001321

Eubanks, M. (2023). Iltn observables. *Interplanetary Trilateration Network Workshop*. http://grailteam.mit.edu/Trilateration/

Exertier, P., Belli, A., Samain, E., Meng, W., Zhang, H., Tang, K., Schlicht, A., Schreiber, U., Hugentobler, U., Prochàzka, I., et al. (2019). Time and laser ranging: A window of opportunity for geodesy, navigation, and metrology. *Journal of geodesy*, *93*, 2389–2404. https://doi.org/10.1007/s00190-018-1173-8

Exertier, P., Bonnefond, P., Deleflie, F., Barlier, F., Kasser, M., Biancale, R., & Ménard, Y. (2006). Contribution of laser ranging to earth's sciences. *Comptes Rendus Geoscience*, *338*, 958–967. https://doi.org/10.1016/J.CRTE.2006.09.019

Faller, J., Alley, C., Bender, P., Currie, D., Dicke, R., Kaula, W., MacDonald, G., Mulholland, J., & Plotkin, H. (1971). 14. laser ranging retroreflector. *Apollo 14 Preliminary Science Report*, *272*, 215.

Farnocchia, D., Chesley, S. R., Takahashi, Y., Rozitis, B., Vokrouhlický, D., Rush, B. P., Mastrodemos, N., Kennedy, B. M., Park, R. S., Bellerose, J., Lubey, D. P., Velez, D., Davis, A. B., Emery, J. P., Leonard, J. M., Geeraert, J., Antreasian, P. G., & Lauretta, D. S. (2021). Ephemeris and hazard assessment for near-earth asteroid (101955) bennu based on osiris-rex data. *Icarus*, *369*, 114594. https://doi.org/10.1016/J.ICARUS.2021.114594

Fayolle, M., Dirkx, D., Lainey, V., Gurvits, L., & Visser, P. (2022). Decoupled and coupled moons' ephemerides estimation strategies application to the juice mission. *Planetary and Space Science*, *219*, 105531. https://doi.org/https://doi.org/10.1016/j.pss.2022.105531

Ferus, M., Žabka, J., Schmidt, N., & Heays, A. (2022). Asteroid prospecting and space mining. In N. Schmidt (Ed.), *Governance of emerging space challenges: The benefits of a responsible cosmopolitan state policy* (pp. 217–232). Springer International Publishing. https://doi.org/10.1007/978-3-030-86555-9_12

Fienga, A. (2023a). Interplanetary laser tri-lateration network: Simulation with inpop planetary ephemerides. https://arxiv.org/abs/2301.06394

Fienga, A., Avdellidou, C., & Hanuš, J. (2020). Asteroid masses obtained with inpop planetary ephemerides. *Monthly Notices of the Royal Astronomical Society*, *492*, 589–602. https://doi.org/10.1093/MNRAS/STZ3407

Fienga, A., Bigot, L., Mary, D., Deram, P., Ruscio, A. D., Bernus, L., Gastineau, M., & Laskar, J. (2019). Evolution of inpop planetary ephemerides and bepi-colombo simulations. *Proceedings of the International Astronomical Union*, *15*, 31–51. https://doi.org/10.1017/S1743921321001277

Fienga, A., Deram, P., Ruscio, A. D., Viswanathan, V., Camargo, J. I. B., Bernus, L., Gastineau, M., & Laskar, J. (2021). *Inpop21a planetary ephemerides* (Scientific and technical notes No. S110). Institut de Mécanique Céleste et de Calculs des Éphémérides (IMCCE). Paris. https://www.imcce.fr/content/medias/recherche/equipes/asd/inpop/inpop21a.pdf

Fienga, A., Deram, P., Viswanathan, V., Ruscio, A. D., Bernus, L., Durante, D., Gastineau, M., & Laskar, J. (2019). *Inpop19a planetary ephemerides* (Scientific and technical notes No. S109). Institut de mécanique céleste et de calculs des éphémérides. Paris. https://hal.science/hal-02470929/document

Fienga, A., Laskar, ·. J., Kuchynka, ·. P., Manche, ·. H., Desvignes, ·. G., Gastineau, ·. M., Cognard, ·. I., Theureau, ·. G., Laskar, J., Kuchynka, P., Manche, H., Gastineau, M., Desvignes, G., & Theureau, G. (2011). The inpop10a planetary ephemeris and its applications in fundamental physics. *Celest Mech Dyn Astr*, *111*, 363–385. https://doi.org/10.1007/s10569-011-9377-8

Fienga, A., Laskar, J., Exertier, P., Manche, H., & Gastineau, M. (2015). Numerical estimation of the sensitivity of inpop planetary ephemerides to general relativity parameters. *Celestial Mechanics and Dynamical Astronomy*, *123*, 325–349. https://doi.org/10.1007/S10569-015-9639-Y/

Fienga, A., Laskar, J., Manche, H., & Gastineau, M. (2016). Constraints on the location of a possible 9th planet derived from the cassini data. *Astronomy & Astrophysics*, *587*, L8. https://doi.org/10.1051/0004-6361/201628227

Fienga, A., Ruscio, A. D., Bernus, L., Deram, P., Durante, D., Laskar, J., & Iess, L. (2020). New constraints on the location of p9 obtained with the inpop19a planetary ephemeris. *Astronomy & Astrophysics*, *640*, A6. https://doi.org/10.1051/0004-6361/202037919

Fienga, A. (2023b). Itln and planetary and lunar ephemerides. *Interplanetary Trilateration Network Workshop*. http://grailteam.mit.edu/Trilateration/

Fienga, A., Avdellidou, C., & Hanuvs, J. (2019). Asteroid masses obtained with inpop planetary ephemerides. *Monthly Notices of the Royal Astronomical Society*. https://api.semanticscholar.org/CorpusID:213946280

Fienga, A., & Minazzoli, O. (2024). Testing theories of gravity with planetary ephemerides. *Living Reviews in Relativity 2024 27:1*, *27*, 1–99. https://doi.org/10.1007/S41114-023-00047-0

Fischbach, E., Sudarsky, D., Szafer, A., Talmadge, C., & Aronson, S. H. (1986). Reanalysis of the eoumltvös experiment. *Phys. Rev. Lett.*, *56*, 3–6. https://doi.org/10.1103/PhysRevLett.56.3

Fischbach, E., & Talmadge, C. L. (1999). *The search for non-newtonian gravity* (1st ed.). Springer. https://doi.org/10.1007/978-1-4612-1438-0

Folkner, W. M., Williams, J. G., Boggs, D. H., Park, R. S., & Kuchynka, P. (2014). The planetary and lunar ephemerides de430 and de431 [revise citation]. *Interplanetary Network Progress Report*, *196*(1), 42–196.

Gaia Collaboration. (2016). The gaia mission⋆. *Astronomy & Astrophysics*, *595*, A1. https://doi.org/10.1051/0004-6361/201629272

Galache, J. L., Beeson, C. L., Mcleod, K. K., & Elvis, M. (2015). The need for speed in near-earth asteroid characterization. *Planetary and Space Science*, *111*, 155–166. https://doi.org/10.1016/j.pss.2015.04.004

Galád, A., & Gray, B. (2002). Asteroid encounters suitable for mass determinations. *Astronomy & Astrophysics*, *391*, 1115–1122. https://doi.org/10.1051/0004-6361:20020810

Gan, W.-Q., Zhu, C., Deng, Y.-Y., Li, H., Su, Y., Zhang, H.-Y., Chen, B., Zhang, Z., Wu, J., Deng, L., Huang, Y., Yang, J.-F., Cui, J.-J., Chang, J., Wang, C., Wu, J., Yin, Z.-S., Chen, W., Fang, C., … Tang, X.-J. (2019). Advanced space-based solar observatory (aso-s): An overview. *Research in Astronomy and Astrophysics*, *19*(11), 156. https://doi.org/10.1088/1674-4527/19/11/156

Genova, A., et al. (2023). Fundamental physics investigation by using interplanetary trilateration. *Interplanetary Trilateration Network Workshop*. http://grailteam.mit.edu/Trilateration/

Genova, A., Mazarico, E., Goossens, S., Lemoine, F. G., Neumann, G. A., Smith, D. E., & Zuber, M. T. (2018). Solar system expansion and strong equivalence principle as seen by the nasa messenger mission. *Nature communications*, *9*(1), 289. https://doi.org/10.1038/s41467-017-02558-1

Gladman, B., & Volk, K. (2021). Transneptunian space. *Annual Review of Astronomy and Astrophysics*, *59*(1), 203–246. https://doi.org/10.1146/annurev-astro-120920-010005

Goffin, E. (2014). Astrometric asteroid masses: A simultaneous determination. *Astronomy & Astrophysics*, *565*, A56. https://doi.org/10.1051/0004-6361/201322766

Gomes, R., Deienno, R., & Morbidelli, A. (2016). The inclination of the planetary system relative to the solar equator may be explained by the presence of planet 9. https://doi.org/10.3847/1538-3881/153/1/27

Gurvits, L. I., Bahamon, T. M. B., Cimò, G., Duev, D. A., Calvés, G. M., Pogrebenko, S. V., de Pater, I., Vermeersen, L. L. A., Rosenblatt, P., Oberst, J., Charlot, P., Frey, S., Tudose, V., Gurvits, L. I., Bahamon, T. M. B., Cimò, G., Duev, D. A., Calvés, G. M., Pogrebenko, S. V., … Tudose, V. (2013). Planetary radio interferometry and doppler experiment (pride) for the juice mission. *EPSC*, *2*, EPSC2013–357. https://ui.adsabs.harvard.edu/abs/2013EPSC....8..357G/abstract

Gurvits, L. I., Cimò, G., Dirkx, D., Pallichadath, V., Akins, A., Altobelli, N., Bocanegra-Bahamon, T. M., Cazaux, S. M., Charlot, P., Duev, D. A., Fayolle, M. S., Fogasy, J., Frey, S., Lainey, V., Calvés, G. M., Perger, K., Pogrebenko, S. V., Said, N. M. M., Vallat, C., … Willner, K. (2023). Planetary radio interferometry and doppler experiment (pride) of the juice mission. *Space Science Reviews 2023 219:8*, *219*, 1–41. https://doi.org/10.1007/S11214-023-01026-1

Hariharan, P., & Hariharan, P. (2007). 1 - introduction. In P. Hariharan & P. Hariharan (Eds.), *Basics of interferometry (second edition)* (Second Edition, pp. 1–2). Academic Press. https://doi.org/https://doi.org/10.1016/B978-012373589-8/50003-1

Hemmati, H., Birnbaum, K., Farr, W., Turyshev, S., & Biswas, A. (2009). Combined laser communications and laser ranging transponder for moon and mars. *Free-Space Laser Communication Technologies XXI*, *7199*, 167–178.

Hertz, H. (1966). The mass of vesta. *International Astronomical Union Circular*, *1983*, 3.

Hilton, J. L., Seidelmann, P. K., & Middour, J. (1996). Prospects for determining asteroid masses. *Astronomical Journal*, *112*, 2319–2329.

Hofmann, F., & Müller, J. (2018). Relativistic tests with lunar laser ranging. *Classical and Quantum Gravity*, *35*, 035015. https://doi.org/10.1088/1361-6382/AA8F7A

Hohmann, M. (2021). Parametrized post-newtonian formalism. In E. N. Saridakis, R. Lazkoz, V. Salzano, P. V. Moniz, S. Capozziello, J. Beltrán Jiménez, M. De Laurentis, & G. J. Olmo (Eds.), *Modified gravity and cosmology: An update by the cantata network* (pp. 357–373). Springer International Publishing. https://doi.org/10.1007/978-3-030-83715-0_24

Holman, M. J., & Payne, M. J. (2016). Observational constraints on planet nine: Astrometry of pluto and other trans-neptunian objects. *The Astronomical Journal*, *152*. https://doi.org/10.3847/0004-6256/152/4/80

Hu, W.-R., & Wu, Y.-L. (2017). The Taiji Program in Space for gravitational wave physics and the nature of gravity. *National Science Review*, *4*(5), 685–686. https://doi.org/10.1093/nsr/nwx116

Hurd, W. J., MacNeal, B. E., Ortiz, G. G., Cheng, E. S., Moe, R. V., Walker, J. Z., Fairbrother, D. A., Dennis, M. L., Eegholm, B., & Kasunic, K. J. (2006). Exo-atmospheric telescopes for deep space optical communications. *IEEE Aerospace Conference Proceedings*, *2006*. https://doi.org/10.1109/AERO.2006.1655834

Imperi, L., Iess, L., & Mariani, M. J. (2018). An analysis of the geodesy and relativity experiments of bepicolombo. *Icarus*, *301*, 9–25. https://doi.org/10.1016/J.ICARUS.2017.09.008

Iorio, L. (2012). Constraining the angular momentum of the sun with planetary orbital motions and general relativity. *Solar Physics*, *281*, 815–826. https://doi.org/10.1007/s11207-012-0086-6

Iorio, L. (2015). Gravitational anomalies in the solar system? *International Journal of Modern Physics D*, *24*(06), 1530015. https://doi.org/10.1142/S0218271815300153

Irbah, A., Mecheri, R., Damé, L., & Djafer, D. (2019). Variations of solar oblateness with the 22 yr magnetic cycle explain apparently inconsistent measurements. *The Astrophysical Journal Letters*, *875*(2), L26. https://doi.org/10.3847/2041-8213/ab16e2

Standard atmosphere (Standard). (1975, May). International Organization for Standardization. Geneva, CH. https://www.iso.org/standard/7472.html

Jones, D. L., Folkner, W. M., Jacobson, R. A., Jacobs, C. S., Dhawan, V., Romney, J., & Fomalont, E. (2014). Astrometry of cassini with the vlba to improve the saturn ephemeris. *The Astronomical Journal*, *149*(1), 28. https://doi.org/10.1088/0004-6256/149/1/28

Kawamura, S., Nakamura, T., Ando, M., Seto, N., Tsubono, K., Numata, K., Takahashi, R., Nagano, S., Ishikawa, T., Musha, M., Ueda, K.-i., Sato, T., Hosokawa, M., Agatsuma, K., Akutsu, T., Aoyanagi, K.-s., Arai, K., Araya, A., Asada, H., … Yoshino, T. (2006). The japanese space gravitational wave antenna—decigo. *Classical and Quantum Gravity*, *23*(8), S125. https://doi.org/10.1088/0264-9381/23/8/S17

Kennewell, J. A., & Vo, B. N. (2013). An overview of space situational awareness. *Proceedings of the 16th International Conference on Information Fusion*, 1029–1036.

Konopliv, A. S., Asmar, S. W., Folkner, W. M., Karatekin, Ö., Nunes, D. C., Smrekar, S. E., Yoder, C. F., & Zuber, M. T. (2011). Mars high resolution gravity fields from mro, mars seasonal gravity, and other dynamical parameters. *Icarus*, *211*, 401–428. https://doi.org/10.1016/J.ICARUS.2010.10.004

Konopliv, A., Park, R., & Ermakov, A. (2020). The mercury gravity field, orientation, love number, and ephemeris from the messenger radiometric tracking data. *Icarus*, *335*, 113386. https://doi.org/https://doi.org/10.1016/j.icarus.2019.07.020

Kral, L., Prochazka, I., & Hamal, K. (2005). Optical signal path delay fluctuations caused by atmospheric turbulence. *Opt. Lett.*, *30*(14), 1767–1769. https://doi.org/10.1364/OL.30.001767

Kretlow, M. (2020). Size, mass and density of asteroids (simda) - a web based archive and data service [Virtual meeting, 21 September–9 October 2020]. *Europlanet Science Congress 2020*, *14*. https://doi.org/10.5194/epsc2020-690

Kucharski, D., Kirchner, G., Lim, H. C., & Koidl, F. (2011). Optical response of nanosatellite blits measured by the graz 2 khz slr system. *Advances in Space Research*, *48*, 1335–1340. https://doi.org/10.1016/J.ASR.2011.06.016

Kuchynka, P., & Folkner, W. M. (2013). A new approach to determining asteroid masses from planetary range measurements. *Icarus*, *222*, 243–253. https://doi.org/10.1016/J.ICARUS.2012.11.003

Kuiper, G. P. (1951). On the origin of the solar system. *Proceedings of the National Academy of Sciences*, *37*(1), 1–14. https://doi.org/10.1073/pnas.37.1.1

Lainey, V., Dehant, V., & Pätzold, M. (2007). First numerical ephemerides of the martian moons. *A&A*, *465*(3), 1075–1084. https://doi.org/10.1051/0004-6361:20065466

Lari, G., Schettino, G., Serra, D., & Tommei, G. (2022). Orbit determination methods for interplanetary missions: Development and use of the orbit14 software. *Experimental Astronomy*, *53*(1), 159–208. https://doi.org/10.1007/s10686-021-09823-8

Lawler, S. M., Shankman, C., Kaib, N., Bannister, M. T., Gladman, B., & Kavelaars, J. J. (2016). Observational signatures of a massive distant planet on the scattering disk. *The Astronomical Journal*, *153*(1), 33. https://doi.org/10.3847/1538-3881/153/1/33

Le, T. (2021). A test of cosmological space–time variation of the gravitational constant with strong gravitational fields. *Chinese Journal of Physics*, *73*, 147–153. https://doi.org/https://doi.org/10.1016/j.cjph.2021.07.004

Lee, J., Kim, Y.-J., Lee, K., Lee, S., & Kim, S.-W. (2010). Time-of-flight measurement with femtosecond light pulses. *Nature photonics*, *4*(10), 716–720. https://doi.org/10.1038/nphoton.2010.175

Lee, J., Lee, K., Lee, S., Kim, S. W., & Kim, Y. J. (2012). High precision laser ranging by time-of-flight measurement of femtosecond pulses. *Measurement Science and Technology*, *23*, 065203. https://doi.org/10.1088/0957-0233/23/6/065203

Li, F., Yuan, Y., Fu, Y., & Chen, J. (2023). Dynamical masses of 20 asteroids determined with gaia dr3 asteroid observations. *The Astronomical Journal*, *166*, 93. https://doi.org/10.3847/1538-3881/ACE52B

Lissauer, J. J., & de Pater, I. (2013). *Fundamental planetary science – physics, chemistry and habitability* (1st ed.). Cambridge University Press.

Liu, N., Zhu, Z., Antoniadis, J., Liu, J. C., & Zhang, H. (2023). Systematics of planetary ephemeris reference frames inferred from pulsar timing astrometry. *Astronomy & Astrophysics*, *674*, A187. https://doi.org/10.1051/0004-6361/202245808

Livadiotti, S., Crisp, N. H., Roberts, P. C., Worrall, S. D., Oiko, V. T., Edmondson, S., Haigh, S. J., Huyton, C., Smith, K. L., Sinpetru, L. A., Holmes, B. E., Becedas, J., Domínguez, R. M., Cañas, V., Christensen, S., Mølgaard, A., Nielsen, J., Bisgaard, M., Chan, Y. A., … Outlaw, R. (2020). A review of gas-surface interaction models for orbital aerodynamics applications. *Progress in Aerospace Sciences*, *119*, 100675. https://doi.org/10.1016/J.PAEROSCI.2020.100675

Lowell, P. (1915). *Memoir on a trans-neptunian planet*. TP Nichols.

Luo, J., Chen, L.-S., Duan, H.-Z., Gong, Y.-G., Hu, S., Ji, J., Liu, Q., Mei, J., Milyukov, V., Sazhin, M., Shao, C.-G., Toth, V. T., Tu, H.-B., Wang, Y., Wang, Y., Yeh, H.-C., Zhan, M.-S., Zhang, Y., Zharov, V., & Zhou, Z.-B. (2016). Tianqin: A space-borne gravitational wave detector. *Classical and Quantum Gravity*, *33*(3), 035010. https://doi.org/10.1088/0264-9381/33/3/035010

Luzum, B., & Petit, G. (2012). The iers conventions (2010): Reference systems and new models. *Proceedings of the International Astronomical Union*, *10*(H16), 227–228. https://doi.org/10.1017/S1743921314005535

Lykawka, P. S., & Mukai, T. (2008). An outer planet beyond pluto and the origin of the trans-neptunian belt architecture. *The Astronomical Journal*, *135*, 1161. https://doi.org/10.1088/0004-6256/135/4/1161

Lykawka, P. S., & Ito, T. (2023). Is there an earth-like planet in the distant kuiper belt? *The Astronomical Journal*, *166*(3), 118. https://doi.org/10.3847/1538-3881/aceaf0

Mariani, V., Minazzoli, O., Gastineau, M., & Laskar, J. (2023). Bayesian test of the mass of the graviton with planetary ephemerides. *Physical Review D*, *108*. https://doi.org/10.1103/PhysRevD.108.024047

Mazarico, E. (2023a). Mission ideas. study at gsfc. *Interplanetary Trilateration Network Workshop*. http://grailteam.mit.edu/Trilateration/

Mazarico, E. (2023b). Science opportunities and possibilities with interplanetary trilateration. *Interplanetary Trilateration Network Workshop*. http://grailteam.mit.edu/Trilateration/

Mecheri, R., Abdelatif, T., Irbah, A., Provost, J., & Berthomieu, G. (2004). New values of gravitational moments j 2 and j 4 deduced from helioseismology. *Solar Physics*, *222*(2), 191–197. https://doi.org/10.1023/B:SOLA.0000043563.96766.21

Meftah, M., Hauchecorne, A., Bush, R., & Irbah, A. (2016). On hmi solar oblateness during solar cycle 24 and impact of the space environment on results. *Advances in Space Research*, *58*(7), 1425–1440. https://doi.org/https://doi.org/10.1016/j.asr.2016.06.003

Mendes, V. B., & Pavlis, E. C. (2004). High-accuracy zenith delay prediction at optical wavelengths. *Geophysical Research Letters*, *31*(14). https://doi.org/https://doi.org/10.1029/2004GL020308

Ming, M., Luo, Y., Liang, Y. R., Zhang, J. Y., Duan, H. Z., Yan, H., Jiang, Y. Z., Lu, L. F., Xiao, Q., Zhou, Z., & Yeh, H. C. (2020). Ultraprecision intersatellite laser interferometry. *International Journal of Extreme Manufacturing*, *2*, 022003. https://doi.org/10.1088/2631-7990/AB8864

Montenbruck, O., & Gill, E. (2001). *Satellite orbits: Models, methods, and applications* (2nd ed.). Springer.

Mouret, S., Hestroffer, D., & Mignard, F. (2007). Asteroid masses and improvement with gaia. *Astronomy & Astrophysics*, *472*, 1017–1027. https://doi.org/10.1051/0004-6361:20077479

Mouret, S., Hestroffer, D., & Mignard, F. (2008). Asteroid mass determination with the gaia mission: A simulation of the expected precisions. *Planetary and Space Science*, *56*, 1819–1822. https://doi.org/10.1016/J.PSS.2008.02.026

Moyer, T. D. (2005). *Formulation for observed and computed values of deep space network data types for navigation*. John Wiley & Sons.

Müller, J., Hofmann, F., Fang, X., & Biskupek, L. (2014). Lunar laser ranging: Recent results based on refined modelling, 447–451. https://doi.org/10.1007/978-3-642-37222-3_59

Murphy, T. W. (2013). Lunar laser ranging: The millimeter challenge. *Reports on Progress in Physics*, *76*(7), 076901. https://doi.org/10.1088/0034-4885/76/7/076901

Murphy, T. (2001). Statistics of photon arrival time. APOLLO Project Document. https://tmurphy.physics.ucsd.edu/apollo/doc/arrival.pdf

Murray, Z. (2023). The challenge of measuring asteroid masses with gaia dr2 astrometry. *The Planetary Science Journal*, *4*, 239. https://doi.org/10.3847/PSJ/AD0BE5

Naess, S., Aiola, S., Battaglia, N., Bond, R. J., Calabrese, E., Choi, S. K., Cothard, N. F., Halpern, M., Hill, J. C., Koopman, B. J., Devlin, M., Mcmahon, J., Dicker, S., Duivenvoorden, A. J., Dunkley, J., Fanfani, V., Ferraro, S., Gallardo, P. A., Guan, Y., … Wollack, E. J. (2021). The atacama cosmology telescope: A search for planet 9. *The Astrophysical Journal*, *923*, 224. https://doi.org/10.3847/1538-4357/ac2307

Neish, C., Nolan, M., Howell, E., & Rivkin, A. (2003). Radar Observations of Binary Asteroid 5381 Sekhmet. *American Astronomical Society Meeting Abstracts*, *203*, Article 134.02, 134.02.

Neumann, G. A., Cavanaugh, J. F., Coyle, D. B., Mcgarry, J., Smith, D. E., Sun, X., Torrence, M., Zagwodski, T. W., & Zuber, M. T. (2006). Laser ranging at interplanetary distances. *Proc. 15th International Workshop on Laser Ranging, Canberra, Australia*.

Neves, R., Cuartielles, J. P. S., Colombo, C., & Alessi, E. M. (2018). Analytical and semi-analytical approaches to the third-body perturbation in nearly co-orbital regimes [1–5 October 2018]. *69th International Astronautical Congress, 2018 (IAC '18)*.

Ni, W.-T. (2013). Astrod-gw: Overview and progress. *International Journal of Modern Physics D*, *22*(01), 1341004. https://doi.org/10.1142/S0218271813410046

Noda, H., Kunimori, H., Mizuno, T., Senshu, H., Ogawa, N., Takeuchi, H., Moore, C., Pollard, A., Yamaguchi, T., Namiki, N., Kase, T., Saiki, T., & Tsuda, Y. (2017). Laser link experiment with the hayabusa2 laser altimeter for in-flight alignment measurement. *Earth, Planets and Space*, *69*, 1–14. https://doi.org/10.1186/S40623-016-0589-8/FIGURES/9

Nordtvedt Jr, K. (1968a). Equivalence principle for massive bodies. i. phenomenology. *Physical Review*, *169*(5), 1014–1016.

Nordtvedt Jr, K. (1968b). Equivalence principle for massive bodies. ii. theory. *Physical Review*, *169*(5), 1017–1025.

Panek, P., Prochazka, I., & Kodet, J. (2010). Time measurement device with four femtosecond stability. *Metrologia*, *47*(5), L13. https://doi.org/10.1088/0026-1394/47/5/L01

Park, R. S., Folkner, W. M., Konopliv, A. S., Williams, J. G., Smith, D. E., & Zuber, M. T. (2017). Precession of mercury's perihelion from ranging to the messenger spacecraft. *The Astronomical Journal*, *153*, 121. https://doi.org/10.3847/1538-3881/AA5BE2

Park, R. S., Folkner, W. M., Williams, J. G., & Boggs, D. H. (2021). The jpl planetary and lunar ephemerides de440 and de441. *The Astronomical Journal*, *161*(3), 105. https://doi.org/10.3847/1538-3881/abd414

Paterno, L., Sofia, S., & Di Mauro, M. (1996). The rotation of the sun's core. *Astronomy & Astrophysics*, *314*, 940–946.

Peron, R. (2023). Gravitation with a solar system trilateration mission: A small collection of ideas. *Interplanetary Trilateration Network Workshop*. http://grailteam.mit.edu/Trilateration/

Petricca, F., & Genova, A. (2022). Sequential processing of inter-satellite doppler tracking for a dual-spacecraft configuration. *Remote Sensing*, *14*(21). https://doi.org/10.3390/rs14215383

Picone, J. M., Hedin, A. E., Drob, D. P., & Aikin, A. C. (2002). Nrlmsise-00 empirical model of the atmosphere: Statistical comparisons and scientific issues. *Journal of Geophysical Research: Space Physics*, *107*(A12), SIA 15-1-SIA 15–16. https://doi.org/https://doi.org/10.1029/2002JA009430

Pijpers, F. P. (1998). Helioseismic determination of the solar gravitational quadrupole moment. *Monthly Notices of the Royal Astronomical Society*, *297*(3), L76–L80. https://doi.org/10.1046/j.1365-8711.1998.01801.x

Pinto, R. F., Brun, A. S., Jouve, L., & Grappin, R. (2011). Coupling the solar dynamo and the corona: Wind properties, mass, and momentum losses during an activity cycle. *The Astrophysical Journal*, *737*, 72. https://doi.org/10.1088/0004-637X/737/2/72

Pitjeva, E. V. (2015). Determination of the Value of the Heliocentric Gravitational Constant ($GM_{\odot}$) from Modern Observations of Planets and Spacecraft. *Journal of Physical and Chemical Reference Data*, *44*(3), 031210. https://doi.org/10.1063/1.4921980

Pitjeva, E. V., & Pavlov, D. (2017). Epm2017 and epm2017h ephemerides [Available online: http://iaaras.ru/en/dept/ephemeris/epm/2017/].

Pitjeva, E. V., Pavlov, D., Aksim, D., & Kan, M. (2019). Planetary and lunar ephemeris epm2021 and its significance for solar system research. *Proceedings of the International Astronomical Union*, *15*(S364), 220–225. https://doi.org/10.1017/S1743921321001447

Pitjeva, E. V., & Pitjev, N. P. (2012). Changes in the sun's mass and gravitational constant estimated using modern observations of planets and spacecraft. *Solar System Research*, *46*, 78–87. https://doi.org/10.1134/S0038094612010054/METRICS

Pitjeva, E. V., & Pitjev, N. P. (2013). Relativistic effects and dark matter in the solar system from observations of planets and spacecraft. *MNRAS*, *432*, 3431–3437. https://doi.org/10.1093/mnras/stt695

Pitjeva, E. V., & Pitjev, N. P. (2014). Development of planetary ephemerides epm and their applications. *Celestial Mechanics and Dynamical Astronomy*, *119*, 237–256. https://doi.org/10.1007/S10569-014-9569-0/TABLES/11

Pitjeva, E. V., & Pitjev, N. P. (2018). Masses of the main asteroid belt and the kuiper belt from the motions of planets and spacecraft. *Astronomy Letters*, *44*, 604–617. https://doi.org/10.1134/S1063773718090050

Pitjeva, E. V., Pitjev, N. P., Pavlov, D. A., & Turygin, C. C. (2021). Estimates of the change rate of solar mass and gravitational constant based on the dynamics of the solar system. *Astronomy & Astrophysics*, *647*, A141. https://doi.org/10.1051/0004-6361/202039893

Poor, C. L. (1905). The figure of the sun. ii. *Astrophysical Journal*, *22*, 305–317. https://doi.org/10.1086/141285

Pravec, P., Scheirich, P., Kušnirák, P., Šarounová, L., Mottola, S., Hahn, G., Brown, P., Esquerdo, G., Kaiser, N., Krzeminski, Z., Pray, D., Warner, B., Harris, A., Nolan, M., Howell, E., Benner, L., Margot, J.-L., Galád, A., Holliday, W., … Kober, G. (2006). Photometric survey of binary near-earth asteroids. *Icarus*, *181*(1), 63–93. https://doi.org/https://doi.org/10.1016/j.icarus.2005.10.014

Prieto, D. M., Graziano, B. P., & Roberts, P. C. (2014). Spacecraft drag modelling. *Progress in Aerospace Sciences*, *64*, 56–65. https://doi.org/10.1016/J.PAEROSCI.2013.09.001

Reinhardt, J. N., Staab, M., Yamamoto, K., Bayle, J.-B., Hees, A., Hartwig, O., Wiesner, K., Shah, S., & Heinzel, G. (2024). Ranging sensor fusion in lisa data processing: Treatment of ambiguities, noise, and onboard delays in lisa ranging observables. *Phys. Rev. D*, *109*, 022004. https://doi.org/10.1103/PhysRevD.109.022004

Rivkin, A., Daly, T., Atchison, J., Barbee, B., Abell, P., Stickle, A., Sotirelis, T. S., King, P. K., Richardson, D., Greenhagen, B., et al. (2021). The case for a planetary defense-optimized neo characterization tour. *Bulletin of the American Astronomical Society*, *53*(4), 336.

Rozelot, J. P., & Damiani, C. (2011). History of solar oblateness measurements and interpretation. *The European Physical Journal H 2011 36:3*, *36*, 407–436. https://doi.org/10.1140/EPJH/E2011-20017-4

Rozelot, J. P., Damiani, C., & Pireaux, S. (2009). Probing the solar surface: The oblateness and astrophysical consequences. *The Astrophysical Journal*, *703*(2), 1791. https://doi.org/10.1088/0004-637X/703/2/1791

Rozelot, J. P., & Fazel, Z. (2014). Revisiting the solar oblateness: Is relevant astrophysics possible? In N. N. Mansour, A. G. Kosovichev, R. Komm, & D. Longcope (Eds.), *Solar dynamics and magnetism from the interior to the atmosphere* (pp. 161–170). Springer New York. https://doi.org/10.1007/978-1-4899-8005-2_10

Sackmann, I., et al. (1993). Our sun. iii. present and future. *Astrophysical Journal v. 418, p. 457*, *418*, 457.

Sagnac, G. (1913). Regarding the proof for the existence of a luminiferous ether using a rotating interferometer experiment. *Comptes Rendus de l'Academie des Sciences*, *157*, 1410–1413.

Sakurai, T., Hotta, H., & Imada, S. (2023). Eleven-year cycle of solar magnetic activity: Observations, theories, and numerical model predictions. In K. Kusano (Ed.), *Solar-terrestrial environmental prediction* (pp. 379–401). Springer Nature Singapore. https://doi.org/10.1007/978-981-19-7765-7_12

Scheirich, P., & Pravec, P. (2009). Modeling of lightcurves of binary asteroids. *Icarus*, *200*(2), 531–547. https://doi.org/https://doi.org/10.1016/j.icarus.2008.12.001

Scholtz, J., & Unwin, J. (2020). What if planet 9 is a primordial black hole? *Phys. Rev. Lett.*, *125*, 051103. https://doi.org/10.1103/PhysRevLett.125.051103

Schreiber, K. U., Kodet, J., Rodrigo, R., Dehant, V., Gurvits, L., Kramer, M., Park, R., Wolf, P., Zarnecki, J., & Schreiber, B. K. U. (2018). The application of coherent local time for optical time transfer and the quantification of systematic errors in satellite laser ranging high performance clocks with special emphasis on geodesy and geophysics and applications to other bodies of the solar system edited. *Space Sci Rev*, *214*, 22. https://doi.org/10.1007/s11214-017-0457-2

Selvan, K., Siemuri, A., Prol, F. S., Välisuo, P., Bhuiyan, M. Z. H., & Kuusniemi, H. (2023). Precise orbit determination of leo satellites: A systematic review. *GPS Solutions*, *27*(4), 178. https://doi.org/10.1007/s10291-023-01520-7

Shankman, C., Kavelaars, J. J., Bannister, M. T., Gladman, B. J., Lawler, S. M., Chen, Y.-T., Jakubik, M., Kaib, N., Alexandersen, M., Gwyn, S. D. J., Petit, J.-M., & Volk, K. (2017). Ossos. vi. striking biases in the detection of large semimajor axis trans-neptunian objects. *The Astronomical Journal*, *154*(2), 50. https://doi.org/10.3847/1538-3881/aa7aed

Shapiro, I. I. (1964). Fourth test of general relativity. *Phys. Rev. Lett.*, *13*, 789–791. https://doi.org/10.1103/PhysRevLett.13.789

Sheard, B. S., Heinzel, G., Danzmann, K., Shaddock, D. A., Klipstein, W. M., & Folkner, W. M. (2012). Intersatellite laser ranging instrument for the grace follow-on mission. *Journal of Geodesy*, *86*, 1083–1095. https://doi.org/10.1007/S00190-012-0566-3/METRICS

Shi, X., Castillo-Rogez, J., Hsieh, H., Hui, H., Ip, W.-H., Lei, H., Li, J.-Y., Tosi, F., Zhou, L., Agarwal, J., et al. (2022). Gauss-genesis of asteroids and evolution of the solar system: A sample return mission to ceres. *Experimental Astronomy*, 1–32. https://doi.org/10.1007/s10686-021-09800-1

Siemes, C. (2023). Assignment 3 instructions. dynamic orbit estimation [Lecture notes in Satellite Orbit Determination. Delft University of Technology].

Siraj, A. (2023). Are there terrestrial planets lurking in the outer solar system? *The Astrophysical Journal Letters*, *959*(2), L17. https://doi.org/10.3847/2041-8213/ad13eb

Siraj, A., & Loeb, A. (2020). Searching for black holes in the outer solar system with lsst. *The Astrophysical Journal Letters*, *898*(1), L4. https://doi.org/10.3847/2041-8213/aba119

Sjogren, W. L., & Wollenhaupt, W. R. (1973). Lunar shape via the apollo laser altimeter. *Science*, *179*(4070), 275–278. https://doi.org/10.1126/science.179.4070.275

Smith, D. E., Zuber, M. T., Mazarico, E., Genova, A., Neumann, G. A., Sun, X., Torrence, M. H., & dan Mao, D. (2018). Trilogy, a planetary geodesy mission concept for measuring the expansion of the solar system. *Planetary and Space Science*, *153*, 127–133. https://doi.org/10.1016/J.PSS.2018.02.003

Smith, D. E., Zuber, M. T., Sun, X., Neumann, G. A., Cavanaugh, J. F., McGarry, J. F., & Zagwodzki, T. W. (2006). Two-way laser link over interplanetary distance. *Science*, *311*, 53. https://doi.org/10.1126/SCIENCE.1120091/SUPPL_FILE/SMITH.SOM.PDF

Somenzi, L., Fienga, A., Laskar, J., & Kuchynka, P. (2010). Determination of asteroid masses from their close encounters with mars. *Planetary and Space Science*, *58*, 858–863. https://doi.org/10.1016/J.PSS.2010.01.010

Standish, E. M., & Hellings, R. W. (1989). A determination of the masses of ceres, pallas, and vesta from their perturbations upon the orbit of mars. *Icarus*, *80*, 326–333. https://doi.org/10.1016/0019-1035(89)90143-7

Standish, E. M. (1993). Planet x-no dynamical evidence in the optical observations. *Astronomical Journal*, *105*, 2000–2006.

Svehla, D. (2018). Model of solar radiation pressure and thermal re-radiation. In *Geometrical theory of satellite orbits and gravity field* (pp. 269–295). Springer International Publishing. https://doi.org/10.1007/978-3-319-76873-1_19

Tapley, B. D., Schutz, B. E., & Born, G. H. (2004). *Statistical orbit determination*. Elsevier Academic Press.

Thorpe, J. I. (2010). Lisa long-arm interferometry. *Classical and Quantum Gravity*, *27*(8), 084008. https://doi.org/10.1088/0264-9381/27/8/084008

Tiesinga, E., Mohr, P. J., Newell, D. B., & Taylor, B. N. (2021). Codata recommended values of the fundamental physical constants: 2018. *Rev. Mod. Phys.*, *93*, 025010. https://doi.org/10.1103/RevModPhys.93.025010

Touboul, P., Métris, G., Rodrigues, M., Bergé, J., Robert, A., Baghi, Q., André, Y., Bedouet, J., Boulanger, D., Bremer, S., Carle, P., Chhun, R., Christophe, B., Cipolla, V., Damour, T., Danto, P., Demange, L., Dittus, H., Dhuicque, O., … Visser, P. (2022). Result of the microscope weak equivalence principle test. *Classical and Quantum Gravity*, *39*(20), 204009. https://doi.org/10.1088/1361-6382/ac84be

Turyshev, S. G., Chiow, S.-w., & Yu, N. (2024). Searching for new physics in the solar system with tetrahedral spacecraft formations. *Phys. Rev. D*, *109*, 084059. https://doi.org/10.1103/PhysRevD.109.084059

Turyshev, S. G., Williams, J. G., Folkner, W. M., Gutt, G. M., Baran, R. T., Hein, R. C., Somawardhana, R. P., Lipa, J. A., & Wang, S. (2013). Corner-cube retro-reflector instrument for advanced lunar laser ranging. *36*, 105–135. https://doi.org/10.1007/s10686-012-9324-z

U.s. standard atmosphere (Technical Memorandum No. NOAA-S/T-76-1562, NASA-TM-X-74335). (1976). National Oceanic and Atmospheric Administration. https://ntrs.nasa.gov/citations/19770009539

Vallado, D. A. (2013). *Fundamentals of astrodynamics and applications* (4th ed.). Microcosm Press; Springer.

van der Zwaard, R., & Dirkx, D. (2022). The influence of dynamic solar oblateness on tracking data analysis from past and future mercury missions. *Remote Sensing*, *14*(17). https://doi.org/10.3390/rs14174139

Verma, A. K., Fienga, A., Laskar, J., Manche, H., & Gastineau, M. (2014). Use of messenger radioscience data to improve planetary ephemeris and to test general relativity. *Astronomy & Astrophysics*, *561*, A115. https://doi.org/10.1051/0004-6361/201322124

Viswanathan, V., Fienga, A., Minazzoli, O., Bernus, L., Laskar, J., & Gastineau, M. (2018). The new lunar ephemeris INPOP17a and its application to fundamental physics. *Monthly Notices of the Royal Astronomical Society*, *476*(2), 1877–1888. https://doi.org/10.1093/mnras/sty096

Vittaldev, V., Mooij, E., & Naeije, M. C. (2012). Unified state model theory and application in astrodynamics. *Celestial Mechanics and Dynamical Astronomy*, *112*, 253–282. https://doi.org/10.1007/S10569-011-9396-5/METRICS

Wakker, K. F. (2015). *Fundamentals of astrodynamics*. TU Delft Repository, Delft.

Walker, M. J. (1986). A set of modified equinoctial orbit elements. *Celestial Mechanics*, *38*, 391–392. https://doi.org/10.1007/BF01238929/METRICS

Walker, M. J., Ireland, B., & Owens, J. (1985). A set modified equinoctial orbit elements. *Celestial Mechanics*, *36*, 409–419. https://doi.org/10.1007/BF01227493/METRICS

Wenxiao, L., Jinsong, P., & Wenzhao, Z. (2021). Comparison and analysis of three kinds of typical solar system planetary ephemeris. *Journal of University of Chinese Academy of Sciences*, *38*(1), Article 114, 114–120. https://doi.org/http://journal.ucas.ac.cn/EN/10.7523/j.issn.2095-6134.2021.01.014

Wilkinson, M., Schreiber, U., Procházka, I., Moore, C., Degnan, J., Kirchner, G., Zhongping, Z., Dunn, P., Shargorodskiy, V., Sadovnikov, M., Courde, C., & Kunimori, H. (2019). The next generation of satellite laser ranging systems. *Journal of Geodesy*, *93*, 2227–2247. https://doi.org/10.1007/s00190-018-1196-1

Will, C. M. (2014). The confrontation between general relativity and experiment. *Living Reviews in Relativity 2014 17:1*, *17*, 1–117. https://doi.org/10.12942/LRR-2014-4

Will, C. M. (2018a). *Theory and experiment in gravitational physics* (1st ed.). Cambridge university press. https://doi.org/10.1017/9781316338612

Will, C. M. (2018b). Solar system versus gravitational-wave bounds on the graviton mass. *Classical and Quantum Gravity*, *35*(17), 17LT01. https://doi.org/10.1088/1361-6382/aad13c

Williams, J. G. (1984). Determining asteroid masses from perturbations on mars. *Icarus*, *57*, 1–13. https://doi.org/10.1016/0019-1035(84)90002-2

Wilson, K., & Lesh, J. (1993). An overview of the galileo optical experiment (gopex). *The Telecommunications and Data Acquisition Report*. https://ntrs.nasa.gov/citations/19940009913

Xu, Y., Shen, Y., Xu, G., Shan, X., & Rozelot, J.-P. (2017). Perihelion precession caused by solar oblateness variation in equatorial and ecliptic coordinate systems. *MNRAS*, *472*, 2686–2693. https://doi.org/10.1093/mnras/stx2122

Yan, J., Yang, X., Ye, M., Li, F., Jin, W., & Barriot, J.-P. (2017). Independent mars spacecraft precise orbit determination software development and its applications. *Astrophysics and Space Science*, *362*(7), 123. https://doi.org/10.1007/s10509-017-3105-0

Ye, J. (2004). Absolute measurement of a long, arbitrary distance to less than an optical fringe. *Opt. Lett.*, *29*(10), 1153–1155. https://doi.org/10.1364/OL.29.001153

Zajdel, R., Sośnica, K., & Bury, G. (2017). A new online service for the validation of multi-gnss orbits using slr. *Remote Sensing*, *9*(10). https://doi.org/10.3390/rs9101049

Zenk, K., Dirkx, D., & Fayolle, M. (2023). *Constraining the ephemeris and interior structure of io using space-based astrometry by juice* [Master's Thesis]. Delft University of Technology [Available at TU Delft repository]. https://repository.tudelft.nl/record/uuid:a583e92a-cfb6-4249-8875-94acc52e7260

Zhou, H., Chen, Y., Hyyppä, J., & Li, S. (2017). An overview of the laser ranging method of space laser altimeter. *Infrared Physics & Technology*, *86*, 147–158. https://doi.org/https://doi.org/10.1016/j.infrared.2017.09.011

Zhu, W. W., Desvignes, G., Wex, N., Caballero, R. N., Champion, D. J., Demorest, P. B., Ellis, J. A., Janssen, G. H., Kramer, M., Krieger, A., Lentati, L., Nice, D. J., Ransom, S. M., Stairs, I. H., Stappers, B. W., Verbiest, J. P. W., Arzoumanian, Z., Bassa, C. G., Burgay, M., … Tiburzi, C. (2018). Tests of gravitational symmetries with pulsar binary J1713+0747. *Monthly Notices of the Royal Astronomical Society*, *482*(3), 3249–3260. https://doi.org/10.1093/mnras/sty2905

Zhu, W., Stairs, I., Demorest, P., Nice, D. J., Ellis, J., Ransom, S., Arzoumanian, Z., Crowter, K., Dolch, T., Ferdman, R., et al. (2015). Testing theories of gravitation using 21-year timing of pulsar binary j1713+ 0747. *The Astrophysical Journal*, *809*(1), 41.

Zhu, X., Liu, L., Liu, S., Xie, P., Gao, W., & Yan, J. (2021). Precise orbit determination of mex flyby phobos using simulated radiometric and image data. *Sensors*, *21*(2). https://doi.org/10.3390/s21020385

Zuber, M. T., Smith, D. E., Mazarico, E., Lunine, J. I., Neumann, G. A., Lemoine, F. G., Genova, A., Goossens, S. J., & Sun, X. (2017). From copernicus to newton to einstein: Toward a dynamical understanding of the solar system. *Planetary Science Vision 2050 Workshop*, *1989*, 8074. https://www.lpi.usra.edu/V2050/presentations/Tuesday/1_8074_Zuber.pdf